Universitat Politècnica de València
Departamento de Máquinas y Motores Térmicos

Doctoral Thesis

Computational and experimental study of the primary atomisation process under different injection conditions

Presented by:
Mr. Lucas Antonio González Montero

Supervised by:
Dr. Francisco Javier Salvador Rubio

in fulfillment of the requirements for the degree of
Doctor of Philosophy

Valencia, September 2022

Ph.D. Thesis

Computational and experimental study of the primary atomisation process under different injection conditions

Written by: Mr. Lucas Antonio González Montero
Supervised by: Dr. Francisco Javier Salvador Rubio

Thesis committee:

Chairman: Prof. Raúl Payri Marín
Secretary: Dr. Daniel Mira Martínez
Member: Prof. François-Xavier Demoulin

Reviewing board:

Prof. Michele Battistoni
Prof. François-Xavier Demoulin
Dr. Oriol Lehmkuhl Barba

Valencia, September 2022

Abstract

The primary atomisation process is the mechanism by which a liquid vein breaks into droplets in a gaseous ambient. This process is present in many engineering applications accomplishing different tasks. Sometimes it is a previous step before being burned, as in the energy or propulsion industry, where the objective is to extract the specific energy of the liquid. In other sectors, such as the coating or fire extinction, the objective is to maximise the area covered by the droplet cloud. However, although atomisation is a fundamental part of several industrial processes, it is far from fully understood. The atomisation process is a mixture of gas-liquid interaction phenomena within a turbulent field that takes place in the near-field, which is the denser region of the spray.

When trying to shed light on the primary atomisation process, the main issue is the lack of definitive physical theories able to link the complex breakup events and the turbulence. The principal impediment that prevents the investigation from breaking through the atomisation process is the inability of the classic optical techniques to provide information from the dense region of the spray. Only in the last years, newer techniques based on X-Ray could provide new information on spray characteristics near the nozzle outlet. This also affects the computational primary atomisation models that, as there is no available experimental information on the dense region, require an accurate calibration of their constants to provide reliable results on the far-field.

This thesis focuses on improving the knowledge of the primary atomisation process, especially on how the injection conditions affect the spray development in the near field from two different standpoints. On the one hand, with a computational approach using Direct Numerical Simulations and on the other hand, experimentally using Near-Field Microscopy.

The computational study is focused on varying the inflow Reynolds and Weber numbers. Results show that increasing the Reynolds number improves the liquid disintegration, exhibiting an increase of generated droplets and a finer droplet cloud. However, the lack of a fully developed inflow turbulent profile leads to characteristic behaviours on the breakup length of the spray that also increases with the Reynolds number. The number of droplets increases when the Weber number increases, but the characteristic droplet sizes remain the same. The breakup length does not vary, suggesting that the surface tension variations affect the droplet and ligament breakup but not the core disintegration itself. With the results obtained from both studies, a phenomenological model is proposed to predict the droplet size distribution depending on the injection conditions.

Additionally, using elliptical nozzles, the number of detected droplets increases compared with the round spray and maintain similar spray apertures. However, when using extremely eccentric nozzles, the inflow turbulence decrease counteracts the elliptical sprays' benefits.

Regarding the experimental analysis, the Near-Field Microscopy magnifies the dense region and analyses the macroscopic features on the spray. So the injection and discharge pressure are varied, and the spotlight is put on the spray angle. The expected increase in the spray angle when increasing both the injection and discharge pressure is observed. Nevertheless, additionally, an analysis of the spray contour perturbations is performed, concluding that increasing the injection pressure, and thus the inflow turbulence, increases the perturbations on the spray contour, especially at lower discharge pressures.

Resumen

El proceso de atomización primaria es el mecanismo por el cual una vena líquida se disgrega en un ambiente gaseoso. Este proceso está presente en muchas aplicaciones de ingeniería realizando diferentes tareas. En ocasiones es un paso previo antes de ser quemado, como en la industria energética o de propulsión, donde el objetivo es extraer la energía específica del líquido. En otros sectores, como el revestimiento o la extinción de incendios, el objetivo es maximizar el área cubierta por el chorro. Sin embargo, aunque la atomización es una parte fundamental de varios procesos industriales, está lejos de comprenderse por completo. El proceso de atomización es una mezcla de fenómenos de interacción gas-líquido dentro de un campo turbulento que tiene lugar en el campo cercano, que es la región más densa del chorro.

Cuando se trata de arrojar luz sobre el proceso de atomización primaria, el problema principal es la falta de teorías físicas definitivas capaces de vincular los complejos eventos de ruptura con la turbulencia. El principal obstáculo que impide investigar el proceso de atomización primaria es la incapacidad de las técnicas ópticas clásicas para proporcionar información de la región densa del chorro. Solo en los últimos años, las nuevas técnicas basadas en rayos X podrían proporcionar nueva información sobre las características de la atomización cerca de la salida de la tobera. Esto también afecta a los modelos computacionales de atomización primaria que, al no disponer de información experimental sobre la región densa, requieren una calibración precisa de sus constantes para proporcionar resultados fiables en el campo lejano.

Esta tesis se centra en mejorar el conocimiento del proceso de atomización primaria, especialmente en cómo las condiciones de inyección afectan el desarrollo del chorro en el campo cercano desde dos puntos de vista diferentes. Por un lado, con un enfoque computacional usando Direct Numerical Simulations y, por otro lado, experimentalmente usando Near-Field Microscopy.

El estudio computacional se centra en variar los números de Reynolds y Weber de inyección. Los resultados muestran que aumentar el número de Reynolds mejora la desintegración del líquido, mostrando un aumento de las gotas generadas y una nube de gotas más fina. Sin embargo, la falta de un perfil turbulento de flujo de entrada completamente desarrollado conduce a comportamientos inesperados en la longitud de ruptura de la vena líquida que también aumenta con el número de Reynolds. El número de gotas también aumenta cuando aumenta el número de Weber, pero los tamaños característicos de las gotas siguen siendo los mismos. La longitud de ruptura no varía, lo que sugiere que las variaciones de la tensión superficial afectan la ruptura de las gotas y los ligamentos, pero no la desintegración del núcleo líquido en

sí. Con los resultados obtenidos de ambos estudios, se propone un modelo fenomenológico que predice la distribución del tamaño de gota en función de las condiciones de inyección.

Además, también se ha estudiado el efecto de usar toberas elípticas. Se ha obtenido que el número de gotas detectadas aumenta en comparación con el chorro redondo manteniendo ángulos de apertura del chorro similares. Sin embargo, cuando se utilizan toberas extremadamente excéntricas, la disminución de la turbulencia del flujo de entrada contrarresta los beneficios de este tipo de inyectores.

En cuanto al análisis experimental, usar Near-Field Microscopy permite magnificar la región densa y analizar las características macroscópicas del chorro. Por lo tanto, se varían las presiones de inyección y descarga, centrándose en el ángulo de apertura del chorro. Se observa el aumento esperado en el ángulo al aumentar tanto la presión de inyección como la de descarga. Sin embargo, adicionalmente, se realiza un análisis de las perturbaciones del contorno del chorro, concluyendo que al aumentar la presión de inyección, y por lo tanto la turbulencia del flujo de entrada, aumentan las perturbaciones en el contorno del rociado, especialmente a presiones de descarga más bajas.

Resum

El procés d'atomització primària és el mecanisme pel qual una vena líquida es disgrega en un ambient gasós. Aquest procés és present en moltes aplicacions d'enginyeria fent diferents tasques. De vegades és un pas previ abans de ser cremat, com ara en la indústria energètica o de propulsió, on l'objectiu és extraure l'energia específica del líquid. En altres sectors, com ara el revestiment o l'extinció d'incendis, l'objectiu és maximitzar l'àrea coberta pel doll. No obstant això, tot i que l'atomització és una part fonamental de diversos processos industrials, està lluny de comprendre's per complet. El procés d'atomització és una barreja de fenòmens d'interacció gas-líquid dins d'un camp turbulent que té lloc en el camp pròxim, que és la regió més densa del doll.

Quan es tracta de donar llum sobre el procés d'atomització primària, el problema principal és la falta de teories físiques definitives capaces de vincular els complexos esdeveniments de trencament amb la turbulència. El principal obstacle que impedeix investigar el procés d'atomització primària és la incapacitat de les tècniques òptiques clàssiques per a proporcionar informació de la regió densa del doll. Només en els últims anys, les noves tècniques basades en raigs X podrien proporcionar nova informació sobre les característiques de l'atomització prop de l'eixida de la tovera. Això també afecta els models computacionals d'atomització primària que, en no disposar d'informació experimental sobre la regió densa, requereixen un calibratge precís de les seues constants per a proporcionar resultats fiables en el camp llunyà.

Aquesta tesi se centra a millorar el coneixement del procés d'atomització primària, especialment en com les condicions d'injecció afecten el desenvolupament del doll en el camp pròxim des de dos punts de vista diferents. D'una banda, amb un enfocament computacional usant Direct Numerical Simulations i, d'altra banda, experimentalment usant Near-Field Microscopy.

L'estudi computacional se centra a variar els nombres de Reynolds i Weber d'injecció. Els resultats mostren que augmentar el nombre de Reynolds millora la desintegració del líquid, tot mostrant un augment de les gotes generades i un núvol de gotes més fi. No obstant això, la falta d'un perfil turbulent de flux d'entrada completament desenvolupat condueix a comportaments inesperats en la longitud de ruptura de la vena líquida que també augmenta amb el nombre de Reynolds. El nombre de gotes també augmenta quan creix el nombre de Weber, però les grandàries característiques de les gotes continuen sent les mateixes. La longitud de ruptura no varia, la qual cosa suggereix que les variacions de la tensió superficial afecten la ruptura de les gotes i els lligaments, però no la desintegració del nucli líquid en ell mateix. Amb els

resultats obtinguts de tots dos estudis, es proposa un model fenomenològic que prediu la distribució de la grandària de gota en funció de les condicions d'injecció.

A més, també s'ha estudiat l'efecte d'usar toveres el·líptiques. S'ha obtingut que el nombre de gotes detectades augmenta en comparació amb el doll redó tot mantenint angles d'obertura del doll similars. No obstant això, quan s'utilitzen toveres extremadament excèntriques, la disminució de la turbulència del flux d'entrada contraresta els beneficis d'aquesta mena d'injectors.

Quant a l'anàlisi experimental, usar Near-Field Microscopy permet magnificar la regió densa i analitzar les característiques macroscòpiques del doll. Per tant, es varien les pressions d'injecció i descàrrega, tot centrant-se en l'angle d'obertura del doll. S'observa l'augment esperat en l'angle en augmentar tant la pressió d'injecció com la de descàrrega. No obstant això, addicionalment, es realitza una anàlisi de les pertorbacions del contorn del doll i es conclou que en augmentar la pressió d'injecció, i per tant la turbulència del flux d'entrada, augmenten les pertorbacions en el contorn del ruixat, especialment a pressions de descàrrega més baixes.

"Life before death. Strength before weakness. Journey before destination"
First ideal of the Knights Radiant

A mi familia

No quiero dejar pasar la oportunidad de agradecer a todas aquellas personas que, de una u otra manera, han formado parte del proceso de realización de este trabajo. En primer lugar, quiero agradecer al instituto CMT por darme la oportunidad de llevar a cabo esta tesis. Desde el director Jose María Desantes, hasta todos los miembros que permiten que el departamento funcione, como Amparo, siempre atenta a todos los trámites burocráticos.

Quiero acordarme de mi tutor y director, Javi Salvador. Su guía ha sido clave para poder encauzar con éxito este trabajo. Nuestras conversaciones analizando datos y tendencias han sido fundamentales para dar sentido a las diferentes partes del proyecto. Siempre dando una visión más profunda de los resultados y proponiendo nuevos enfoques donde aplicar las metodologías de estudio.

Mención especial al grupo de inyección, desde que llegué tanto profesores como doctorandos hicieron un inmejorable ambiente de trabajo. A los profesores Marcos, Pedro, Joaquín, Gabriela y Jaime, con Raúl a la cabeza, a quienes he tenido que recurrir en bastantes ocasiones con dudas de todo tipo y siempre me ayudaron en todo lo que pudieron. Gracias a Jose Enrique y Omar, los técnicos que hicieron posible todas y cada uno de los ensayos experimentales realizados durante la tesis.

También a los doctorandos del grupo de inyección que han coincidido conmigo estos años: Mary, María, Jesús, Kike, Javi, Víctor, Rami, Tomás, Alberto, César, Santiago, Vincenzo, Armando y Borja. Que decir de los compañeros de despacho, Marco fue fundamental durante los dos primeros años de la tesis. Me dio todas las herramientas que el desarrolló durante 4 años para poder entender y realizar tanto las simulaciones como sus análisis. Por otro lado, está Mario, contigo no faltaban las risas en el despacho, ni las largas charlas tan necesarias en algunos momentos. A Carlos le he visto crecer como investigador, primero como alumno TFM de Mario y luego uniéndose al loco grupo del DNS. Y bueno, Alejandro, el último en llegar, solo puedo darte ánimos y que te sirva de algo lo que te he enseñado.

Mención especial a Pau, Alberto y Nico, con los que he compartido los 11 años de estudio y han sido imprescindibles para sobrellevar todas y cada una de las etapas. No me olvido de Fabio, Juancho y Miguel ángel, sus compañeros de despacho y, por extensión casi también los míos.

No puedo obviar a mucha gente que, aunque no forme parte del mundo de la investigación, me ha aguantado durante estos 5 años y que, de manera indirecta, han sido partícipes de este trabajo.

A mis padres y mi hermano, por estar ahí en todo momento. A Pedro y a

Víctor por su amistad desde hace ya casi 20 años. A Sara, Alba Carlos y Yorx que me han permitido desconectar y recargar las pilas cuando lo necesitaba. Y para concluir quiero tener unas palabras especiales para Irene. Gracias por estar a mi lado todos estos años. Gracias por aguantarme cuando las cosas salían bien y no paraba de hablar del trabajo. Y cuando las cosas salían mal, que tampoco paraba de hablar del trabajo, aunque más enfadado. Gracias por escucharme pacientemente, aunque no tenías ni la menor idea de lo que hablaba. Sin vosotros esta tesis no habría sido posible.

Contents

List of Figures

List of Tables

Nomenclature

Acronyms

AMR	Adaptive Mesh Refinement.
ANL	Argonne National Lab.
APS	Advanced Photon Source.
CFD	Computational Fluid Dynamics.
CFL	Courant-Friedrichs-Lewy number.
CIAM	Calcul d'Interface Affine par Morceaux.
CR	Computational Requirements.
DBI	Diffused Backlight Illumination.
DNS	Direct Numerical Simulation.
DPM	Discrete Particle Model.
ECN	Engine Combustion Network.
ELSA	Eulerian Lagrangian Spray Atomization.
FT	Front Tracking.
HF	Height Function.
HPC	High Performance Computing.
KL	Optical thickness.
LED	Light Emitting Diode.
LES	Large Eddy Simulation.
LS	Level-Set.
MBC	Mapped Boundary Condition.
NFM	Near-Field Microscopy.

PARIS	PArallel Robust Interface Simulator.
PCI	Phase Contrast Imaging.
PDF	Probability Density Function.
PISO	Pressure Implicit with Splitting of Operators.
PIV	Particle Image Velocimetry.
PLIC	Piecewise Linear Interface Calculation.
RANS	Reynolds-Averaged Navier-Stokes.
SBC	Synthetic Boundary Condition.
SGS	Sub-Grid Scales.
SLIPI	Structured Laser Illumination Planar Imaging.
SMD	Sauter Mean Diameter.
SR	Storage Requirements.
SSE	Sum Squared Error.
VOF	Volume of Fluid.
VTK	Visual Tool-Kit.
WALE	Wall-Adapting Local Eddy-viscosity.

Greek symbols

Δ	Width of the LES filter.
δ	Dirac Function.
ϵ	Turbulent dissipation rate.
η	Kolmogorov scale.
$\hat{\mu}$	Mean of $\ln(d_v)$.
$\hat{\sigma}$	Standard deviation of $\ln(d_v)$.
κ	Surface curvature.
λ_2	Lambda 2 criterion variable.
μ	Dynamic Viscosity.
ν	Kinematic viscosity.
ν_t	Turbulent Viscosity.
Ω	Antisymmetric rate-of-rotation tensor.
ω^+_{wall}	Cell size in azimuthal direction on the wall, in wall units.
ρ	Density.
σ	Surface tension.
τ_ω	Wall shear stress
θ	Azimuthal direction.

ξ	Dimensionless distance from the wall.
ξ^+	Dimensionless distance from the wall in wall units.

Latin symbols

A	Advection term.
a	Ellipse major axis.
b	Ellipse minor axis.
C	VOF color function.
C_w	WALE model constant.
D	Diffusion term.
D_{32}	Sauter mean diameter.
D_h	Hydraulic diameter.
D_n	Pipe/Nozzle diameter.
d_v	Volumetric diameter.
e	Eccentricity factor.
F	Forces source term.
f	Friction factor.
IQ_k	Index of quality based on the resolved turbulent kinetic energy in LES.
k_{mod}	Modelled Turbulent kinetic energy in LES.
k_{res}	Resolved Turbulent kinetic energy in LES.
L	Pipe length.
N_{cell}	Number of cells.
N_{drops}	Number of droplets detected.
N_s	Number of vortex structures.
Oh	Ohnesorge number.
p	Pressure.
P_{back}	Discharge pressure of the atomiser.
$\bar{p}$	LES modified kinetic pressure.
P_{inj}	Injection pressure of the atomiser.
r	Radial position.
$r_{0.01}$	Radial distance where the value is the 1% of the centreline value.
$r_{1/2}$	Radial distance where the value is the half of the centreline value.
R^2	Coefficient of determination.
Re_D	Reynolds number.

Re_τ	Kármán number.
R_n	Pipe/nozzle radius.
S	Symmetric strain rate tensor.
s_{ij}	Strain tensor of the fluctuating velocity.
$\bar{S_{ij}}$	LES resolved strain rate tensor.
U_b	Bulk velocity.
U_c	Averaged centreline axial velocity.
u_d	Droplet axial velocity.
$\bar{u_i}$	LES resolved velocity vector.
u_r	Radial velocity.
u_{tau}	Friction velocity.
u_x	Axial velocity.
u_x^+	Axial velocity in wall units.
We_D	Weber number.
x_b	Breakup length.
x_i	External non-perturbed length.
y^+	Dimensionless distance to the wall.

Subscripts

θ	Azimuthal component.
C	Liquid Volume Fraction.
c	Centreline statistics.
g	Gas phase.
l	Liquid phase.
m_c	Mass concentration.
x	Axial component.
y	Transversal component.
z	Transversal component.

Chapter 1

Introduction

1.1 General context

The atomization process is understood as the conversion of a liquid bulk into small liquid particles in a gaseous ambient. This phenomenon has been widely studied in the past, as is present in almost all engineering and industrial applications. One of the most spread research lines of the atomization process is the combustion, present in engines and energy generation, that have pushed the requirements of the design of the atomizers to the most critical operating conditions. In these fields, the main objective of the spray formation is to generate heat by its combustion, so the droplet distribution and sizes are essential to predict the combustion conditions and, thus, the efficiency and the pollutants generated in different atomizers.

However, there are many applications that are not related to any combustion process. In a society increasingly aware of pollutant emissions, electrification is becoming essential to the industry. This electrification requires developing more efficient batteries and miniaturizing electronic components for typical applications such as particular transportation, satellite electronics, or computer electronics. Thermal management starts becoming an issue when using bigger batteries as thermal runaway appears. To avoid this phenomenon and increase the life of the batteries, approaches like spray cooling [1–3] have emerged. This technique consists of spraying refrigerant liquid in specific regions to cool down the most sensible components before reaching thermal critical conditions.

Furthermore, spraying liquid on a solid is also used in different applications applications such as the surface coating. In this context, the spray paint industry has been involved in many other atomizer developments [4]. Here, the characteristic sizes of these atomizers are bigger to cover the maximum area to paint. Also, this kind of spray uses the electromagnetic field by polarizing the liquid and the target surface to make them attractive, decreasing the amount of paint that misses the objective and, therefore, wasted.

Another application is the pharmacology industry. Here the sprays are studied to optimize the drug-delivery devices [5, 6], such as the pressured Metered Dose Inhalers [7], the Dry Powder Inhaler [8], or the spacers [9]. These researches are carried out both experimentally and numerically and focus on the proper dose delivery, avoiding the drug deposit within the mouth or the throat, which decreases the amount of drug delivered to the lungs.

Also, when taking into account the thermal balance, some spray applications are based on the solidification of the injected liquid to produce a powder cloud. This kind of process is present in the pharmaceutical applications, with the spray-drying systems [10] or in the metallurgic industry [11], where the molten liquid metal is atomized assisted with supersonic gas, which breaks up the liquid vein and cools down the metal droplets until the spray becomes metal dust.

Outside the industry application, the atomization process is present in nature constantly around us. The most typical example, which has increased its importance exponentially on these days [12], is the spray formation present on the sneezes and coughs. These sprays, usually called aerosols, consist of a few saliva droplets advected with the airflows provoked by sneezes or coughs, which carry pathogens and are responsible for transmitting many diseases. In this framework, the study of the transport of these droplets is directly related to the range of contagion. Furthermore thus, the turbulence of the gas ambient can strongly affect the spreading of the droplets.

All the presented applications bring different particularities to the atomization process: electromagnetic fields, liquid-solid interaction, heat transfer, natural buoyancy... In recent years, this variety of configurations and applications has increased the interest in delving into the fundamentals of the liquid breakup, both from an experimental and computational standpoint. The last advances in experimental techniques and the development of better measuring instruments as optical devices or high-speed cameras have allowed the scientific community to measure and analyse many spray conditions and applications in great detail [13]. On the other hand, the emergence of High Performance Computing (HPC) as an affordable tool has lead to an increase of numerical

studies using the Computational Fluid Dynamic (CFD) approach, which has become more frequent as an instrument to shed light on the insights of the phenomena as it can extract information that the experimental tools are not able to provide. However, as in other applications, both approaches are required, and the computational study can not entirely replace the experimental studies.

1.2 Atomization

When studying the primary atomization process, there are many parameters that determine the liquid disintegration. Those parameters can be grouped in different non-dimensional numbers, which represent the physical problem. The most commonly used in this kind of flows are:

- **Density ratio**: this relates the densities of the ambient gas and the injected liquid. Higher density rations increase the liquid-gas interaction favouring the mixture.

$$\rho_g/\rho_l \tag{1.1}$$

- **Reynolds number (Re)**: this number relates the inertial and the viscous forces. Higher values of Reynolds number imply more turbulent flows as the lower values are usually related to laminar flows.

$$Re = \frac{Inertial\ forces}{Viscous\ forces} = \frac{\rho u D}{\mu} \tag{1.2}$$

- **Weber number (We)**: this number relates the inertial and the surface tension forces. For higher values of the Weber number the liquid surface breakup is easier than for the lower values.

$$We = \frac{Inertial\ forces}{Surface\ tension\ forces} = \frac{\rho u^2 D}{\sigma} \tag{1.3}$$

Where u and D are the characteristic velocity and length scale, respectively; ρ and μ are the density and dynamic viscosity of the fluid of the reference fluid, and σ is the surface tension between the gas and the liquid phases. The physical properties in simple atomizers, as in the cases studied in this document, refer to the liquid phase. However, there are other types of configurations, such as air-assisted atomizers, which can refer these properties

to the injecting gas phase or the liquid phase. Hence, this selection is key to characterize the flow. Additionally, both Reynolds and Weber numbers can be replaced by other non-dimensional numbers composed by their combination. Typically the two other dimensionless numbers are:

- **Ohnesorge number (Oh)**: this number combines both previous non-dimensional numbers as it relates the viscous forces with the surface tension forces.

$$Oh = \frac{Viscous\ forces}{Surface\ tension\ forces} = \frac{\sqrt{We}}{Re} \tag{1.4}$$

- **Taylor number (Ta)**: this number presents the ratio between the surface tension forces and the viscous forces in a different approach.

$$Ta = \frac{Surface\ tension\ forces}{Viscous\ forces} = \frac{Re}{We} \tag{1.5}$$

When it comes to simple liquid atomization, where there are no additional flows that perturb the liquid surface, the atomization process can be characterized by the Reynolds and Weber number, and the density ratio between the liquid and gas phases [14]. In the literature, the atomization behaviour is usually categorised in different atomization regimes, which can be related to the average injection velocity [15]:

- **Rayleigh regime**: it takes place at relatively low velocities, where the instabilities of the liquid surface increase during its propagation on the injected liquid core until its growth leads to the breakup. This regime is characteristic of placing the atomization on the liquid tip and generating droplets with a diameter almost twice the nozzle size. Originally, this breakup regime was proposed by Lord Rayleigh [16], and it has been widely addressed in the literature.

- **First wind-induced regime**: the velocity is slightly higher than in the previous regime. In this case, the effect of surface tension is augmented, provoking instabilities with higher amplitude and frequency. The breakup length is reduced, but the atomization is still located at the spray tip. The number of droplets generated increases, and the characteristic size is comparable to the nozzle diameter.

- **Second wind-induced regime**: increasing the relative velocity between the liquid and the gas also increases the shear stress in the liquid surface. These forces combined with the surface disturbances lead to the liquid breakup along the liquid core surface, in contrast to the previous two regimes where the atomization occurs at the liquid tip. In this regime, the resulting droplets are much smaller than the nozzle diameter, being comparable to the surface instabilities amplitudes.

- **Atomization**: when the injection velocity is sufficiently high, the liquid core surface is completely disrupted at the nozzle exit. The liquid vein is mostly atomized in this regime, but some liquid mass is still attached to the nozzle exit. This amount of liquid is called *breakup length* and its size depends on the Reynolds and Weber number. This kind of sprays can also be divided into incomplete atomization and complete atomization, depending on the breakup length and the spray angle, as depicted in Figure 1.1.

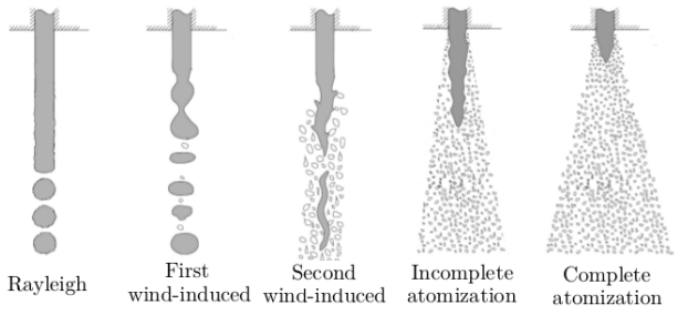

Figure 1.1: Sketch of the different atomization regimes.

However, recently B. Trettel performed an exhaustive analysis of several experimental studies present in the literature [17, 18] where he questioned the accuracy and validity of the classic atomisation regime chart. He argued that some of the boundaries from the classic regimes are based only on a few points and focused on superficial characteristics that are not accurate enough to determine the atomisation regime correctly. So he designed an atomisation regime chart that depends on the Reynolds and Weber number given a density ratio. This chart is outlined in Figure 1.2 from [18]. This diagram shows that a clear division is made depending on whether the nozzle outflow is turbulent or not. So the Rayleigh regime is divided between turbulent and laminar Rayleigh regimes, and the first and second wind-induced regimes are

substituted by the downstream transition and turbulent surface breakup, respectively. Apart from performing an analysis of a vast number of experiments to determine the different regimes, he also based the boundaries of the regimes on the turbulence intensity on the nozzle outlet.

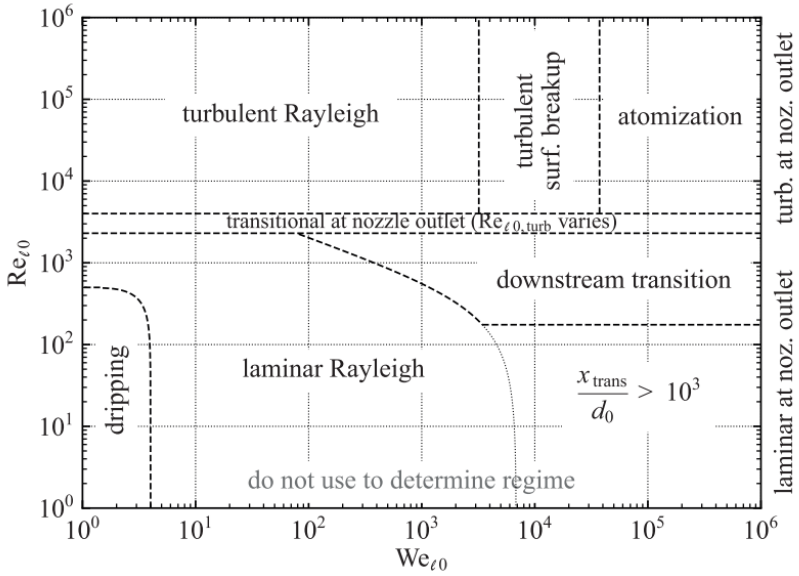

Figure 1.2: Schematic regime diagram from Trettel [18].

As already exposed in the previous section, the industrial applications of the sprays are mostly taken in the context of finer droplet production (e.g., to achieve better gas-liquid mixing or finer powder). For this reason, the atomisation regime has become the object of study in the scientific community. However, when increasing the relative velocity and, thus, the flow complexity, more processes are taking place simultaneously. So, the effects of the mechanisms that promote atomization are mixed, hindering the identification of the contribution of each one. That is the reason why the exact development of the atomization process is far from being fully known, only understanding some of them in a qualitative manner [14, 15]. Those mechanisms can be organized into different categories:

1. **Inflow turbulence**: the internal flow previous to the injection plays a key role in the atomization development as it determines the shape of the velocity profile. The effect of having a laminar, semi-turbulent, or turbulent velocity profile will deeply affect the evolution of the spray.

The nozzle turbulence thus is one of the most important factors that promote the liquid breakup, according to Lefebvre and Mcdonell [15]. However, the turbulent study of the internal flow is quite complex, and the direct quantification of its importance is not trivial.

2. **Velocity profile relaxation**: when the liquid is still inside the nozzle, the velocity profile is constrained to be zero at the walls. Once the liquid goes through the nozzle exit, this imposition is removed, and then radial velocity components appear. Those radial components widen the velocity profile, disturbing the liquid surface and eventually causing ligament formation and breakup.

3. **Aerodynamic instabilities**: the relative velocity (Kelvin-Hemholtz instabilities) and the density ratio (Rayleigh-Taylor instabilities) between both phases affect the way that the disturbances of the liquid surface growth or dump. When the high frequency instabilities perturb the liquid core surface, waves appear in the vein. Then, those waves are deformed until forming ligaments and droplets after the breakup.

4. **Cavitation**: this phenomenon occurs when the liquid reaches pressure values below the saturation point. This condition is strongly dependant to the nozzle geometry. In those cases, the liquid flow separates the wall a the internal flow, generating vapour bubbles that enhance the turbulence. Also, the bubbles can implode and cause perturbations on the liquid surface, ultimately generating ligaments and droplets. The cavitating sprays present earlier atomization and a wider spray cone angle [19]. However, the exact quantification of the induced turbulence and the contribution of the bubble implosions to the jet breakup is challenging.

Figure 1.3 depicts an ideal spray which will be used to explain the main parameters that can define it. First, focusing on the dense region, there is a big liquid structure connected to the nozzle called the liquid core. This structure can be characterized by its length at the centreline x_b, also called the breakup length or the intact core length, and the length where the instabilities breakup the liquid surface x_i, usually called the non-perturbed length. Furthermore, the core cone angle θ_i and the spray angle θ can be defined. The dense region also presents significant liquid structures, detached from the liquid core and near the spray centreline. At a certain axial distance from the nozzle, the atomization pattern changes to a finer droplet cloud without big

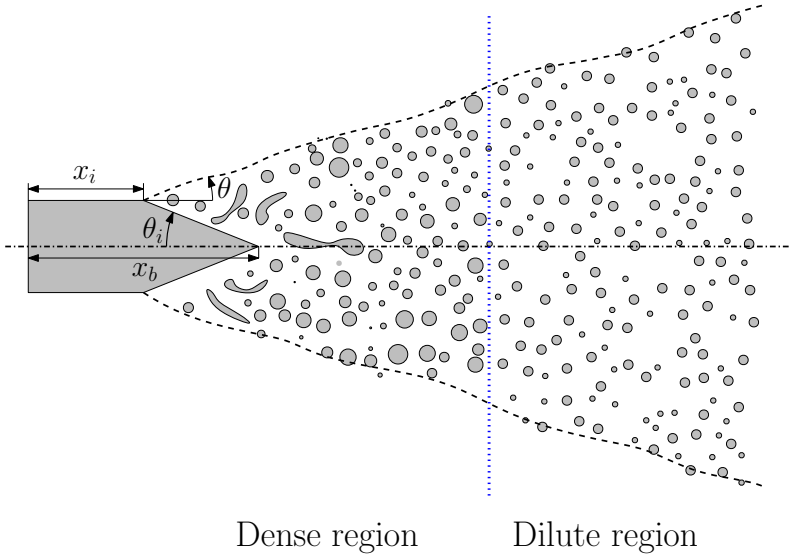

Figure 1.3: Scheme of a full atomized spray.

liquid ligaments, and the mass concentration at the centreline decreases drastically on the so-called dilute region. The limit between both regions is still a bit unclear. Firsts spray studies located the threshold at an axial distance of $25 < x/D < 30$, corresponding to the distance where a single-phase jet starts to show an auto-similar behaviour. The dense region has been usually omitted when studying the turbulence field using hot-wire anemometry, so this information is scarce in the literature. What is really known is that the turbulence is not developed until $x/D > 30$. From that point on, the majority of the flow properties of any location can be scaled by the respective centreline value.

1.3 Literature review

In order to give an actual context of the state of the art of spray dense region findings, a review of the previous studies will be resumed in this section. The reviewed works will be sorted depending on whether the studies are performed with an experimental or computational approach, in the latter case, focusing on DNS studies.

Nevertheless, before starting the review, there are some particularities associated with the study of the primary atomization process that are worth mentioning. Regarding the experimental works, the research performed over

last years aims at industrial applications, where the operating conditions usually present very high Reynolds and Weber numbers. However, when it comes to the near field, there are a few drawbacks to consider, which are the reasons for the gap of understanding of the physical phenomena that generate the liquid breakup:

- **Characteristic length scales:** in order to generate proper atomization, the injection velocity and the nozzle length have to be high enough to develop turbulence within the internal flow and the sufficient shear stress on the outflow. However, many industrial applications present small nozzles combined with high injection pressures, leading to short length scales. So, regarding the optical devices, powerful microscopes are needed to zoom in the first 2-3 mm from the nozzle exit with enough resolution. Also, due to the droplet velocities, the camera shutter has to be sufficiently fast to freeze each instant and avoid blurry images. Condition than only the fast cameras fulfil. Finally, with short camera shutter times, high power light pulses are needed, which are achieved with high frequency pulsating laser or high frequency pulsated LEDs. Those limitations increase the costs of the typical optical setups.

- **High optical density:** as already mentioned in the previous section, the primary atomization process takes place in the dense region, near the nozzle exit. There are optical techniques that are able to extract information about droplet population in the dilute region as Phase Doppler Particle Analysis, Mie-Scattering or Schlieren among others. Nevertheless, those techniques fail when applied in the dense region due to the high number of liquid structures detached from the core that remain close to the spray axis, making them only suitable to extract macroscopic information as the spray penetration and spray angle. Recently, new techniques have appeared that are able to get information from inside the spray. Among them are worth mentioning the optical connectivity to measure the intact core length and the X-ray to measure the liquid concentration of the spray. However, those techniques require even more sophisticated devices and setups than the classic techniques, increasing the costs drastically. Therefore the amount of this kind of facilities are really scarce and so, the number of works using these techniques.

On the other hand, regarding the computational approach, DNS of high-velocity sprays require fine grids to capture all turbulence scales, and short

timesteps to make the simulations stable. Those requisites lead to a radical increase of the computational costs. That is the reason why, traditionally, the DNS spray simulations have been applied to fundamental studies, with small computational domains and low injection velocities, aiming the study of the shear stress influence on ligament breakup or the droplet formation mechanisms.

1.3.1 Computational studies of liquid atomization

This subsection aims to provide state-of-the-art DNS for the primary atomization process study. Nevertheless, it is essential to give a context of the application of CFD to the atomization process. The CFD has proven to be a valuable research tool to complement the experimental studies, providing information that can not be acquired with the experimental approach. The computational study of the atomization process is deeply influenced by the multiphase nature of the problem, which requires special treatment. Traditionally, the first approaches to computational studies of this problem have been performed using Reynolds Averaged Navier Stokes (RANS) methods. Those methods require implementing different models to simulate the liquid breakup and atomization. There are many models developed to this end, depending on the Lagrangian or Eulerian approach. Dos Santos and Le Moyne reviewed the main atomization models from RANS methods on [20], among the Lagrange methods are worth mentioning the Blob model developed by Reitz and Diwakar [21], the Kelvin-Helmholtz Break-Up Model developed by Reitz [21] and the Distribution Functions [22]. On the other side, some Eulerian methods are developed as the Interactive Cross-sectional Averaged Spray (ICAS) by Wan and Peters [23], or the one proposed by Vallet et al. [24]. Another approach to this problem is using a combined approach as the Eulerian-Lagrangian Spray Atomization (ELSA) [25] that is widely spread in the scientific community, using the Lagrangian approach to compute the droplet advection and the Eulerian framework for the carrier phase. However, although those models can give fairly accurate results, they require a manual calibration of their several tunning constants to fit the experimental results. When using LES approaches, the same division can be done. On the one hand, Bharadwaj et al. [26] developed a non-evaporative Eulerian model, which showed good agreement in high-speed Diesel sprays. On the other hand, the Lagrangian approach using Volume-Of-Fluid (VOF) or Level-Set (LS) methods is also present in the literature. Finally, as in RANS simulations, models based on the Eulerian-Lagrangian approach, as the Discrete Phase Model (DPM), are present in many software.

Recently, the growth of computational power has allowed the scientific community to start using DNS in specific problems. When it comes to multiphase flows, the numerical framework differs significantly depending on the application. Also, as the majority of DNS studies aim to shed light down to the fundamental physics, their use are mostly limited to research centres. Furthermore, many research centres develops its computational code, appropriate to their needs. Nevertheless, some aspects are common in most of these implementations , e.g., the incompressible flow assumption, as the computational requirements strictly limit the simulated velocities. Further details about the numerical methods and fluid advection can be found in Chapter 2 (emphasizing the ones used on the simulations performed in this document). So in the following pages, a framework of the computational studies performed with DNS tools will be presented.

There are many applications where primary atomization plays a key role and many injector designs that influence the development of this phenomenon. Since the DNS studies focus on studying the fundamental processes that take place during the primary atomization event, the configurations of the simulations are often simplifications to reproduce the phenomenon. So, the most common simulations available in the literature are the canonical flows as the round sprays [27, 28] and liquid sheets [29], often adding supplementary gas flows to assist the atomization as in [30, 31] studying round jets under crossflow configurations or [32, 33] focused on prefilmer airblast atomizers.

As the possibility of using DNS as a viable tool to study the primary atomization process is reasonably recent, the majority of the available literature has been published in the last 15 years. However, to study the intrinsic phenomena of ligament formation, some works addressed this topic from a more fundamental standpoint. These works often simplify the problem where some liquid structure is placed within a periodical box and perturbed with a coflowing gas. On the literature, there are two main approaches: on the one hand, the liquid structure is a cylinder, as depicted in Figure 1.4a; whereas on the other hand, the liquid structure is a sheet, as depicted in Figure 1.4b. Both methodologies focus on the aerodynamic interaction between the liquid and the gas, neglecting additional sources that can disturb the surface and avoiding the need to calculate the transient phase. Also, the simplification of the study alleviates the computational requirements, allowing to perform simulations with various flow conditions (focusing on the Reynolds and Weber number and density and viscosity ratios).

In this line, Lozano et al. [36] published an early research of this problem that inspired this kind of fundamental approach. In this work, they developed

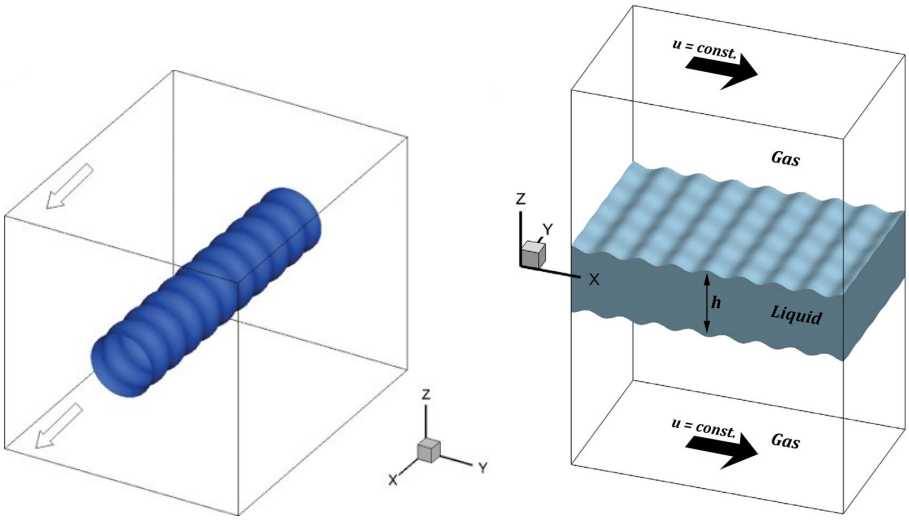

(a) Round jet setup from Jarrahbashi and Sirignano [34]

(b) Liquid sheet setup from Zandian et al. [35]

Figure 1.4: Typical simplified setups of DNS for ligament breakup studies

a 3D model to study the liquid breakup caused by the growth of the instabilities on the liquid interface. This study and the ligament study from Shinjo [37] et al. inspired Jarrahbashi et al. [34] to perform a comparison between a spray simulation (accounting the internal flow), an axisymmetric model, and a 3D model approach as depicted in Figure 1.4a. This work emphasized the apparition of a counter-rotating vortex, similar to the hairpin vortex, that induced the lobe formation and afterwards the ligament breakup. Later, in [38] the same research group revisited the 3D model and performed simulations varying the non-dimensional number to study their influence on the breakup mechanisms. They provide a relationship between the vortex dynamics and the surface wave dynamics to explain the different lobe and ligament generation. On the other hand, regarding the liquid sheet approach, Zandian et al. [35, 39, 40] recently performed a study of the influence of flow conditions on the liquid sheet breakup. In [35] they approached the topic by identifying the consecutive phenomena that take place during the ligament breakup under different density ratios. They pointed out that, depending on the flow conditions, the particular shapes prior to the ligament detachment are different, and they called them liquid cascades. In their next work [39] they focused on the relationship between the vortex dynamics and the breakup mechanisms, emphasizing the streamwise vorticity. Finally, in the last work [40] they pro-

vided PDFs from the liquid length-scale distribution and an estimation of the spray angle. Also, studying the influence of the main flow parameters on the detached liquid structures size, spray aperture, and the liquid cascade. One of the main advantages of using a liquid sheet instead of a cylindrical shape is avoiding axisymmetry behaviours that increase the complexity of the computations. To end up with the fundamental approach, another interesting study is the one performed by Canu et al. [41] to study the droplet collision and curvature in different axial positions of the spray. In this work, they used a Homogeneous Isotropic Turbulence box seeded with different volume fractions to replicate diverse axial locations of the droplet cloud from the simulation of Menard et al. [42]. The droplet collision and population are studied in each box, also focusing on the curvature distribution. Figure 1.5 shows the different liquid interfaces for total volume fractions of 10%, 50% and 90%.

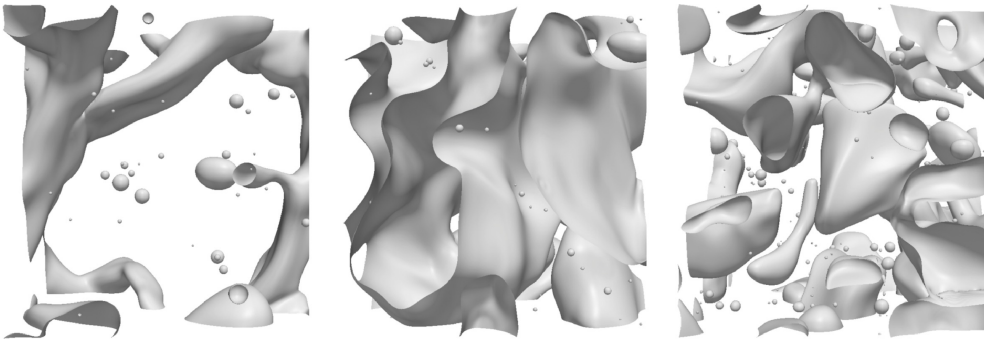

Figure 1.5: Liquid interface contour from left to right: 10%, 50% and 90%, of total liquid fraction, obtained from Canu et al. [41].

Moving to the proper primary atomization DNS simulations, one of the first steps on applying this approach was published on [43], but the accurate description of the simulation and the code was in [42, 44]. Those simulations were performed coupling VOF/LS and the ghost fluid methods to capture the interface and using a digital filter from Klein et al. [45] to generate synthetic turbulent inflow boundary conditions, a snapshot from [42] is shown in Figure 1.6. The main objectives of those works were related to the standpoint of the numerical methods, although they gave some interesting results on the axial mass concentration and velocity decay. Afterwards, they used the DNS simulations to improve and validate results obtained by the ELSA model [27, 28].

Shinjo and Umemura that previously were focused on the single ligament behaviour and breakup, performed one of the largest DNS simulations of primary atomization, reaching the 6 billion cells [37]. That research and the later

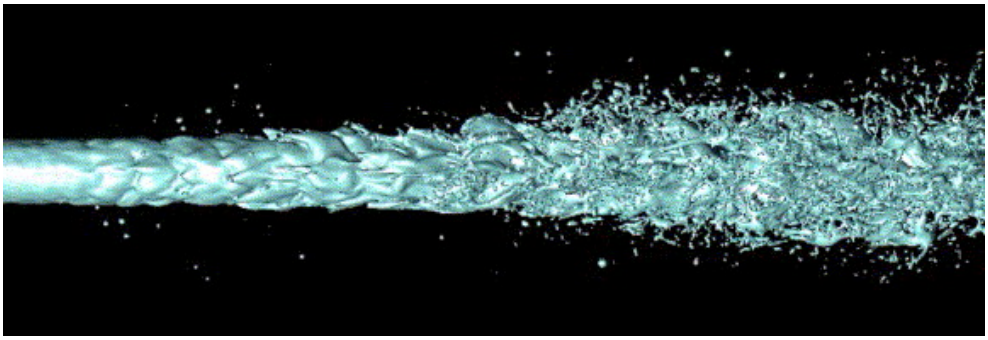

Figure 1.6: Liquid jet breakup from Menard et al. [42].

one [46] shed light on the breakup mechanisms on the round jet. However, some simplifications of the problem were made to be able to perform that challenging computation, being one of them using a planar velocity profile on the inflow boundary condition. The main objective of those studies was to investigate the breakup mechanisms at both the spray tip and the liquid core during the transient state. They pointed out the influence of the Weber number on the ligament size, how the short-wave instabilities enhance the droplet formation at the spray tip, and the importance of the local vortices that provoke the shear stress on the liquid surface. Although the results presented on those works have motivated lots of research afterwards, some drawbacks have to be considered. Apart from addressing only the transient phase, the experimental validation is likely impossible due to the simplifications as there is no way to replicate the inflow conditions. Nevertheless, with the simulations performed on those studies and its analysis, they were able to develop a mathematical model of a Sub-Grid Scale model for LES simulations on [47, 48].

One of the open topics regarding DNS simulations of primary atomization is the inflow boundary condition. Some works use simplified inlet boundary conditions as [37, 46] where a plain velocity profile is injected, neglecting the effect of the inflow turbulence on the liquid breakup. Another approach is using mathematical filters to generate synthetic turbulence, as in [27, 42, 49], which allows taking into account the effects of the inflow turbulence on the atomization with low computational cost. The last standard methodology is feeding the spray with a computed turbulent time-varying velocity profile to trigger the breakup process. This turbulent profile can be achieved by simulating the internal flow coupled with the external flow or mapping results from other internal flow simulations as inflow conditions to the external flow computations (usually called Mapped Boundary Conditions (MBC)). Several

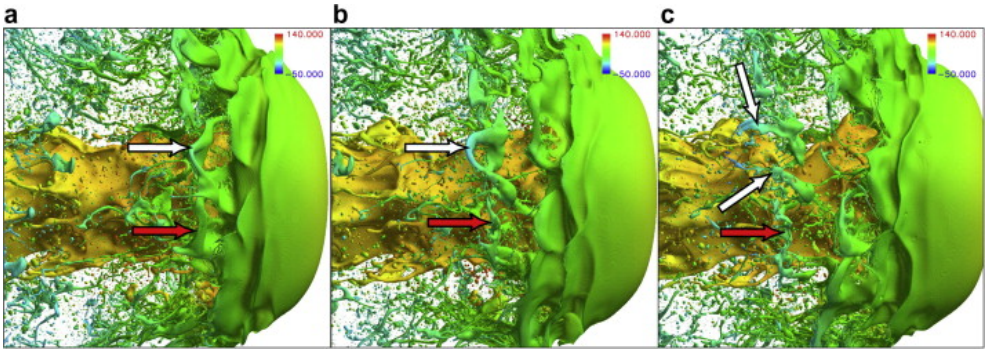

Figure 1.7: From left to right the breakup of a ligament formed in the spray tip, from Shinjo and Umemura [37].

works pointed out the significance of the origin of the inflow turbulence. Hermann in [50] used an MBC obtained from a DNS of a periodical pipe flow to study the influence of the mesh size on the primary atomization process. It concluded that, despite the DNS resolves the Navier Stokes equations, the mesh refinement should be enough to provide accurate results, showing a good droplet convergence for droplet sizes from 6 grid points. However, the main drawback of using MBC is the increase of computational cost, but Payri et al. [51] investigate the differences between the structures generated by the mathematical filter and the ones obtained by simulating the internal flow. The first case showed isotropic structures, whereas the typical structures of wall-bounded flows are strongly anisotropic, as can be seen in Figure 1.8 where the perturbations on the liquid core are clearly different. The results showed an increase in the number of droplets generated when using the Mapped Boundary Conditions.

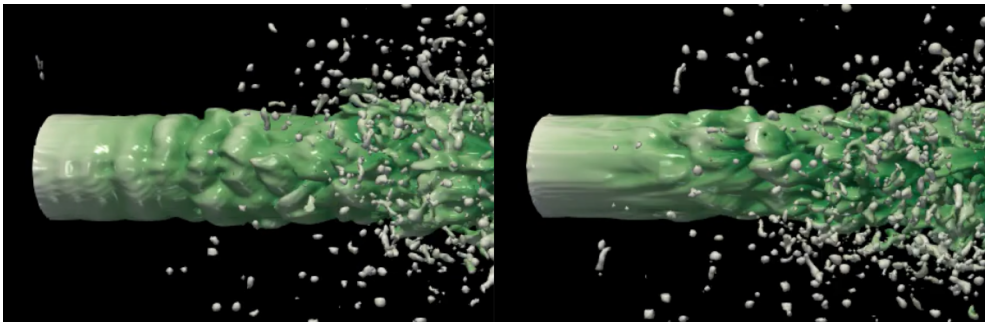

Figure 1.8: Effects of injected structures shape on liquid core perturbation for left: Synthetic Boundary Condition, right: Mapped Boundary Condition.

Even so, Synthetic Boundary Conditions are still useful to perform studies on this field as it saves computational resources. One of the recent studies performed with this configuration is the one by Hasslberger et al. [52]. Here, a parametric study with different injection conditions was carried out by varying the Reynolds and the Weber number and using a numeric filter to generate the inflow turbulence. The main objective of this document was to study the influence of the inflow boundary conditions on the liquid topologies generated downstream. They concluded that even though both non-dimensional numbers were important to the jet breakup, the Reynolds number was dominant regarding the flow topology.

All the previous studies agree that one of the limitations of DNS studies lies in having extremely refined meshes restricting the operating conditions and the computational domains. So, in order to minimize the computational costs when increasing the complexity of the study, Adaptive Mesh Refinement (AMR) algorithms have been developed. To highlight one, the Octree method from Popinet [53] that has been tested in different configurations (including primary atomization) in [54] showing good agreement with experimental data.

One example of a DNS study using AMR algorithms is the one recently performed by Zhang et al. [55]. One of the particularities of this work is that, in contrast to the majority of the DNS studies that aim to investigate simplified configurations, and their main objective is to understand the phenomena behind the liquid breakup, the objective of this study is to replicate a more realistic configuration. The geometry presented in this research and the operating conditions correspond to a single-hole injector with counterbore, adapted from the Spray G geometry from the Engine Combustion Network (ECN) [56]. They add an angle to the inflow velocity to generate a non-axisymmetric behaviour of the spray and put their efforts into studying the droplet size distribution and how the initial inflow conditions affect this parameter on the azimuthal direction. Figure 1.9 shows the liquid interface obtained from this configuration.

Finally, this thesis is a continuation of the works performed by CMT-Motores Termicos on [49, 51, 57, 58] gathered in Crialesi's thesis [59]. As already introduced earlier in the document, on Salvador et al. [49], the SBC approach was chosen to study the influence of the inflow turbulence on the atomization process. The turbulence was created using a numerical filter based on Klein et al. [45] and tuned to feed the jet with three different turbulent intensities. On Payri et al. [51] the first comparison between MBC and SBC was shown. This study highlighted the differences between the shapes of the turbulent structures injected in the domain and how they affect droplet

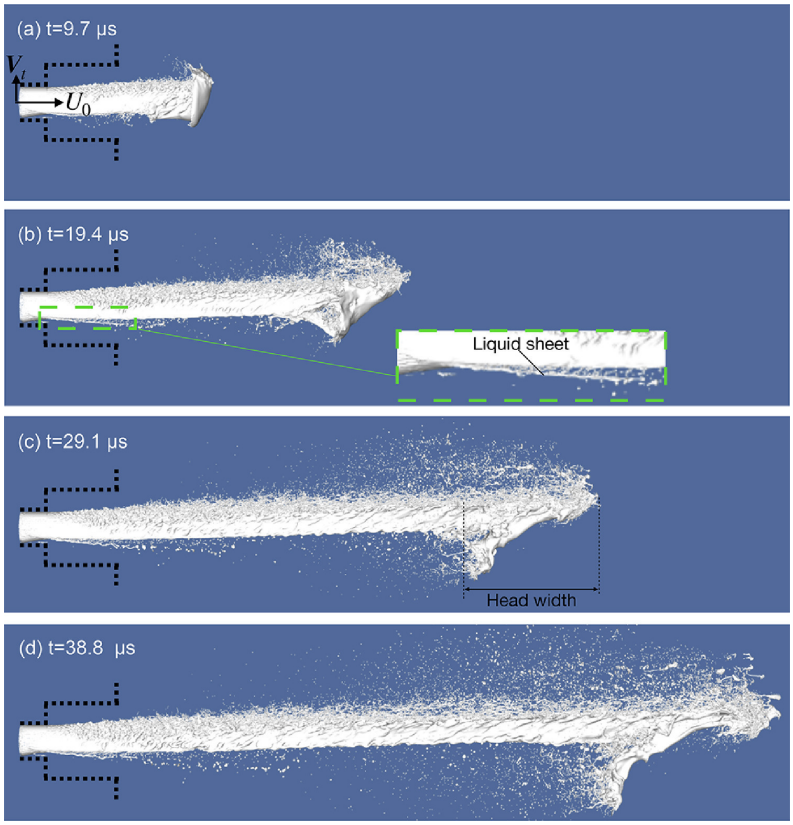

Figure 1.9: Evolution of a gasoline surrogate jet of a counterbore injector computed with DNS, from Zhang et al. [55].

production. To ensure the accuracy of the computations, and as there is no experimental data to validate the results obtained, on Torregrosa et al. [57] the computation of fundamental turbulent parameters was performed, including the Kolmogorov scale, the dissipation rate, and the energy cascade on the MBC case. Finally, Crialesi et al. [58] compared both SBC and MBC cases in turbulent terms and on droplet production, showing similar results on both cases, but emphasizing the higher droplet production rate obtained on the MBC. All these results and research is used as a starting point to perform the different studies proposed in this document.

1.3.2 Experimental studies on the near-field

Before explaining the latest techniques used when addressing the dense region study, it is worth mentioning why this space is a hard-measuring zone

in optical terms, as explained above in the section. The optical density can be quantified using the Beer-Lambert-Bougher law, which describes the attenuation of a light travelling through a medium, up to a limited density [60]. This quantification is performed using the Optical Thickness (KL) that can be expressed based on the light intensity detected by the camera, I, and the background illumination I_0, as shown in Equation 1.6. So, as the opacity of a medium increases, do the amount of scatterers bodies that the light beam will find. Each scattering event refracts the light beam, modifying its trajectory, and, in some cases, the new trajectories can not reach the optical objective, decreasing the amount of light registered by the camera sensor. Figure 1.10 presents a scheme from the light scattering through an opaque medium.

$$KL = -ln\left(\frac{I}{I_0}\right) \tag{1.6}$$

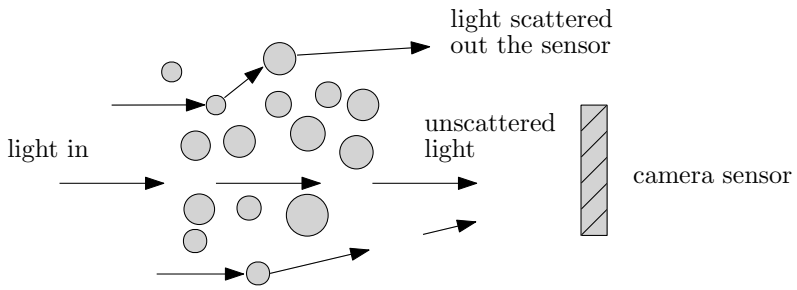

Figure 1.10: Scheme of the light scattering through a medium.

When it comes to sprays, the scattering events are the interaction between the light beams and the droplets. There is a proportional relationship between the number of scattering events per unit volume and the KL value. Depending on the KL value, some considerations have to be taken into account when choosing the experimental technique.

- **KL** $\approx$ **1** $-$ **2**: here, there is not much light scattering. Simple techniques as shadowgraphy with basic light sources can achieve excellent results.
- **KL** $\approx$ **2** $-$ **5**: the amount of scatter events increases. The basic optical techniques are not enough to depict what is happening inside the spray.
- **KL** $\approx$ **5** $-$ **10**: the mediums that correspond to this range of values require imaging techniques.

- **KL $\geq$ 10**: The amount of light scattering generates a diffused illumination. The possibility of imaging the internal part of the spray is nearly impossible. The dense region of Diesel spray in non-evaporative conditions often are located at this range.

So, when the KL values of the problem are high enough, the traditional techniques fail to give helpful information on the liquid breakup inside the spray. However, to overcome these issues, new imaging techniques have appeared. The following pages will present the last developments on optical techniques with the relevant publications about its application to the near field of the spray.

Near-field microscopy

The Near-field Microscopy (NFM) appears as an evolution of the traditional technique called Diffused Backlight Illumination (DBI). It first application to sprays was presented by Sjöber and co-workers [61]. The central idea of Near-field Microscopy is to illuminate the spray from one side and record its shadow with a camera on the opposite side (same as the DBI technique). So, being the same idea as previous techniques, its novelty lies in adding a long-distance microscope to zoom into the dense region and use high-quality components. Measuring the near field with this technique requires short light pulses with high intensity, a high-quality magnifying lens, and a high-speed camera. To comply with those requirements, the light source should be a high-frequency pulse laser used along a diffuser to cover all the measuring area (although good results have been achieved using high-frequency LEDs with a light pipe [62]), a long-distance microscope able to magnify the first millimetres of the spray with a good spatial resolution, and a high-speed camera with a frame rate around 150 kfps. Figure 1.11 presents a render of the optical setup from Crua et al. [63] which uses a laser light source.

The main drawback of this technique is that, when the liquid core starts to breakup and the atomization starts, the amount of scattered light increases and the intensity captured by the camera sensor is not enough to discern on the spray core. However, it provides notable results when applied to first moments of the spray as it penetrates into the domain. Being interesting for the comparison with numerical results. This technique has been applied to high pressure sprays by different workgroups [62–64] and also to study the cavitation phenomenon [65]. Figure 1.12 shows the results obtained by [63] proving its potential to give useful information from the transient state.

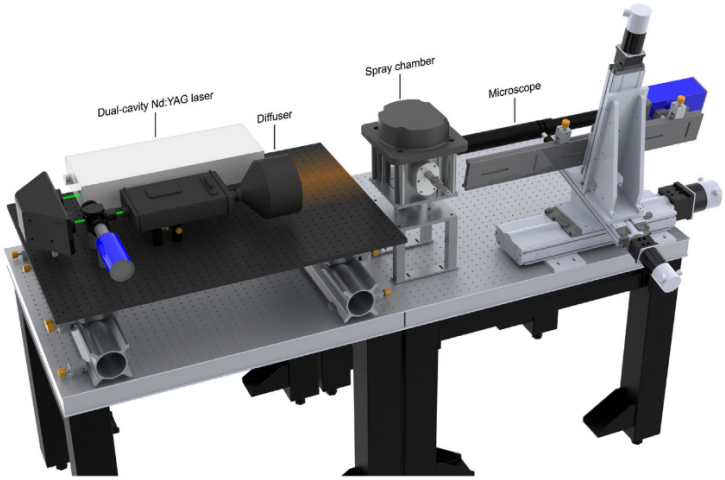

Figure 1.11: Render of the optical set-up for high-resolution microscopic imaging from Crua et al. [63].

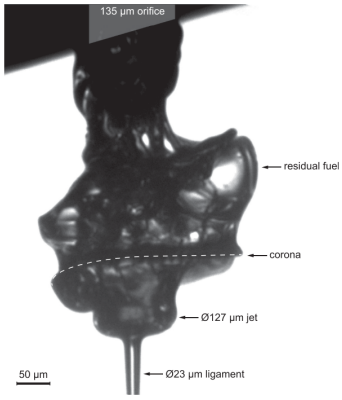

Figure 1.12: Transient snapshot of a fuel spray from Crua et al. [63].

Ballistic imaging

The ballistic imaging [66, 67] is also an optical technique based on the line-of-sight that uses a laser as a light source. This technique is similar to laser-based shadowgraphy as it uses an expanded laser beam to go through the spray and then capture a shadowgram of the liquid structures on an opposing fast camera. The main difference lies in the discrimination of the photons received on the camera sensor. While on laser shadowgraphy, the image is built using all the photons received, the Ballistic imaging filters the photons to select only the less scattered ones. Figure 1.13 shows a sketch of ballistic imaging applied to a spray. Each photon from the input beam can face up three different scenarios when passing through the spray:

1. **Ballistic photons**: there is a small portion of photons that, then passing through the dense region, do not interact with any liquid structures. They maintain the same polarization from the original laser beam and are the first to reach the camera sensor.

2. **Quasi-ballistic photons**: other much larger portions of the emitted photons are slightly scattered by only a few liquid structures. They reach the camera sensor right after the ballistic photons.

3. **Corrupted light**: the majority of the photons are heavily scattered when passing across the spray. The more the corrupted light is rejected to create the image, the better the result is.

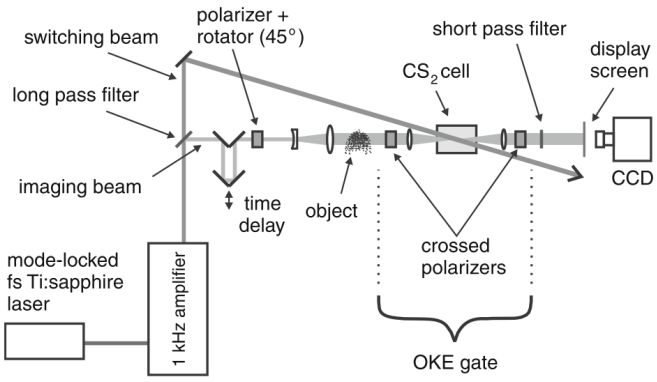

Figure 1.13: Sketch of single-shot Ballistic imaging from Linne et al. [68].

As one may think, when addressing the dense region of the spray, the amount of ballistic photons is too low to reconstruct a proper shadowgram.

So, in order to get proper spray images, the quasi-ballistic photons are also taken into account. If calibrated correctly, the liquid structures will be marked in black on the image, with sufficient spatial resolution to extract curvatures, wavelengths, ligament sizes, and distributions. Also, using double-image ballistic imaging is possible to compute the velocities of the drops [69].

Finally, this technique has been applied to the primary atomization process in fully atomized Diesel spray [70, 71], effervescent sprays [68], and other configurations. Some results from [68] are depicted in Figure 1.14 to show the data provided by this kind of technique.

Figure 1.14: Result of an effervescent spray from Linne et al. [68].

Structured Laser Illumination Planar Imaging

The main idea of this technique is using a laser light sheet to illuminate the spray, which is doped with a fluorescent to enhance the light scattering, and capture the scattered photons with a camera sensor located at 90° from the laser sheet. This kind of illumination approach is similar to the one used in Particle Image Velocimetry (PIV), but when addressing dense environments, the secondary scattering on the drops located outside the plane increases, complicating the droplet identification. To mitigate this problem, the Structured Laser Illumination Planar Imaging (SLIPI) has been recently developed [72]. This technique spatially modulates the laser sheet with a sinusoidal wave and then it uses three consecutive images shifting the modulating signal $2\pi/3$, creating a 'signature' (some new approaches have reduced this number to two shots [73] and the signal shift to $2\pi/2$). One requisite of this method is taking the different images within a short time range to reduce to the minimal the drop motion between the snaps. Once the partial images are obtained, a pair-wise difference is computed to get the final reconstructed image. Figure 1.15 present a typical SLIPI experimental set-up.

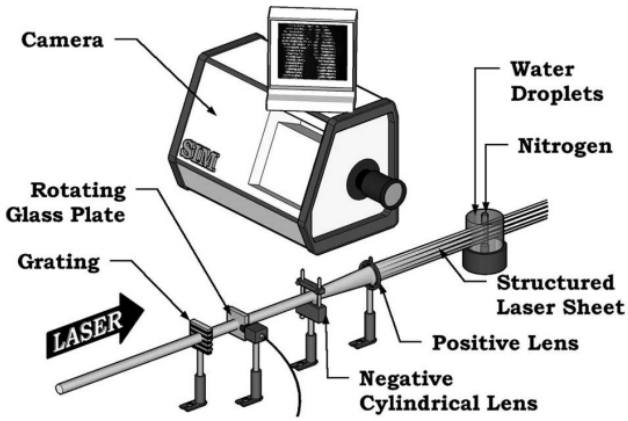

Figure 1.15: Sketch of SLIPI set-up from Kristensson et al. [74].

When imaging with planar laser light, one of the most known disadvantages is that, as the sheet goes through the spray, the amount of non-scattered photons decreases, so the results tend to be polarized towards the first side of the spray to be illuminated, as also can be seen in Figure 1.16 where the laser sheet goes from left to right of the image.

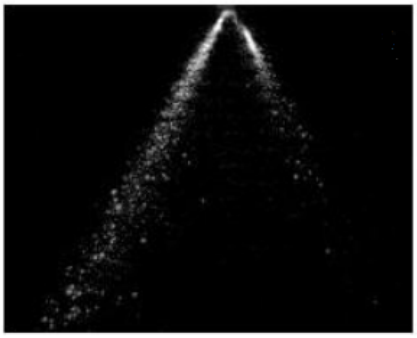

Figure 1.16: Result of a hollow cone water spray from Berrocal et al. [72].

Using SLIPI combined with Mie-Scattering can provide Sauter Mean Diameters (SMD) results, as the fluorescent scattering from the SLIPI depends on the droplet volume, and the Mie-Scattering depends on the mean surface area. Some results have been obtained with this combined methodology [75].

Optical Connectivity

As already presented earlier in the atomization section, apart from the droplet cloud, the internal core length of the spray is an essential parameter of the atomization process. By definition, the liquid core is surrounded by all the drops and ligaments detached from it, and thus, when illuminating the spray from outside, most of the light that penetrates the spray is scattered before reaching it.

In this context, the idea of illuminating the spray from inside the injection nozzle has recently increased its interest as it can give useful information about the liquid core length and shape. From this idea, Charalampous et al. [76, 77] developed a new technique called Optical Connectivity. This technique uses a fluorescent doped liquid illuminated with a light source (commonly guided with optical fibre) so that, when the light goes through the nozzle exit, the refractive index of the liquid surface keeps the light beams inside the liquid core until it breaks up. This provides a neat measurement of the liquid mass connected to the nozzle exit. Figure 1.17 shows a simple schematic representation of this technique.

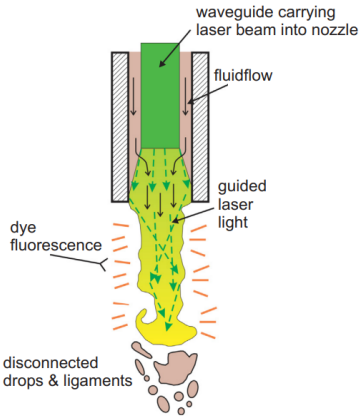

Figure 1.17: Sketch of Optical Connectivity set-up from Linne et al. [13].

The application of this technique requires having access, utilizing optical fibre or internal windows, to the inside of the nozzle. This requires the modification of the injector or the design of specific injectors with those optical accesses. Also, if optical fibres are used, the modification of the internal flow and its turbulence can cause different behaviour of the atomization process. However, if the experiment and the simulation have the same setup, the results provided by this technique can be used to validate the results obtained

using numerical simulations. Optical Connectivity has been applied in different experiments, primarily to coaxial airblast atomizers [77, 78], but also to automotive injectors [79]. Figure 1.18 depicts the comparison between Shadowgraphy and Optical Connectivity of a coaxial airblast atomizer from [78].

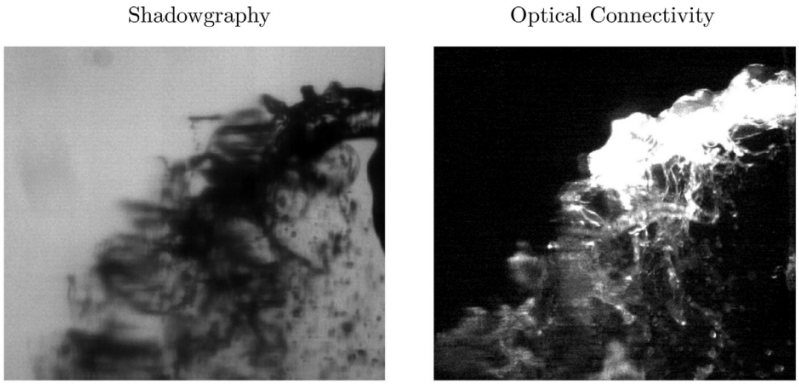

Figure 1.18: Comparison between Shadowgraphy and Optical connectivity of an air-blast atomizer from Patil and Sahu [78].

X-ray phase contrast

The continuous efforts to get images from inside the spray on the dense region moved the optical developments to use X-ray as a light source. The X-ray Phase Contrast Imaging (PCI) is the most recent technique developed that uses X-ray to go through the dense region in a similar manner that typical shadowgraphy technique does. It uses a synchrotron that circulates electrons in packs generating pulses of around 150 ps with a 1.59 μs of interval between pulses. Those pulses are tuned in a photon energy level that is not absorbed by the liquid and are refracted when going through the interface of the spray. Figure 1.19 represents a sketch of the experimental setup of the PCI technique. As can be appreciated in the figure, the X-ray illuminates the spray but needs to be converted to photon energy by a scintillator crystal in order to be captured by the camera sensor. There are two ways to detect the wave-fronts patterns [13]:

- **Analyzer-based imaging:** one device, such as an interferometer or diffractometer, is used to remove the background light, allowing a clear image of the spray.

- **Propagation-based image:** does not require any additional devices to remove the background light as it mitigates it by increasing the distance that the light has to propagate. However, this technique needs data post-processing in order to provide clear images.

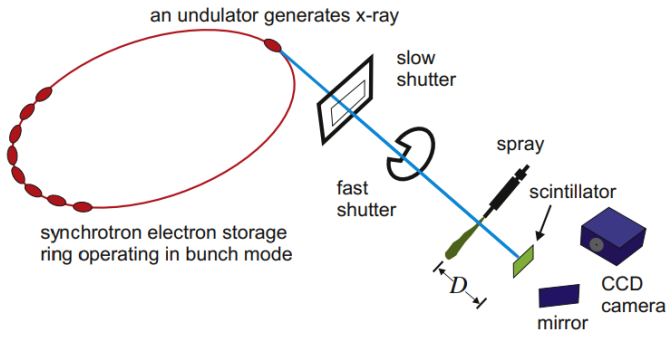

Figure 1.19: PCI setup schematics from Linne et al. [13] adapted from Wang et al. [80].

The main drawback of this technique is the cost of the required devices to make it work (mainly due to the synchrotron); thus, there are only a few laboratories that own one. One of the most important laboratories is the Advanced Photon Source (APS) from the Argonne National Lab (ANL), who are also the developers of the PCI. There are many studies using this technique, some of them focusing on the transient phase, as Wang et al. [80] that compared the spray transient using DBI with laser light source against PCI results. This comparison has been depicted in Figure 1.20a to show the clear improvement in the spray detection with the PCI technique, where the spatial resolution is higher and also the ligaments can be easily identified. Another application of this technique, and in the authors' opinion the best, is the study of the stationary near field of the spray as performed by Moon et al. [81] and shown in Figure 1.20b.

X-ray radiography

The X-ray radiography also uses a synchrotron to generate an X-ray beam to pass through the spray core. However, unlike the X-ray PCI, where the photons are tuned to non-absorbing energy to base the contour detection by its phase change, the X-ray radiography uses the absorption of the liquid mass of the spray (accounting liquid core, ligaments, and droplets) to determine

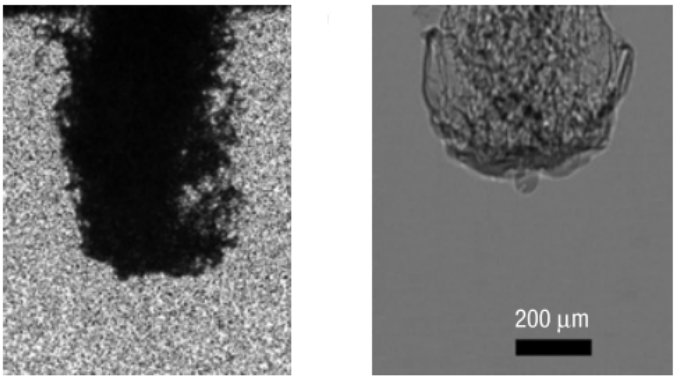

(a) Experimental data from Wang et al. [80]

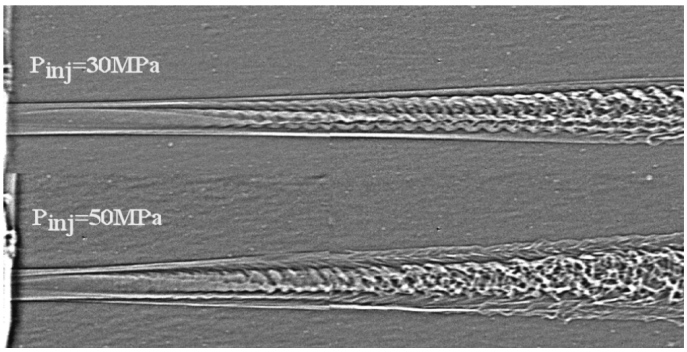

(b) Experimental data from Moon et al. [81]

Figure 1.20: Experimental results using PCI.

the amount of mass the beam has passed through. This technique allows having a 2D picture of the spray showing in some manner the projected mass of the spray in the beam direction. The light absorption from the X-ray is also quantified by the Beer-Lambert-Bougher law as with the traditional techniques. Figure 1.21 shows a schematics of a X-ray radiography setup. As this technique is based on the absorption of the liquid, it requires doping the liquid to increase its absorption to achieve clearer images [13]. Also, to achieve proper average values, several injections must be performed.

The X-ray radiography results have high diffusion among the CFD community as spray simulations can easily obtain the mass-to-area ratio (specifically in RANS and LES applications). As well as in the case of the PCI, the need for an X-ray light source narrows down the number of laboratories able to

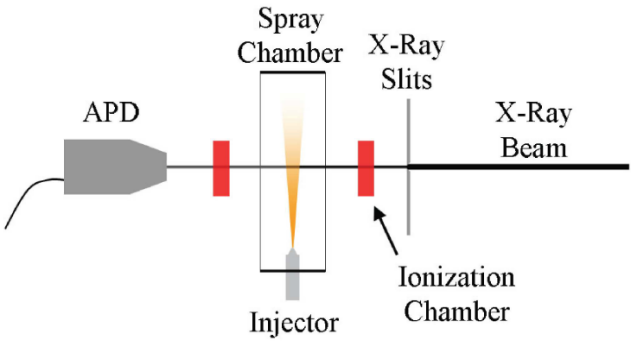

Figure 1.21: Experimental setup of X-ray radiography technique from Kastengren and Powell [82].

perform this kind of study. That is why the APS collaborates in most of the publications that apply this technique to spray [83–85]. Figure 1.22 shows the typical results obtained when applied this technique to spray research, extracted from [86]. Apart from studying the 2D distribution of the light absorption in the axial direction, the cross-section tomography of the liquid volume fraction can be provided as shown by Pickett et al. [64], and also the study of the axial velocity distribution [87]

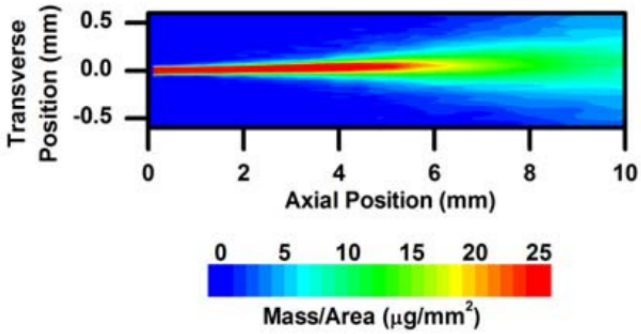

Figure 1.22: Experimental results using X-ray radiography from Kastengren et al. [85].

USAXS

Both PCI and X-ray radiography are based on the phase-shifting and absorption of the incident beam. This is because the scattering of the X-ray beam is

significantly low and difficult to measure. However, the Ultra-Small-Angle X-ray Scattering [88] technique, recently developed, is able to capture the small changes of the X-ray beam and reconstruct the spray interface and, after a data analysis [89], provide a projected surface area per beam area. The optical setup and foundations of this technique are more complex in comparison to the previous presented, and the reader can be referred to [88] for more specific information. A Sketch of a USAXS approach is drawn in Figure 1.23. The USAXS can provide the projected area of the spray by scanning it along the axial axis.

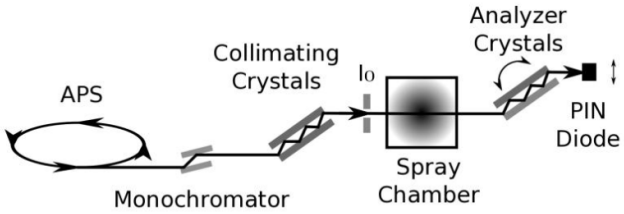

Figure 1.23: Sketch of the experimental setup of USAXS technique from Kastengren et al. [90].

This technique has been applied to the study of the spray core [90, 91], and some of the typical results are shown in Figure 1.24a. It is worth mentioning that, combining the projected volume provided by X-ray radiography and the projected area given by USAXS, it is possible to compute the SMD in the measured section, as can also be noticed in Figure 1.24b.

1.4 Objectives

The different studies presented in this thesis aim to increase the knowledge of the primary atomization process in the near field, either using a more fundamental approach or directly simulating the spray development. As it has been exposed in the literature review, historically, the study of this process has been performed both from the computational and the experimental standpoints. This encourages the study to not focus only on one methodology but try to approach the problem in both directions.

However, each approach has its own characteristics and particularities that make it nearly impossible to perform exactly the same study on both approaches. DNS simulations provide information that can not be acquired by

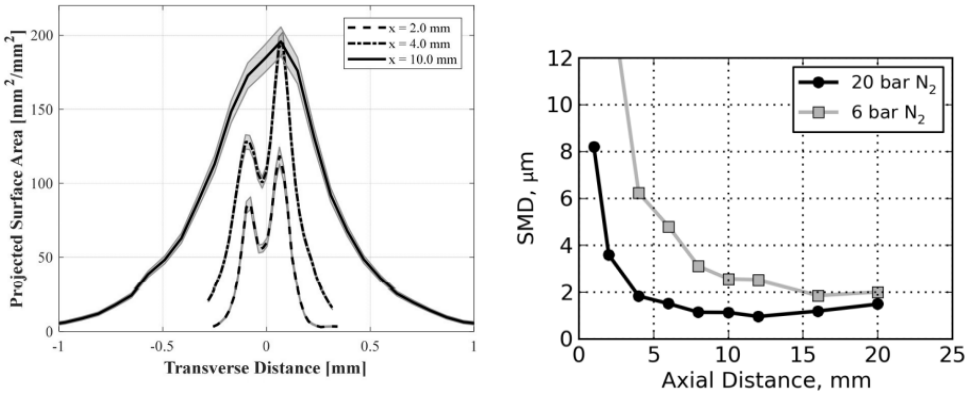

(a) Experimental data from Battistoni et al. [91] *(b) Experimental data from Kastengren et al. [90]*

Figure 1.24: Experimental results using USAXS.

any experimental methodology (as the insights of the droplet formation), but the operating conditions have to be restricted to lower Reynolds numbers. Experimental studies can be performed in realistic operating conditions, providing actual data of the spray development, but are restricted to the optical capabilities. Also, in this particular context, the injector used in this thesis could not inject at very low pressure, and thus, it can not achieve the average injection velocity used on the DNS simulations.

Due to this limitation, both studies will aim for different purposes, and therefore the objectives of each one will be addressed separately in the following subsections.

1.4.1 Computational study

As already commented above, the restrictions of the DNS simulations make computing real industrial applications quite complicated. However, DNS has proved to be an exceptional tool to provide extensive and high-detailed information on both the velocity and scalar fields, which can be used to develop physical knowledge and theories.

Resolving all scales of motion within the computational domain allows connecting the atomization process with the turbulence associated. A DNS calculation is practically an information generator, which leads to a high amount of data that can be unmanageable (up to 12 TeraBytes per simulation). So is essential to have a well-defined methodology for analysing the results. Otherwise, the computational requirements for the post-processing tasks can be even more demanding than the computation itself. This means that sometimes

is needed to know in advance the particularities of the problem and the main results required to extract from the simulations. In this case, many methodologies implemented in Marco's thesis [59] are used, with some modifications and additions to adapt them, in this study.

In this framework, the main purpose of the computational study is to shed light on the influence of the operating conditions on the primary atomization process in the dense region. This analysis has been divided into three different parameters to isolate their effects:

- **Reynolds number,** this parameter is one of the most important when studying the turbulence field of any flow. It is usually used as an indicator of turbulence, and the range of motion scales is directly dependent on it. The features of the DNS calculations that allow the resolution of the smallest motion scales are also limited from low to moderate Reynolds numbers because of the exponential increase of computational resources.
- **Weber number,** when studying two-phase flows, this parameter became crucial to determine also the atomization regime. It correlates the inertial forces with the surface forces, so it is involved with the ligaments breakup and droplet formation. It is also limited with the cell size, being that the definition of a droplet requires at least six grid points to be considered resolved.
- **Nozzle shape,** this study is focused on elliptical nozzles, where the eccentricity factor plays a key role in the turbulence field injected. The non-axisymmetry of these nozzles leads to new motions and new turbulent phenomena that provoke non-uniform atomization in the azimuthal direction. These effects have been addressed already on the far-field, but there are not many detailed studies at the near-field.

This study aims to investigate the influence of these parameters in order to generate a phenomenological model of the primary atomization process, which can be used to improve the knowledge of this phenomenon or the models used on low-detailed simulations.

1.4.2 Experimental study

As reviewed early in the document, several experimental methodologies are developed that use optical diagnosis to study the primary atomization and the spray formation. Among them, DBI is chosen to perform the experiments due to its affordability and its capability to give reliable data on the macroscopic

spray contour. In order to be able to zoom in the near field, a long-distance microscope is used along with a high-speed camera to record the first millimeters of the injection.

The atomizer used for this experiment is a mono-orifice injector, with a high conicity angle to avoid cavitation, with a nozzle exit equal to the one used on the DNS simulations.

The main objective of the experimental study of this document is to correlate the turbulence induced by the injection pressure with the spray opening angle as well as its standard deviation, which can be considerer as a marker for the oscillations in the spray boundary. To this end, different injection pressures and discharge pressures have been used to create an experimental matrix able to study the influence of both parameters separately.

1.5 Thesis outline

The present thesis is organised into ten chapters. The present chapter introduces the atomisation process, focusing on the near-field. A literature review is presented to show the studies performed on the computational and experimental aspects of this process. Finally, the main objectives of this thesis are presented. In Chapter 2, the numerical methods for the DNS simulations are exposed, emphasising the algorithms used in the performed studies.

Chapter 3 focuses on the inflow boundary condition generation for the DNS simulations. Fundamentals of pipe flow are presented there to explain the turbulent characteristics of this kind of flow. The numerical method and turbulence model used on LES simulations are described, as well as the simulation parameters and boundary conditions. These computations are validated with theory, experiments and DNS computations. Then, a study of the turbulent structure generation is performed to closely examine the influence of the Reynolds number and cross-section shape on the vortexes' volume and position.

The last introductory chapter is Chapter 4. There, the main post-processing techniques are explained. Introducing a few concepts of the turbulence associated with this kind of flow and describing the methodologies of droplet detection and characterisation.

As far as the computational study is concerned, it is divided into four chapters, from 5 to 8. Chapter 5 focuses on the Reynolds number variation, with three different levels at a constant Weber number and density ratio. Here the influence of the inflow conditions is studied on the spray disintegration and

droplet formation, as well as on the flow field statistics along the computational domain. The same analysis structure is followed in Chapter 6, but increasing the Weber number at a constant Reynolds number and density ratio (using the lower condition from the previous study). In Chapter 7, the phenomenological model is proposed using the droplet size distributions obtained from Chapters 5 and 6. Finally, Chapter 8 follows a similar structure to Chapters 5 and 6 but analysing the effect of having elliptical nozzle shapes.

On the other hand, Chapter 9 exposes the experimental results obtained by using DBI with a long-distance microscope on an ad-hoc nozzle. These experiments are focused on the spray angle obtained from a Dodecane fuel under different operating conditions on the near-field. Apart from the well-known effect of increasing the spray angle when increasing the injection pressure, the study showed an influence of the injection Reynolds number on the deviation of the detected spray angle, increasing this deviation as the injection pressure increased.

Finally, Chapter 10 exposes this thesis's main conclusions, summarising the investigation's main results and proposing possible directions on which orient the DNS study of primary atomisation.

References

[1] Silk, Eric A., Golliher, Eric L., and Paneer Selvam, R. "Spray cooling heat transfer: Technology overview and assessment of future challenges for micro-gravity application". In: *Energy Conversion and Management* 49.3 (2008), pp. 453–468. DOI: 10.1016/j.enconman.2007.07.046.

[2] Liang, Gangtao and Mudawar, Issam. "Review of spray cooling - Part 1: Single-phase and nucleate boiling regimes, and critical heat flux". In: *International Journal of Heat and Mass Transfer* 115 (2017), pp. 1174–1205. DOI: 10.1016/j.ijheatmasstransfer.2017.06.029.

[3] Liang, Gangtao and Mudawar, Issam. "Review of spray cooling - Part 2: High temperature boiling regimes and quenching applications". In: *International Journal of Heat and Mass Transfer* 115 (2017), pp. 1206–1222. DOI: 10.1016/j.ijheatmasstransfer.2017.06.022.

[4] Hines, R. L. "Electrostatic Atomization and Spray Painting". In: *Journal of Applied Physics* 37 (1966), pp. 2730–2736.

[5] Ruzycki, Conor A., Javaheri, Emadeddin, and Finlay, Warren H. "The use of computational fluid dynamics in inhaler design". In: *Expert Opinion on Drug Delivery* 10.3 (2013), pp. 307–323. DOI: 10.1517/17425247.2013.753053.

[6] Stein, Stephen W., Sheth, Poonam, Hodson, P. David, and Myrdal, Paul B. "Advances in metered dose inhaler technology: Hardware development". In: *AAPS PharmSciTech* 15.2 (2014), pp. 326–338. DOI: 10.1208/s12249-013-0062-y.

[7] Gavtash, B. et al. "A model of transient internal flow and atomization of propellant/ethanol mixtures in pressurized metered dose inhalers (pMDI)". In: *Aerosol Science and Technology* 52.5 (2018), pp. 494–504. DOI: 10.1080/02786826.2018.1433814.

[8] Milenkovic, Jovana, Alexopoulos, Aleck H., and Kiparissides, Costas. "Optimization of a DPI Inhaler: A Computational Approach". In: *Journal of Pharmaceutical Sciences* 106.3 (2017), pp. 850–858. DOI: 10.1016/j.xphs.2016.11.008.

[9] Ogrodnik, Nicholas, Azzi, Victor, Sprigge, Elizabeth, Fiset, Sandra, and Matida, Edgar. "Nonuniform deposition of pressurized metered-dose aerosol in spacer devices". In: *Journal of Aerosol Medicine and Pulmonary Drug Delivery* 29.6 (2016), pp. 490–500. DOI: 10.1089/jamp.2015.1257.

[10] Ziaee, Ahmad et al. "Spray drying of pharmaceuticals and biopharmaceuticals : Critical parameters and experimental process optimization approaches". In: *European Journal of Pharmaceutical Sciences* 127.November (2018), pp. 300–318. DOI: 10.1016/j.ejps.2018.10.026.

[11] Mates, S. P. and Settles, G. S. "A study of liquid metal atomization using close-coupled nozzles, part2: atomization behavior". In: *Atomization and Sprays* 15 (2005), pp. 41–60.

[12] Pendar, Mohammad Reza and Páscoa, José Carlos. "Numerical modeling of the distribution of virus carrying saliva droplets during sneeze and cough". In: *Physics of Fluids* 32.8 (2020). DOI: 10.1063/5.0018432.

[13] Linne, Mark. "Imaging in the optically dense regions of a spray: A review of developing techniques". In: *Progress in Energy and Combustion Science* 39.5 (2013), pp. 403–440. DOI: 10.1016/j.pecs.2013.06.001.

[14] Reitz, Rolf D. and Bracco, Frediano V. "Mechanism of atomization of a liquid jet". In: *Physics of Fluids* 25.10 (1982), pp. 1730–1742. DOI: 10.1063/1.863650.

[15] Lefebvre, Arthur H and McDonell, Vincent G. *Atomization and Sprays*. 2nd Ed. Boca Raton, FL: CRC Press, 2017.

[16] Rayleigh, Lord. "On The Instability Of Jets". In: *Proceedings of the London Mathematical Society* s1-10.1 (1878), pp. 4–13. DOI: 10.1112/plms/s1-10.1.4.

[17] Trettel, Ben. "Reevaluating the jet breakup regime diagram". In: *Atomization and Sprays* 30.7 (2020), pp. 517–556. DOI: 10.1615/ATOMIZSPR.2020033171.

[18] Trettel, Ben. "Conditional damped random surface velocity model of turbulent jet breakup". In: *Atomization and Sprays* 30.8 (2020), pp. 575–606. DOI: 10.1615/AtomizSpr.2020033172.

[19] Payri, Francisco, Bermúdez, Vicente, Payri, Raul, and Salvador, Francisco Javier. "The influence of cavitation on the internal flow and the spray characteristics in diesel injection nozzles". In: *Fuel* 83.4-5 (2004), pp. 419–431. DOI: 10.1016/j.fuel.2003.09.010.

[20] Santos, F. dos and Moyne, L. le. "Spray atomization models in engine applications, from correlations to direct numerical simulations". In: *Oil and Gas Science and Technology* 66.5 (2011), pp. 801–822. DOI: 10.2516/ogst/2011116.

[21] Reitz, Rolf D. and Diwakar, Ramachandr. "Structure of high-pressure fuel sprays". In: *SAE Paper 870598* (1987).

[22] Levy, N., Amara, S., and Champoussin, J. C. "Simulation of a diesel jet assumed fully atomized at the nozzle exit". In: *SAE Technical Papers* 724 (1998). DOI: 10.4271/981067.

[23] Wan, Yuepeng and Peters, Norbert. "Scaling of spray penetration with evaporation". In: *Atomization and Sprays* 9.2 (1999), pp. 111–132. DOI: 10.1615/AtomizSpr.v9.i2.10.

[24] Vallet, A., Burluka, A. A., and Borghi, Roland. "Development of a eulerian model for the "atomization" of a liquid jet". In: *Atomization and Sprays* 11.6 (2001), pp. 619–642. DOI: 10.1002/fld.1650080906.

[25] Pandal, Adrian. "Implementation and Development of an Eulerian Spray Model for CFD simulations of diesel Sprays". PhD thesis. 2016.

[26] Bharadwaj, N., Rutland, C. J., and Chang, S. "Large eddy simulation modelling of spray-induced turbulence effects". In: *International Journal of Engine Research* 10.2 (2009), pp. 97–119. DOI: 10.1243/14680874JER02309.

[27] Lebas, R., Menard, T., Beau, P.A., Berlemont, A., and Demoulin, François-Xavier. "Numerical simulation of primary break-up and atomization: DNS and modelling study". In: *International Journal of Multiphase Flow* 35.3 (2009), pp. 247–260. DOI: 10.1016/j.ijmultiphaseflow.2008.11.005.

[28] Duret, B, Reveillon, J, Menard, T, and Demoulin, François-Xavier. "Improving primary atomization modeling through DNS of two-phase flows". In: *International Journal of Multiphase Flow* 55 (2013), pp. 130–137. DOI: 10.1016/j.ijmultiphaseflow.2013.05.004.

[29] Klein, M. "Direct numerical simulation of a spatially developing water sheet at moderate Reynolds number". In: *International Journal of Heat and Fluid Flow* 26.5 (2005), pp. 722–731. DOI: 10.1016/j.ijheatfluidflow.2005.01.003.

[30] Herrmann, Marcus. "The influence of density ratio on the primary atomization of a turbulent liquid jet in crossflow". In: *Proceedings of the Combustion Institute* 33.2 (2011), pp. 2079–2088.

[31] Mukundan, Anirudh Asuri et al. "DNS and LES of primary atomization of turbulent liquid jet injection into a gaseous crossflow environment". In: *Proceedings of the Combustion Institute* 38.2 (2021), pp. 3233–3241. DOI: 10.1016/j.proci.2020.08.004.

[32] Sauer, B., Sadiki, A., and Janicka, J. "Embedded DNS concept for simulating the primary breakup of an airblast atomizer". In: *Atomization and Sprays* 26.3 (2016), pp. 187–217. DOI: 10.1615/AtomizSpr.2014011019.

[33] Warncke, K. et al. "Experimental and numerical investigation of the primary breakup of an airblasted liquid sheet". In: *International Journal of Multiphase Flow* 91 (2017), pp. 208–224. DOI: 10.1016/j.ijmultiphaseflow.2016.12.010.

[34] Jarrahbashi, D. and Sirignano, W. A. "Invited Article: Vorticity dynamics for transient high-pressure liquid injection". In: *Physics of Fluids* 26.10 (2014). DOI: 10.1063/1.4895781.

[35] Zandian, A., Sirignano, W. A., and Hussain, F. "Planar liquid jet: Early deformation and atomization cascades". In: *Physics of Fluids* 29.6 (2017). DOI: 10.1063/1.4986790.

[36] Lozano, Antonio, García-Olivares, Antonio, and Dopazo, César. "The instability growth leading to a liquid sheet breakup". In: *Physics of Fluids* 10.9 (1998), pp. 2188–2197. DOI: 10.1063/1.869740.

[37] Shinjo, J. and Umemura, Akira. "Simulation of liquid jet primary breakup: Dynamics of ligament and droplet formation". In: *International Journal of Multiphase Flow* 36.7 (2010), pp. 513–532. DOI: 10.1016/j.ijmultiphaseflow.2010.03.008.

[38] Jarrahbashi, D., Sirignano, W. A., Popov, P. P., and Hussain, F. "Early spray development at high gas density: hole, ligament and bridge formations". In: *Journal of Fluid Mechanics* 792 (2016), pp. 186–231. DOI: 10.1017/jfm.2016.71.

[39] Zandian, A., Sirignano, W. A., and Hussain, F. "Understanding liquid-jet atomization cascades via vortex dynamics". In: *Journal of Fluid Mechanics* 843 (2018), pp. 293–354. DOI: 10.1017/jfm.2018.113.

[40] Zandian, Arash, Sirignano, William A., and Hussain, Fazle. "Length-scale cascade and spread rate of atomizing planar liquid jets". In: *International Journal of Multiphase Flow* 113 (2019), pp. 117–141. DOI: 10.1016/j.ijmultiphaseflow.2019.01.004.

[41] Canu, Romain et al. "Where does the droplet size distribution come from?" In: *International Journal of Multiphase Flow* 107.January 2019 (2018), pp. 230–245. DOI: 10.1016/j.ijmultiphaseflow.2018.06.010.

[42] Ménard, T, Tanguy, S, and Berlemont, A. "Coupling level set/VOF/ghost fluid methods: Validation and application to 3D simulation of the primary break-up of a liquid jet". In: *International Journal of Multiphase Flow* 33.5 (2007), pp. 510–524. DOI: 10.1016/j.ijmultiphaseflow.2006.11.001.

[43] Beau, Pierre-Arnaud et al. "Numerical jet atomization: part II-modeling information and comparison with DNS results". In: *Fluids Engineering Division Summer Meeting*. Vol. 47500. 2006, pp. 555–563.

[44] Desjardins, Olivier, Moureau, Vincent, and Pitsch, Heinz. "An accurate conservative level set/ghost fluid method for simulating turbulent atomization". In: *Journal of Computational Physics* (2008). DOI: 10.1016/j.jcp.2008.05.027.

[45] Klein, M., Sadiki, A., and Janicka, J. "A digital filter based generation of inflow data for spatially developing direct numerical or large eddy simulations". In: *Journal of Computational Physics* 186.2 (2003), pp. 652–665. DOI: 10.1016/S0021-9991(03)00090-1.

[46] Shinjo, J. and Umemura, Akira. "Surface instability and primary atomization characteristics of straight liquid jet sprays". In: *International Journal of Multiphase Flow* 37.10 (2011), pp. 1294–1304. DOI: 10.1016/j.ijmultiphaseflow.2011.08.002.

[47] Shinjo, J., Xia, J., and Umemura, Akira. "Droplet/ligament modulation of local small-scale turbulence and scalar mixing in a dense fuel spray". In: *Proceedings of the Combustion Institute* 35.2 (2015), pp. 1595–1602. DOI: 10.1016/j.proci.2014.06.088.

[48] Umemura, Akira and Shinjo, Junji. "Detailed SGS atomization model and its implementation to two-phase flow LES". In: *Combustion and Flame* 195 (2018), pp. 232–252. DOI: 10.1016/j.combustflame.2018.01.026.

[49] Salvador, Francisco Javier, Ruiz, Santiago, Crialesi-Esposito, Marco, and Blanquer, Ignacio. "Analysis on the Effects of Turbulent Inflow Conditions on Spray Primary Atomization in the Near-Field by Direct Numerical Simulation". In: *International Journal of Multiphase Flow* 102 (2018), pp. 49–63. DOI: 10.1016/j.ijmultiphaseflow.2018.01.019.

[50] Herrmann, Marcus. "On Simulating Primary Atomization Using the Refined Level Set Grid Method". In: *Atomization and Sprays* 21.4 (2011), pp. 283–301. DOI: 10.1615/AtomizSpr.2011002760.

[51] Payri, Raul, Salvador, Francisco Javier, Gimeno, Jaime, and Crialesi-Esposito, Marco. "Comparison of mapped and synthetic inflow boundary conditions in Direct Numerical Simulation of sprays". In: *ILASS - Europe 2019, 29th Conference on Liquid Atomization and Spray Systems*. Paris, France, 2019.

[52] Hasslberger, Josef, Ketterl, Sebastian, Klein, Markus, and Chakraborty, Nilanjan. "Flow topologies in primary atomization of liquid jets: A direct numerical simulation analysis". In: *Journal of Fluid Mechanics* 859 (2019), pp. 819–838. DOI: 10.1017/jfm.2018.845.

[53] Popinet, Stéphane. "An accurate adaptive solver for surface-tension-driven interfacial flows". In: *J. Comput. Phys.* 228.16 (2009), pp. 5838–5866. DOI: 10.1016/j.jcp.2009.04.042.

[54] Fuster, Daniel et al. "Simulation of primary atomization with an octree adaptive mesh refinement and VOF method". In: *International Journal of Multiphase Flow* 35.6 (2009), pp. 550–565. DOI: 10.1016/j.ijmultiphaseflow.2009.02.014.

[55] Zhang, Bo, Popinet, Stephane, and Ling, Yue. "Modeling and detailed numerical simulation of the primary breakup of a gasoline surrogate jet under non-evaporative operating conditions". In: *International Journal of Multiphase Flow* 130 (2020), p. 103362. DOI: 10.1016/j.ijmultiphaseflow.2020.103362.

[56] ECN. *Engine Combustion Network*. Online. 2010.

[57] Torregrosa, Antonio J., Payri, Raul, Javier Salvador, F., and Crialesi-Esposito, Marco. "Study of turbulence in atomizing liquid jets". In: *International Journal of Multiphase Flow* 129 (2020), p. 103328. DOI: 10.1016/j.ijmultiphaseflow.2020.103328.

[58] Crialesi-Esposito, Marco, Gonzalez-Montero, L. A., and Salvador, F. J. "Effects of isotropic and anisotropic turbulent structures over spray atomization in the near field". In: *International Journal of Multiphase Flow* 150.November 2021 (2022), p. 103891. DOI: 10.1016/j.ijmultiphaseflow.2021.103891.

[59] Crialesi-Esposito, Marco. "Analysis of primary atomization in sprays using Direct Numerical Simulation". PhD thesis. Universitat Politècnica de València, 2019.

[60] Berrocal, Edouard, Sedarsky, David L., Paciaroni, Megan E., Meglinski, Igor V., and Linne, Mark. "Laser light scattering in turbid media Part I: Experimental and simulated results for the spatial intensity distribution". In: *Optics Express* 15.17 (2007), p. 10649. DOI: 10.1364/oe.15.010649.

[61] Sjöberg, Henrik, Manneberg, Göran, and Cronhjort, Andreas. "Long-working-distance microscope used for diesel injection spray imaging". In: *Optical Engineering* 35.12 (1996), p. 3591. DOI: 10.1117/1.601113.

[62] Manin, Julien, Bardi, Michele, Pickett, Lyle M, Dahms, R N, and Oefelein, Joseph C. "Development and mixing of diesel sprays at the microscopic level from low to high temperature and pressure conditions". In: *THIESEL 2012 Conference on Thermo and Fluid-dynamic Processes in Diesel Engines*. 2012.

[63] Crua, Cyril, Heikal, Morgan R, and Gold, Martin R. "Microscopic imaging of the initial stage of diesel spray formation". In: *Fuel* 157 (2015), pp. 140–150. DOI: 10.1016/j.fuel.2015.04.041.

[64] Pickett, Lyle M., Manin, Julien, Kastengren, Alan L, and Powell, Christopher F. "Comparison of Near-Field Structure and Growth of a Diesel Spray Using Light-Based Optical Microscopy and X-Ray Radiography". In: *SAE Technical Paper 2014-01-1412* 7.2 (2014), pp. 1044–1053. DOI: 10.4271/2014-01-1412.

[65] Manin, Julien, Pickett, Lyle M, and Yasutomi, K. "Transient cavitation in transparent diesel injectors". In: *ICLASS 14th Triennial International Conference on Liquid Atomization and Spray Systems*. Chicago, 2018, pp. 1–9.

[66] Linne, Mark, Paciaroni, Megan E, Hall, Tyler, and Parker, Terry. "Ballistic imaging of the near field in a diesel spray". In: *Experiments in Fluids* 40.6 (2006), pp. 836–846. DOI: 10.1007/s00348-006-0122-0.

[67] Meyer, Terrence R, Brear, Michael, Jin, Seong Ho, and Gord, James R. "Formation and diagnostics of sprays in combustion". In: *Handbook of Combustion: Online* (2010), pp. 291–322.

[68] Linne, Mark, Sedarsky, David, Meyer, Terrence, Gord, James, and Carter, Campbell. "Ballistic imaging in the near-field of an effervescent spray". In: *Experiments in Fluids* 49.4 (2010), pp. 911–923. DOI: 10.1007/s00348-010-0883-3.

[69] Sedarsky, David, Gord, James, Carter, Campbell, Meyer, Terrence, and Linne, Mark. "Fast-framing ballistic imaging of velocity in an aerated spray." In: *Optics letters* 34.18 (2009), pp. 2748–50. DOI: 10.1364/OL.34.002748.

[70] Linne, Mark et al. "Correlation of internal flow and spray breakup for a fuel injector used in ship engines". In: *8th US National Combustion Meeting 2013* 2 (2013), pp. 1–8.

[71] Duran, S P, Porter, J M, and Parker, T E. "Ballistic Imaging of Sprays at Diesel Relevant Conditions". In: *ICLASS 2012*. 2012, pp. 1–5.

[72] Berrocal, Edouard, Kristensson, Elias, Richter, Mattias, Linne, Mark, and Aldén, Marcus. "Multiple scattering suppression in planar laser imaging of dense sprays by means of structured illumination". In: *Atomization and Sprays* 20.2 (2010), pp. 133–139. DOI: 10.1615/AtomizSpr.v20.i2.30.

[73] Kristensson, Elias, Berrocal, Edouard, and Aldén, Marcus. "Two-pulse structured illumination imaging". In: *Optics Letters* 39.9 (2014), p. 2584. DOI: 10.1364/ol.39.002584.

[74] Kristensson, E., Berrocal, E., Richter, M., Pettersson, S.-G., and Aldén, M. "High-speed structured planar laser illumination for contrast improvement of two-phase flow images". In: *Optics Letters* 33.23 (2008), p. 2752. DOI: 10.1364/ol.33.002752.

[75] Berrocal, E., Kristensson, E., Hottenbach, P., Aldén, M., and Grünefeld, G. "Quantitative imaging of a non-combusting diesel spray using structured laser illumination planar imaging". In: *Applied Physics B: Lasers and Optics* 109.4 (2012), pp. 683–694. DOI: 10.1007/s00340-012-5237-9.

[76] Charalampous, Georgios, Hardalupas, Yannis, and K. P. Taylor, A. M. "Novel Technique for Measurements of Continuous Liquid Jet Core in an Atomizer". In: *AIAA Journal* 47.11 (2009), pp. 2605–2615. DOI: 10.2514/1.40038.

[77] Charalampous, Georgios, Hadjiyiannis, C, Hardalupas, Yannis, and Taylor, A.M.K.P. "Measurement of continuous liquid jet length in atomizers with optical connectivity, electrical conductivity and high-speed photography techniques". In: *ILASS Europe 2010*. September. Brno, Czech Republic, 2010, pp. 1–10.

[78] Patil, Shirin and Sahu, Srikrishna. "Liquid jet core characterization in a model crossflow airblast atomizer". In: *International Journal of Multiphase Flow* 141 (2021), p. 103688. DOI: 10.1016/j.ijmultiphaseflow.2021.103688.

[79] Kaiser, Max, Heilig, Ansgar, and Dinkelacker, Friedrich. "Application of the Optical Connectivity Method to a Real Size Heavy Duty CIDI-Injector". In: *COMODIA 2012*. Comodia. 2012, pp. 506–511.

[80] Wang, Yujie et al. "Ultrafast X-ray study of dense-liquid-jet flow dynamics using structure-tracking velocimetry". In: *Nature Physics* 4.4 (2008), pp. 305–309. DOI: 10.1038/nphys840.

[81] Moon, S. et al. "Ultrafast X-ray Phase-Contrast Imaging of High-Speed Fuel Sprays from a Two-Hole Diesel Nozzle". In: *22nd Annual Conference on Liquid Atomization and Spray Systems (ILASS Americas 2010)* May (2010).

[82] Kastengren, Alan L and Powell, Christopher F. "Spray density measurements using X-ray radiography". In: *Proceedings of the Institution of Mechanical Engineers, Part D: Journal of Automobile Engineering* 221.6 (2007), pp. 653–662. DOI: 10.1243/09544070JAUTO392.

[83] Cai, Wenyi et al. "Quantitative analysis of highly transient fuel sprays by time-resolved x-radiography". In: *Applied Physics Letters* 83.2003 (2003), pp. 1671–1673. DOI: 10.1063/1.1604161.

[84] El-Hannouny, Essam M. et al. "Near-Nozzle Spray Characteristics of Heavy-Duty Diesel Injectors". In: *SAE Technical Paper 2003-01-3150* 724 (2003).

[85] Kastengren, Alan L, Powell, Christopher F, Liu, Z., and Wang, J. "Time resolved, three-dimensional mass distribution of diesel sprays measured with x-ray radiography". In: *SAE Technical Paper 2009-01-0840* 4970 (2009), SAE Paper no. 2009–01–0840.

[86] Kastengren, A. L. et al. "Time-resolved X-ray radiography of sprays from Engine Combustion Network spray a diesel injectors". In: *Atomization and Sprays* 24.3 (2014), pp. 251–272. DOI: 10.1615/AtomizSpr.2013008642.

[87] Kastengren, Alan L. et al. "Determination of diesel spray axial velocity using X-ray radiography". In: *SAE Technical Papers* 2007.724 (2007). DOI: 10.4271/2007-01-0666.

[88] Ilavsky, Jan et al. "Ultra-small-angle X-ray scattering at the Advanced Photon Source". In: *Journal of Applied Crystallography* 42.3 (2009), pp. 469–479. DOI: 10.1107/S0021889809008802.

[89] Ilavsky, Jan and Jemian, Peter R. "Irena: Tool suite for modeling and analysis of small-angle scattering". In: *Journal of Applied Crystallography* 42.2 (2009), pp. 347–353. DOI: 10.1107/S0021889809002222.

[90] Kastengren, Alan L et al. "Measurements of droplet size in shear-driven atomization using ultra-small angle x-ray scattering". In: *International Journal of Multiphase Flow* 92 (2017), pp. 131–139. DOI: 10.1016/j.ijmultiphaseflow.2017.03.005.

[91] Battistoni, Michele et al. "Experimental and Computational Investigation of Subcritical Near-Nozzle Spray Structure and Primary Atomization in the Engine Combustion Network Spray D". In: *SAE Technical Paper* 2018-01-0277 (2018), pp. 1–15. DOI: 10.4271/2018-01-0277.

Chapter 2

Computational Methodology

2.1 Introduction

Using DNS to perform computational studies is relatively new in the scientific community. However, back at the end of the XX century, Reynolds [1], and Moin [2] already exposed some potential benefits of using this numerical approach to solve the Navier-Stokes equations (gathered on [3]). However, to be able to resolve these equations is necessary to have a very fine spatial mesh along with a sufficiently small time resolution in order to capture the smallest scales and the fastest frequencies. With these limitations, the physical problems that can be studied with this approach are dependent on the computer architectures, being unfeasible, as of today, the resolution of big complex domains. Nevertheless, the evolution of the High Performance Computers (HPC) and the development of new codes have allowed starting using DNS to study different physical problems, as the multiphase flows.

Therefore, as the turbulence of the problem defines the minor flow structures, it is the limiting factor for DNS. That is why most of the studies performed with DNS have typically low or moderate Reynolds numbers. However, Fuster and Popinet [4] developed an All-Mach method able to perform DNS with compressible effects. This method has been applied to fundamental problems on single phase simulations and multiphase flows with the droplet/shock interaction. Even so, the application to more complex problems is still ongoing.

When choosing the numerical methods, one of the most important features is spatial discretisation. The resolution of the smallest turbulent and multiphase scales is prone to provoke a rapid increase in the number of cells, leading to an extensive simulation that will likely not be affordable. Among all the mesh types that exist, Cartesian meshes are the most extended type due to their simplicity (see works presented in Chapter 1 [5–7]). In these meshes, the cells are cuboids, and the computational domains are usually prisms. This configuration allows splitting the computational load evenly among the processes, leading to quite good strong and weak scalability. Also, as the output data is sorted, its post-processing is often straightforward. However, the amount of data produced in this kind of meshes is huge and typically needs previous knowledge of the problem to select the specific data needed to avoid an unmanageable amount of information. Some multiphase flows DNS codes that use this kind of meshes are ARCHER [8], FS3D [9], and PARIS Simulator [10].

Since the high amount of information that can generate the DNS simulations can be a significant drawback to simulating larger domains, some solutions have arisen to overcome this problem. Adaptive Meshing Techniques (AMR) provide an effective way to decrease the mesh size, maintaining the accuracy of the results. This kind of algorithm often refines the mesh due to velocity gradients or density variations, which in theory comprises the mechanisms of multiphase flows. However, the local refinement can cause new drawbacks in these simulations as the larger cells may act as low-pass filters, losing information from the smallest waves. Also, as the mesh is dynamically adapted to the flow, the number of cells varies during the simulation requiring an efficient load balancing between processors to achieve proper scalability when using thousands of cores. Although codes as Gerris [11] or Basilisk [12] (both based on the Octree refinement) have demonstrated their suitability to perform simulations on this kind of flows [13, 14], these uncertainties and the added difficulty to perform the post-processing of the output data, have dissuaded its usage from performing the study of this thesis. Nevertheless, as the study presented in this document has shed some light on the processes within the atomization, they might be helpful to calibrate the refinement algorithms and remove some of the uncertainties in the future.

Finally, the numerical code chosen for this thesis is PARIS Simulator as this thesis is a continuation of the previous study performed by Crialesi on [15]. This code offers a structure that can be easily modified to add features such as the boundary conditions reader or the option of HDF5 data format to store the output information, besides an efficient parallelisation. Further code features will be presented following in this Chapter.

This section will present the main numerical methods, focusing on the methods applied to multiphase flows. This explanation aims to give an overview of the numerical methods (emphasizing the ones used on PARIS Simulator) without explaining the full implementation ([16] presents an in-depth presentation of the different methods). So, first, in Section 2.2, the governing equations for multiphase flows are presented, presenting the fluid problem. Section 2.3 presents the different numerical methods used to resolve each term of the momentum equation. As the gas-liquid interaction is the characteristic feature of multiphase flows, Section 2.4 focuses on the different methods to deal with the liquid advection and the surface tension forces. Finally, Section 2.5 presents the methods implemented on PARIS Simulator and, more specifically, the ones used to perform the simulations presented in this thesis.

2.2 Governing equations for multiphase flows

Computational studies are often performed under isothermal and adiabatic conditions when addressing more fundamental studies. Although most engineering applications present temperature changes, many experiments can be carried out under these conditions. With this approach, the need to solve the energy equation is removed, maintaining its accuracy. Regarding the compressibility effects, this study will be focused on incompressible flows. The assumption of this hypothesis leads to the following expression for the continuity equations:

$$\nabla \cdot \mathbf{u} = 0 \tag{2.1a}$$

$$\rho \left(\partial_t \mathbf{u} + \mathbf{u} \cdot \nabla \mathbf{u} \right) = -\nabla p + \mu \nabla \cdot \left(\partial_i u_j + \partial_j u_i \right) + \sigma \kappa \delta_s \mathbf{n} \tag{2.1b}$$

Where $\mathbf{u}$ is the velocity field, which is divergence-free due to the incompressibility nature of the problem as stated in Equation 2.1a. The physical properties of the fluids ρ and μ are the density and the dynamic viscosity, respectively. The Equation 2.1b is expressed to include both fluids in a single equation, avoiding the necessity of having two formulas with jump conditions to couple the solution on the interface; this is known as the one-fluid approach. The pressure is represented by p.

Finally, the one-fluid formulation requires a term to add the surface tension of the interface as a body force. To this end, the last term of Equation 2.1b is added, allocating the stresses on the surface, where the Dirac function δ is one.

However, this allocation requires an infinitesimal grid size to detect a sharp interface, which can not be achieved in numerical simulation. Thus a special treatment is necessary to locate the surface. The stresses within the interface are computed using the surface tension σ, the liquid surface curvature κ, and the normal vector of the surface $\mathbf{n}$.

When studying multiphase flows, one of the main particularities is to detect the interface between two fluids and estimate their physical properties. There are several ways to describe the interface location and its tracking during the simulation (some will be discussed later). However, many of them use a Heaviside function as a marker, defined as a discontinuous function by Equation 2.2.

$$H(\mathbf{x}) = \begin{cases} 1 & \text{if inside a closed interface;} \\ 0 & \text{if outside a closed interface.} \end{cases} \tag{2.2}$$

Usually is defined that $H = 1$ for the liquid and $H = 0$ for the gas. So this function can be accurately used to describe the sharp interface between both fluids by computing the physical properties as:

$$\rho(x) = \rho_l H(x) + \rho_g(1 - H(x)) \tag{2.3a}$$

$$\mu(x) = \mu_l H(X) + \mu_g(1 - H(x)) \tag{2.3b}$$

A more extensive explanation of the equations and terms can be found at [16].

2.3 Numerical solution for the Navier-Stokes equations

The main feature of DNS is that they directly resolve the Navier-Stokes equations numerically. This resolution can be performed with different methods. In this section, the spotlight will be put on the method used in the PARIS code, which is the one used to perform all the simulations of this research. This code is based on finite volume computations and, thanks to the one-fluid formulation, the resolution is similar to the single-phase flows but accounting for the physical properties (generally the density and viscosity) change between phases and the location of the interface. As a starting point, the

momentum equation (Eq. 2.1b) is rewritten in a different style to address during the explanation as:

$$\rho\partial_t\mathbf{u} + \rho\mathbf{A} = -\nabla p + \mathbf{D} + \mathbf{F} \tag{2.4}$$

where $\mathbf{A}$ is the advection term, $\mathbf{u}\cdot\nabla\mathbf{u}$, $\mathbf{D}$ is the diffusion term, $\mu\nabla\cdot(\partial_i u_j + \partial_j u_i)$, and F is the all other forces, in this case will only take account of the surface forces (as the gravity is neglected in this study).

The numerical resolution will be addressed in the following sections by separating the different parts to improve the readability. Starting with the temporal integration, followed by the spatial discretisation, then the advection and the viscous terms and finally the pressure equation. However, the following explanations can be found widely discussed on [16].

2.3.1 Temporal integration

There are several methods to perform the time integration as the well-known Pressure Implicit with Splitting Operators (PISO) or the Semi-Implicit Method for Pressure Linked Equations (SIMPLE). However, regarding DNS multiphase flows, the Chorin projection method [17] is one of the most widely chosen to perform this task.

This method has two steps. First, the velocity field is computed ignoring the pressure gradient. The resulting velocity field is not usually divergence-free, so the second step uses the pressure gradient to correct the first result. This last step is the projection onto a space of divergence-free velocity field, hence the method's name. Although all the simulations performed in this thesis used a second-order accurate time and space integration, the method will be presented in a first-order formulation to improve readability and comprehension. First, the expression of the first-order explicit, forward-in-time for the velocity field time derivatives can be expressed as:

$$\partial_t\mathbf{u} = \frac{(\mathbf{u}^{n+1} - \mathbf{u}^*) + (\mathbf{u}^* - \mathbf{u}^n)}{\Delta t} \tag{2.5}$$

here the superscripts n and $n+1$ refer to the current and the next time-steps, respectively. $\mathbf{u}^*$ is the temporal velocity field that will be computed on the first step of the method, and Δt is the time-step. Therefore, the first step of the method would be solving the second parenthesis of Equation 2.5 ignoring the pressure effects.

$$\frac{(\mathbf{u}^* - \mathbf{u}^n)}{\Delta t} = -\mathbf{A}^n + \frac{\mathbf{D}^n + \mathbf{F}^n}{\rho^n} \tag{2.6}$$

Once the preliminary velocity field is obtained, the rest of the Equation 2.4 can be expressed to perform the projection step as:

$$\frac{(\mathbf{u}^{n+1} - \mathbf{u}^*)}{\Delta t} = \frac{-\nabla p}{\rho^n} \tag{2.7}$$

Up to this point, the only thing remaining to obtain before is the pressure gradient that ensures that the velocity of the next time-step is divergence-free. So the divergence of Equation 2.7 is taken to express the pressure as:

$$\nabla \cdot \left(\frac{\nabla p}{\rho^n}\right) = \frac{\nabla \mathbf{u}^*}{\Delta t} \tag{2.8}$$

Being Equation 2.8 the Poisson equation for the pressure where the dependence of $\mathbf{u}^{n+1}$ is removed.

Finally, the simplest way to achieve the second-order extension can be done by repeating the algorithm proposed twice and averaging the results. So, the first $\mathbf{u}^{n+1}$ obtained is now called as a temporal field $\mathbf{u}^{tmp}$, used to compute the Right Hand side of Equation 2.4. Then with the new temporal conditions, apply the same algorithm to obtain the new velocity field, $\mathbf{u}^{n+2}$. In the end, the resulting velocity field is the average between the initial velocity field and the last one:

$$\mathbf{u}^{n+1} = 0.5 \cdot (\mathbf{u}^n + \mathbf{u}^{n+2}) \tag{2.9}$$

note that $n + 2$ refers to the second resolution of the velocity and is not a temporal one. It is also worth mentioning that a further extension of this method can be found in [18] where the changes in material properties are taken into account.

2.3.2 Spatial integration

The governing equations are discretised using the finite volumes approach, applying mass and momentum conservation principles on small control volumes. PARIS uses a fixed Cartesian mesh, meaning that the small control volumes are cubes, leading to an easy automatic way of mesh generation and parallelisation. However, there are two main approaches regarding the way

that variables are stored within the cells. On the one hand, *collocated* grids storage all the variables at the cell centres, while the *staggered* grids storage the pressure and material properties at the cell centres, and the velocity fields are stored at the cell faces.

Using *staggered* grids provide three main advantages over using *collocated grids*. One is that the production of conservative methods is relatively simpler to produce in *staggered* grids. The second one is accuracy. Being that the variables are stored both on cell centres and faces in *staggered* grids, the solution is performed on a finer grid. The third and last, *staggered* grids provide tighter coupling between variables, producing lower numerical fluctuations.

For these reasons, and because it has proved to be more suitable for incompressible flows, the *staggered* grid is chosen as the spatial discretisation. Note that the full numerical discretisation of Equation 2.4 has been omitted because of its tedious mathematical elaboration. Again it can be found at [16].

2.3.3 Advection term

Now the different terms that appear on Equation 2.4 will be exposed separately, starting with the advection term **A**. This term is based on the derivatives of the velocity, which means that its calculation is the same for multiphase flows that for single flows. The original Markers-And-Cells (MAC) formulation [19] used single explicit first-order projection for the time integration and centred differencing for all spatial variables. Later, centred second-order schemes appeared and provided more accurate results. However, the best results were obtained in fully-resolved flows, producing non-physical oscillations when the flow was not fully resolved. Also, when computing inviscid flows along the time integration explained at Section 2.3.1, the behaviour is unstable if there are not any diffusion terms that stabilize it (extremely limiting the time-step).

Currently, there are some methods used to avoid these behaviours when computing the advection terms:

- **Quadratic Upstream Interpolation for Convective Kinematics (QUICK):** a third-order upwind-biased polynomial method, developed by Leonard [20]. Although it does not remove all the numerical oscillations at high-velocity gradients, they are much more robust and accurate than the first-order upwind method and spread in many CFD codes.

- **Essentialy Non-Oscillating (ENO):** developed by Shu and Osher [21]. It is based on extrapolating the edge values from the known values at the center of the control volumes. To this end, uses the slope limiter MINMOD by Sweby [22]. This method is even more robust than QUICK method, and despite being its basic version second-order, it can be implemented in higher order versions. A further modification of this method was performed by Liu et al. [23] developing the weighted version WENO.
- **Bell-Collela-Glaz (BCG):** is a variant of the ENO approach and developed by Bell et al. [24]. This method is used in various DNS codes [11, 12].

2.3.4 Viscous term

Continuing with the terms of Equation 2.4, the viscous term **D** will be introduced in this section. As presented earlier in this document, the viscous term depends on the velocity field and the dynamic viscosity. When it comes to resolving multiphase flows, the dynamic viscosity is space dependant. So, if the viscosity is constant in each fluid but varies across the interface, it can be expressed as in Equation 2.3b. The main problem appears when the viscosity ratio between both fluids is high, which leads to a discontinuity of the velocity derivative. Thus, the results obtained are not consistent when applying the numerical derivatives using second-order centred differences.

In order to face this problem, different approaches have been studied, as using only the values from one side of the interface. Other approaches use the harmonic or the arithmetic mean to compute the viscosity. Each method presents different drawbacks when resolving high viscosity ratios. The harmonic mean enhances the lowest viscosity, while the arithmetic mean favours the largest viscosity. In practice, the arithmetic mean moves the interface towards the small viscosity region, creating a high viscosity region around the interface, which may have a dumping effect on the short-wavelength instabilities on the liquid surface, avoiding its perturbation. A consistent second-order method has not been published to overcome this problem [16].

2.3.5 Solving the pressure equation

Once obtained the advection term **A**, the viscous term **D**, the body forces **F** (this term will be studied in-depth on the following section), the preliminary velocity field $\mathbf{u}^*$ can be computed using Equation 2.6. Then the Poisson equation (Equation 2.8) is all defined and can be reorganised to isolate the

pressure term. In one dimension, staggered grids can be expressed as Equation 2.10.

$$p_i = \frac{\frac{1}{\Delta x^2} \cdot \left(\frac{p_{i+1}}{\rho^n_{i+1} + \rho^n_i} + \frac{p_{i-1}}{\rho^n_i + \rho^n_{i-1}} \right) + \frac{\left(u^*_{i+1/2} - u^*_{i-1/2} \right)}{2\Delta t \Delta x}}{\frac{1}{\Delta x^2} \cdot \left(\frac{1}{\rho^n_{i+1} + \rho^n_i} + \frac{1}{\rho^n_i + \rho^n_{i-1}} \right)} \tag{2.10}$$

This equation can be extended to higher dimensions, as presented in [3, 16]. Different methods have been developed to resolve this equation, heavily based on iterating until reaching the convergence of the pressure value. Those methods are highly influenced by the density ratio between fluids, requiring more elaborated developments to obtain the pressure field accurately. However, as the density ratios present in this study are sufficiently low the Succesive Over Relaxation (SOR) method will be presented below.

The Successive Over Relaxation (SOR) is a straightforward approach to resolve the pressure iteratively. In this case, the pressure values from the previous iteration are used and weighted to compute the pressure on the next iteration as shown in Equation 2.11: b

$$p^{\alpha+1}_i = \beta \cdot \frac{\frac{1}{\Delta x^2} \cdot \left(\frac{p^\alpha_{i+1}}{\rho^n_{i+1} + \rho^n_i} + \frac{p^\alpha_{i-1}}{\rho^n_i + \rho^n_{i-1}} \right) + \frac{\left(u^*_{i+1/2} - u^*_{i-1/2} \right)}{2\Delta t \Delta x}}{\frac{1}{\Delta x^2} \cdot \left(\frac{1}{\rho^n_{i+1} + \rho^n_i} + \frac{1}{\rho^n_i + \rho^n_{i-1}} \right)} + (1 - \beta) p^\alpha_i \tag{2.11}$$

where α is the iteration step, and β is the relaxation parameter, usually taking values between 1.2 - 1.5. When initializing the simulation, the pressure values are set to 0 to start the iteration process, but once the simulation has started, the pressure values from the previous timestep are usually an excellent estimation to speed up the iteration process. This formulation requires storing the pressure for the current timestep and the previous one ($p^{\alpha+1}$ and p^α), increasing its computational cost. However, the convergence speed can be improved by applying the *Gauss-Seidel* method. This method resolves the pressure on $\alpha + 1$ orderly along the i direction so that it can use $p^{\alpha+1}_{i-1}$ instead of the p^α_{i-1} in Equation 2.11. With this approach, the solution is "propagated" during the pressure computation, being more memory-efficient and storing only one pressure field.

2.4 Fluid interface advection

The central theme of this thesis is the study of multiphase flows, so it is mandatory to study in-depth the particularities of this kind of flows. So far, the numerical methods already described are well-known in CFD. However, the interface treatment in multiphase flows has been developed mainly in the last 40 years and requires further explanation.

There is not a unique way to describe a liquid surface. Depending on the definition of the surface and its motion, the are two main methods: the *interface-tracking*, based on the Lagrangian approach; and the *interface-capturing*, based on the Eulerian approach. As already introduced in section 2.2, many methods use a marker function as the Heaviside function to get rid of having two meshes to define the solution. So, advecting the Heaviside function shown on Equation 2.2, the motion of the surface can be written as:

$$\partial_t H(x) + \mathbf{u}\nabla H(x) = 0 \tag{2.12}$$

In this case, the formulation is intrinsically Eulerian, and the surface position must be determined, hence the name of *interface-capturing* methods. From this category, VOF and LS are highlighted for being the ones that are more extended.

On the other hand, when the topological changes are not important, the surface can be defined as a function of position. Being all the points of the surface defined x_S, the surface motion can be expressed as:

$$\frac{dx_S}{dt} = \mathbf{u}(x_s, t) \tag{2.13}$$

This equation applied is entirely a Lagrangian method. Among these methods, the Front-Tracking method (FT) requires an Eulerian mesh to follow the surface points obtained on a Lagrangian mesh. This method will be presented below.

As previously exposed, several methods have been developed to describe the interface location and motion. Since all the computations presented in this work have been performed using the VOF method, it will be described in more detail. Nevertheless, other approaches will also be presented to give a broader perspective of how this problem has been addressed from another point of view.

Volume-Of-Fluid (VOF)

This method uses the color function C instead of the Heaviside function as a marker function. This function is an approximation of the Heaviside function in order to be able to work with it computationally. Thus, the color function varies between 0 and 1, corresponding to the fluids studied. It can be directly defined as already presented with the Heaviside function on Equations 2.2, 2.3 and 2.12. So basically, is the average value of the Heaviside function in each computational cell, leading to the following expression on a rectangular two dimensional cell:

$$C_{ij} = \frac{1}{\Delta x \Delta y} \int_V H(x, y) dx dy \tag{2.14}$$

In these methods, the interface cells, which are partially occupied, present values of the color function of $0 < C < 1$. So, the main issue of this method is computing the advection part of the equation to solve the propagation of the interface. While in one-dimensional problems, the solution is trivial, being that the interface is normal to the propagation direction and its location is at $\Delta x C$ when it comes to two or three dimensions, the solution is way more complicated. In this context, different approaches have been developed to overcome this issue:

- **Simple Line Interface Calculation (SLIC):** proposed by Noh and Woodward [25], the marker function is advected by time splitting. The advection is performed in each direction dividing the cell, normal to the propagation direction, into the empty and full parts, depending on the surrounding cells.
- **Hirt and Nichols approach:** [26] they proposed a simpler approach, also using straight lines parallel to the coordinate axis, but using the same orientation to advect in all directions. To determine the direction of the interface, the method studied the color function values on the neighbouring cells to compute the normal of the surface on that cell and then, select the direction that was more aligned. However, the results obtained with this method were not relevantly more accurate than those obtained with the SLIC method. Furthermore, both methods present a considerable amount of artificial breakup.
- **Piecewise Linear Interface Calculation (PLIC):** developed by DeBar [27] and Youngs [28]. The previous methods pointed out the importance of reconstructing the cell interface using the color function of

both the cell and the neighbouring cells. So, being insufficient to describe the interface using the normal cells directions, the PLIC method uses a straight line segment in each cell but can be orientated in any direction. Therefore, the key of this method is to find the correct surface normal **n** which is non-trivial, and many authors have developed different complex algorithms. Among these algorithms emphasize the Youngs' finite-difference method [29, 30], the height method [16], the ELVIRA method [31] and the least-squares fit method [32].

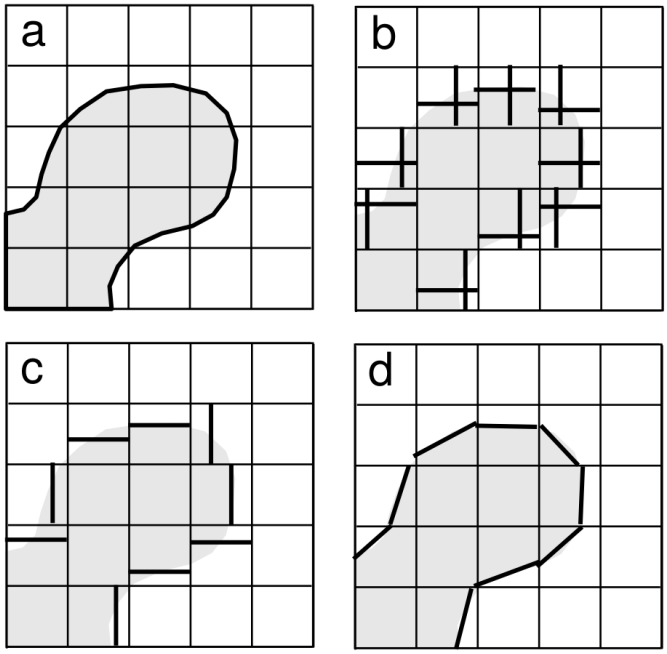

Figure 2.1: Different VOF surface reconstruction methods in 2D (from [16]). ***a)*** *The original interface,* ***b)*** *SLIC reconstruction,* ***c)*** *the method proposed by Hirt and Nichols and* ***d)*** *the PLIC reconstruction.*

A graphical overview of these methods is well represented at Figure 2.1, extracted from [16] which is indeed an adaptation from Rudman [33].

Level-Set (LS)

The LS method is also a *interface-capturing* method but, unlike VOF method, uses a smooth marker function identified as $F(\mathbf{x}, t)$. This function varies from positive values in one fluid to negative values in the other fluid. So the interface

between both fluids is defined by the curve $F(\mathbf{x}, t) = 0$. This function moves with the fluid so it can be advected as Equation 2.12, replacing the Heaviside function, H, with the LS function F.

The surface motion only depends only on the normal velocity component of the interface. This direction is directly computed as:

$$\mathbf{n} = -\frac{\nabla F}{|\nabla F|} \tag{2.15}$$

This equation means that there is no surface reconstruction method necessary, as opposed to the VOF method as exposed above. In addition, due to the smoothness of the function, its advection can be computed using any standard method for hyperbolic equations (as the ENO method). However, in order to reconstruct the physical properties on the interface, a Heaviside function is needed and can be expressed as:

$$I(F) = \begin{cases} 1 & \text{if } F < -\alpha_{LS}\Delta x; \\ \frac{1}{2}(F/\alpha_{LS}\Delta x) + \frac{1}{\pi} sin(\pi F/\alpha_{LS}\Delta x))/\pi & \text{if } F \leq \alpha_{LS}\Delta x; \\ 0 & \text{if } F > \alpha_{LS}\Delta x; \end{cases} \tag{2.16}$$

where α_{LS} is a coefficient that represents the thickness of the interface. It can be adjusted as wished and often is set to 3.

The simplicity of the method and the fact that there is no need to use additional methods to reconstruct the liquid surface have given the LS method high popularity when resolving multiphase flows, specially for sprays. However, its early implementations demonstrate to have considerable problems regarding the mass-conservation. To overcome this problem, more accurate methods have been developed increasing the complexity of the method, as the Accurate Conservative Level-Set (ACLS) [34] and also coupling with the VOF methods known by its acronym CLSVOF [35] or with the Ghost Fluid Method [36]. Nevertheless, this added complexity diminishes the main appeal of the original LS method of simplicity and performance.

Front-Tracking (FT)

In this kind of method, the interface is represented by connected marker particles that are advected by the fluid velocity. These particles are interpolated from the fixed grid, where the governing equations for the fluid flow are solved.

In fact, how the front interacts with the fixed grid is the main difference between the methods that implement this approach. Regarding low to moderate Reynolds number on multiphase flows, a first model has developed by Unverdi, and Triggvason [37] using the front to modify the marker function and to add the surface tension. Later this method was extended by Triggvason et al. in [38].

Although these methods require an additional grid to locate the marker particles, the requirements to manage this grid are usually minor compared to the effort needed to perform the simulation. Also, as the interface position is known, the determination of the surface curvature and forces are simpler than in other methods. However, front-tracking methods present some limitations to handle topological changes, where the fluid region breaks up or merges. These methods can not resolve these events automatically, requiring manual intervention. The interfaces will not fuse in these methods unless something special is done.

These drawbacks prove the incompatibility of these methods when studying the atomization process by DNS. Nevertheless, it has demonstrated its suitability to perform fundamental studies being its accuracy in defining the liquid surface.

2.4.1 Surface tension treatment

Returning to the govern equations (Equation 2.4), the only term that is left to explain is the body forces term $\mathbf{F}$, that, being that the gravity is not accounted in this document, can be wrote as:

$$\mathbf{F} = \sigma\kappa\delta_s\mathbf{n} \tag{2.17}$$

Considering σ a constant physical property and δ_s the Dirichlet function to apply the forces at the surface, the main problem of computing this term relies on the estimation of the curvature κ and the surface normal direction $\mathbf{n}$.

There are different ways to compute the surface forces, depending on if the fluid interface is obtained by *interface-capturing* methods or *interface-tracking* methods. As this study is performed using the VOF method, the explanation will focus on those used in this study. However, further information on the different existing methods can be found at [16] and [39].

Continuous Surface Force method (CSF)

The original CSF model was first introduced by Brackbill et al. [40] and interpreted the surface tension as a continuous volume force in the surroundings of the interface. This method can be almost directly applied with both VOF and LS approaches. Focusing on the VOF application, the δ_s can be approximated by $|\nabla C|$ since the color function C is the numerical approximation of the Heaviside function. This leads to the following expression for the surface forces:

$$\mathbf{F} = \sigma\kappa|\nabla C|\mathbf{n} \tag{2.18}$$

Here, the curvature κ needs to be found. There are different approaches that use the curvature of the surface or the local curvature. In this case, the curvature of the surface can be calculated with the following expression:

$$\kappa = -\nabla\mathbf{n} \tag{2.19}$$

As the VOF color function is not continuous, sometimes it is necessary to smooth the δ function. Nevertheless, a simple method that results without any smoothing can provide a very accurate balance between pressure and surface tension in special cases as spherical droplets or round cylinders. When smoothed the field, the method is called *smoothed* CSF. Although this method is remarkably simple, it leads to noise and spurious current propagations.

This method has derived into new approaches as the Continuous Surface Stress (CSS), a conservative method that does not need to compute the curvature. However, the computation of the pressure drop along the interface is not simple.

Also, the original CSF can be improved by the Proper Representation Of Surface Tension (PROST) method introduced by Renardy and Renardy [41] which uses a quadratic curvature fitting to the color function C in a 3x3 block. The main drawback is the computational requirements needed to obtain the least-squares curve.

Height Function method (HF)

The HF curvature calculation was initially proposed by Torrey et al. [42] and has gained importance in the last years because it has been proved its ability to achieve accurate curvature estimations. The HF approach has been used to perform curvature computations in several studies [43–45], and is based on three simple steps:

1. Estimate the interface orientation, by determining the maximal component of the **n**, to choose a stencil (3x7 or 3x7) where the curvature will be evaluated.

2. Build the height function by summing the volume fractions in each column or file (depending the stencil's orientation).

3. Calculate the local curvature with the centred finite differences using the following expression:

$$\kappa = \frac{h''}{(1 + h'^2)^{3/2}} \tag{2.20}$$

Figure 2.2 (from [16]) shows the schematics of the stencil used in this method for the case where the normal is oriented along the x direction. So, applying central differences to Equation 2.20 the curvature can be wrote as:

$$\kappa = \frac{(x_{j+1} - 2x_j + x_{j+1})/h^2}{(1 + [(x_{j+1} - x_{j-1})/2h]^2)^{3/2}} \tag{2.21}$$

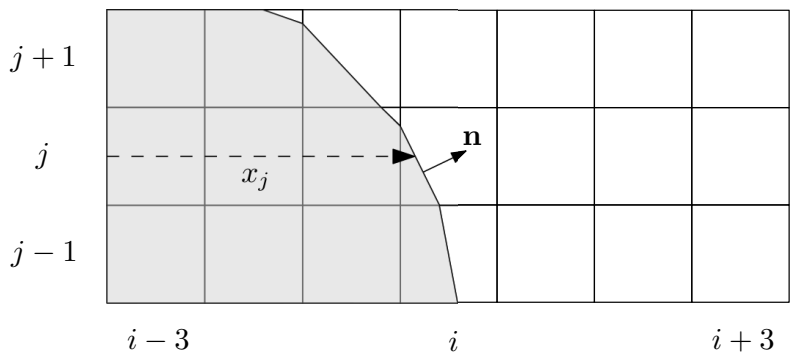

Figure 2.2: Computing the height function in a 7 x 3 stencil when $|n_x| > |n_y|$.

However, one of the main drawbacks of this methodology is that it becomes inconsistent when the radius of curvature is comparable to the mesh size, which often takes place when dealing with topology changes. To deal with this problem, Popinet [45] proposed a code where, if the HF method fails to reconstruct the surface curvature because the C field is too irregular, it uses a fitting curve through these points to give an estimation of the curvature.

2.5 PARIS Simulator Code

In this section, the PARIS code will be presented since it is the one chosen to perform the different atomization simulations. PARIS is a free code for the study of Computational Fluid Dynamics or multiphase flows. It has implemented many ideas and methods discussed above that can be selected depending on its suitability for the problem to resolve.

Among the main features of the code [10], the following characteristics can be highlighted: is written in Fortran 90, it uses a fixed Cartesian staggered Mesh for the finite volume discretisation. The computational domains are prismatic and use MPI and a regular array of subdomains for parallelisation, improving the code performance. Figure 2.3 from [15] shows the good scalability of the code on Marconi (Bologna, Italy) and Marenostrum4 (Barcelona, Spain) supercomputers.

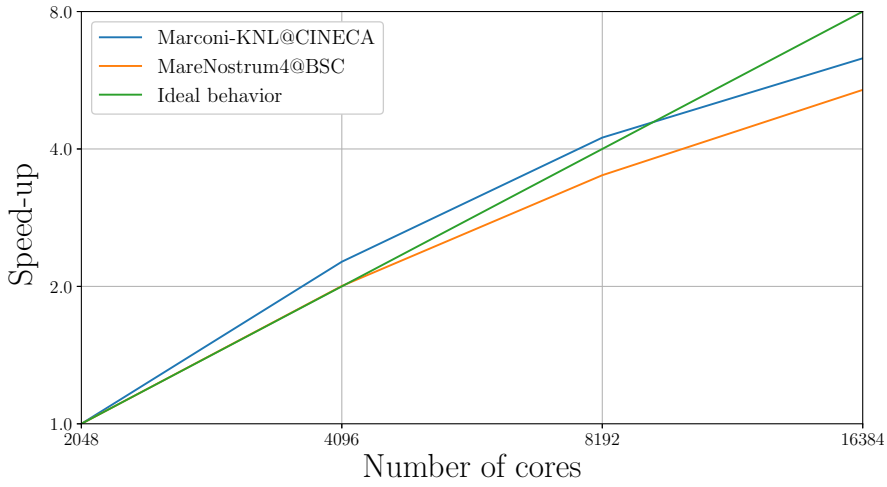

Figure 2.3: PARIS Simulator code scalability on Marconi and MareNostrum4 supercomputers, from Crialesi [15].

For the temporal solution, the code uses the Chorin projection method in its second-order predictor-corrector formulation. The pressure iteration is computed with the internal Poisson solver with over-relaxation since preliminary studies have proved more stability.

It implements different methods to compute the advection term as QUICK, ENO, Superbee, or Verstappen. The QUICK method is used for this study, and the diffusive flux is solved using a second-order central scheme.

Regarding the fluid interface advection, VOF and FT methods are implemented to follow interfaces. Due to the complexity of the interface of the spray simulations and the inability of the FT to handle such topology changes, the VOF method is chosen. Among the methods developed to reconstruct the interface, PARIS uses a modification of the PLIC method called Calcul d'Interface Affine par Morceaux (CIAM)[30]. The surface tension contribution is calculated using a Balanced CSF method along with HF (Popinet [45]) for the curvature computations and surface tension forces.

References

[1] Narasimha, R and Lumley, J. "Whither turbulence? Turbulence at the crossroads". In: *Lecture Notes in Physics, Proceedings of a workshop held at Cornell University, Ithaca New York, March*. 1989, pp. 22–24.

[2] Moin, Parviz and Mahesh, Krishnan. "DIRECT NUMERICAL SIMULATION: A Tool in Turbulence Research". In: *Annual Review of Fluid Mechanics* 30.1 (1998), pp. 539–578. DOI: 10.1146/annurev.fluid.30.1.539.

[3] Versteeg, H K and Malalasekera, W. *An introduction to computational fluid dynamics*. 2nd. Pearson Education Limited, 2007.

[4] Fuster, Daniel and Popinet, Stéphane. "An all-Mach method for the simulation of bubble dynamics problems in the presence of surface tension". In: *Journal of Computational Physics* 374 (2018), pp. 752–768. DOI: 10.1016/j.jcp.2018.07.055.

[5] Shinjo, J. and Umemura, Akira. "Simulation of liquid jet primary breakup: Dynamics of ligament and droplet formation". In: *International Journal of Multiphase Flow* 36.7 (2010), pp. 513–532. DOI: 10.1016/j.ijmultiphaseflow.2010.03.008.

[6] Hasslberger, Josef, Ketterl, Sebastian, Klein, Markus, and Chakraborty, Nilanjan. "Flow topologies in primary atomization of liquid jets: A direct numerical simulation analysis". In: *Journal of Fluid Mechanics* 859 (2019), pp. 819–838. DOI: 10.1017/jfm.2018.845.

[7] Payri, Raul, Salvador, Francisco Javier, Gimeno, Jaime, and Crialesi-Esposito, Marco. "Comparison of mapped and synthetic inflow boundary conditions in Direct Numerical Simulation of sprays". In: *ILASS - Europe 2019, 29th Conference on Liquid Atomization and Spray Systems*. Paris, France, 2019.

[8] CORIA. *Archer code*. 2005.

[9] University of Stuttgart. *FS3D code*. 2010.

[10] Zaleski, S, Tryggvason, G, and Scardovelli, R. *ParisSimulator code*. 2013.

[11] Popinet, Stéphane. *Gerris code*. 2010.

[12] Popinet, Stéphane. *Basilisk code*. 2014.

[13] Fuster, Daniel et al. "Simulation of primary atomization with an octree adaptive mesh refinement and VOF method". In: *International Journal of Multiphase Flow* 35.6 (2009), pp. 550–565. DOI: 10.1016/j.ijmultiphaseflow.2009.02.014.

[14] Zhang, Bo, Popinet, Stephane, and Ling, Yue. "Modeling and detailed numerical simulation of the primary breakup of a gasoline surrogate jet under non-evaporative operating conditions". In: *International Journal of Multiphase Flow* 130 (2020), p. 103362. DOI: 10.1016/j.ijmultiphaseflow.2020.103362.

[15] Crialesi-Esposito, Marco. "Analysis of primary atomization in sprays using Direct Numerical Simulation". PhD thesis. Universitat Politècnica de València, 2019.

[16] Tryggvason, Grétar, Scardovelli, Ruben, and Zaleski, Stéphane. *Direct Numerical Simulations of Gas-Liquid Multiphase Flows*. 1st ed. Cambridge University Press, 2011.

[17] Chorin, Alexandre Joel. "Numerical solution of the Navier-Stokes equations". In: *Mathematics of Computation* 22 (1968), pp. 745–762. DOI: 10.2307/2004575.

[18] Kim, J and Moin, P. "Application of a fractional-step method to incompressible Navier-Stokes equations". In: *Journal of Computational Physics* 59.2 (1985), pp. 308–323. DOI: 10.1016/0021-9991(85)90148-2.

[19] Harlow, Francis H and Welch, J Eddie. "Numerical calculation of time-dependent viscous incompressible flow of fluid with free surface". In: *The physics of fluids* 8.12 (1965), pp. 2182–2189.

[20] Leonard, B.P. Brian P. "A stable and accurate convective modelling procedure based on quadratic upstream interpolation". In: *Computer methods in applied mechanics and engineering* 19.1 (1979), pp. 59–98. DOI: 10.1016/0045-7825(79)90034-3.

[21] Shu, Chi-Wang and Osher, Stanley. "Efficient implementation of essentially non-oscillatory shock-capturing schemes, II". In: *Journal of Computational Physics* 83.1 (1989), pp. 32–78. DOI: 10.1016/0021-9991(89)90222-2.

[22] Sweby, Peter K. "High resolution schemes using flux limiters for hyperbolic conservation laws". In: *SIAM journal on numerical analysis* 21.5 (1984), pp. 995–1011.

[23] Liu, Xu-Dong, Osher, Stanley, and Chan, Tony. "Weighted Essentially Non-oscillatory Schemes". In: *Journal of Computational Physics* 115.1 (1994), pp. 200–212. DOI: 10.1006/jcph.1994.1187.

[24] Bell, John B, Colella, Phillip, and Glaz, Harland M. "In this paper we develop a second-order projection method for the incom- pressible Navier-Stokes equations". In: *Journal of Computational Physics* 283 (1989), pp. 257–283.

[25] Noh, W.F. and Woodward, P. *SLIC (simple line interface calculation). [Usable in 1, 2, or 3 space dimensions].* Tech. rep. Livermore, CA: Lawrence Livermore National Laboratory (LLNL), 1976. DOI: 10.2172/7261651.

[26] Hirt, C.W W and Nichols, B.D D. "Volume of fluid (VOF) method for the dynamics of free boundaries". In: *Journal of Computational Physics* 39.1 (1981), pp. 201–225. DOI: 10.1016/0021-9991(81)90145-5.

[27] DeBar, R. "Fundamentals of the KRAKEN code". In: *Technical Report UCIR-760* (1974).

[28] Youngs, David L. "Time-dependent multi-material flow with large fluid distortion". In: *Numerical Methods for Fluid Dynamics* (1982).

[29] Youngs, David L. "An interface tracking method for a 3D Eulerian hydrodynamics code". In: *Atomic Weapons Research Establishment (AWRE) Technical Report* 44.92 (1984), p. 35.

[30] Li, Jie. "Calcul d'interface affine par morceaux". In: *Comptes rendus de l'Académie des sciences. Série II, Mécanique, physique, chimie, astronomie* 320.8 (1995), pp. 391–396.

[31] Pilliod Jr, James Edward and Puckett, Elbridge Gerry. "Second-order accurate volume-of-fluid algorithms for tracking material interfaces". In: *Journal of Computational Physics* 199.2 (2004), pp. 465–502.

[32] Scardovelli, R and Zaleski, S. "Interface Reconstruction with Least-Square Fit and Split Lagrangian-Eulerian Advection". In: *Int J. Numer. Meth. Fluids* 41 (2003), pp. 251–274.

[33] Rudman, Murray. "Volume-tracking methods for interfacial flow calculations". In: *Int. J. Numer. Meth. Fluids* 24.7 (1997), pp. 671–691. DOI: 10.1002/(SICI)1097-0363(19970415)24:7<671::AID-FLD508>3.0.CO;2-9.

[34] Desjardins, Olivier, Moureau, Vincent, and Pitsch, Heinz. "An accurate conservative level set/ghost fluid method for simulating turbulent atomization". In: *Journal of Computational Physics* (2008). DOI: 10.1016/j.jcp.2008.05.027.

[35] Sussman, Mark and Puckett, Elbridge Gerry. "A Coupled Level Set and Volume-of-Fluid Method for Computing 3D and Axisymmetric Incompressible Two-Phase Flows". In: *Journal of Computational Physics* (2000). DOI: 10.1006.

[36] Fedkiw, Ronald P., Aslam, Tariq, Merriman, Barry, and Osher, Stanley. "A Non-oscillatory Eulerian Approach to Interfaces in Multimaterial Flows (the Ghost Fluid Method)". In: *Journal of Computational Physics* 152.2 (1999), pp. 457–492. DOI: 10.1006/jcph.1999.6236.

[37] Unverdi, S O and Tryggvason, G. "A front-tracking method for viscous, incompressible, multi-fluid flows". In: *J. Comput. Phys.* 100 (1992), pp. 25–37.

[38] Tryggvason, G. et al. "A Front-Tracking Method for the Computations of Multiphase Flow". In: *Journal of Computational Physics* 169.2 (2001), pp. 708–759. DOI: 10.1006/jcph.2001.6726.

[39] Popinet, Stéphane. "Numerical Models of Surface Tension". In: *Annual Review of Fluid Mechanics* 50.1 (2017), pp. 49–75. DOI: 10.1146/annurev-fluid-122316-045034.

[40] Brackbill, J.U U, Kothe, D.B B, and Zemach, C. "A continuum method for modeling surface tension". In: *Journal of Computational Physics* 100.2 (1992), pp. 335–354. DOI: 10.1016/0021-9991(92)90240-Y.

[41] Renardy, Yuriko and Renardy, Michael. "PROST a parabolic reconstruction of surface tension for the volume-of-fluid method". In: *Journal of computational physics* 183.2 (2002), pp. 400–421.

[42] Torrey, Martin D, Cloutman, Lawrence D, Mjolsness, Raymond C, and Hirt, C W. "NASA-VOF2D: a computer program for incompressible flows with free surfaces". In: *NASA STI/Recon Technical Report N* 86 (1985), p. 30116.

[43] Sussman, Mark. "A second order coupled level set and volume-of-fluid method for computing growth and collapse of vapor bubbles". In: *Journal of Computational Physics* 187.1 (2003), pp. 110–136.

[44] Cummins, Sharen J, Francois, Marianne M, and Kothe, Douglas B. "Estimating curvature from volume fractions". In: *Computers & structures* 83.6-7 (2005), pp. 425–434.

[45] Popinet, Stéphane. "An accurate adaptive solver for surface-tension-driven interfacial flows". In: *J. Comput. Phys.* 228.16 (2009), pp. 5838–5866. DOI: 10.1016/j.jcp.2009.04.042.

Chapter 3

Inflow Boundary Conditions

3.1 Introduction

As already mentioned in Section 1.4.1, in all the DNS of atomization presented in this study Mapped Boundary Condition (MBC) are used as an inflow velocity field. This requires generating a boundary condition database to feed each operating condition. This chapter focuses on validating and studying the different internal flow LES from which the data is extracted to feed DNS computations.

The main objective of the internal flow simulations is to provide a fully-developed turbulent pipe flow. The pipe flow is one of the three canonical wall-bounded flows, besides the spatially evolving boundary layer, and the channel flow. In these kinds of flows, the presence of the wall affects the velocity profile, having significant viscous effects near the wall with a scaling factor depending on the friction velocity $u_\tau = \sqrt{\tau_w/\rho}$ and the wall-length scale ν/u_τ, where τ_w is the wall shear stress, and ρ and ν are the fluid density and viscosity, respectively. In the outer region, the velocity scale remains to be u_τ whereas the appropriate length scale is the pipe radius R [1, 2]. Many different studies have been performed on pipe flows, both experimental [3, 4] and computational [5].

There are two essential parameters to define a pipe flow simulation, one is the ratio of the pipe length to the pipe radius, L_p/R, and the Reynolds number. The first one determines the range of turbulent structures captured within the domain. Several studies have focused their efforts on this field, as

Kim et al. [6] who concluded that a length of $7.5 \cdot L/D$ should be enough to capture all the turbulent structures in pipe flows. The second one determines the operating condition and, thus, the turbulent field associated. One of the most known computational studies of this influence at low Reynolds conditions is the one performed by El Khoury et al. [5], in which different DNS simulations from low to moderate Reynolds number were performed and validated their results with other DNS studies of pipe flows [7, 8] and other wall-bounded flows [4, 9].

There are fewer studies about this kind of flow regarding the elliptical pipes. In elliptical duct study, the eccentricity factor plays a critical role in the flow development within the domain, along with the Reynolds number, as in the pipe flow. First studies of non-circular ducts predicted the appearance of secondary motions on the transversal direction [10]. When it comes to the high-fidelity numerical studies, one of the most complete is the one performed by Nikitin et al. [11], where a comparison between a circular pipe flow and two different elliptical pipes with different eccentricity factors was performed, showing the behaviours of the mean statistics and capturing the secondary motions of this kind of geometries. This work was extended by Voronova et al. [12], studying the influence of the Reynolds number on a given elliptical duct. More recently, Spalart et al. [13] focused on the computation of the skin friction in non-circular ducts, including the elliptical cross-section pipes.

This chapter explains the numerical method and the turbulence model used to perform the internal flow simulations. Then, the chosen initial and the boundary conditions are presented, describing when the simulations are considered fully developed. Moving to the cases of study, the main parameters that define the simulation are presented as the fluid properties or the geometrical specifications. The computational meshes are also shown, along with an index of quality study to ensure the correct resolution. Following the configuration sections, the average velocity field results are validated by comparing them with the theory, experiments, and other calculations. Once the results are validated, a turbulent analysis intends to do a deeper study on the turbulence side to understand the influence of the operating conditions and the geometry on the vortex size and distribution.

3.2 Numerical methods

This kind of simulations have been performed using OpenFOAM 3.0.0 [14] with the standard PISO (Pressure Implicit with Splitting Operator) solver,

proposed by Issa [15] to solve the isothermal incompressible flow governing equations:

$$\frac{\partial}{\partial x_i}(\bar{u_i}) = 0 \tag{3.1}$$

$$\frac{\partial \bar{u_i}}{\partial t} + \frac{\partial}{\partial x_j}\left(\bar{u_i}\bar{u_j}\right) = -\frac{1}{\rho}\frac{\partial \bar{p}}{\partial x_j} + \frac{\partial}{\partial x_j}\left((\nu + \nu_t)\left(\frac{\partial \bar{u_i}}{\partial x_j} + \frac{\partial u_j}{\partial x_i}\right)\right) \tag{3.2}$$

Where $\bar{u}$ is the resolved velocity field, $\bar{p}$ is the modified kinetic pressure and ν_t is the Subgrid Scale viscosity, used to the closure of Equation 3.2, which is a non-linear term that needs to be modelled. Many models have been developed to estimate the energy dissipation in the subgrid range. In this case, due to the objective of the study, the Wall Adapting Local Eddy-viscosity (WALE) model [16] is chosen. This model is based on the square of the velocity tensor to compute the estimation of the local eddy viscosity using Eq. 3.3.

$$\nu_t = (C_w\Delta)^2 \cdot \frac{(\bar{S}^d_{ij}\bar{S}^d_{ij})^{3/2}}{(\bar{S}_{ij}\bar{S}_{ij})^{5/2} + (\bar{S}^d_{ij}\bar{S}^d_{ij})^{5/4}} \tag{3.3}$$

Where C_w is the constant of the WALE model used to calibrate the subgrid energy dissipation, Δ is the width of the LES filter, $\bar{S}^d_{ij}$ is the traceless symmetric part of the squared gradient tensor, and $\bar{S}_{ij}$ is the resolved strain rate tensor. The last term behaves as a cubic function of the wall-distance (y^3) and depends on the rotation and strain rates. This characteristic allows this model to reproduce the near-wall scaling without using any dynamic procedure and is able to reproduce the turbulent flow behaviour in pipes, as proved in [16]. Finally, the constant C_w is set to 0.5 as proposed by their developers [16] for this flow topology.

3.3 Simulation parameters

Two main types of pipe flow simulations have been performed during this study: circular cross-section pipes and elliptical-cross section ducts. Both studies have the same pipe length L_p of 720 µm, corresponding with 16 times the circular pipe radius R_p.

In order to reach a fully developed turbulent flow within the computational domain, a cyclic boundary condition is applied to both the inlet and the outlet surfaces. So, the outflow values are used as an inflow condition. Also, different

channel simulations are performed to get preliminary turbulent flows that will be mapped on pipe simulations. These preliminary simulations are triggered using the boxTurb tool from OpenFOAM. Additionally, in order to avoid the pressure loss within de domain, a momentum source is added to maintain the bulk velocity.

After mapping the preliminary turbulent field, it is necessary to compute for around 200 washouts (being a washout, the interval that a particle remains in the computational domain before passing through the outflow section). Once this computation is done, the turbulent field within the pipe is considered fully adapted, and the main calculations are performed.

3.4 Cases of study

As already presented, this thesis aims at studying the influence of the injection conditions on droplet generation. In this framework, three main parameters are varied, the Reynolds number, the Weber number, and the nozzle shape.

The first parameter is the Reynolds number. This parameter is delicate as it depends on the velocity, and, as already addressed in Chapter 2, DNS simulations have a substantial limitation on simulating high velocities. So, to ensure the computational cost of atomisation simulations is manageable, the bulk velocity will be kept constant at $U_b = 100$ m/s. This requires varying the physical properties of the liquid to modify the operating Reynolds number. With this approach, the Reynolds number will range from $5,037$ to $9,000$. Table 3.1 lists the physical properties of the fluids used. Note that the lower Reynolds number liquid properties correspond to the Dodecane and are employed to design the other two pseudo-fluids. Those pseudo-fluids are modified to provide an equally-spaced sweep of Reynolds number.

Table 3.1: Physical properties from each case of study when varying the Reynolds number

$\mathbf{Re}_D$	5,037	7,000	9,000
$\boldsymbol{\rho}$ **[kg/m^3]**	750	750	690
$\boldsymbol{\mu}$ **[Pa ·s]**	$1.34 \cdot 10^{-3}$	$0.964 \cdot 10^{-3}$	$0.69 \cdot 10^{-3}$
$\boldsymbol{\nu}$ **[m^2/s]**	$1.786 \cdot 10^{-6}$	$1.285 \cdot 10^{-6}$	$1 \cdot 10^{-6}$

On the other hand, the Weber number can be modified by just increasing or decreasing the surface tension. So for that study, the same inflow boundary condition is used.

Finally, regarding the nozzle geometries, both the Reynolds and the Weber number studies used a nozzle with 90 µm of diameter, whereas for the nozzle shape study, two elliptical pipes are simulated with two different eccentricity factors e. Those eccentricity factors are chosen to match the bulk velocity and the injection area from the round pipes and the physical properties of the fluid matching to the lower Reynolds number case (Dodecane). The main parameters are gathered in Table 3.2. The eccentricity factor is computed as $e = \sqrt{a^2 - b^2}/a$, where a and b are the major and minor axes, respectively. It is noticeable that, as the definition of Reynolds number on elliptical pipes is based on the hydraulic diameter D_h, the obtained values are slightly lower but are sufficiently closer to be comparable.

Table 3.2: Geometric parameters of the elliptical ducts

e	0.85	0.92
a [µm]	63.32	72.65
b [µm]	32.82	28.12
D_h [µm]	84.30	77.28
Re	4,718	4,325

3.5 Computational meshes

Figure 3.1 depicts the characteristic meshes from both round and elliptical pipes used. It can be seen that for both cases, the meshing strategy is the so-called o-grid. When performing wall-bounded flows simulations, the refinement required in the normal direction of the surface is higher than in the other parts of the domain. Although all cases use the same mesh strategy, the refinement parameters are set according to the first y^+, directly depending on the Reynolds number.

Table 3.3 summarizes the grid parameters and the total amount of cells from the round pipe cases. In this table, N_{cell} is the number of cells of the mesh, Δr^+_{wall}, $\Delta \omega^+_{wall}$ and Δx^+ are the sizes of the wall cells in the normal, azimuthal and axial directions, respectively (in wall units).

Those parameters are based on the work performed by Nicoud and Ducrous [16]. Regarding the elliptical configurations, as the Reynolds numbers are similar to the lower Reynolds case from the round pipe cases, the main sizes are maintained, leading to 1,632,000 cells for both cases. However, an index

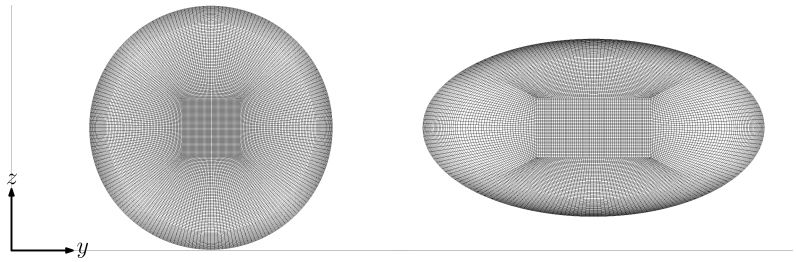

Figure 3.1: Characteristic meshes for left, round cases, and right elliptical cases.

Table 3.3: Mesh parameters from the round pipe cases

$\mathbf{Re}_D$	5,037	7,000	9,000
$\mathbf{N}_{cell}$	1,650,000	2,010,000	2,250,000
$\boldsymbol{\Delta r}^+_{wall}$	0.86	0.89	0.9
$\boldsymbol{\Delta \omega}^+_{wall}$	9.5	9.2	9
$\boldsymbol{\Delta x}^+$	24	24	24

of quality, IQ_k, has been computed to ensure the LES resolution's quality. This index can be calculated based on three different parameters: kinetic energy, length scales, and viscosity. In this case, the quality assessment of the simulations is performed using the resolved kinetic energy, so the IQ_k can be expressed as:

$$IQ_k = \frac{k_{res}}{k_{tot}} = \frac{k_{res}}{k_{res} + k_t + k_{num}} \tag{3.4}$$

where k_{res} is the resolved kinetic energy, k_t is the turbulent kinetic energy modelled by the subgrid model, and k_{num} is the kinetic energy related to the numeric error. The resolved kinetic energy can be computed using Equation 3.5; the modelled part can be calculated with Equation 3.6 as proposed by Sagaut [17]; and finally, the numerical part can be approximated as the same as the modelled part, as suggested by Celik et al. [18].

$$k_{res} = \frac{1}{2}\left(u^2_{x,rms} + u^2_{y,rms} + u^2_{z,rms}\right) \tag{3.5}$$

$$k_t = \frac{1}{(C_m \Delta)^2}\nu_t^2 \tag{3.6}$$

Where C_m is a model constant set to 0.091, and Δ is the characteristic filter size related to the cell volume. As can be observed in Equation 3.5, it is necessary to compute the temporal statistics of the velocity field to obtain the IQ_k. A plane is sampled at half the pipe domain with high frequency to achieve smooth temporal statistics on the velocity field. Regarding the round pipes, due to their axi-symmetry, the information can be collapsed into a single radial profile by performing an azimuthal average. On the contrary, elliptical ducts have particular characteristics, so their temporal statistics will be collapsed onto a single quadrant for better understanding. Beginning with the round cases, Figure 3.2 shows the IQ_k distribution against the radial profile, defined as $\xi = (R_p - r)/R_p$. Note that ξ is equal to 0 at the wall and 1 at the pipe centre. All the radial profiles show a common shape, presenting higher values near the wall and at the pipe centre, but a minimum around $\xi = 0.2$. The lowest values presented in each case are located where the subgrid model is modelling more energy. However, it is commonly accepted that values of the IQ_k greater than 0.8 imply a good resolution. All round cases show values higher than the standard, assessing the accuracy of the computations.

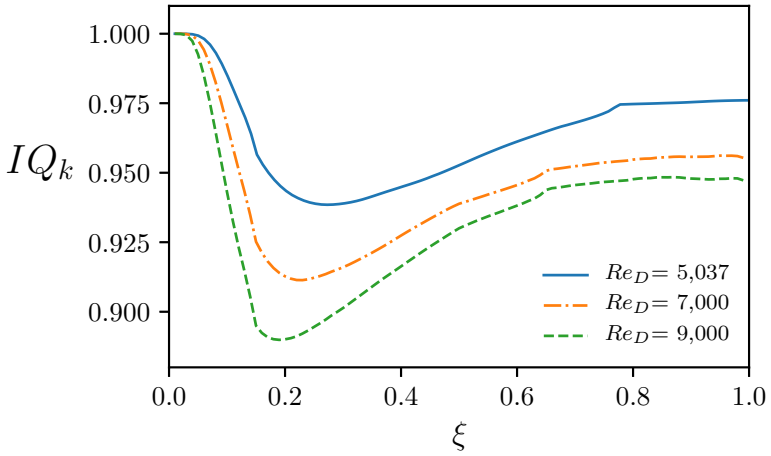

Figure 3.2: Index of Quality profile based on the turbulence resolution for the round pipe cases.

On the other hand, Figure 3.3 depicts the IQ_k fields for the ellipse pipe cases. The upper geometry corresponds to the lower eccentricity factor, while the bottom geometry refers to the higher eccentricity factor. It can be noticed that the minimum values are around 0.92 and 0.98 for the lower and the higher eccentric ducts, respectively. The same as for the round cases, the minimum values are higher than 0.8, proving the quality of the resolution.

Also, the distribution between cases is reasonably similar, presenting high values around the wall and at the pipe centre, and the lowest values around the half of both semi-axes. It is interesting to point out that the obtained values from the most eccentric case are often considered DNS resolutions as they are resolving almost 98% of the kinetic energy of the problem. This is caused because the turbulence within the domain decreases (as the Reynolds number decreases), leading to an over-refinement. Nevertheless, the computational resources required to perform these simulations are far from being significant compared to the atomizations DNS simulations. With this analysis, the LES quality has been assessed for all conditions and constitutes the first validation of the results.

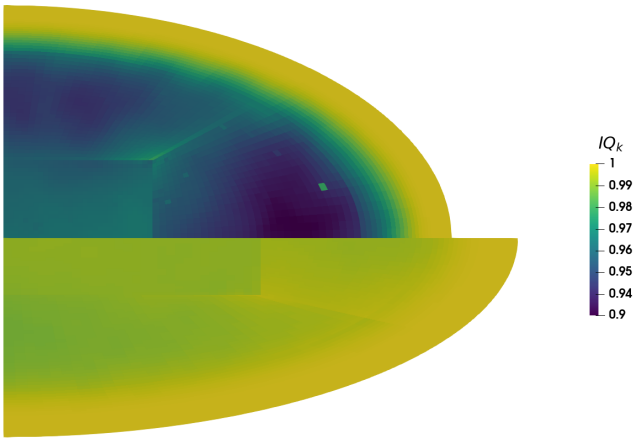

Figure 3.3: Index of Quality profile based on the turbulence resolution for the elliptic pipe cases. Top: $e = 0.85$*; bottom:* $e = 0.92$

3.6 Validation

This study aims to generate a reliable boundary condition database for the DNS simulations. To this end, several parameters based on the mean velocity statistics will be assessed in the present section. As in the previous section, the round cases will be presented in their radial profile, while the elliptical cases will be plotted in their first quadrant. It is worth mentioning that the validation for the circular pipes will be more accessible due to the amount of information available in the bibliography. Taking into account these differences between the cases, the validation is split into two parts, first, the round cases validation, and then the validation for the elliptical cases.

3.6.1 Round cases

First of all, to validate the results is mandatory having a fully developed velocity profile that ensures that the simulations have reached a steady state. To achieve this state, after the initial 1 ms (around 200 washouts), a plane normal to the flow direction is sampled to perform the mean statistics of the velocity field. As already commented above, the study will be collapsed in the azimuthal direction to provide radial profiles for the different statistics.

Having a smooth mean axial velocity profile is a symptom of having good mean statistics. To this end, Figure 3.4 shows the mean axial velocity profile, normalized with the centreline velocity against the radial position ξ, defined in the previous section. It can be seen that the velocity profiles collapse at the pipe center, and near the wall, the velocity profile shifts to a more squared velocity profile when the Reynolds number increases, characteristic of turbulent velocity profiles. This behaviour is well-known and already addressed in the literature [19].

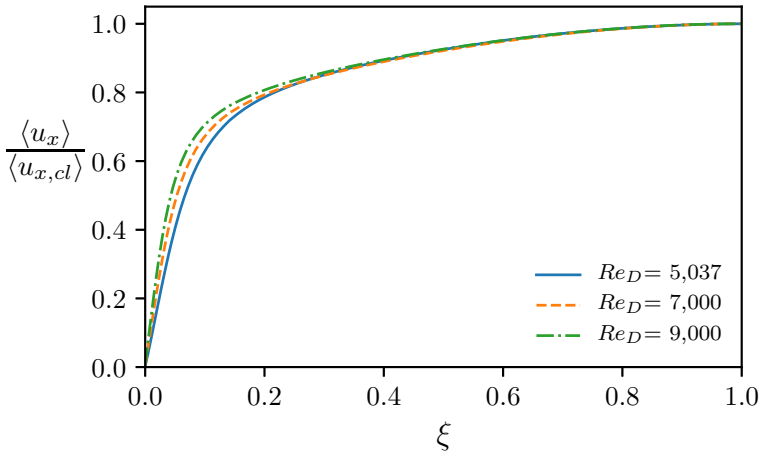

Figure 3.4: Mean axial velocity profile.

From the mean velocity field, it is possible to compute the friction parameters in order to assess the reliability of the results. Table 3.4 present the results concerning the friction velocity, u_τ, and the Kármán number, Re_τ. The results exhibit a decrease in the friction velocity to bulk velocity ratio as the Re increases, which is in agreement with the trend presented at [5].

The friction velocity can be used to express the velocity and the radial distance in wall units as $u_x^+ = u_x/u_\tau$ and $\xi^+ = \xi \cdot u_\tau/\nu$, respectively. This

Table 3.4: Friction velocity and Karman number for all round cases

$\mathbf{Re}_D$	5,037	7,000	9,000
$\boldsymbol{u_\tau}$	6.83	6.52	6.35
$\boldsymbol{Re_\tau}$	171.73	228.06	285.92

is known as the law-of-the-wall and allows to compare the non-dimensional velocity profile with the known theoretical behaviour. For the case of the round pipes, results are compared with DNS data [5] and experimental data [3]. The results obtained for the round pipe shown in Figure 3.5 present an excellent agreement as to the theoretical law-of-the-wall and reference results. It is worth mentioning that the values of the parameters that define the logarithmic region are $B = 2.5$ and $\kappa = 0.41$, as suggested on [20].

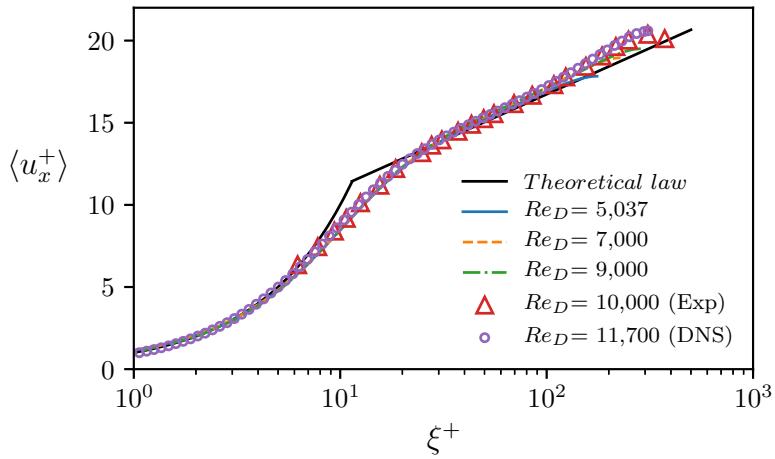

Figure 3.5: Mean axial velocity profile in wall units for the round pipe cases. Experimental data from Den Toonder et al. [3] and DNS data from El Khoury et al. [5].

The following parameter that will be studied is the turbulence intensity, which will be analyzed through the axial component of the root mean squared velocity, $\sqrt{\langle u'^2 \rangle}$. Again, for the round pipe, the results obtained will be compared with the DNS data from El Khoury et al. [5], and the experimental data from den Toonder et al. [3]. Figure 3.6 depicts the values obtained for the round cases. It can be seen that all the conditions present the maximum peak at the same location (when expressed in wall units) and coincide with the location of the DNS and experimental results. Also, the maximum value

increases with the Reynolds number, behaviour already reported in different studies [5, 7, 8], but it remains as an open question.

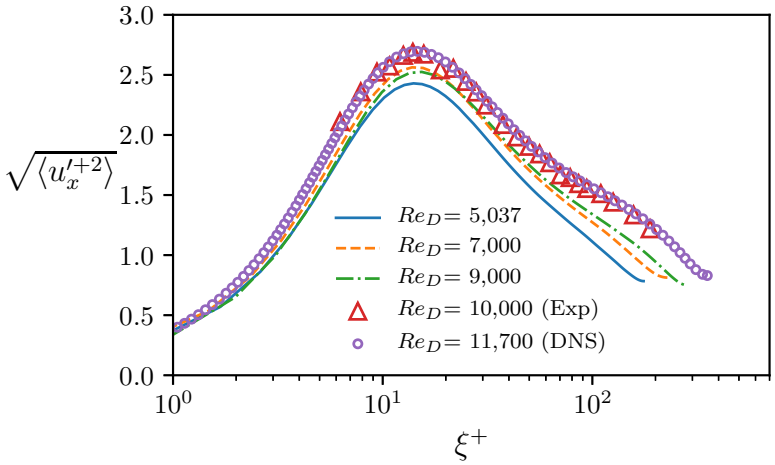

Figure 3.6: Axial component of the root mean squared velocity in wall units for the round pipe cases. Experimental data from Den Toonder et al. [3] and DNS data from El Khoury et al. [5].

Finally, the last verification performed on the round pipes is the friction factor, evaluated from the friction velocity as $f = 8u_\tau^2/U_b^2$. The obtained results will be compared with the Blasius and Colebrook laws [21]. Those results are plotted in Figure 3.7. The results present a good agreement to both laws (particularizing the Colebrook law for a roughness factor equal to 0).

3.6.2 Elliptical cases

In order to assess the accuracy of the results obtained from this simulation, it is necessary to check that the mean velocity profile is correctly developed. Figure 3.8 shows the mean resolved velocity profile for both cases. It can be seen that both sections present a smooth velocity profile and, regarding the centre axial velocity, both cases present a similar value, being the difference of 0.74% higher for the most eccentric case. This figure is also helpful to visually compare the geometries from both cases.

There is no such global velocity friction in the elliptical ducts as it changes in the azimuthal direction. In fact, a friction velocity distribution can be obtained along the azimuthal direction. Figure 3.9 depicts the computed friction velocity, made dimensionless by its average value, against θ, which is defined

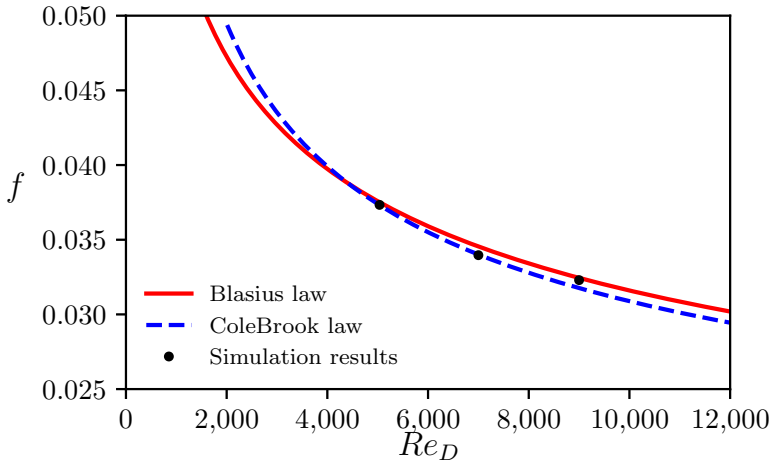

Figure 3.7: Friction factor for the circular pipe cases.

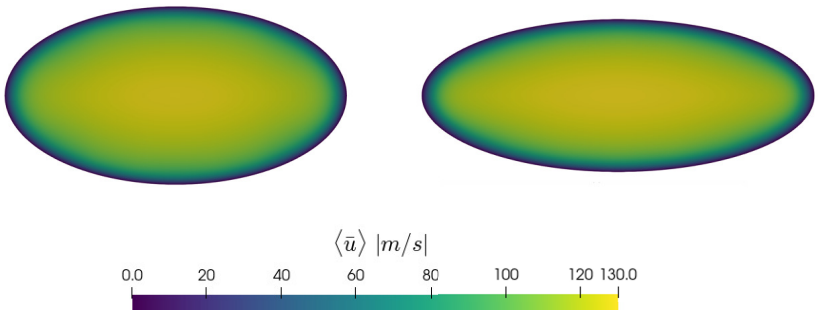

Figure 3.8: Mean resolved velocity field for left:, $e = 0.85$ and right: $e = 0.92$.

as the non-dimensional distance that is 0 at the minor axis and 1 at the major axis, so it gathers the information from all the perimeter of the ellipses. From these results, it can be seen that the obtained values are higher at the minor axis and lower at the major axis for both cases. This behaviour has already been addressed in [11, 12] and is caused by the velocity profile having less length to adapt itself at the minor axis.

As there is not a global friction velocity, the axial component of root mean squared velocity will be computed without expressing it in wall units. The values obtained for both cases are presented on the left fields from Figure 3.10, corresponding to the top geometry for the lower eccentricity factor and the bottom for the higher eccentricity factor. It can be noticed that the

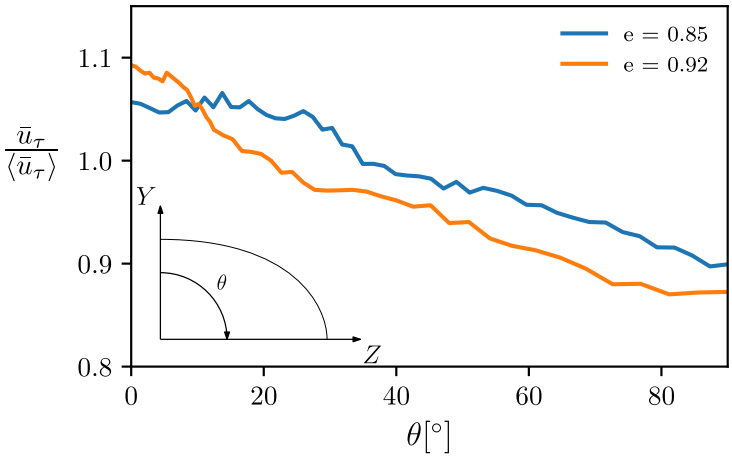

Figure 3.9: Azimuthal friction velocity distribution for the elliptical cases

higher values are located near the walls for both cases (as expected, being the region where the shear stresses are maximum). However, the most interesting behaviour is that the values are maximum at the minor axis and decrease in the azimuthal direction towards the major axis. In terms of the values obtained, the lower eccentricity case presents an almost 5% higher value of this parameter than the other case.

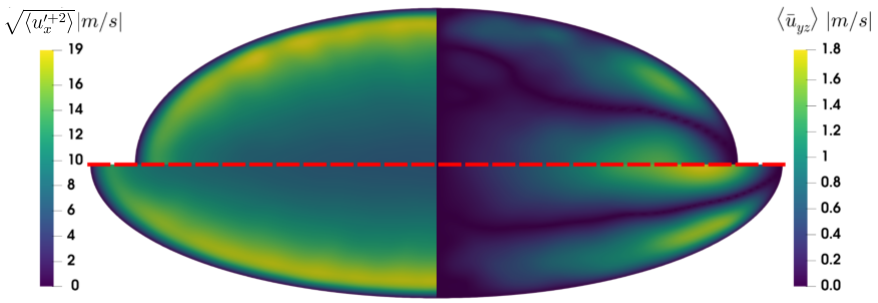

Figure 3.10: Left: root mean squared velocity in the streamwise direction; right: secondary flow resolved velocity. Upper: e = 0.85 case; bottom: e = 0.92 case.

The main particularities of elliptical pipes are the apparition of secondary movements characteristics of non-axisymmetric ducts. It is important, thus, to ensure that these motions are well captured as they will be of great importance on spray development. First of all, the transversal motion is computed as $\bar{u}_{yz} = \sqrt{\bar{u}_y^2 + \bar{u}_z^2}$ and has been plotted on the right fields from Figure 3.10. Again, the top geometry corresponds to the lower eccentricity case, while the bottom corresponds to the most eccentric geometry. In this case, the maximum values obtained of the secondary movements are in agreement with [11] where predicted around 1.5% of the bulk velocity, depending on the eccentricity factor. Also, Figure 3.11 presents the streamlines corresponding to the secondary movement. This allows to visualize the secondary movement, and the location of the movement axis, which also agrees with computational data [11, 12].

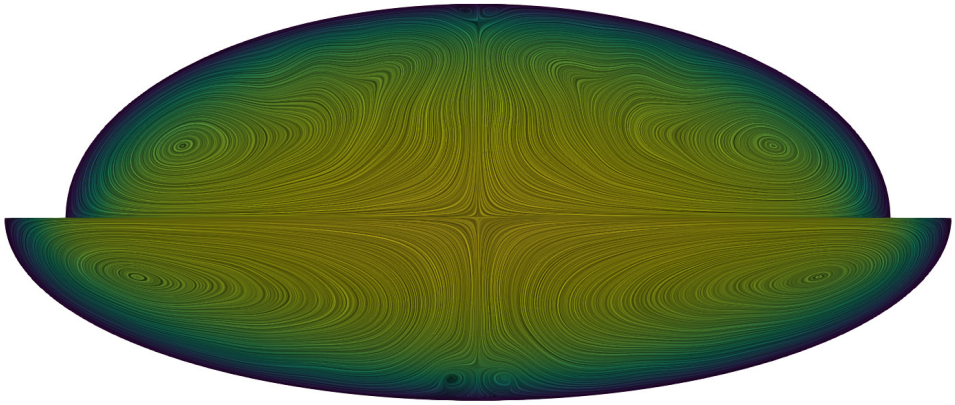

Figure 3.11: Streamlines from the secondary motion.

Finally, once the internal flow results are validated, a plane located at the half of the pipe is sampled every 100 ns. Then, these planes are interpolated into a cartesian mesh whose cell size matches the one corresponding to the DNS atomisation simulation, and stored in a boundary condition database.

3.7 Detection and analysis of vortex

As already mentioned before, one of the main ideas is to link the phenomena that occur in the internal flow to the phenomena that take place in the atomization simulation. In order to do so, a study of the size, shape, and location of vortex structures is performed. Several methods exist to detect vortex core, mainly based on the velocity gradient tensor analysis. Jeong and Hussain proposed the λ_2 criterion [22] which decompose the velocity gradient tensor into a symmetric rate-of-strain tensor S and an antisymmetric rate-of-rotation tensor Ω. Once the viscous effects and the unsteady irrotational straining are neglected, the symmetric part of the gradient of the incompressible Navier-Stokes equation can be expressed as Equation 3.7:

$$S^2 + \Omega^2 = -\frac{1}{\rho}\nabla^2 p \tag{3.7}$$

Hence, $S^2 + \Omega^2$ is a real and symmetric matrix and implies the existence of a local minimum of pressure and that it has 3 eigenvalues ($\lambda_1 \geqslant \lambda_2 \geqslant \lambda_3$). So this method states that a vortex core is a connected zone with two negative eigenvalues, which is equivalent to saying that a connected zone with $\lambda_2 < 0$ can be considered a vortex structure.

So, the λ_2 criterion allows studying the distribution of vortex core by using iso-contours set by a certain threshold. It must be noted that the values of λ_2 obtained, when applying the method to this kind of study, usually fall in a wide range. Therefore, two different approaches have been taken into account to compare the distribution of vortex core for all the cases. On the one hand, a single threshold value has been set for all conditions. However, if the selected value were too high, no vortex would appear at a lower Reynolds number; on the contrary, if it were too low, the different vortex would start merging, leading to a chaotic pattern at higher Reynolds values that are not representative. With this limitations, the threshold value for this approach is set to $\lambda_2 = -1e^{13}$. On the other hand, considering that the range of values obtained changes with the Reynolds number, a relative threshold has also been used to have a proportional vortex definition for all cases. In this case, a 10% of the averaged maximum detected is chosen as the relative threshold. In the round pipe study, the selected thresholds are $-0.87e^{13}$, $-1.25e^{13}$ and $-1.4e^{13}$ when increasing the Reynolds number. The relative threshold loses sense regarding the eccentricity analysis as the λ_2 range is quite similar. Thus, only the absolute threshold will be applied.

First, some qualitative results demonstrate the influence of the Reynolds number and eccentricity factor on the generation of turbulent structures.

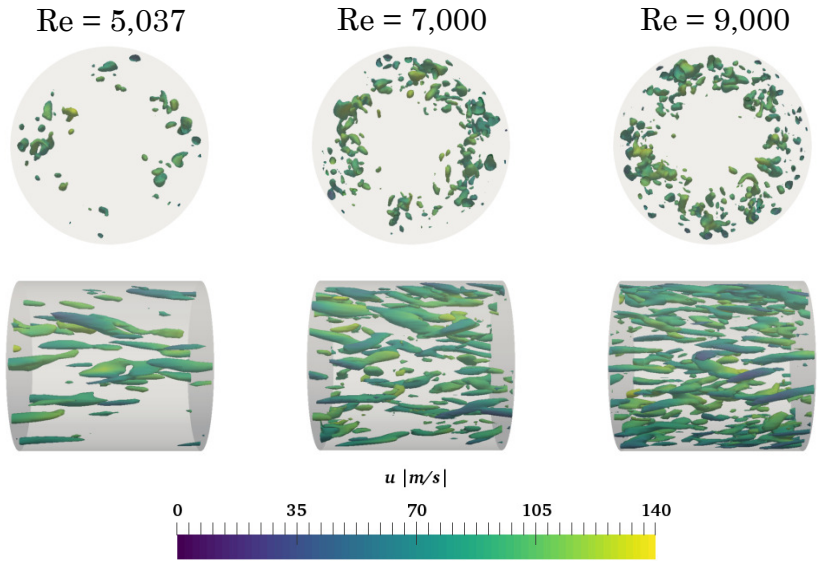

Figure 3.12: Iso-contours of $\lambda_2 = -1e^{13}$ for all round cases, top: YZ plane, bottom: XY plane.

Note that all the qualitative results correspond to the absolute threshold of $\lambda_2 = -1e^{13}$. Figure 3.12 represents the contours of λ_2 in a section of the round pipe cases for all conditions. The top row shows the structures in its radial distribution, whereas the bottom row presents the vortexes in the axial direction. It can be noticed that, as the Reynolds number increases, so does the number of structures, and its volume seems to decrease. Also, when focusing on the radial distribution, the increase of the Reynolds number seems to spread the vortex location to the pipe centre.

On the other hand, Figure 3.13 shows the λ_2 contours for the elliptical pipe cases. Again, the top row corresponds to the radial distribution, and the bottom row shows the structures in the axial direction. In this case, being that the Reynolds number is very similar, there are not huge differences between both geometries, but it can be seen that the majority of the structures are located on the region closest to the minor axis.

Once shown the qualitative studies, a vortex detection algorithm is used to count these structures and sort them by volume and distribution. In order to achieve a reliable time-averaged distribution, one snapshot per washout has been post-process during 200 consecutive washouts. As can be appreciated in both Figure 3.12 and 3.13, there are some structures with a minimal volume, just defined by a few points, which appear when computing the iso-surface

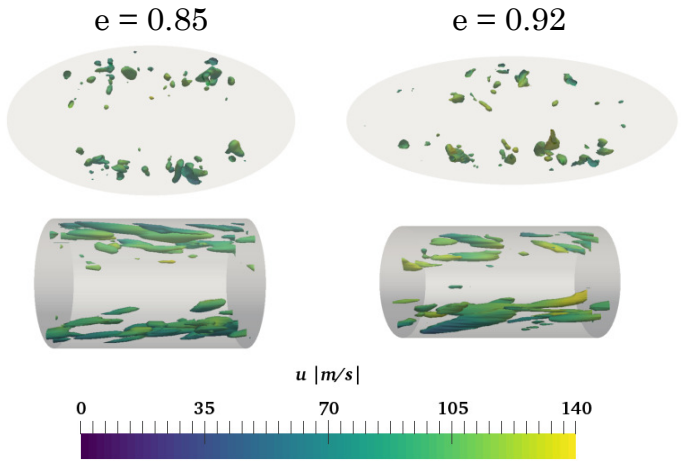

Figure 3.13: Iso-contours of $\lambda_2 = -1e^{13}$ for all elliptical ducts, top: YZ plane, bottom: XY plane.

extraction. These structures have a numerical base and should be discarded for the analysis, so a minimum volume of twice the characteristic cells is set to avoid numerical noise.

Apart from detecting the structures, Probability Density Functions (PDF) are performed to get the distribution for both volume and position. The PDF diminishes the effect of the total amount of structures to allow the direct comparison of the cases. Again, for clarity, the results are divided by the domain type.

Beginning with the round pipe study, Figure 3.14 depicts the obtained results of applying the vortex detection algorithm in terms of volume distribution for both the absolute threshold (left column) and the relative threshold (right column) criteria. Also, the top row plots show the number of vortex structures (N_s), whereas the bottom row plots the PDFs, both cases sorted by their volumes. Concerning the total amount of structures, the absolute threshold shows an increase of the total amount of vortexes with the Reynolds number for the majority of the sizes, as could be suggested in Figure 3.12. On the contrary, the bigger structures disappear when applying the relative threshold as the Reynolds number increases. This behaviour is caused because the relative thresholds are higher than the absolute threshold, excluding the lower Reynolds case. So, the less turbulent structures corresponding with lower λ_2 values are filtered when increasing the threshold value. However, when studying the shape of the resulting PDFs, same trends are obtained regardless threshold used, being the values related to the bigger structures are higher as

the Reynolds number decreases. This agrees with the fact that qualitatively on Figure 3.12 the structures seemed to be bigger at low Reynolds.

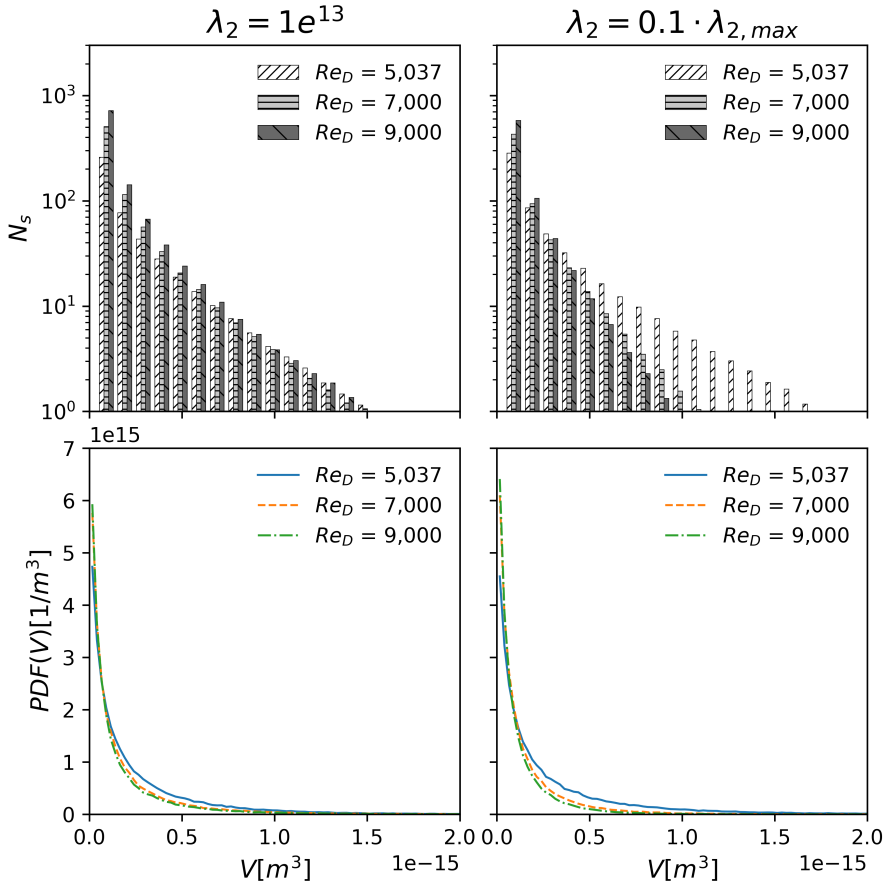

Figure 3.14: Left: absolute threshold criterion; right: relative threshold criterion. Upper: time-averaged number of structures sorted by its volume; bottom: volume PDF.

On the other hand, Figure 3.15 presents the same composition from Figure 3.14 but applied to the radial distribution (obtained by the radial position of the vortex core). Here, as already exposed earlier in the chapter, ξ is a non-dimensional radius which is 0 at the wall and 1 at the pipe centre. So, with respect to the total number of structures on each radial location, the absolute threshold criterion shows an increase in the number of structures with the Reynolds number for all radial positions. This leads to a spread of the radial distribution both towards the wall and the pipe centre. However, when applying the relative threshold criterion, the amount of structures located near

the wall increases at the expense of the structures located near the pipe centre, which disappear. This means, applying the same reasoning from the volume distribution, that the structures near the pipe centre are less turbulent and filtered by increasing the threshold. Regarding the PDFs, when applying the absolute threshold, the peak values are similar for all cases, and its location shifts towards the wall, which is consistent with the theory as the maximum values obtained for the $u^+_{x,rms}$ on Figure 3.6 were located at the same ξ^+ which decreases with the Reynolds number. Analogous results are obtained using the relative threshold, but peak values decrease with the Reynolds number and decrease near the pipe centre.

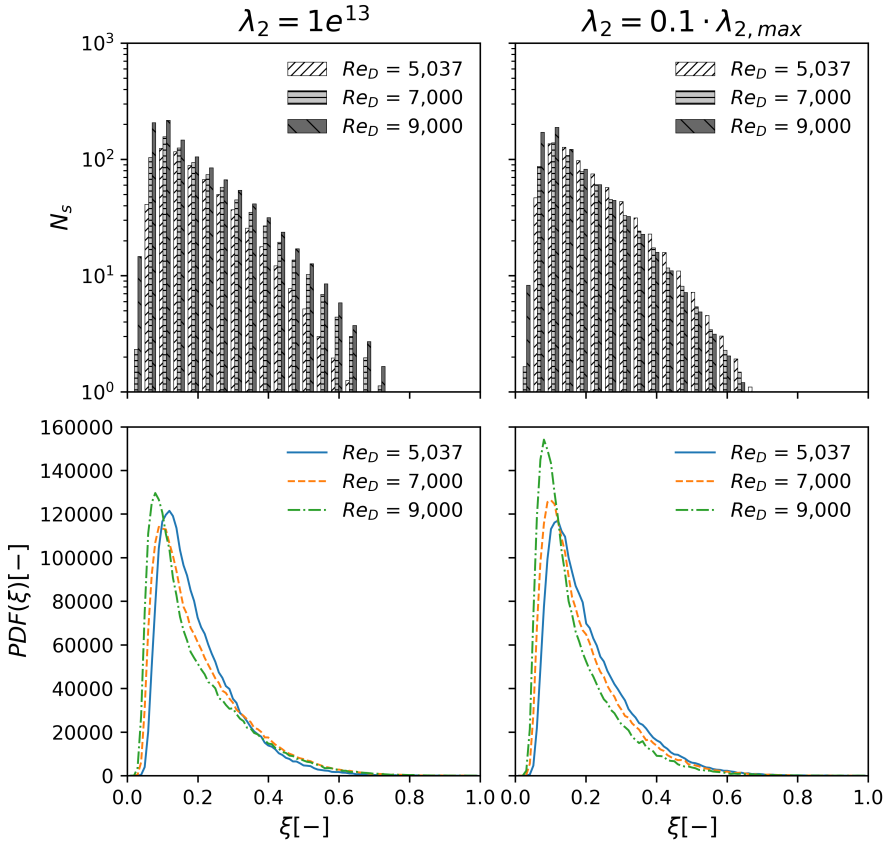

Figure 3.15: Left: absolute threshold criterion; right: relative threshold criterion. Upper: time-averaged number of structures sorted by its radial position; bottom: radial position PDF.

Finally, the same approach is performed on the elliptical study where Figure 3.16 gathers the volume distribution results in terms of the total amount

of structures sorted by its volume in the left, and the PDF distribution of their volumes in the right. Here, the round pipe corresponding to the lower Reynolds number is referred as $e = 0$. Regarding the number of structures detected per volume, it is noticeable that the medium eccentricity factor presents more structures for all volume ranges. In contrast, the higher eccentricity factor shows fewer structures for all volumes. As shown in Table 3.2, the Reynolds number slightly decreases with the eccentricity factor. However, the secondary movements induced by the non-axi-symmetry allow maintaining the turbulence within the domain when the eccentricity factor is moderate, decreasing when this parameter reaches extreme values. Nevertheless, as the Reynolds number is quite similar, the PDFs computed for all cases are nearly identical. These results agree with the qualitative results presented earlier, where no considerable difference was noticed regarding the number and size of the structures.

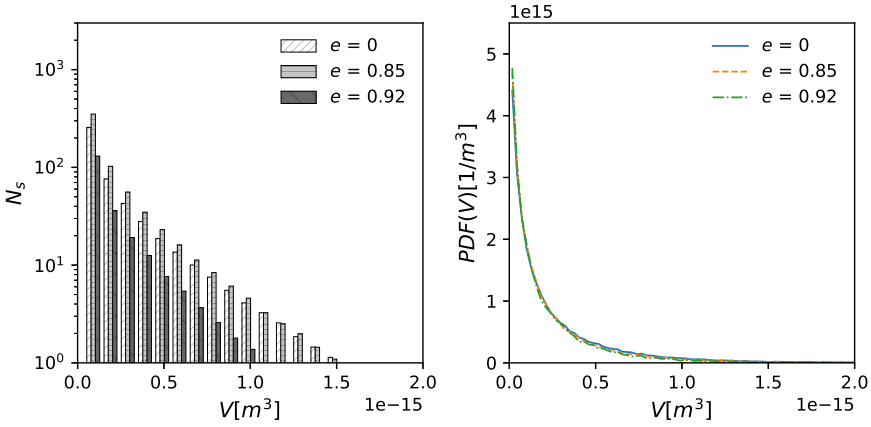

Figure 3.16: Structures distribution from the elliptical study in terms of time-averaged number of structures sorted by its volume (left) and volume PDF (right).

Finally, to check the distribution of the vortexes on the elliptical cases, the azimuthal distribution is studied instead of performing a radial distribution. Figure 3.17 depicts on the left the number of structures along the azimuthal direction, expressed as θ, and on the right the PDF of that distribution. The angle, θ, starts at 0° in the minor semiaxis and ends at 90°, on the major semiaxis. The round pipe shows a quasi-constant value of detected structures as expected due to its axi-symmetry. On the other hand, the elliptical pipes present a maximum value that shifts towards the minor axis as the eccentricity factor increases. This is in line with what is observed in Figure 3.13, where

the structures appear near the minor axis. Regarding the PDF, just like in the previous graph, the round cases describes a constant distribution. The maximum values on the elliptical case increase with the eccentricity factor, which means that the number of structures collapsed on the minor axis are relatively higher for the $e = 0.92$ case.

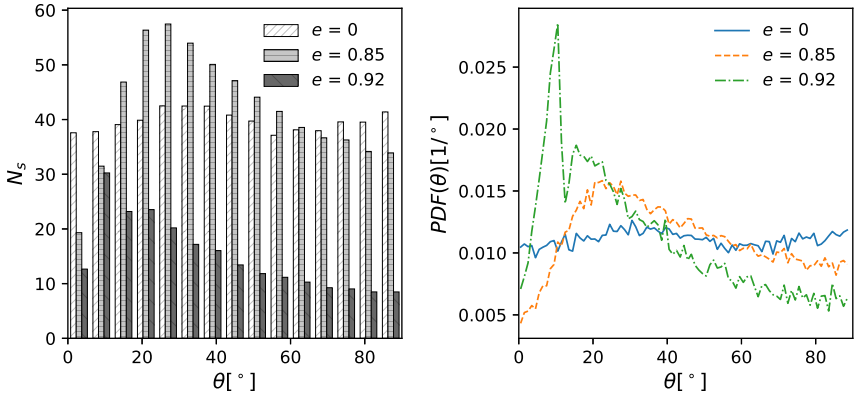

Figure 3.17: Structures distribution from the elliptical study in terms of left: time-averaged number of structures sorted by its azimuthal position; right: azimuthal position PDF.

3.8 Main conclusions

This chapter has presented the different LES simulations of periodical pipes used to generate the boundary conditions to be mapped into the atomisation DNS simulations. One of the main goals has been to validate the results to ensure that the turbulence fields used to feed the different external flow simulations are coherent and well-resolved.

This validation has been performed by analysing many parameters, starting with the Index of Quality of the mesh, reporting values greater than 0.8 in all cases studied, followed by the flow's mean statistics. The round pipe cases have shown a good agreement with experimental, computational, and theoretical data regarding friction velocity, law-of-the-wall, root-mean squared velocity, and friction factor. On the other hand, regarding the elliptical cases, both configurations have demonstrated capturing the secondary movements of the flow, characteristic of non-circular ducts, and the friction velocity distribution on the azimuthal direction fits with the expected behaviour.

However, the analysis of these simulations has been continued further away by studying the vortex formation using the λ_2 criterion. When it comes to the round pipe configurations, two approaches have been used to extract the volume and radial distribution of the vortexes. On the one hand, an absolute threshold has been applied to all conditions. On the other hand, a relative threshold depending on the maximum λ_2 values for each case has been used. From this study, the following states can be extracted:

- The number of detected structures increases as the Reynolds number increases. Regardless of the approach.
- The relative threshold exhibits a decrease in the maximum volume detected as the Reynolds number increases, becoming more restrictive.
- The absolute threshold detects that the radial distribution spreads towards the wall and the pipe centre when increasing the Reynolds number. The relative threshold presents the majority of the structures closer to the wall.
- The bigger structures detected with lower threshold values, which are located near the pipe centre, correspond to less turbulent structures.

Two different eccentricities have been compared against a round pipe under the same conditions regarding the elliptical pipe cases. As the resulting Reynolds numbers were similar, only one threshold has been used to perform this analysis, from which the following conclusions have been noticed:

- The secondary movements tend to generate more vortexes than round pipes at moderate eccentricity factors. However, at higher values, this effect disappears.
- Although the number of vortexes detected is different for each case. The volume PDF collapse into the same distribution. As the Reynolds number is quite similar between cases.
- Qualitative studies pointed out the redistribution of the vortex cores, moving from the major axis towards the minor axis on the elliptical ducts.
- The azimuthal distributions agree with the qualitative results, showing a relatively higher percentage of structures in the minor axis as the eccentricity factor increases.

As pointed out in [23], the inflow structures shape is fundamental to trigger the atomisation in DNS simulations correctly. This analysis will be helpful to understand how the inlet turbulence affects the liquid breakup in the DNS simulations on the different studies gathered in this document.

References

[1] Townsend, A. A. *The Structure of Turbulent Shear Flow*. 2nd. Cambridge University Press, 1976.

[2] Marusic, I. et al. "Wall-bounded turbulent flows at high Reynolds numbers: Recent advances and key issues". In: *Physics of Fluids* 22.6 (2010), pp. 1–24. DOI: 10.1063/1.3453711.

[3] Den Toonder, J. M.J. and Nieuwstadt, F. T.M. "Reynolds number effects in a turbulent pipe flow for low to moderate Re". In: *Physics of Fluids* 9.11 (1997), pp. 3398–3409. DOI: 10.1063/1.869451.

[4] Örlü, R. et al. "Reynolds stress scaling in pipe flow turbulence - First results from CICLoPE". In: *Philosophical Transactions of the Royal Society A: Mathematical, Physical and Engineering Sciences* 375.2089 (2017). DOI: 10.1098/rsta.2016.0187.

[5] El Khoury, George K. et al. "Direct numerical simulation of turbulent pipe flow at moderately high reynolds numbers". In: *Flow, Turbulence and Combustion*. Vol. 91. 3. 2013, pp. 475–495. DOI: 10.1007/s10494-013-9482-8.

[6] Kim, K. C. and Adrian, R. J. "Very large-scale motion in the outer layer". In: *Physics of Fluids* 11.2 (1999), pp. 417–422. DOI: 10.1063/1.869889.

[7] Chin, C., Ooi, A. S.H., Marusic, I., and Blackburn, H. M. "The influence of pipe length on turbulence statistics computed from direct numerical simulation data". In: *Physics of Fluids* 22.11 (2010). DOI: 10.1063/1.3489528.

[8] Klewicki, J., Chin, C., Blackburn, H. M., Ooi, A., and Marusic, I. "Emergence of the four layer dynamical regime in turbulent pipe flow". In: *Physics of Fluids* 24.4 (2012). DOI: 10.1063/1.3702897.

[9] Jiménez, Javier and Hoyas, Sergio. "Turbulent fluctuations above the buffer layer of wall-bounded flows". In: *Journal of Fluid Mechanics* 611 (2008), pp. 215–236. DOI: 10.1017/S0022112008002747.

[10] Speziale, Charles G. "On turbulent secondary flows in pipes of noncircular cross-section". In: *International Journal of Engineering Science* 20.7 (1982), pp. 863–872. DOI: 10.1016/0020-7225(82)90008-8.

[11] Nikitin, Nikolay and Yakhot, Alexander. "Direct numerical simulation of turbulent flow in elliptical ducts". In: *Journal of Fluid Mechanics* 532 (2005), pp. 141–164.

[12] Voronova, T. V. and Nikitin, N. V. "Results of direct numerical simulation of turbulent flow in a pipe of elliptical cross-section". In: *Fluid Dynamics* 42.2 (2007), pp. 201–211. DOI: 10.1134/S0015462807020068.

[13] Spalart, P. R., Garbaruk, A., and Stabnikov, A. "On the skin friction due to turbulence in ducts of various shapes". In: *Journal of Fluid Mechanics* 838 (2018), pp. 369–378. DOI: 10.1017/jfm.2017.911.

[14] *OpenFOAM v3.0.0*. 2015.

[15] Issa, R I. *Solution of the Implicitly Discretised Fluid Flow Equations by Operator-Splitting*. Tech. rep. 1985.

[16] Nicoud, F. and Ducros, F. "Subgrid-Scale Stress Modelling Based on the Square of the Velocity Gradient Tensor". In: *Flow, Turbulence and Combustion* 62.3 (1999), pp. 183–200. DOI: 10.1023/A:1009995426001.

[17] Sagaut, Pierre. *Large eddy simulation for incompressible flows: an introduction*. Springer Science & Business Media, 2006.

[18] Celik, I., Klein, M., and Janicka, J. "Assessment measures for engineering LES applications". In: *Journal of Fluids Engineering, Transactions of the ASME* 131.3 (2009), pp. 0311021–03110210. DOI: 10.1115/1.3059703.

[19] Wagner, C., Hüttl, T. J., and Friedrich, R. "Low-Reynolds-number effects derived from direct numerical simulations of turbulent pipe flow". In: *Computers and Fluids* 30.5 (2001), pp. 581–590. DOI: 10.1016/S0045-7930(01)00007-X.

[20] Nagib, Hassan M. and Chauhan, Kapil A. "Variations of von Kármán coefficient in canonical flows". In: *Physics of Fluids*. Vol. 20. 10. American Institute of Physics Inc., 2008. DOI: 10.1063/1.3006423.

[21] Moody, LF and Princeton, NJ. "Friction Factors for Pipe Flow". In: *Transactions of the ASME* 66.8 (1944), pp. 671–684.

[22] Jeong, Jinhee and Fazle, Hussain. *On the identification of a vortex*. Tech. rep. 1995, pp. 69–94.

[23] Crialesi-Esposito, Marco. “Analysis of primary atomization in sprays using Direct Numerical Simulation”. PhD thesis. Universitat Politècnica de València, 2019.

Chapter 4

Post-processing methodologies

4.1 Introduction

Performing DNS simulations generates a high amount of data, so it is essential to consider which outputs are necessary and when they must be sampled before running the simulations. A correct strategy of output writing allows optimising the storage requirements and avoids rerunning the computations to extract additional data. This is particularly important in the studies gathered in this document as the storing requirements and computational resources needed to perform the simulations and post-process are highly restrictive, as seen in Table 4.1 where CR and SR are the computational and storing requirements, respectively. The simulations range from 60 kch to near 1 Mch to complete and from 4 to 12 TB for storing the generated data.

Table 4.1: Computational resources and storing requirements to perform all DNS simulations presented on this document.

		Reynolds number			Weber number		Nozzle shape	
		5,037	7,000	9,000	60,000	90,000	0.85	0.92
CR	[kch]	80	300	950	80	80	90	120
SR	[TB]	4	7	12	4	4	5	6

In this context, this chapter presents the different post-processing strategies followed to extract the maximum data, optimising the costs of storing and computing. To do so, three different outputs have been stored with different sampling frequencies:

- **Centreline**: the velocity and volume fraction values from the centreline are stored each timestep once the simulation has reached the steady state. Those results help analyse the axial velocity decay and the breakup length of the core.
- **Transversal plane**: the velocity and volume fraction are stored on a plane located at $x/D_n \approx 25$, this plane has 2 cells width to be able to compute the gradients in the axial direction, which is used to compute the turbulence statistics. Like the centreline output, each timestep is stored once the simulation has reached a steady state.
- **Domain**: all variables are stored within the whole domain. This output has several applications, first to plot the spray contour and check the spray morphology development, then the flow field study and finally, the droplet detection. As this output is the largest, the sampling frequency is 0.5 µs during the transient state and decreased to 10 µs during the steady state.

From those outputs, there are some straightforward post-processing, such as the temporal statistics performed on the centreline, the plane and the domain. However, some calculations deserve previous explanations, such as the turbulent statistics on the plane or the droplet detection algorithm. So, in this chapter, those methodologies will be extensively discussed, starting with the plane study and concluding with the droplet detection algorithm.

4.2 Flow field post-processing

4.2.1 Introduction to turbulence

The turbulence is present in almost every engineering application and is the reason why turbulent flows display chaotic behaviour. Although an extensive explanation of the turbulence theory is out of the scope of this thesis, it is interesting to provide an overall context and a few terms to understand certain concepts mentioned throughout this document.

First of all, the randomness observed in turbulent flows is linked to the behaviour of the velocity field, which displays different values under the same

conditions at different times. This can be contradictory to the fact that the Navier-Stokes equations that describe the fluid motion are deterministic. However, the equations are highly sensitive to the boundary conditions and perturbations that modify the local conditions of the flow. Those perturbations lead to different values, although the flow conditions at a macroscopic level are constant. Moreover, as those perturbations are not strictly huge, the variability of the obtained results is constrained to a particular range.

When observing turbulent flows, many sizes of motion can be distinguished, from the bigger movements to the smallest swirls in the so-called '*energy cascade*'. One of the first mentions of the fractal behaviour of the turbulent structures was made by Richardson [1]. He proposed that the kinetic energy of the turbulent flow enters through the largest motion scales and is then transferred to the smallest scales until it is diffused by the viscous effects. Later on, Kolmogorov extend the '*energy cascade*' concept by proposing its hypotheses on [2]. Those hypotheses focused on quantifying the energy transfer between scales and the smallest scale where the viscous effects are high enough to dissipate the kinetic energy. Further explanations of the specific hypotheses can be found in [3]. However, explaining two of the keys of these hypotheses is required to understand part of the turbulent analysis that will be performed later on.

Following Kolmogorov's hypothesis, the flow statistics at the smallest scales only depend on the kinematic viscosity, ν and the dissipation rate, ε, so that scales can be computed using Equations 4.1.

$$\eta \equiv \left(\frac{\nu^3}{\varepsilon}\right)^{1/4} \tag{4.1a}$$

$$u_\eta \equiv (\varepsilon\nu)^{1/4} \tag{4.1b}$$

$$\tau_\eta \equiv (\nu/\varepsilon)^{1/2} \tag{4.1c}$$

Where u_η and τ_η are the velocity and time scales respectively, from the Kolmogorov scales. Additionally, the dissipation rate is usually defined as:

$$\varepsilon = 2\nu\langle s_{i,j} s_{i,j}\rangle \tag{4.2}$$

where s_{ij} corresponds to the strain tensor of the fluctuating velocity expressed as $s_{ij} = \left(\partial_i u_j + \partial_j u_i\right)/2$. However, as it is applied on a multiphase

flow configuration, ν is not constant, and further considerations have to be taken into account.

Moreover, when addressing turbulent problems using CFD, especially with DNS, a priori knowledge of the Kolmogorov scale is essential. This is because it is used to determine the grid size and thus, estimate the feasibility of the simulations. However, without any prior experiment or calculation, this information is challenging to obtain as the dissipation rate requires a well spatial and temporal discretisation of the domain. To overcome this difficulty and be able to size up the computational grid, the approximation given by S. Pope in [3] is commonly used. This approximation requires the characteristic Reynolds number to provide a Kolmogorov scale to flow characteristic length scale, as seen on Equation 4.3.

$$\eta/l_0 \sim Re^{-3/4} \tag{4.3}$$

Where l_0 is referred to the largest scales of the domain. Although this approximation is often used in the literature to size the domain grid, its lack of dependence on the dissipation rate makes it fail to provide reliable results when analysing the turbulent flows. In this context, DNS of multiphase flows can provide the velocity field required to compute the stress tensor of the fluctuating velocity as long as the temporal interval is long enough to get reliable statistics. However, although the Kolmogorov scale can be used as a parameter to size up the cell size of the problem, the reality is that it actually is a scalar field and presents different values depending on the position.

Additionally, having a multiphase flow leads to a non-uniform ν distribution both spatially and temporally. This has consequences when computing the Kolmogorov scale and the dissipation rate once the simulation is completed. Equation 4.2, requires having a constant and characteristic value for ν. Usually, on DNS simulations where the spatial discretisation is high enough to express the dissipation rate as:

$$\varepsilon = 2\langle \nu s_{ij} s_{ij} \rangle \tag{4.4}$$

However, using the one-fluid formulation allows expressing the local properties as a function of the time and position, so the viscosity can be expressed using the Reynolds decomposition as the sum of the mean and the time-dependence, leading to the Equation 4.5. Furthermore, the term related to the pulsating component of the viscosity can be neglected by the pseudo-fluid approach and confirmed in Crialesi [4].

$$\varepsilon = 2\left(\langle\nu\rangle\langle s_{ij}s_{ij}\rangle + \langle\nu' s_{ij}s_{ij}\rangle\right) \tag{4.5}$$

4.2.2 Flow field methodology

As already exposed, the multiphase nature of the sprays raises many open questions when studying the turbulence field in the dense region. There are neither experimental nor computational works devoted to this task. Nevertheless, there exist some works about the turbulence field of gaseous jets [5–7] that inspired this kind of approach on multiphase sprays as [4, 8, 9] which are the foundation of the present document. There, the authors made a straightforward analogy between both configurations, considering that the viscous interaction leads to a velocity decay as the injected flow goes through the quiescent domain. Since the momentum has to be conserved, the surrounding gas is accelerated. In these cases, there are two directions where the flow is changing considerably: the axial and the radial directions. This means that the flow is statistically stationary in the azimuthal direction, given an axial and a radial position.

Those previous studies did an in-depth analysis of the turbulence field in terms of the statistics convergence, dissipation rate, Kolmogorov scale and energy spectrum. This research helped size the grid and the computational domain size, considering the amount of energy resolved results. However, this document focuses on the influence of the injection conditions on flow field distributions and droplet formation. Thus, the turbulence statistics are limited to the study of the dissipation rate and the Kolmogorov scale as a way to check the accuracy of the resolution.

As already mentioned in the introduction, different types of outputs can be extracted from the simulations, and each has its purpose and post-process pipeline. The centreline values are just temporally averaged to analyse the axial distribution of the main flow fields. However, when it comes to the plane and the domain outputs, the high amount of data (both spatial and temporal) requires previous management to provide readable results.

When it comes to the Reynolds and Weber number studies, where round sprays are analysed, the axi-symmetric behaviour along the azimuthal direction allows to collapse all the information in a single radial profile (similarly as done in Chapter 3). So when post-processing both the plane and the domain data, apart from the temporal average, an azimuthal average is performed at each axial position, as seen schematically in Figure 4.1. This allows the study to express the variations of the flow field and turbulent statistics, and droplet location in terms of axial and radial positions.

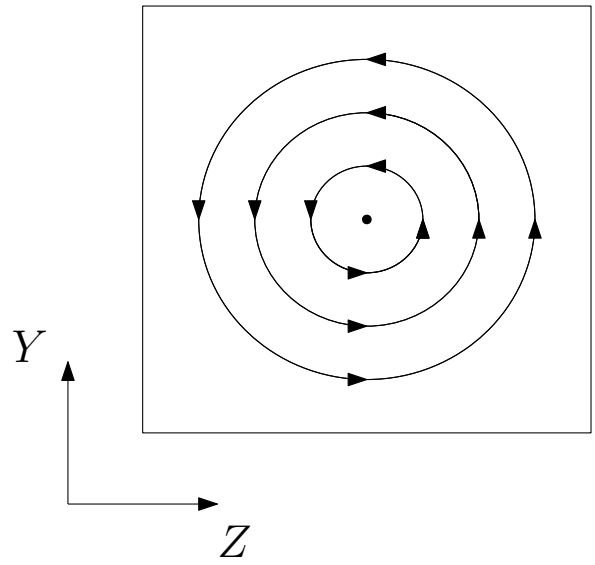

Figure 4.1: Scheme of the azimuthal average procedure on both the plane and the domain outputs.

Regarding the nozzle shape study, the elliptical sprays do not exhibit the axi-symmetric behaviour along the azimuthal direction. Instead, two planes aligned with the ellipse's major and minor axis can be set as regions of interest. With this, two main approaches have been followed to post-process the elliptical sprays. On the one hand, parameters such as the spray aperture are analysed on the planes of interest, directly comparing both directions. On the other hand, the transversal information as droplet position is collapsed into a single quadrant to provide information on the droplet cloud shape.

4.3 Droplet post-processing

4.3.1 Droplet analysis in the literature

As exposed earlier in the document, droplet formation is fundamental knowledge that the scientific community strives to obtain. Therefore, this section is devoted to providing an overview of how droplet detection has been addressed in DNS literature. Traditionally, the droplet concept has been related to a liquid structure with a spheric shape, which is true when the surface tension becomes dominant, and no external forces disturb their topology. However, in many cases, the droplets are affected by different shear stresses when the breakup occurs, deforming the liquid structure into ligaments or non-spherical

droplets. Nonetheless, the sphere approximation is widely spread in droplet detection studies, characterising them using their diameter.

As droplet characterisation is challenging, many approaches have arisen during the last decades. Early in century XXI, Subramaniam suggested in [10, 11] a method for initialising multiphase LES and DNS simulations with physically reliable conditions by correctly using the point-process theory, along with statistical mechanics. This initialisation was characterised by droplet spatial distribution and properties (such as velocity and size). However, the description of a droplet cloud using the point-process theory can be used to obtain physical information from the droplet distributions. In [10] the author explains that a droplet can be defined by its position vector, velocity vector and radius, summing a total of 7 parameters. So being a droplet cloud an ensemble of droplets, the fine-grained density function can be expressed in two different approaches, the Klimontovich and the Louisville descriptions. This statistical approach to the droplet description, precisely the Klimontovich formulation, inspired the analysis performed on previous works.

However, before analysing the droplet generation is mandatory to detect the droplets present within the computational domain. When it comes to the droplet detection in the numerical framework, one of the open arguments refers to the minimum diameter that can be considered a well-resolved droplet, depending on the grid size. In the mixing layer, where the turbulence increases and most of the breakup occurs, many droplets appear characterised with hardly higher than 2 cells. Shinjo and Umemura [12] stated that the detected droplets with a diameter smaller than 4 cells were numerical debris and could be neglected. Zhang et al. [13] used an AMR code to study the gasoline spray and set a cutoff diameter corresponding to 8 volume cells. Other studies that compared computational simulations with experimental results on prefilmer airblast atomisers set the minimum resolved droplet depending on the experiment resolution [14]. Those smallest droplets can be caused by numerical pinch-off, satellite atomisation, or even well-resolved breakups, so the criteria can vary depending on the objective of the study. In these terms, Ling et al. [15] studied the influence of the mesh size on the atomisation description, comparing the obtained droplet size PDFs with the log-normal and gamma distribution models. Those results exhibit that the more the mesh is refined, the more the distribution tends to present a log-normal pattern. Moreover, according to the author, although the most refined mesh demonstrated to resolve up to the Kolmogorov scale [16], the mesh convergence seemed not reached.

Many of the atomisation studies in the literature aim to obtain droplet

size distributions to analyse the breakup events. Shinjo and Umemura [12] provided the droplet size distribution depending on the inflow velocity. They were showing an increase in droplet production and obtaining finer droplets. Furthermore, they stated that the transient phase provided atomisation only on the tip of the spray (as no inflow turbulence was present), being not relevant when studying the statistically stationary state.

An interesting approach was proposed by Herrmann [17], combining an Eulerian-Lagrangian approach, where the liquid core was captured and resolved on the Eulerian mesh, while the disconnected liquid structures were extracted and computed in a Lagrangian coupled mesh. This method was used in different studies as on Herrmann [18] where the mesh dependency on the droplet diameter, volume and area distribution is analysed. In addition, Herrmann also studied the influence of the density ratio on droplet generation on a liquid jet in crossflow [19].

A similar procedure was proposed by Ling et al. [20]. Here, they proposed a droplet detection methodology where the bigger structures (as ligaments, liquid core and big droplets) were resolved using the VOF method and the smaller droplets (with diameters around 4 to 6 cells) were transferred to a Lagrange-Point-particle model to be resolved. Primary efforts were put into coupling the momentum conversion between the Lagrange-Point Particle and the resolved flow, validating the results against full resolved DNS simulations and experimental data on a gas-liquid mixing layer.

Other works, such as the one from Warncke et al. [14] compared DNS simulations of a simplified prefilmer airblast atomiser against experimental data under the same operating conditions. The results were promising, showing comparable results between both approaches. However, the mesh refinement was probably not sufficient enough.

To summarise, the droplet detection and analysis are in the spotlight of multiphase flows computational studies, and the research gathered in the literature has raised the main topics that have to be considered when addressing this particular problem:

- **Droplet resolution**: the different studies reported liquid structures smaller than the mesh resolution, even on a priori low turbulence scenarios [12]. The mesh convergence of the droplet distribution is still unclear, and the treatment of the smallest droplets depends on the analysis performed.
- **Experimental comparability**: the comparison with experimental data is also sensitive to the used technique and the detection resolu-

tion. Techniques such as Particle Image Velocimetry (PIV) or Phase Doppler Anemometry (PDA) fail to give accurate information on dense mediums and focus on providing droplet distributions in the far field. This leads to requiring large computational domains out of the possibility of DNS or focusing on more straightforward configurations of actual atomisers (e.g. [14]) to validate their results with experiments.

- **Resources required**: the droplet detection itself requires analysing the computational domain looking for connected cells with liquid. This analysis can be performed on the snapshots provided during the simulation or be calculated on the fly. Performing the study on the snapshots allows carrying out a sensitivity study of the detection method without increasing the computational time of the simulation. However, a high-frequency sample time resolution is required to provide enough temporal information. This usually leads to a hardly manageable required storage space for each snapshot. On the other hand, on-the-fly statistics allow increasing the time-resolution of the detected droplets without impacting the storage requirements. Nevertheless, performing this approach can be more time-consuming, slowing down the simulation, and does not allow performing sensitivity studies without re-running the simulation.

4.3.2 Droplet detection algorithm

As previously introduced, many techniques address droplet detection and characterisation in the computational approach. Tagging functions usually directly provide droplet sizes and positions, approximating all liquid structures to spheric droplets. Codes as Basilisk [21] provide tagging functions to obtain the droplet distribution while the simulation is running, which can also be used to delete the smallest droplets considered as debris and improve the code stability [13]. On the other hand, many codes provide the liquid fields and have to be post-processed.

PARIS Simulator (which is the used code in this research) provides the VOF field, which needs to be analysed to extract the droplet information. In previous works [4, 8, 22] a recursive algorithm was developed to scan the snapshots provided by the code and identify the connected structures. This algorithm performed an average of each cell centre and velocity, weighted with the volume fraction, on all cells corresponding to the same liquid structure. Then the information was collapsed into a spherical droplet with the same volume, velocity and centre location. Although this methodology disposes of the topology features from the original liquid structure, it simplifies the process and is almost a direct way to compare DNS results with Discrete Droplet

Methods (DDM). However, the recursive method proved to be time-consuming as the number of cells increased, requiring a complex parallelisation of the spatial domain. Besides, that method exhibited two extreme cases that failed to identify liquid structures correctly. On the one hand, the maximum recursive loops allowed were far lower than the number of cells on the liquid core, requiring special and time-consuming treatment to remove it from the droplet cloud. On the other hand, some ligaments near the liquid core exhibit complex geometries and the algorithm divided them into smaller droplets. Although the last situation was not crucial in the overall spray analysis, the droplet detection algorithm was changed to improve the post-processing efficiency.

The new post-processing routine avoids the recursive approach of applying VTK [23] filters to identify the liquid structures. Like the previous methodology, the procedure is based on the study of the VOF field and requires setting a threshold, C_{th}, to check whether the cell is full or empty. Figure 4.2 shows the result of applying a *Threshold Filter* to a VOF field obtained from a snapshot. Among the many filters present on VTK, the *Connectivity filter* detects connected cells. So, once the *Threshold filter* is applied on the domain, the *Connectivity filter* ascribes the same value to the cells belonging to the same liquid structure. This task is based on the connectivity vector that internally uses VTK to assemble the mesh and the field values and has been proved as a faster option than the recursive approach. Indeed, this method has no limitations for detecting large liquid structures and handling the liquid core identification smoothly.

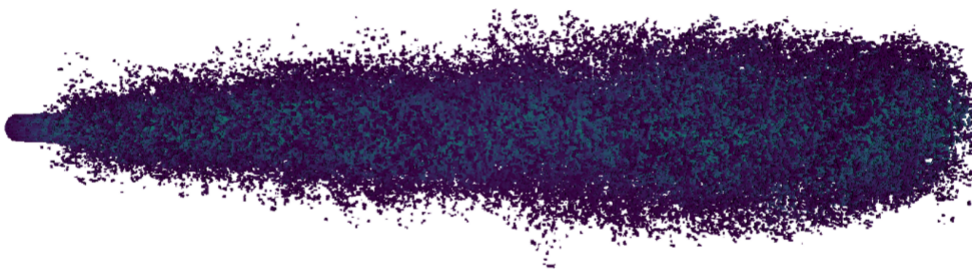

Figure 4.2: Spray morphology obtained after applying the Threshold filter.

Once the filter has provided each cell with a droplet identification value, they can be grouped to compute the droplet statistics. In the same manner as in the previous methodology, the volumetric diameter, d_v is used to characterise the droplet size and is computed as $d_v = \sqrt[3]{6V_d/\pi}$, being V_d the total

volume of the droplet, computed with the VOF values and the cell volume. The same procedure is applied to the velocity and the centre of mass, obtained using a weighted average of the values of each cell belonging to the same droplet. With this approach, the liquid core is easily distinguished, as it has the highest volume of all liquid structures and can be isolated to perform specific studies.

So, to be able to apply this post-processing methodology to the simulation snapshots, only the threshold value of the colour function, C_{th}, has to be defined. This threshold will dictate whether the cell is considered part of a droplet or not, so it is of fundamental importance. Crialesi et al. [8] performed a parametric study of the influence of the threshold value on the droplet size distribution detected. Figure 4.3 depicts the different droplet size distributions depending on the threshold value, ranging from 0.05 to 0.4. It can be noticed that for most of the droplet sizes ($6.71 \leq d_v \leq 22.72$), the number of detected droplets N_{drop} is quite similar, regardless of the threshold value. However, when focusing on the distribution sides, the trends are inverse. The lower the C_{th} value is chosen, the fewer number of small droplets are detected, but the higher number of large drops are counted. This particular behaviour is explained by the existence of thin ligaments that connect the liquid structures, so, as the C_{th} increases, the liquid structures are more prone to be split into two or more structures. Nonetheless, the thin ligaments that are taken into account on lower C_{th} values are presumed to be breaking up soon, so counting as separate droplets could be not so deceiving as it could seem.

As already introduced, one of the main limitations of this type of procedure is the demanding storage requirements. So, choosing the sampling frequency is key to optimising the saved data and avoiding having an unmanageable number of files. There are two phases during the atomisation simulation that are distinguishable. On the one hand, the transient phase encompasses from the start of the injection until the spray tip goes through the axial outflow boundary of the domain, located at 2.4 mm (corresponding to $x/D_n \approx 27$). In this state, a high sampling frequency is required to capture the dynamics that cause the spray formation, so a snapshot is analysed every 0.5 µs. On the other hand, the statistically stationary phase starts right after the transient phase and lasts until the end of the simulation. As this phase lasts longer than the transient phase, the sampling frequency increases to 10 µs. This also allows significant time for the liquid structures to leave the domain while new droplets and ligaments are generated.

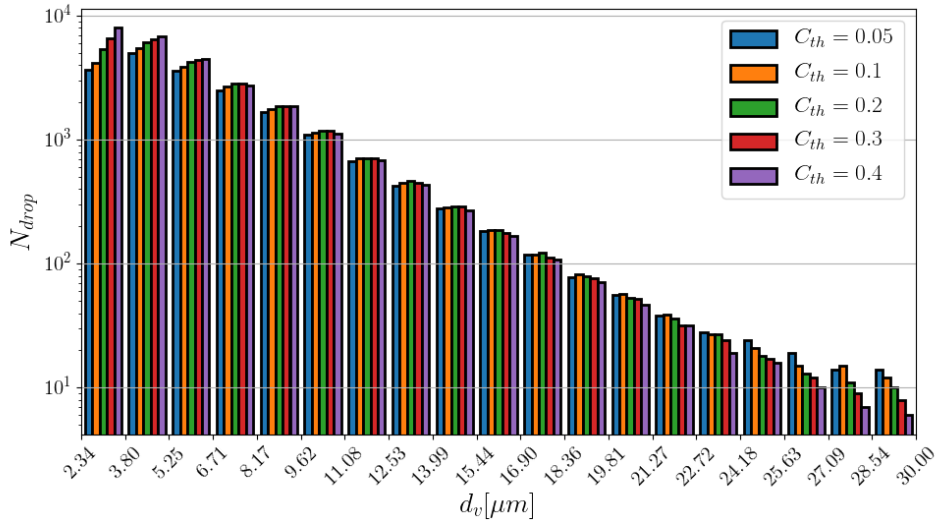

Figure 4.3: Parametric analysis of the C_th parameter during the statistically stationary state of the reference simulation from Crialesi [4].

References

[1] Richardson, Lewis F. "Weather prediction by numerical process, second edition". In: *Weather Prediction by Numerical Process, Second Edition* (1922), pp. 1–236. DOI: 10.1017/CBO9780511618291.

[2] Kolmogorov, A. "On the log-normal distribution of particles sizes during breakup process". In: *Dokl. Akad. Nauk.* XXXI.4 (1941), pp. 99–101.

[3] Pope, Stephen B. *Turbulent flows*. IOP Publishing, 2001.

[4] Crialesi-Esposito, Marco. "Analysis of primary atomization in sprays using Direct Numerical Simulation". PhD thesis. Universitat Politècnica de València, 2019.

[5] Corrsin. *SPECTRA AND DIFFUSION IN A ROUND TURBULENT JET*. Tech. rep. 8. 1943, pp. 399–405.

[6] Hussein, Hussein J., Capp, Steven P., and George, William K. "Velocity measurements in a high-Reynolds-number, momentum-conserving, axisymmetric, turbulent jet". In: *Journal of Fluid Mechanics* 258 (1994), pp. 31–75.

[7] Craske, John, Debugne, Antoine L R, and Van Reeuwijk, Maarten. "Shear-flow dispersion in turbulent jets". In: *Journal of Fluid Mechanics* 781 (2015), pp. 28–51. DOI: 10.1017/jfm.2015.417.

[8] Crialesi-Esposito, Marco, Gonzalez-Montero, L. A., and Salvador, F. J. "Effects of isotropic and anisotropic turbulent structures over spray atomization in the near field". In: *International Journal of Multiphase Flow* 150.November 2021 (2022), p. 103891. DOI: 10.1016/j.ijmultiphaseflow.2021.103891.

[9] Torregrosa, Antonio J., Payri, Raul, Javier Salvador, F., and Crialesi-Esposito, Marco. "Study of turbulence in atomizing liquid jets". In: *International Journal of Multiphase Flow* 129 (2020), p. 103328. DOI: 10.1016/j.ijmultiphaseflow.2020.103328.

[10] Subramaniam, S. "Statistical representation of a spray as a point process". In: *Physics of Fluids* 12.10 (2000), pp. 2413–2431. DOI: 10.1063/1.1288266.

[11] Subramaniam, S. "Statistical modeling of sprays using the droplet distribution function". In: *Physics of Fluids* 13.3 (2001), pp. 624–642. DOI: 10.1063/1.1344893.

[12] Shinjo, J. and Umemura, Akira. "Simulation of liquid jet primary breakup: Dynamics of ligament and droplet formation". In: *International Journal of Multiphase Flow* 36.7 (2010), pp. 513–532. DOI: 10.1016/j.ijmultiphaseflow.2010.03.008.

[13] Zhang, Bo, Popinet, Stephane, and Ling, Yue. "Modeling and detailed numerical simulation of the primary breakup of a gasoline surrogate jet under non-evaporative operating conditions". In: *International Journal of Multiphase Flow* 130 (2020), p. 103362. DOI: 10.1016/j.ijmultiphaseflow.2020.103362.

[14] Warncke, K. et al. "Experimental and numerical investigation of the primary breakup of an airblasted liquid sheet". In: *International Journal of Multiphase Flow* 91 (2017), pp. 208–224. DOI: 10.1016/j.ijmultiphaseflow.2016.12.010.

[15] Ling, Yue, Fuster, Daniel, Zaleski, Stéphane, and Tryggvason, Grétar. "Spray formation in a quasiplanar gas-liquid mixing layer at moderate density ratios: A numerical closeup". In: *Physical Review Fluids* 2.1 (2017), p. 014005. DOI: 10.1103/PhysRevFluids.2.014005.

[16] Ling, Y et al. "A two-phase mixing layer between parallel gas and liquid streams: multiphase turbulence statistics and influence of interfacial instability". In: *Journal of Fluid Mechanics* 859 (2019), pp. 268–307. DOI: 10.1017/jfm.2018.825.

[17] Herrmann, Marcus. "A parallel Eulerian interface tracking/Lagrangian point particle multi-scale coupling procedure". In: *Journal of Computational Physics* 229.3 (2010), pp. 745–759. DOI: 10.1016/j.jcp.2009.10.009.

[18] Herrmann, Marcus. "On Simulating Primary Atomization Using the Refined Level Set Grid Method". In: *Atomization and Sprays* 21.4 (2011), pp. 283–301. DOI: 10.1615/AtomizSpr.2011002760.

[19] Herrmann, Marcus. "The influence of density ratio on the primary atomization of a turbulent liquid jet in crossflow". In: *Proceedings of the Combustion Institute* 33.2 (2011), pp. 2079–2088.

[20] Ling, Y., Zaleski, Stéphane, and Scardovelli, Ruben. "Multiscale simulation of atomization with small droplets represented by a Lagrangian point-particle model". In: *International Journal of Multiphase Flow* 76 (2015), pp. 122–143. DOI: 10.1016/j.ijmultiphaseflow.2015.07.002.

[21] Popinet, Stéphane. *Basilisk code*. 2014.

[22] Payri, Raul, Salvador, Francisco Javier, Gimeno, Jaime, and Crialesi-Esposito, Marco. "Comparison of mapped and synthetic inflow boundary conditions in Direct Numerical Simulation of sprays". In: *ILASS - Europe 2019, 29th Conference on Liquid Atomization and Spray Systems*. Paris, France, 2019.

[23] *VTK*.

Chapter 5

The Influence of Reynolds Number

5.1 Introduction

This chapter will be focused on the study of the influence of Reynolds number on the spray formation in the near region, up to 2.4 mm from the injection orifice. Three different DNS simulations have been carried out to perform this study, ranging this parameter from 5,037 to 9,000.

The low Reynolds condition will be taken as the reference case as it has been designed following the Engine Combustion Network (ECN) [1] Spray A configuration, except for the fuel mean velocity which is reduced to be feasible for DNS computations. This condition has been widely used to perform experimental studies during the last years and is suited to be used to validate simulation results in the future, when both the experimental and computational injection conditions are comparable. Table 5.1 gathers the configuration parameters used for all the simulations. This case has already been addressed in previous studies [2–4], performing in-depth studies on both turbulent statistics and droplet generation. Thus, it will be used as the reference case.

As already mentioned early in the document, varying the Reynolds number without increasing the bulk velocity or increasing the nozzle diameter requires changing the fluid physical properties. Additionally, those physical properties have been changed so that the Weber number is also maintained. With this limitations, three different fluids will be simulated to perform this study and

their properties are gathered on Table 5.2. Note that the reference case corresponds to a real fluid (Dodecane) while the other cases are pseudo-fluids designed to increase the Reynolds number.

Table 5.1: Spray A configuration

Fuel mean velocity	$\langle U_b \rangle$ [m/s]	100
Nozzle diameter	D_n [µm]	90
Nitrogen viscosity	μ_g [Pa·s]	$1.85 \cdot 10^{-5}$
Nitrogen density	ρ_g [km/m^3]	22.8

Table 5.2: Simulation parameters for the Reynolds study

Reynolds number	Re [-]	5,037	7,000	9,000
Fuel viscosity	μ_l [kg/m^3]	$1.34 \cdot 10^{-3}$	$0.964 \cdot 10^{-3}$	$0.69 \cdot 10^{-3}$
Fuel density	ρ_g [kg/m^3]	750	750	690
Surface tension	σ [kg/s^2]	0.025	0.025	0.023
x - length	l_x [mm]	2.4	2.4	2.4
y,z - length	l_y, l_z [mm]	1.2	1.5	1.6
Cell size	d_x [µm]	2.34	1.87	1.56
Timestep	d_t [ns]	4	2	2
Number of cells	N_{cells} [-]	$268 \cdot 10^6$	$768 \cdot 10^6$	$1,610 \cdot 10^6$

This approach allows simulating moderate Reynolds number without requiring reducing significantly both the cell size and the timestep to keep moderate values of the Courant number. However, as the Reynolds number increases the turbulent processes gain significance, leading to smaller eddies scales. This leads to the decrease of the characteristic Kolmogorov scale η, which requires a consequent reduction of the cell size to try to capture those motion scales. Since there is no way to accurately compute the Kolmogorov scale a priori, nor there is any previous computational or experimental study that can be used to derive an approximation, the well-known expression from Pope [5] is used to get an initial estimation (already addressed in Chapter 4). This initial estimation is used to set the cell size for each case. This approach was already applied on the reference case on Torregrosa et al. [3], where the Kolmogorov scale was estimated a priori and computed a posteriori, leading

to an acceptable ratio between the cell size and the calculated Kolmogorov scale. Thus, has been also applied for the rest of the cases presented on this study.

Preliminary studies performed increasing the reference case Reynolds number exhibit some flow structures around the spray tip during the transient time that were not fully captured within the domain. These non-closed structures provoked non-physical spray breakup, generating high number of static droplets located far away from the spray. This phenomenon forced to increase the domain size with the Reynolds number, otherwise the transient phase of the simulation, and thus the statistically stationary phase, would not be realistic. This means that, when increasing the Reynolds number, the cell size has to decrease while the domain has to increase, leading to an exponential growth of the total number of cells. Finally, maintaining the CFL lower than 0.3 requires lower timesteps, and this is one of the main reasons to maintain the average velocity field on the simulations. Although the timestep has to decrease with the Reynolds number, as the velocity is maintained, the timestep can be sufficiently high to make those simulations affordable.

Finally, regarding the boundary conditions, two different types are used. On the one hand, the inflow boundary condition is perpendicular to the axial direction. The velocity is set according to the LES mapped condition and placed in the middle of the face. The rest of the boundary conditions are set as an outflow.

During this chapter the results will be divided in three different approaches: first a study of the velocity and the density fields will be developed. On the one hand, a study of the effects of the inflow boundary conditions on the spray morphology will be presented, putting emphasis on the liquid core perturbations. Then, using the domain snapshots and the centreline probes to analyse the axial distribution of important parameters as the spray aperture, centreline velocity decay and the centreline liquid concentration. Additionally, a turbulence study will be performed on a transversal plane located at $x/D_n = 25$, focusing on the dissipation rate and the Kolmogorov scale distributions. This is of fundamental importance as it will be used to check the accuracy of the simulations. Finally, the main efforts will be devoted to the analysis of the droplet cloud in terms of size, position and velocity distribution.

5.2 Spray morphology study

The first approach to the atomisation results is made by examining the overall spray morphology. To this end, two different snapshots are chosen to be

analysed. On the one hand, one corresponds to the transient phase, where the spray is still penetrating the domain; and on the other hand, one where the statistically stationary state is reached, so the spray is completely developed.

Figure 5.1 shows the overall aspect of the spray during the transient phase, specifically at T = 12.5 µs, for all three cases. Sorted from top to bottom as the Reynolds number increases, the liquid surface has been reconstructed using an iso-surface with $C_{th} = 0.05$. The first thing to notice is that all cases present a spray tip with a high disintegration rate, so the 'mushroom tip' is barely visible. This is caused because the injected turbulence disrupts the liquid surface of the tip earlier than the liquid-gas friction, perturbing the characteristic mushroom shape. In fact, in normal conditions, the first instants of the injection the liquid is at rest inside the nozzle, so the initial injection would present less turbulence and the 'mushroom tip' would be less perturbed. Regarding the droplet sizes, they are finer as the Reynolds number increases. However, the droplet cloud seems more significant at lower Reynolds. Finally, as the injection bulk velocity is the same in all cases, the penetration showed by the three conditions is nearly the same.

Moving to the statistically stationary phase, in Figure 5.2 the spray morphology at T = 150 µs is represented fot all the cases when they are fully developed. Just like in the previous Figure, the cases are sorted from top to bottom by increasing the Reynolds number, and the spray is represented as an iso-surface where $C_{th} = 0.05$. Increasing the Reynolds number does not affect the spray aperture but the droplet size and generation. The higher Reynolds case presents a finer droplet cloud and apparently generates more droplets than the lower Reynolds number cases. It is also interesting to point out the existence of relatively big spherical droplets located in the spray periphery in all conditions. Another noticeable effect is that the atomization seems to start earlier in the axial distance by increasing the Reynolds number.

This earlier atomization is caused by the increase of the perturbations on the liquid core surface. So, the liquid core is extracted with the droplet detection algorithm to study the surface perturbations without the noise induced by the presence of the droplets. Figure 8.6 shows a zoom in the liquid core at the nozzle exit for all cases, increasing the Reynolds number from left to right. All snapshots have been taken at T = 150 µs, and applying a contour filter with $C_{th} = 0.95$.

Results show how the perturbations on the liquid core surfaces increase as the Reynolds number increases. Those perturbations are responsible for forming ligaments and, consequently, the breakup of the liquid core into droplets. Indeed, all cases present two different regions, the first one closer to the nozzle

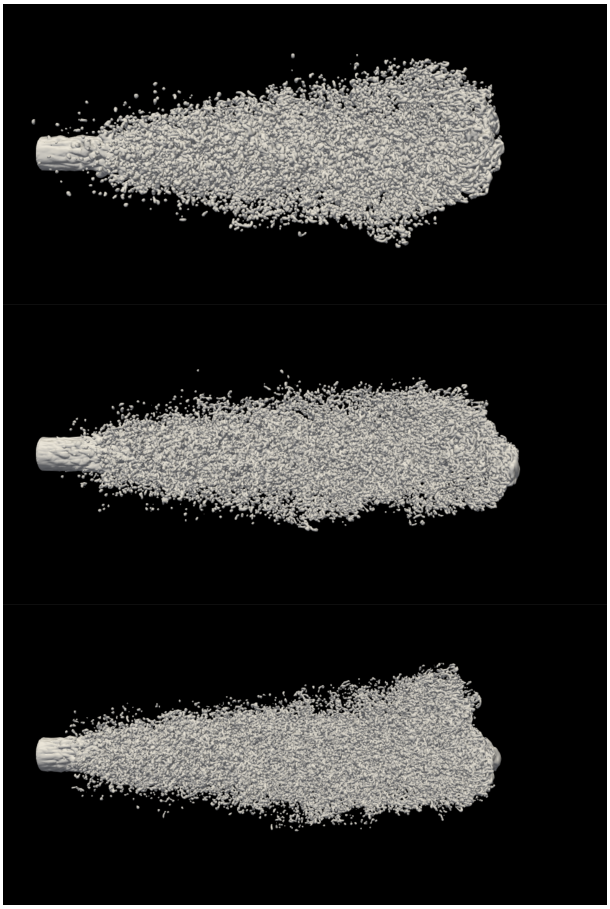

Figure 5.1: Spray morphology during the transient state at $T = 12.5$ μs. Increasing Reynolds number from top to bottom.

where the cylindrical shape is maintained. This region corresponds to the intact region, where the core presents perturbations mainly caused by the inflow turbulence. It can be seen that, as the Reynolds number increases, the perturbations present on the liquid surface have less amplitude, but their number increases. In Chapter 3 the vortex generation was studied within the internal flow, showing an increase of turbulent structures and their shifting towards the pipe wall as the Reynolds number increased, which is coherent with the behaviour depicted on the snapshots. As the axial distance increases, the perturbations disrupt the liquid core, leading to a chaotic core contour, indicating the size of the external non-perturbed length x_i where the atomization occurs.

Visually, the x_i can be estimated at 1.8, 1.2 and 1 times the nozzle diameter

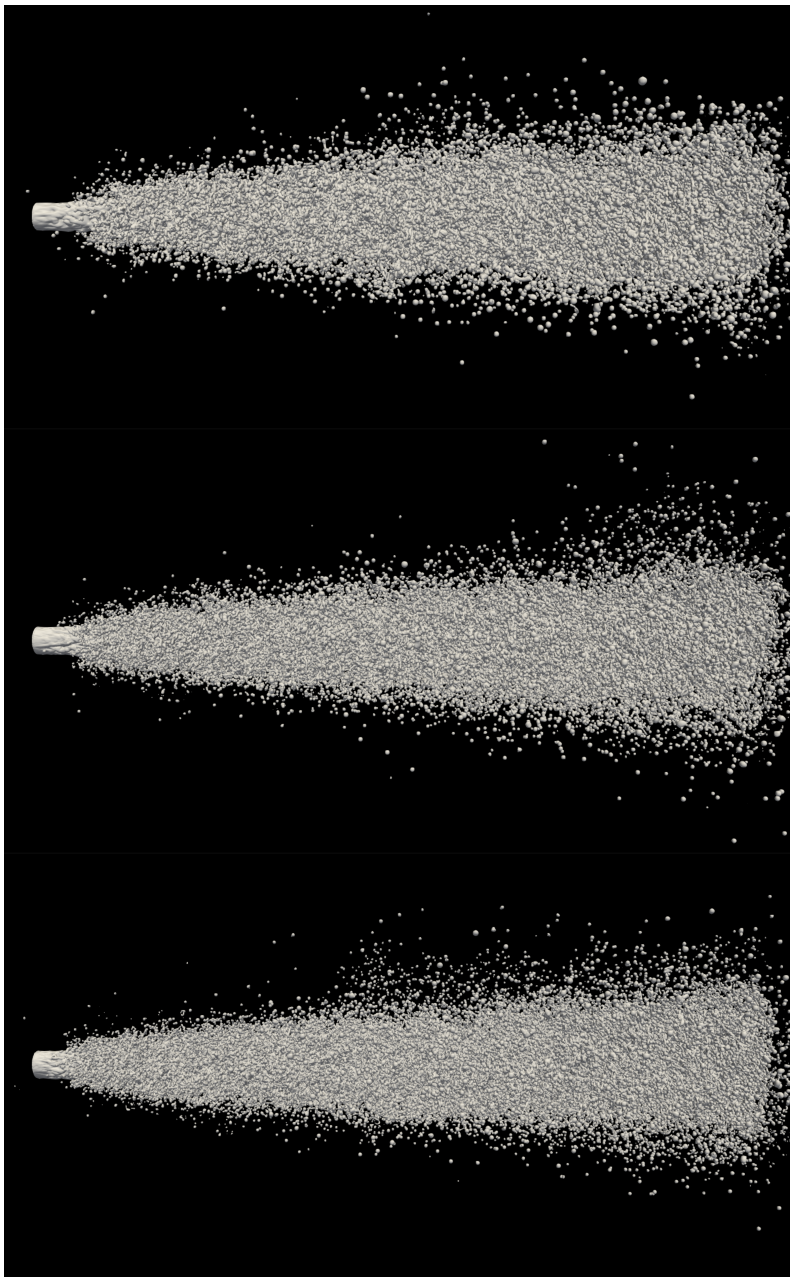

Figure 5.2: Spray morphology during the statistically stationary state at $T = 150\ \mu s$. Increasing Reynolds number from top to bottom.

Figure 5.3: Spray core extracted from the full spray at $T = 150$ µs. Increasing Reynolds number from left to right.

as the Reynolds number increases. However, further analysis is performed on the topology of the liquid core by detecting the instantaneous contour and studying the deviation of the surface. The contour detection is performed on different planes along the azimuthal direction using a cylindrical mesh, similar to the one used to study the planes and explained in Chapter 4. In each azimuthal plane, the core contour is detected each 10 µs at the statistically stationary state, and then the standard deviation is studied as a marker of the perturbations of the liquid surface at that axial position. Then, an average of the standard deviation is performed in the azimuthal direction to obtain a smoother axial distribution. Figure 5.4 depicts the mean contour, shaded with the standard deviation along the axial direction, focused on the nozzle outlet. It can be seen that the first region up to $x \approx 1.4$ presents a higher standard deviation for the highest Reynolds number case, followed by a region up to $x \approx 2$ where the medium Reynolds case is the one exhibiting the higher standard deviation.

So, the x_i can be computed by setting a threshold where the standard deviation reaches the 10% the nozzle radius (i.e. 0.0045 mm). With this, Figure 5.5 shows the standard deviation of the core radius r_c along with the axial distance, and in grey is plotted the said threshold. The obtained values are 1.3, 1.1 and 0.96 as the Reynolds number increases. Compared with the results obtained by the visualization, they are slightly lower (particularly at the lowest Reynolds number), but overall are really similar, and the trend is maintained.

5.3 Flow field analysis

This section mainly focuses on studying the velocity, liquid volume fraction, and mass concentration fields during the statistically stationary state. Start-

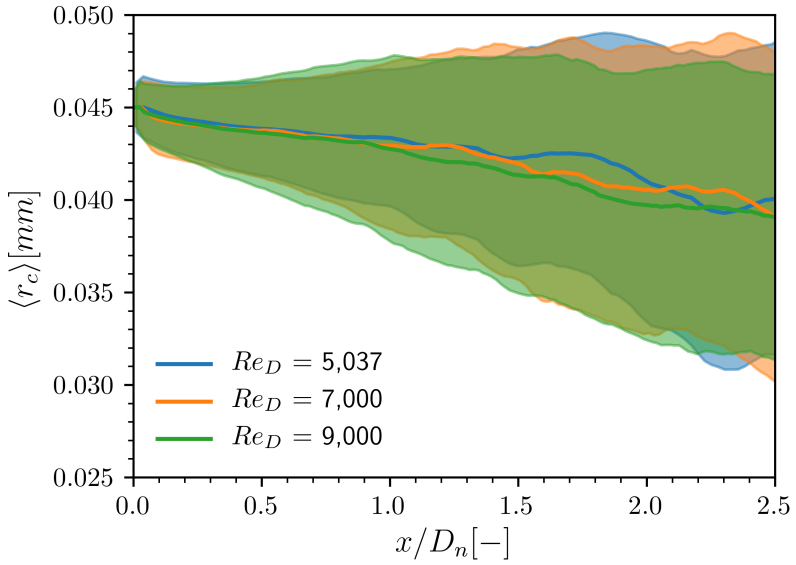

Figure 5.4: Axial distribution of the average core radius, shaded with the standard deviation.

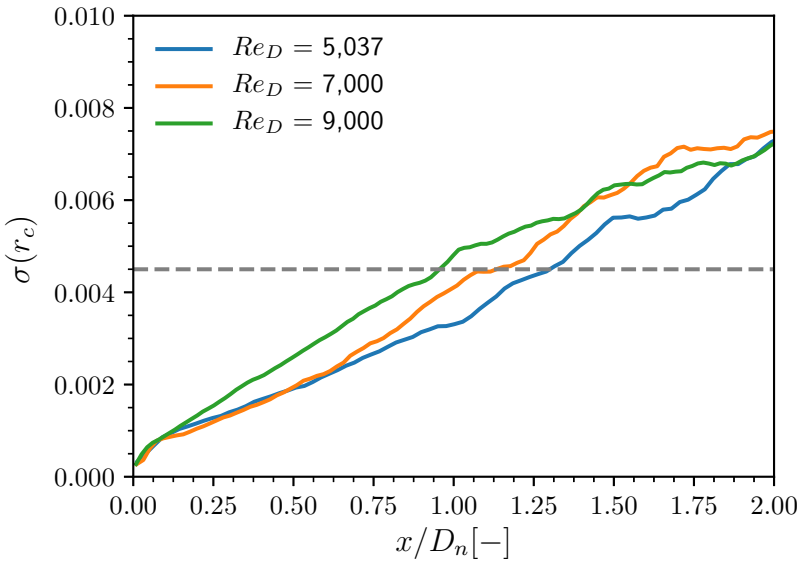

Figure 5.5: Axial distribution of the standard deviation of the core radius.

ing with the centreline values, followed by the axial distribution of the spray aperture and concluding with the analysis of a plane located at $x/D_n = 25$.

5.3.1 Centreline statistics

The velocity and liquid distribution along the spray axis are of fundamental importance as they can be used to estimate the amount of momentum and mass transferred to the medium. So, in order to achieve accurate statistics, the centreline is sampled every timestep once the simulations have reached the statistically stationary state, and then the temporal average is performed. The centreline analysis will be focused on the axial velocity decay and the liquid mass concentration.

Figure 5.6 depicts the average axial component of centreline velocity, $u_{x,c}$, distribution on the axial direction. First of all, focusing on the nozzle exit, it is noticeable that as the Reynolds number increases, the average values of the centreline velocity decrease. As already explained in Chapter 3, as the Reynolds number increases, the axial velocity profile tends to a more squared distribution, as seen in Figure 3.4 and [6]. So, as the bulk velocity is maintained in all conditions (100 m/s), the values around the pipe centre have to be lower as the profile adapts to the squared shape. When looking at the overall trends, it can be seen that all cases present two different slopes, one steeper up to $x/D_n \approx 7$ and then one smoother up to the end of the domain. Both trends can be characterised by linear regression.

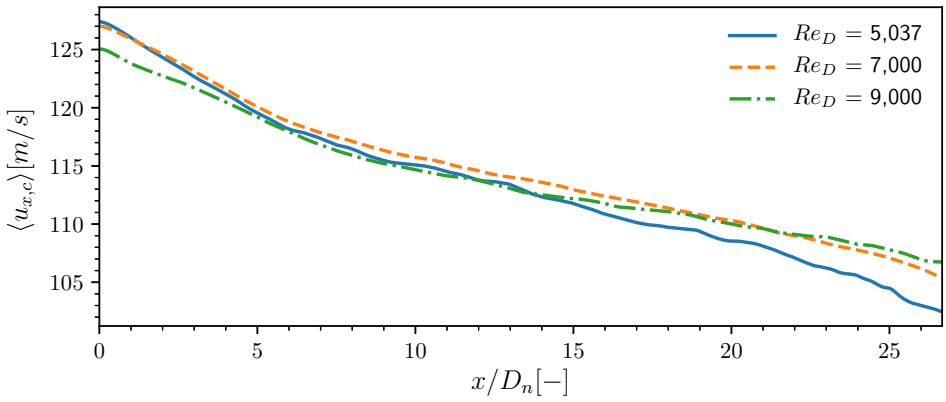

Figure 5.6: Axial distribution of the centreline axial velocity.

Table 5.3 gathers the linear regression parameters for all cases, where m, n are the regression slope and the intercept point, respectively, and R^2 is the coefficient of determination. Subscripts 1 and 2 refer to the first and

the second trend seen when moving along the axial direction, and d is the non-dimensional axial distance where both regressions intersect. So as the Reynolds number increases, both slopes are less prominent, and the transition takes place later in the axial direction. This means that the lower the Reynolds number is, the easier is the momentum transfer from the spray axis. This can be non-intuitive as the turbulence should act as a mass and momentum mixer, but the fact that the velocity profile is not fully developed leads to unexpected behaviours that will be extensively discussed in this chapter.

Table 5.3: Linear regression parameters of the axial distribution of the centreline velocity for all Reynolds cases.

$\mathbf{Re}_D$	5,037	7,000	9,000
$\mathbf{m}_1$	-1.512	-1.423	-1.184
$\mathbf{n}_1$	127.60	127.33	125.13
$\mathbf{R}_1^2$	0.999	0.998	0.998
$\mathbf{m}_2$	-0.706	-0.581	-0.457
$\mathbf{n}_2$	122.30	121.67	119.16
$\mathbf{R}_2^2$	0.996	0.996	0.996
$\mathbf{d}$	6	6.6	8

Regarding the liquid fraction, C, distribution along the spray centreline, Figure 5.7 presents the C values obtained after averaging during all the statistically stationary states of the simulations. As expected, the values near the nozzle are equal to 1, meaning that only liquid is present in that region. When moving further from the nozzle, the mean values start to decrease when the liquid-gas mixing reaches the centreline of the spray. It can be seen that the mass transfer from the centreline takes place earlier as lower the Reynolds number is. This is in line with the velocity results shown before, so as the velocity decreases in the centreline, both the momentum and the mass are transferred through the radial direction.

In addition to the liquid volume fraction study, the liquid mass concentration, m_c will also be computed to analyse the liquid axial distribution. This decision is based on the fact that the experiments able to provide information on the spray centreline are based on X-rays, and those experiments provide the local spray mass concentration as on [7, 8]. So, in order to give comparable data, the liquid mass concentration is computed using the Equation 5.1 on the centreline.

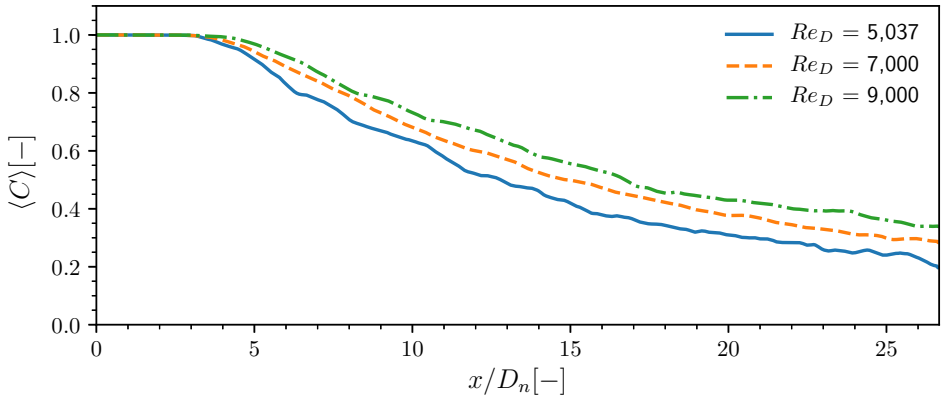

Figure 5.7: Axial distribution of the liquid volume fraction.

$$m_c(x) = \frac{C(x) \cdot \rho_l}{C(x) \cdot \rho_l + (1 - C(x)) \cdot \rho_g} \tag{5.1}$$

Figure 5.8 shows the liquid mass concentration value on the centreline. It can be noticed that the results show the same trends as on the liquid volume fraction analysis when analysing the Reynolds influence. Nevertheless, two details are worth mentioning. On the one hand, the axial values where the liquid mass concentration drops below 0.99 are higher than those obtained by the liquid volume fraction field. On the other hand, the decay seems to follow a more linear distribution than the shape presented in the liquid volume fraction figure.

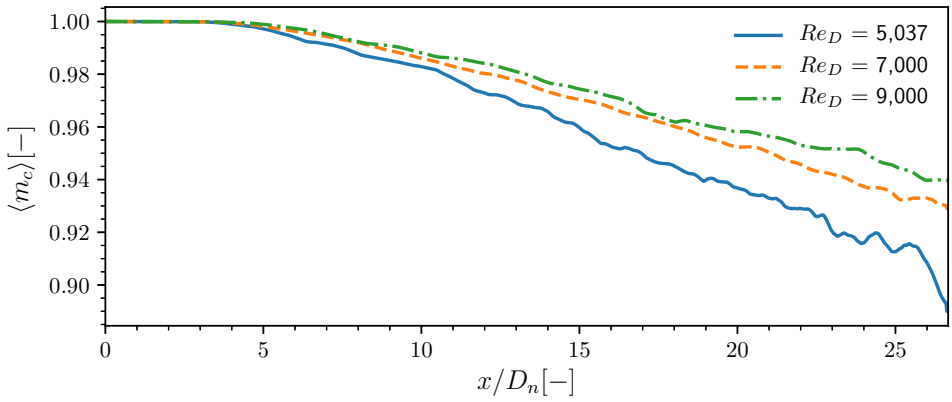

Figure 5.8: Axial distribution of the liquid mass concentration, m_c.

Furthermore, it is possible to set a criterion to determine the breakup length on the centreline by setting a certain threshold on the liquid volume fraction and mass concentration distributions. Table 5.4 gathers the breakup lengths, x_b, obtained by applying three different thresholds to both C and m_c for all considered conditions. It can be seen that, as is visible in Figures 5.7 and 5.8, as the Reynolds number increases, so do the breakup length, independently of the parameter or the threshold value selected. Indeed, the trends presented on each threshold value are practically identical. Also, the values obtained by applying the threshold to the m_c are significantly higher than those obtained by the C.

Table 5.4: Breakup length using different thresholds on C and m_c.

	C			m_c		
$\mathbf{Re}_D$	5,037	7,000	9,000	5,037	7,000	9,000
$x_b/D_{n\ (Th=0.99)}$	3.36	3.69	4.25	7.52	8.62	9.37
$x_b/D_{n\ (Th=0.98)}$	3.7	4.05	4.64	10.73	12.18	13.25
$x_b/D_{n\ (Th=0.95)}$	4.5	4.86	5.44	16.96	21.06	24.05

These trends contradict the classical knowledge where, when the spray reaches the atomisation regime, the breakup length decreases until the atomisation is completely developed, and then, this value remains nearly constant. However, as already mentioned in Chapter 1, B. Trettel broadly argued on [9, 10], how the classic breakup regimes need to be revisited, putting the spotlight on additional parameters beyond the non-dimensional numbers. He focused on the influence of the turbulence intensity on the breakup regime, proposing a redistribution of the diagram and adding new regimes, such as the turbulent breakup regime. Although the diagrams proposed on [9] and shown in Figure 1.2 back in Chapter 1 can not be directly used to situate our simulated points, they inspired to dig into the possibility of re-evaluating the trends and studying the influence of an additional parameter that B. Trettel mentions on [9], the inlet velocity profile. As shown in Figure 3.4, the average axial velocity profile distribution is still changing as the Reynolds number increases, meaning that the flows are located in a not-fully developed turbulent region. This is key to understanding that the studied cases can not be located in a fully atomised regime, and this factor will heavily influence many aspects of the spray development. Indeed, the breakup length is known to be dependent on the Area Coefficient C_a [11, 12], which increases with the Reynolds number and can be a possible explanation for this behaviour. Additionally,

the discharge coefficient is also variable in this Reynolds number range. So it would be expected that, when moving to actual fully-developed turbulent flows, coefficients such as the area, velocity or discharge should normalise, shifting the trends to the expected ones on the fully atomised regime. In the following sections, the evolution of the velocity profile is studied with a more depth study of its influence on mass and momentum transfer.

5.3.2 Axial distributions

Analysing the centreline of the spray provides valuable information regarding the spray axis behaviours as the mass and momentum transfer reaches the spray centre. However, essential parameters, such as the spray aperture, require analysing the radial profiles along the axial direction and can not be discerned using only the centreline results. This section will be devoted to studying how the radial profiles of the velocity, liquid volumetric fraction, and mass concentration vary along the axial direction. As already pointed out in Chapter 4, sampling domain snapshots are high storage demanding, so all results shown in this section are obtained after performing both temporal and azimuthal averages of each field. This allows collapsing all radial profile information changes along the axial direction.

The first parameter studied is the spray aperture in terms of the velocity field. There are different approaches to defining a velocity aperture angle. In this case, two methodologies have been considered. Both are based on computing the radial distance where the velocity drops below a certain percentage of the centreline velocity at a certain axial distance. On the one hand, $r_{1/2}$ refers to the radial distance where the axial velocity drops 50%, and on the other hand, $r_{0.01}$ refers to the radial distance where the axial velocity drops 99%. The $r_{1/2}$ is a widely known parameter to characterise the spray, and the $r_{0.01}$ provides an aperture more accurate to characterise the spray in terms of far-field measurements [11, 12]. So by computing the axial distributions of these parameters, a spray contour can be reconstructed to analyse the different behaviours along the axial direction.

Starting with the $r_{1/2}$, Figure 5.9 depicts the axial distribution obtained for all cases. Both the $r_{1/2}$ and the axial distance x are made non-dimensional by dividing by the nozzle diameter, D_n. It is important to highlight that the average axial centreline velocity values used to compute the $r_{1/2}$ correspond to the ones presented in the previous section, as they have been averaged with higher sampling frequency and provide more accurate values. Regarding the $r_{1/2}$ distributions, it can be noticed that up to $x/D_n = 4$, the aperture is slightly higher as the Reynolds number increases, but after $x/D_n = 5$ the trend

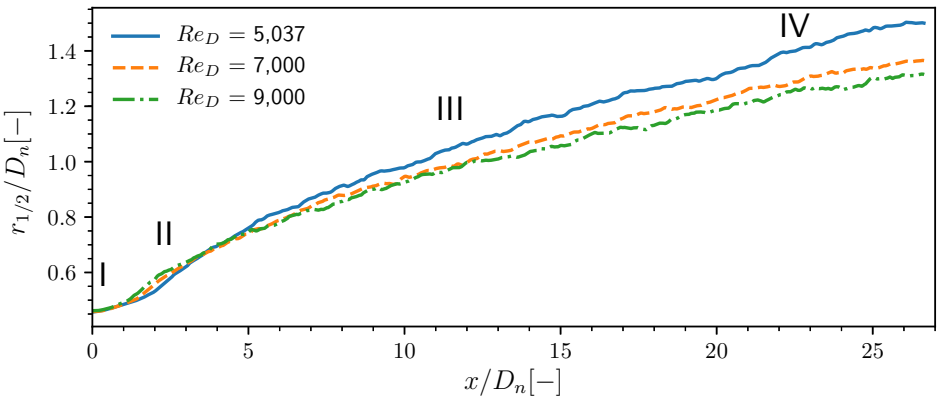

Figure 5.9: Axial distribution of $r_{1/2}$.

inverts, and the lower Reynolds shows the highest aperture. This aperture can be quantified by applying a linear regression of the developed region ($x/D_n > 5$). This leads to a half aperture angle, $\theta_{r_{1/2}}$, of 3.84°, 3.25° and 3° as the Reynolds number increases.

This may contradict the literature's theories that show that increasing the Reynolds number increases the spray angle slightly. However, some particularities of this study can explain this behaviour. As already pointed out in Chapter 3, the non-dimensional mean velocity profile hinted that the velocity profile has not reached the fully developed shape [6]. In order to shed light on this behaviour, Figure 5.10 shows the radial profiles of the mean axial velocity at positions marked on Figure 5.9 corresponding to axial distances of $x/D_n = 0$, 2.25, 10 and 20. The first axial position corresponds to the nozzle outlet (analogous to Figure 3.4); here, it can be seen that because the bulk velocity is maintained, the velocity values on the pipe centre are higher at the Reynolds number decreases in the 80% of the pipe diameter as the profile tends to be more parabolic. The next axial position is located at $x/D_n = 2.25$ where the $r_{1/2}$ increases with the Reynolds number. It can be seen that, as the Reynolds number increases, the velocity profile spreads towards the radial direction. Moving to the location III, it can be noticed that the velocity profiles are nearly the same up to $r/D_n = 0.75$. Further to that point, the momentum transfer to the gas increases as the Reynolds number decreases. Finally, on position IV, the velocity profiles show smoother distributions, increasing the profile width with the Reynolds number, as expected from the results of Figure 5.9.

The same procedure is used to compute the $r_{0.01}$ whose axial distribution are plotted on Figure 5.11. Again made dimensionless by dividing by

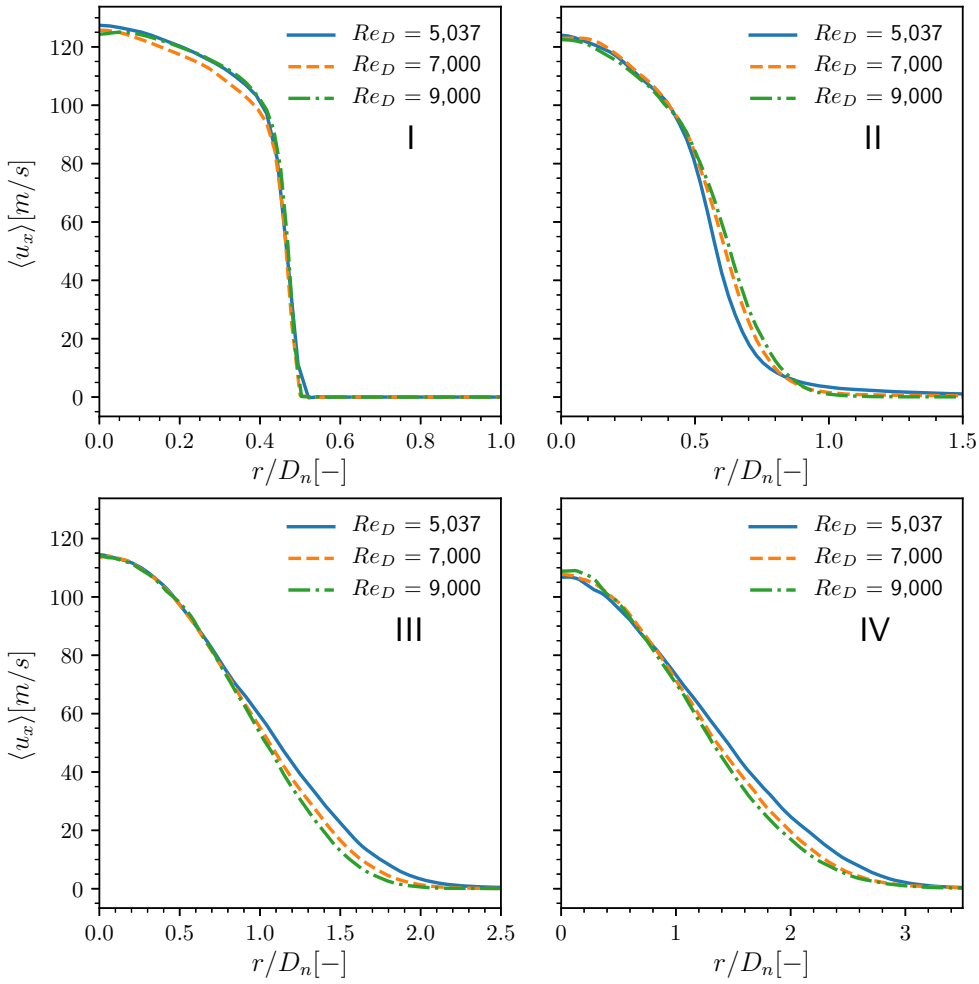

Figure 5.10: Mean axial velocity profiles at different axial positions: I) the nozzle outlet, II) at $x/D_n = 2.25$, III) at $x/D_n = 12.25$, and IV) at $x/D_n = 22.25$.

the nozzle diameter. A particular behaviour appears near the nozzle, up to $x/D_n = 5$, where the values increase up to a maximum to drop immediately after. Following that region, the distributions exhibit increasing trends so that the spray aperture angle can be computed with a linear regression using the same axial range as for the previous case. From those linear regressions, the obtained half spray angle aperture, $\theta_{r_{0.01}}$, are 10.60°, 10.60° and 10.80° as the Reynolds number increases. In this case, although the $r_{0.01}$ values were slightly increasing with the Reynolds number, it can be seen that the spray angle remains almost constant.

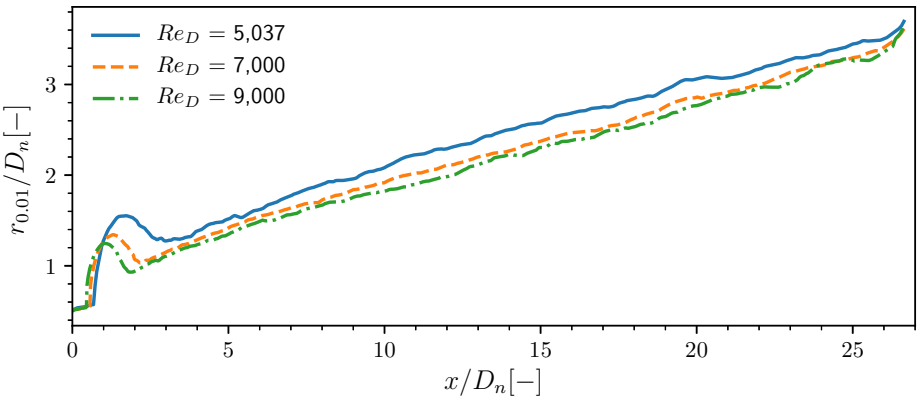

Figure 5.11: Axial distribution of $r_{0.01}$.

With respect to the near nozzle behaviour displayed on the $r_{0.01}$, some aspects are worth being discussed. First of all, this parameter shows a deeply dependence on how the momentum is mixed near the interface as it determines the radial distance where the air is being accelerated. As already introduced in Chapter 3, as the Reynolds number increases, the amount of vortex generated increases and spreads towards the pipe wall. As seen when studying the core topology, as the Reynolds number increases, so do the perturbations on the liquid surface. Indeed, the axial distance where the detected velocity contour suddenly increases reduces with the Reynolds number and the size of the region where this behaviour occurs shrinks.

Finally, a similar analysis is performed on the liquid volume fraction and mass concentration to extract the liquid aperture angle. In this case, only one radial parameter is defined $r_{0.01,C}$, for the liquid volume fraction and $r_{0.01,m_c}$ for the mass concentration. Figures 5.12 and 5.13 show the axial distribution of the liquid volumetric fraction and mass concentration, respectively. It can be seen that both parameters depict similar results, presenting earlier apertures

as the Reynolds number increases but higher apertures at lower Reynolds numbers. Regarding the half spray aperture angles, same procedure than for the velocity angle is followed, obtaining for $\theta_{r_{0.01,C}}$ values of 14.69°, 12.03° and 9.93° and for $\theta_{r_{0.01,m_c}}$ 15.56°, 15.08° and 13.03° in both cases as the Reynolds number increases.

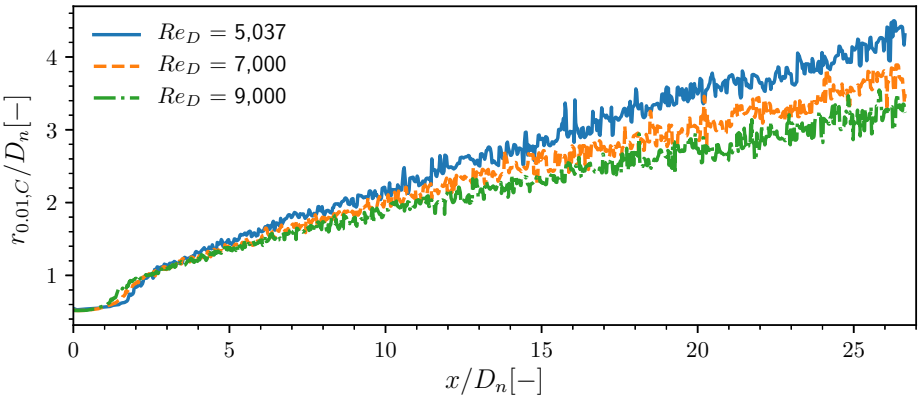

Figure 5.12: Axial distribution of $r_{0.01,C}$.

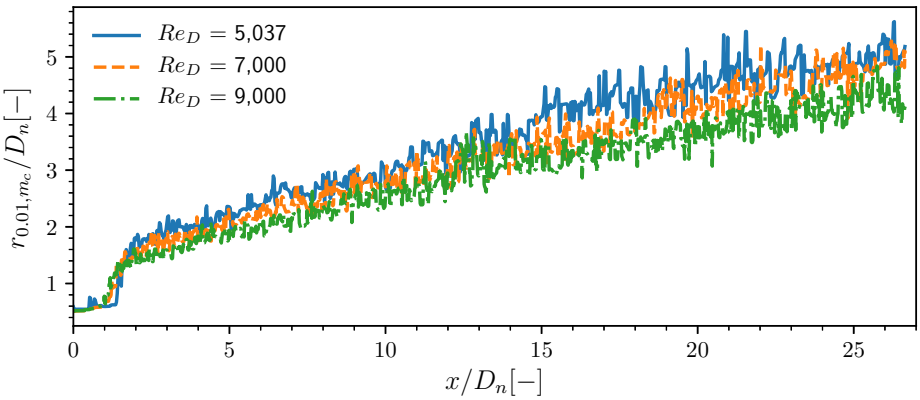

Figure 5.13: Axial distribution of $r_{0.01,m_c}$.

All the particular trends can be explained by one of the main mechanisms presented in Chapter 1, the velocity profile relaxation. As the fluid reaches the nozzle exit, the wall-bounded velocity profile faces no radial restriction, starting the momentum transfer to the surrounding medium. The average velocity profiles injected are still not fully developed, so they present different shapes and thus, can not be expected the same relaxation along the axis direction. Those relaxation differences affect the way the mass and momentum are

mixed. This becomes apparent putting together the centreline liquid volume fraction and mass concentration, the spray aperture and the axial velocity profiles. One of the conclusions extracted from the turbulent analysis performed in Chapter 3 was that the turbulence and the number of vortex cores not only increase with the Reynolds number but its location shifts towards the pipe wall. When the liquid goes through the nozzle exit, the momentum transfer to the surrounding gas starts from the radial position near the liquid surface. So, being that the vortex structures are located closer to the surface as the Reynolds number increases, it is expected that the momentum transfer will take place earlier on the axial distance. Focusing on the $r_{1/2}$ axial distribution can be observed that the spray aperture slightly increases with the Reynolds number on axial positions up to 3.25 x/D_n, which corresponds to where the lower Reynolds condition reaches the linear trend of $r_{0.01}$. Beyond this point, the momentum transfer reaches the central part of the spray. In this region, the lowest Reynolds conditions presents higher injection velocities, having more momentum and enhancing the radial transfer, thus, varying the trends of the $r_{1/2}$ and $r_{0.01}$. This also affects the trends of $r_{0.01,C}$ and $r_{0.01,m_c}$ since the liquid aperture starts earlier as the Reynolds number increases, but also inverts at $x/D_n > 5$. Finally, this behaviour can be related to the liquid volume fraction distribution on the centreline, where it can be seen that it drops to 0.99 at around $x/D_n \approx 3.25 - 4.25$, suggesting that the mass transfer has reached the spray centreline.

5.3.3 Turbulent statistics on $\mathbf{x/D_n \approx 25}$

Once the main parameters have been evaluated both in the centreline and the axial domain, the analysis is centred on the flow statistics on a plane located at $x/D_n = 25$. The main reason for this study is having a well time-sampled dataset in a location where the spray starts exhibiting the self-similar behaviour. It is said that the spray or jet reaches the self-similar region somewhere around $25 \leq x/D_n \leq 30$, but due to the domain limitations of DNS simulations, the plane has been located sufficiently far from the nozzle exit and from the outlet boundary condition to ensure the accuracy of the results.

To start this study, the main average radial profiles are gathered in Figure 5.14. Figure 5.14a depicts the axial velocity profiles for all considered cases. As the previous section shows, the centreline velocity increases with the Reynolds number, but the profile spreads to greater radial positions as the Reynolds decreases. In Figure 5.14b the radial velocity profiles are plotted, there it can be seen in two clear regions. In the first region located from the centreline to around $r/D_n \approx 1.5$, the radial velocities are positive, meaning that the liquid

inside the spray is being transferred to the gas medium. At higher radial positions, the radial velocities are negative and represent the air entrainment of the spray. Moving to Figure 5.14c, the radial profile of the liquid volume fraction, C, is shown. Again, results show the same trends on the centreline. Regarding the distribution, the C values rapidly drop when moving from the spray axis up to radial distances of $r/D_n \approx 1$. Finally, transforming VOF results into mass concentration changes the distribution notably, as can be seen in Figure 5.14d, where the values seem to decrease slower than the velocity results.

It has been widely proved [5, 13] that a fully developed turbulent jet displays a Gaussian behaviour on the radial mean axial velocity profile and the mass concentration. The Gaussian behaviour can be written as the correlation expressed on Equation 5.2, provided by Desantes et al. [11, 12, 14].

$$g(x,r) = g_c(x) \cdot exp\left(-\alpha\left(\frac{r}{r_{ref}}\right)^2\right) \tag{5.2}$$

Where g is a generic field that can be both the axial velocity profile or the mass concentration, the subscript c refers to the centreline value of the field $g(x,r)$, α is the shape coefficient for the Gaussian radial profile and r_{ref} is the radial distance take into account to set the shape coefficient.

Figure 5.15 shows the dimensionless averaged radial profile of the axial velocity (made dimensionless with the corresponding centreline velocity), along with the Gaussian fit for two different configurations: on the left using $r_{ref} = r_{1/2}$ and on the right using $r_{ref} = r_{0.01}$. To fit the Gaussian profile when using $r_{1/2}$ the α coefficient is set to $-ln(0.5)$, while to fit using $r_{0.01}$ is set to $-ln(0.01)$. All cases seem to fit with the Gaussian distributions, focusing on the left plot, showing minor discrepancies on radial positions greater than 1.5 at lower Reynolds conditions. However, when fitting with $r_{0.01}$, those discrepancies are far more important. While the highest Reynolds number condition fits perfectly on the whole radial range, the lower Reynolds conditions present higher values for radial positions higher than 0.2. These results show that the distance where the spray reaches the self-similar behaviour decreases as the Reynolds number increases.

As far as the radial velocity profile is concerned, Figure 5.16 shoes the radial velocity component profile along the dimensionless radial distance (made non-dimensional by dividing by $r_{1/2}$. When analysing against this parameter, all cases collapse into the same behaviour, turning all the cases from positive to negative radial velocities at $r/r_{1/2} = 1$ and presenting the maximums and

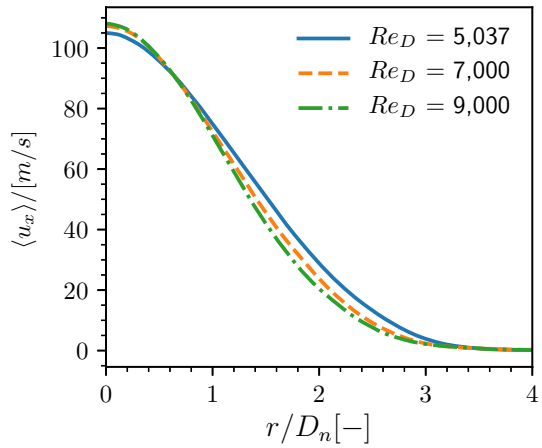

(a) Average radial profile of axial velocity

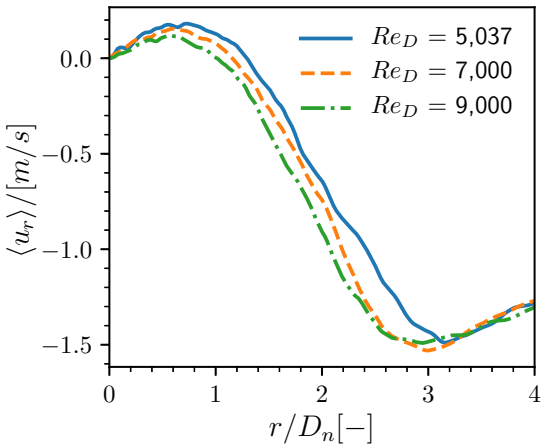

(b) Average radial profile of radial velocity

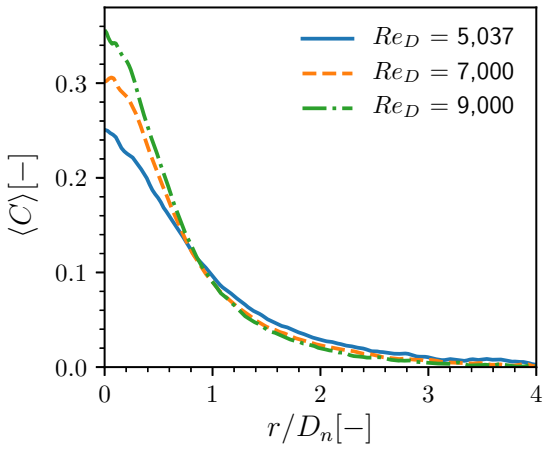

(c) Average radial profile of liquid volume fraction

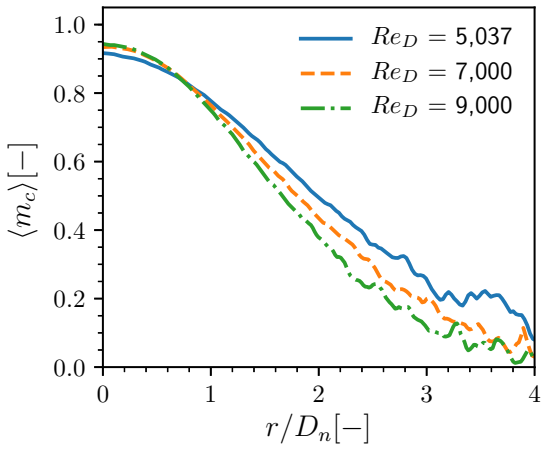

(d) Average radial profile of mass concentration

Figure 5.14: Average radial profiles of main flow fields on a plane located at $x/D_n = 25$.

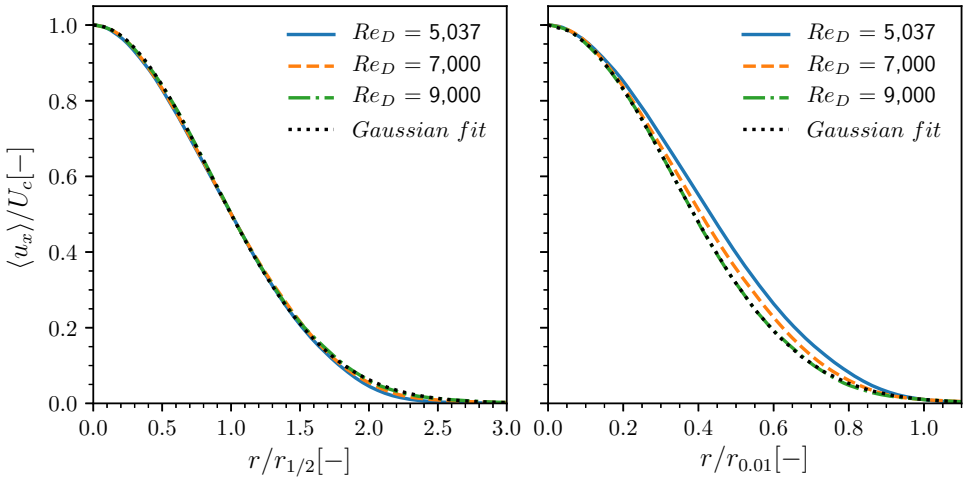

Figure 5.15: Self-similar radial profile of the dimensionless mean axial velocity at x/D_n = 25 made non dimensional with: left, $r_{1/2}$ and right, $r_{0.01}$.

minimums nearly at the same radial distances. This behaviour is coherent with the LDA data presented by Hussein et al. [13], where both the maximum and minimum are located at those radial distances. Regarding the values themselves, lower Reynolds conditions show higher values in the positive region and lower in the negative region, meaning that the liquid is moving away faster but the air entrainment is poorer in comparison with higher Reynolds number. It is interesting also to point out that the values obtained for all cases collapse between the maximum and the minimum of the curves. However, when comparing the values with the LDA results, the maximum values are far below, while the negative peaks are more similar, which means that the spray is attracting the surrounding air, but the liquid still has mainly axial motion. Nevertheless, it is essential to mention that the experimental results are performed on a gaseous jet and taken at a higher axial position, where the spray is entirely in the self-similar region, so it is possible that at farther positions, the radial profile shown in Figure 5.16 may present higher positive radial velocities. Here, is worth mentioning that a clear significance is noticed around the $r_{1/2}$ distance, as is able to be used as a reference to obtain the Gaussian profile of the axial velocity, or the fact that the radial velocities are nearly 0, which means that both the liquid and the surrounding gas are attracted to this region. So, with this evidences, the region around $r_{1/2}$ will be referred herein as the mixing region.

Regarding the liquid field, the first parameter studied is the liquid volume fraction. Like with the radial velocity component, the C field does not show

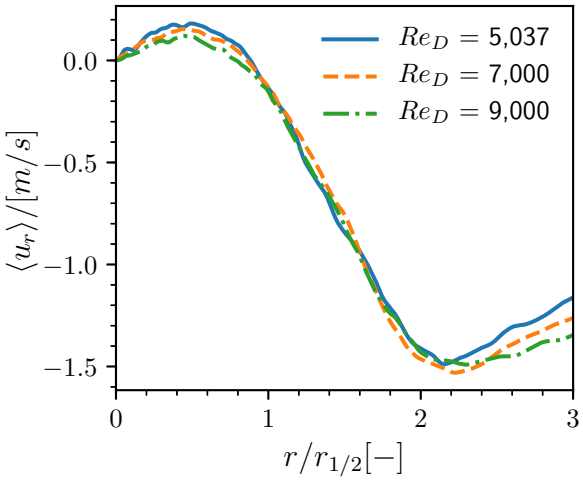

Figure 5.16: Radial profile of the mean radial velocity at $x/D_n = 25$.

a Gaussian behaviour as it drops rapidly from the centreline values. However, it is interesting to plot the radial distributions against $r_{1/2}$ to check the trends with the axial velocity profile. Figure 5.17 depicts that distribution, showing similar behaviours than those in Figure 5.14c, but an interesting feature is that in this case, all distributions collapse at radial distances higher than $r/r_{1/2} = 1$.

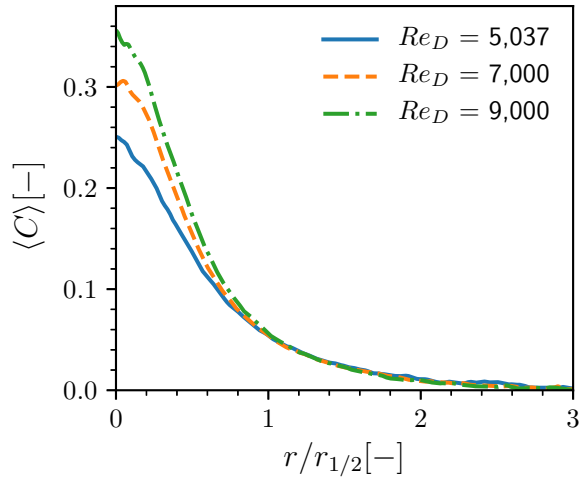

Figure 5.17: Radial profile of the mean radial velocity at $x/D_n = 25$.

Moving to the mass concentration, it is expected to follow a Gaussian profile. So, in the same manner that is done to the axial velocity profile,

Figure 5.18 depicts the radial profile of the mass concentration using the same reference radius. On the left, the $r_{1/2}$ and on the right $r_{0.01}$. Regarding the left plot, all cases show good agreement with the Gaussian fit up to radial distances of $r/r_{1/2} = 1.5$. On further radial position, the highest Reynolds number continues to fit the Gaussian distribution, but the lower cases start diverging, especially the lowest Reynolds number case. Indeed, the smoothness of the distributions at lower Reynolds numbers decreases. The right plot shows worse fitting for all cases, presenting lower values in all radial positions. Nevertheless, the further the radial position is, the noisier the profile is, so the shape coefficient fit is harder to adjust correctly. This hints that the liquid field could be not perfectly stable at the furthest radial locations during the sampling period.

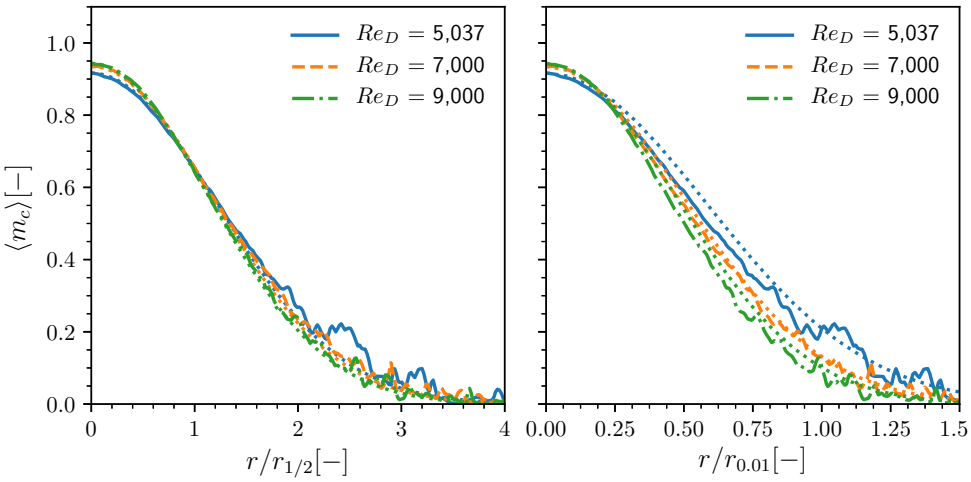

Figure 5.18: Self-similar radial profile of the mean mass concentration at $x/D_n = 25$ made non dimensional with: left, $r_{1/2}$ and right, $r_{0.01}$.

Finally, the plane study is focused on studying the turbulent behaviour of the spray at this location by analysing the radial profiles of both the dissipation rate and the Kolmogorov scale.

The dissipation rate has been computed as explained in Chapter 4. Figure 5.19 depicts the radial profile of the dimensionless dissipation rate against the dimensionless radial distance. The dissipation rate has been made non-dimensional by multiplying by $r_{1/2}/U_c^3$. It can be noticed that the centreline values decrease with the Reynolds number, with a higher decrease between the lowest and the medium levels of Reynolds than between the medium and the highest levels. Then the values increase until the maximum is reached

near the $r/r_{1/2} = 1$. The exact location of the maximum shifts towards the $r/r_{1/2} = 1$, and the obtained values of the peak increase with the Reynolds number. Finally, all cases tend to 0 as moving away from the spray axis. The position of the maximum is coherent as it is located near where the maximum interaction between the liquid and the gas is taking place and the momentum is being transferred.

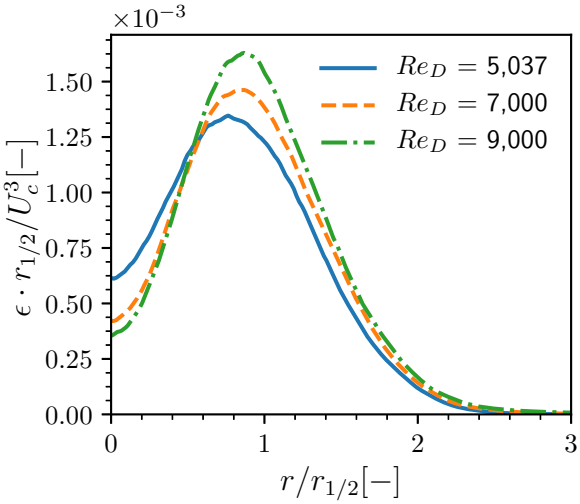

Figure 5.19: Radial profile of the dimensionless dissipation rate at $x/D_n = 25$.

Concluding with the plane analysis, although the Kolmogorov scale η is initially estimated to select the cell size of each simulation, after all computations, it can be calculated. Figure 5.20 shows the η radial distribution against the non-dimensional radial position. It can be seen that all cases present practically the same distribution, decreasing the values when increasing the Reynolds number. The location of the minimum value is nearly the same for all cases, being situated near $r/r_{1/2} = 1$, where the turbulence peak is located as the momentum transfer is taking place. This is in agreement with all the behaviours shown so far. Comparing the minimum value with the cell size leads to a ratio of $\eta_{min}/d_x \approx 0.25$ in all conditions. Even though this value can seem slightly high, further spectral analysis was performed for the low Reynolds condition in [3] showing that the energy loss of the smallest scales was not determinant to affect the spray development.

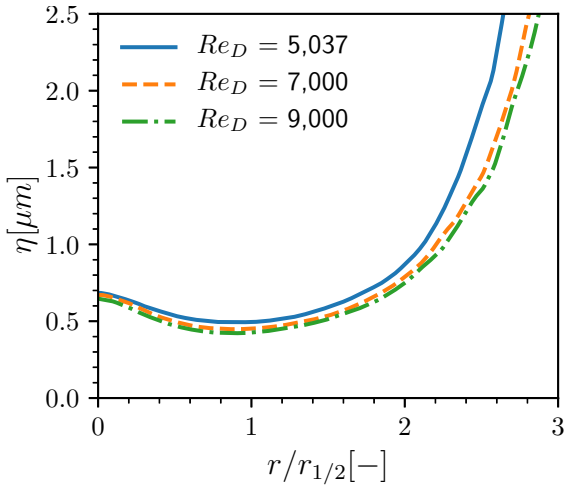

Figure 5.20: Radial profile of the computed Kolmogorov scale at $x/D_n = 25$.

5.4 Droplet cloud study

Once the flow statistics have been analysed, the final study is centred on the influence of the inflow Reynolds number on the droplet generation and the characterisation of the resulting droplet cloud. In this terms, the first approach to this study is counting the total amount of droplets located within the domain in each case. Figure 5.21 depicts the evolution of the number of droplets detected after applying the droplet detection algorithm during the simulation time. It is interesting to highlight that all cases present their maximum peak simultaneously. This maximum is related to the time when the spray tip reaches the end of the domain. The reason behind the existence of this maximum is that the spray tip generates a high number of droplets when advancing through the domain, and when it goes through the outflow boundary, this droplet production disappears. From this point on, the droplet production is mostly provoked by the spray core disintegration and the breakup of ligaments. Focusing on the number of droplets generated, the total number of detected droplets increases as the Reynolds number increases. Finally, Table 5.5 presents the averaged values obtained by averaging the number of droplets when T $>$ 60 μs. There is an increase of around 52% from the low Reynolds condition to the medium condition and a 30% from the medium condition to the high condition.

Those results are in agreement with the snapshots shown during the morphological study, where the droplet cloud seems denser as the Reynolds number increases. However, in order to shed light on the droplet cloud character-

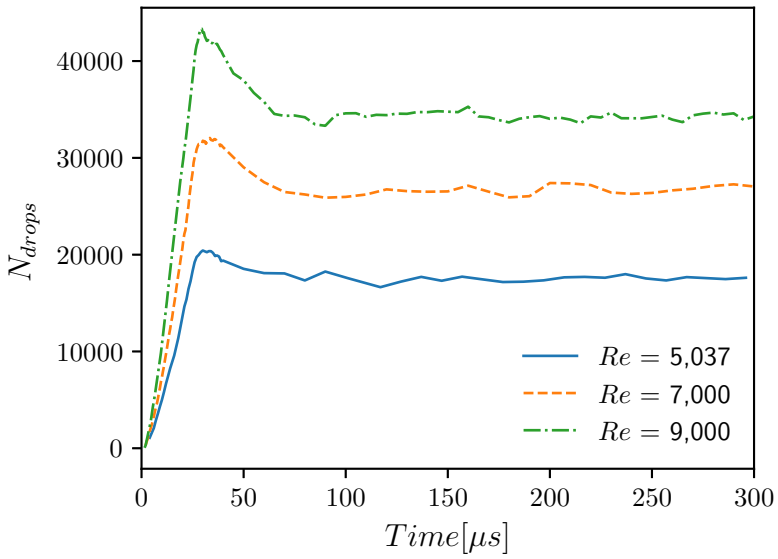

Figure 5.21: Evolution of the number of droplets detected during the whole simulation time.

Table 5.5: Average of droplets detected during the steady state ($T > 60$ μs) for all Reynolds conditions.

Reynolds number	5,037	7,000	9,000
Average droplets detected	17,530	26,610	34,300

istics, a further study is performed in the following subsections, focusing on the size and position distribution of the droplets.

5.4.1 Size distribution

In order to provide more global results, the droplets are characterized by their volumetric diameter. The number of droplets of each size is counted for each timestep and averaged during the statistically steady state. Figure 5.22 shows the average droplet size distribution for all the cases. It can be seen that the overall distribution is similar for all conditions, having their peaks located at small values and decreasing as the diameter increases. Indeed, the lowest Reynolds condition presents the maximum number of droplets located at higher droplet sizes than the higher cases (from 4.5 to 3.2 µm). Also, the amount of small droplets increases considerably with the Reynolds number, whereas this trend inverts when moving towards bigger diameter values.

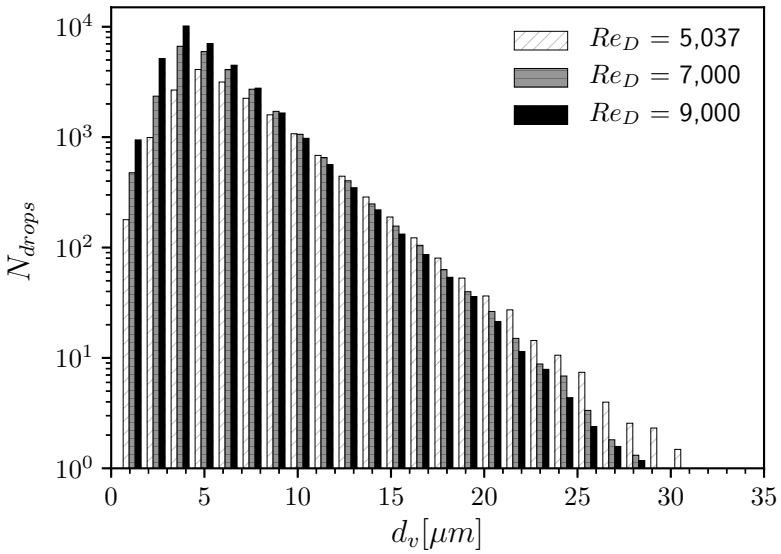

Figure 5.22: Average number of droplets detected for all Reynolds conditions, sorted by their volumetric diameter.

Same trends are observed when computing the PDF from the size distribution, as can be noticed in Figure 5.23. In this case, the diameters are made non-dimensional with the nozzle diameter to provide more global results, defined as d_v/D_n. Here, thanks to the better resolution it can be noticed that the peak location shifts towards smaller diameters also between the medium level and highest level of Reynolds number, being the maximums located at 0.046, 0.38 and 0.33 as increasing the Reynolds number. Additionally, the number of bigger liquid structures decrease as the Reynolds number increases. Also, the peak value increases with the Reynolds number. So Figures 5.22 and 5.23 show that increasing the turbulence in the nozzle exit leads to a higher droplet generation with more population of small droplets. Furthermore, the PDF shows that the relative proportion among small and big droplets also increases with the Reynolds number. These results imply that, when increasing the turbulence, the energy driving the breakup process allows for a finer droplet cloud by splitting ligaments and droplets.

To ensure that the breakup process is stabilised, the production ratio is computed for the different droplet sizes, apart from having a constant total number of droplets. Figure 5.24 represents the average variation of the number of droplets detected for the different sizes. This parameter is expressed as a percentage of the average droplets detected from each size. The results show

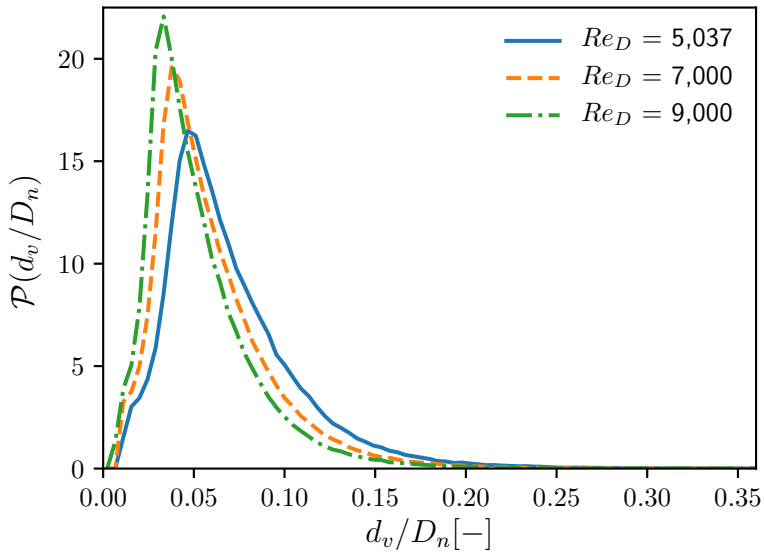

Figure 5.23: Average Probability Density Function of the non-dimensional diameter from the detected droplets for all Reynolds conditions.

that, for sizes up to 0.2 d_v/D_n, the production ratio is under 2.5%, which is almost negligible. Nevertheless, the production ratio increases with a chaotic pattern as the diameter increases. This is caused by the lower number of droplets detected at those sizes, so ratio variation becomes more sensible. However, as previously shown in Figures 5.22 and 5.23, those structures are negligible to the droplet size distribution.

When addressing the multiphase flow resolution, the liquid structures whose diameter is lower than twice the cell size can not be accurately resolved, and the results are unreliable. In order to diminish its influence, a filter is applied to not take into account those droplets. Figure 5.25 represents the average number of droplets detected for all Reynolds conditions as in Figure 5.22 with the filter applied.

The results presented in this subsection expose a clear trend on the influence of the Reynolds number condition in the droplet generation behaviour once the steady-state is reached. On the one hand, increasing the inflow turbulence leads to a higher droplet generation, especially in the smaller diameter population. Additionally, the proportion between bigger structures and smaller droplets also decreases. This means that, when increasing the turbulence of the process, the increase of the energy of the flow that drives the ligament breakup allows producing finer droplets generation.

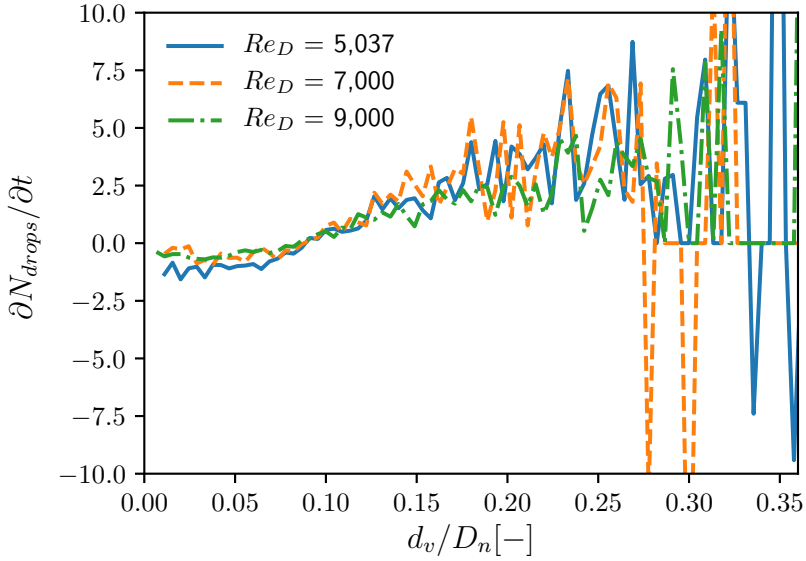

Figure 5.24: Droplet production for the diameters detected within the domain during the steady state. Results expressed as a percentage of the average droplets detected on each size interval.

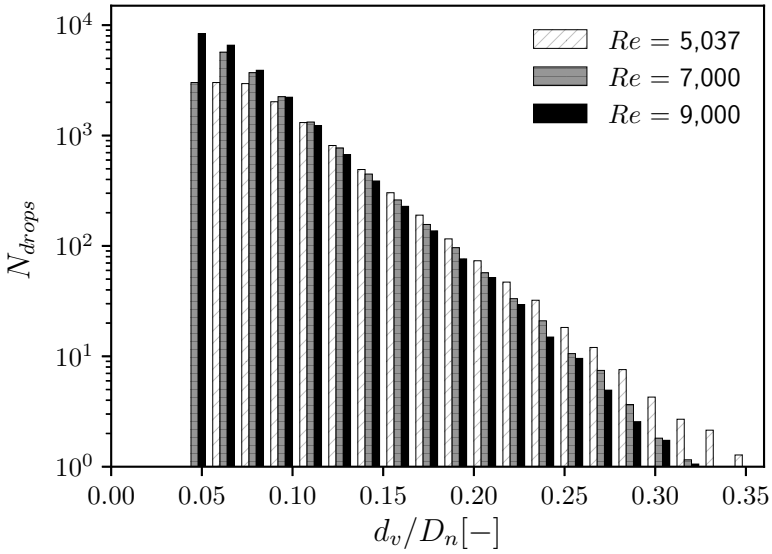

Figure 5.25: Droplet size distribution after filtering the non-resolved droplets.

5.4.2 Radial distribution

Once the size distribution has been studied, the droplets are characterised by their radial position in order to analyse how they are located concerning the spray axis and relate their position to the spray aperture. Figure 5.26 shows the PDF of the non-dimensional radial position (made non-dimensional by dividing with the nozzle diameter) of the droplet cloud for all cases tested. As expected from the aperture results shown earlier in the document, the maximum location moves to the spray axis as the Reynolds number increases, so the spray aperture is slightly lower. The peak value increases with the Reynolds number, and the distribution width decreases, meaning that the droplets are closer, so the density of the droplet cloud increases.

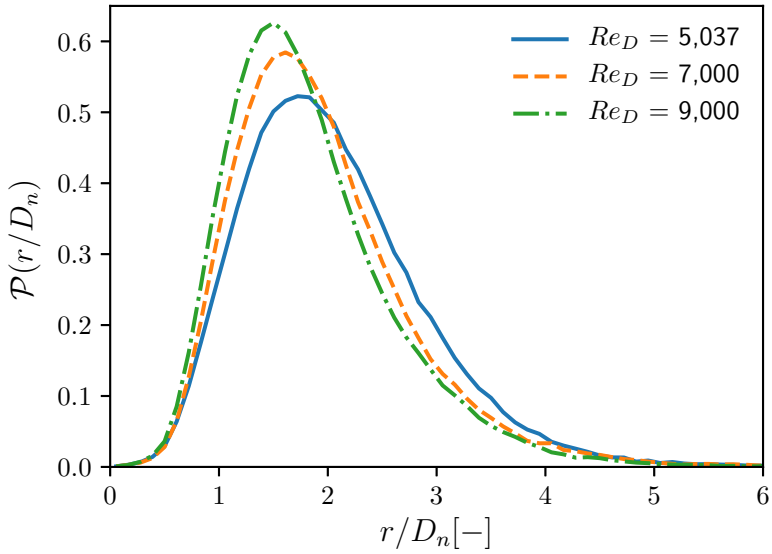

Figure 5.26: Probability Density Function of droplet radial position for all Reynolds conditions.

As previous analyses have demonstrated, studying the radial distribution, taking into account the $r_{1/2}$ provides interesting conclusions. Thus, the radial distance of each droplet has been made non-dimensional by dividing their value by the one corresponding to the value of $r_{1/2}$ at the same axial location extracted from Figure 5.9. Figure 5.27 depicts the PDF of the droplet radial position with respect to the $r_{1/2}$. In contrast with the results shown in Figure 5.26, the radial distributions exhibit a more similar pattern, having nearly the same width and being only slightly different in the peak location of the highest Reynolds number case, which is shifted from $r/r_{1/2} = 1.5$ to $r/r_{1/2} = 1.46$.

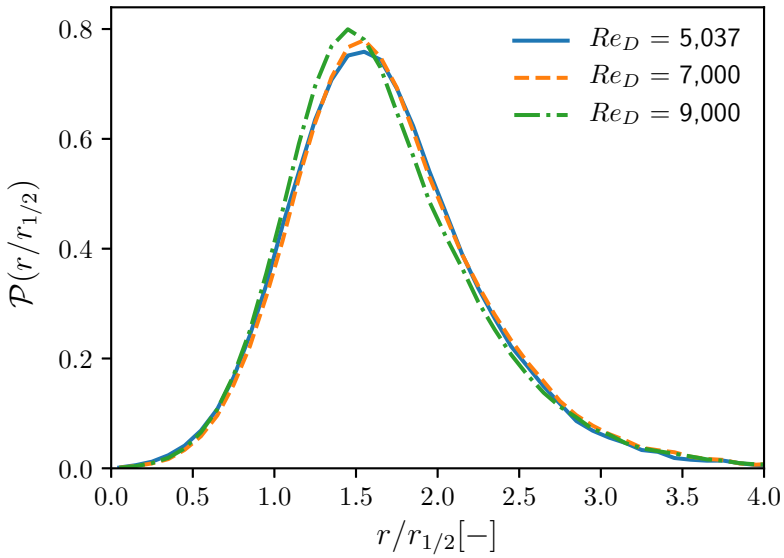

Figure 5.27: Probability Density Function of droplet non-dimensional radial position for all Reynolds conditions.

A combination of droplet size and radial position data is gathered in Figure 5.28, where the radial PDF is computed separately for different droplet sizes. From black to grey as the droplet diameter increases, matching with the droplet sizes shown on the bars from Figure 5.22. Regarding the smaller droplets, it can be seen that the distributions are smoother than the ones corresponding to bigger sizes, and their right tail extends to values up to $r/r_{1/2} = 4$. As the droplet size increases, the distributions are rougher as the droplet population decreases, and the right tail tends to reach zero values earlier. This behaviour is expected as the bigger structures are usually ligaments that appear as a first breakup liquid structure from the core and are subsequently divided into droplets when the shear stresses from the turbulence located around the mixing layer act on the ligament surface.

5.4.3 Velocity distribution

Regarding the droplet movement, Figure 5.29 shows the PDF of the droplet axial velocity made non-dimensional with the injection bulk velocity. Focusing on velocities higher than 10% of the injection bulk velocity, the probability of finding a droplet slightly increases with the Reynolds number. Although the injection bulk velocity is the same for all cases, the turbulence increases so

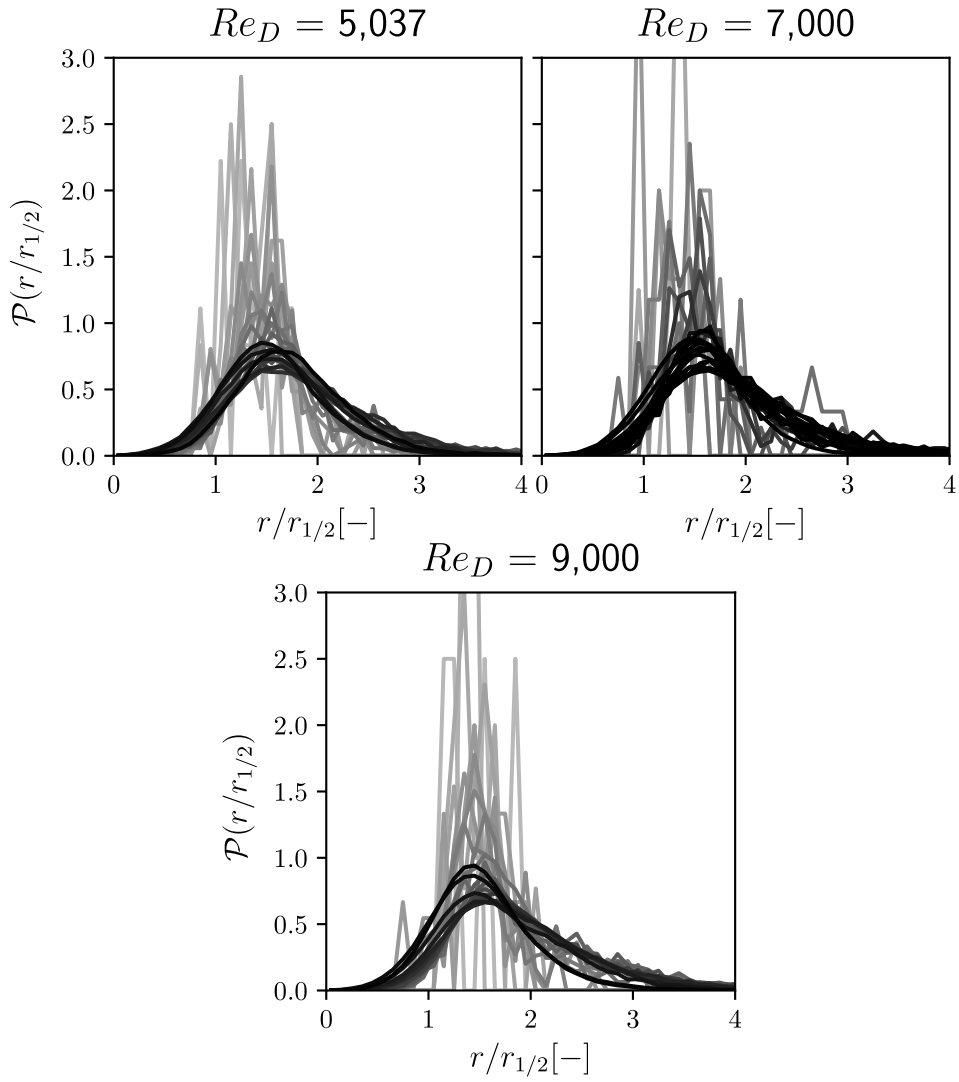

Figure 5.28: Probability Density Function of droplet non-dimensional radial position for different droplet sizes. From black to grey as the droplet size increases. The series correspond to the bars from Figure 5.22.

the momentum transfer to the droplets is higher, providing the droplets with high velocity.

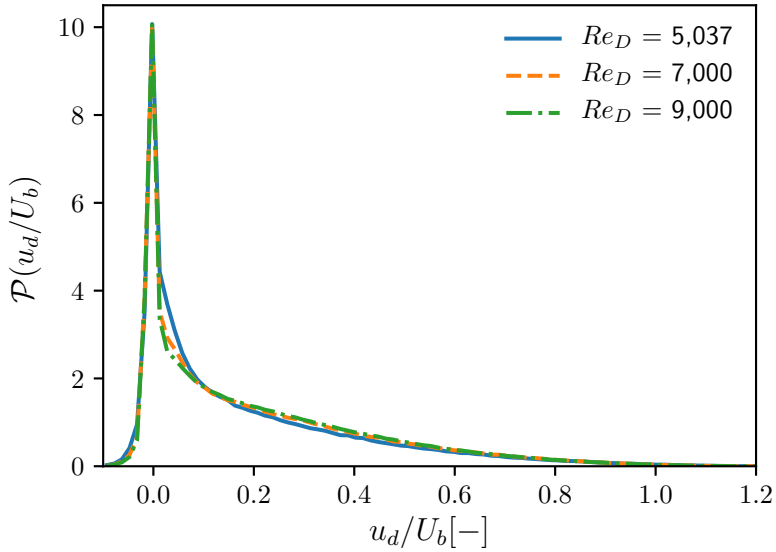

Figure 5.29: Probability Density Function of droplet axial velocity for all Reynolds conditions.

Interestingly, most cases present a peak near zero velocity, and some droplets have negative velocity. Although that could lead to the thought that almost the majority of the droplets are almost motionless, they only account for nearly the 20% of the total droplets detected for each case. The fact that they are located in a narrower band of velocities, leads to a higher PDF values. However, considering the area corresponding to the higher velocities it can be seen that there are a higher amount of droplets with non-zero velocities. The reason for having those low velocities can be hinted from Figures 5.30 and 5.31 that correspond to the radial and axial distribution of the droplets with zero or negative axial velocity, respectively. When the breakup occurs, those droplets are displaced towards the spray periphery as seen in Figure 5.30, where it can be noticed that the peak location is around $r_{0.01} = 1$. There the velocity field is not high enough to advect them again into the dense region remaining quasi-static, being called *'satellite drops'*. Regarding the axial distribution of Figure 5.31, it shows that they are equally distributed along with the domain. However, the majority of drops generated are advected with the flow.

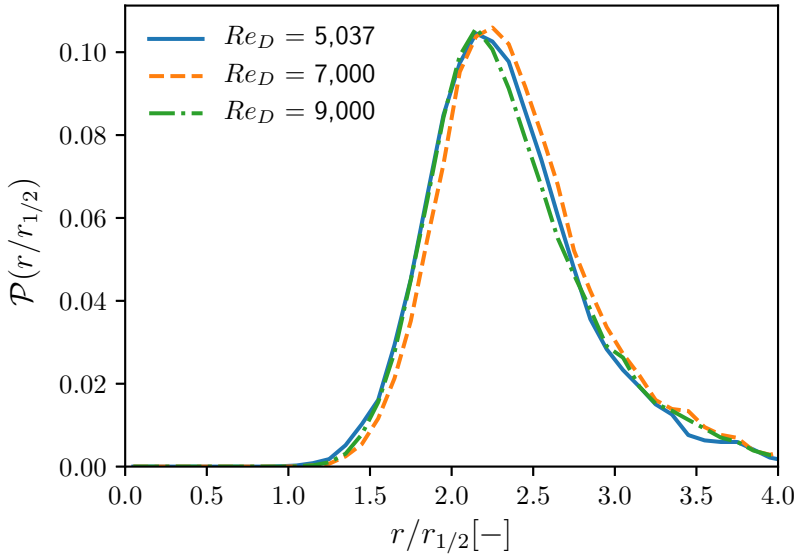

Figure 5.30: Probability Density Function of droplet non-dimensional radial position of the quasi-static droplets.

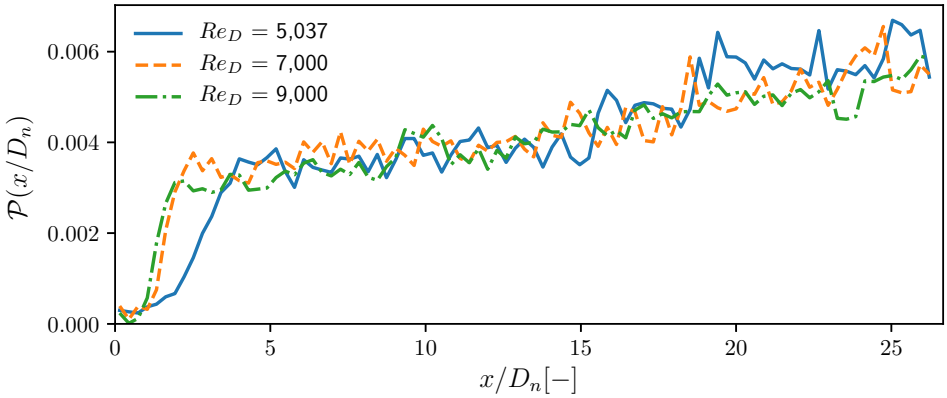

Figure 5.31: Probability Density Function of droplet non-dimensional axial position of the quasi-static droplets.

5.4.4 Axial distribution

Figure 5.32 depicts the probability of having a droplet along with the axial position. As expected, as the axial distance increases, so does the number of droplets generated. Hence, the probability of having a droplet is higher. When comparing the different cases, it can be seen that, as the Reynolds number increases, the minimum axial position where it can be found droplets is reduced. As already pointed out in Section 5.2, the non-perturbed length is reduced with the Reynolds number, which agrees with having droplets earlier in the axial position.

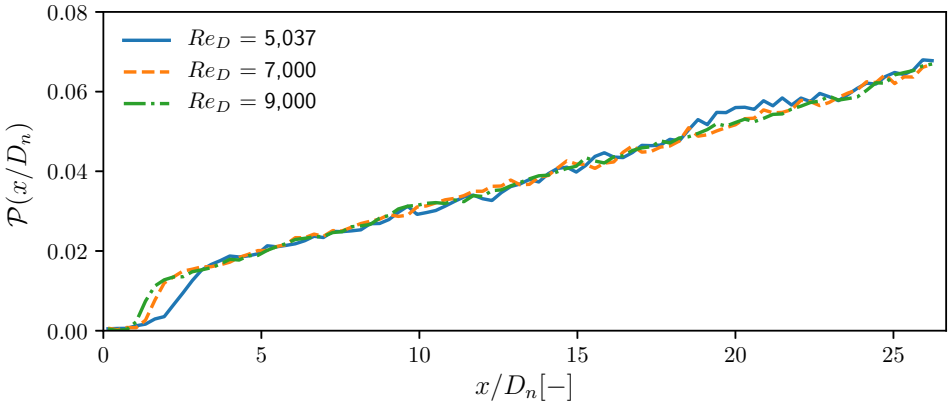

Figure 5.32: Probability Density Function of droplet non-dimensional axial position for all Reynolds conditions.

Just like done before with the radial distribution. Figure 5.33 presents the PDF axial droplet distribution discretised by the droplet diameter. Again, from black to grey as the diameter increases, using the same discretisation. Here, the smallest droplet sizes present an interesting behaviour as they are the first series to increase from zero, but then the distribution remains constant for the other axial positions. Regarding the rest of the diameters, the droplet production increases with the axial distance in a similar trend.

As can be seen in 5.32, the amount of droplets increases as moving from the nozzle exit. However, as seen in the previous section, the spray is still developing along the axial direction. For this reason, apart from having an overall characterization of the entire droplet cloud, it is interesting to check how those distributions change along the axial direction. In these terms, Figure 5.34 represents the droplet size distribution for different axial divisions from the nozzle exit to the end of the domain, from grey to black as the distance to the nozzle increases. All cases present similar trends are found

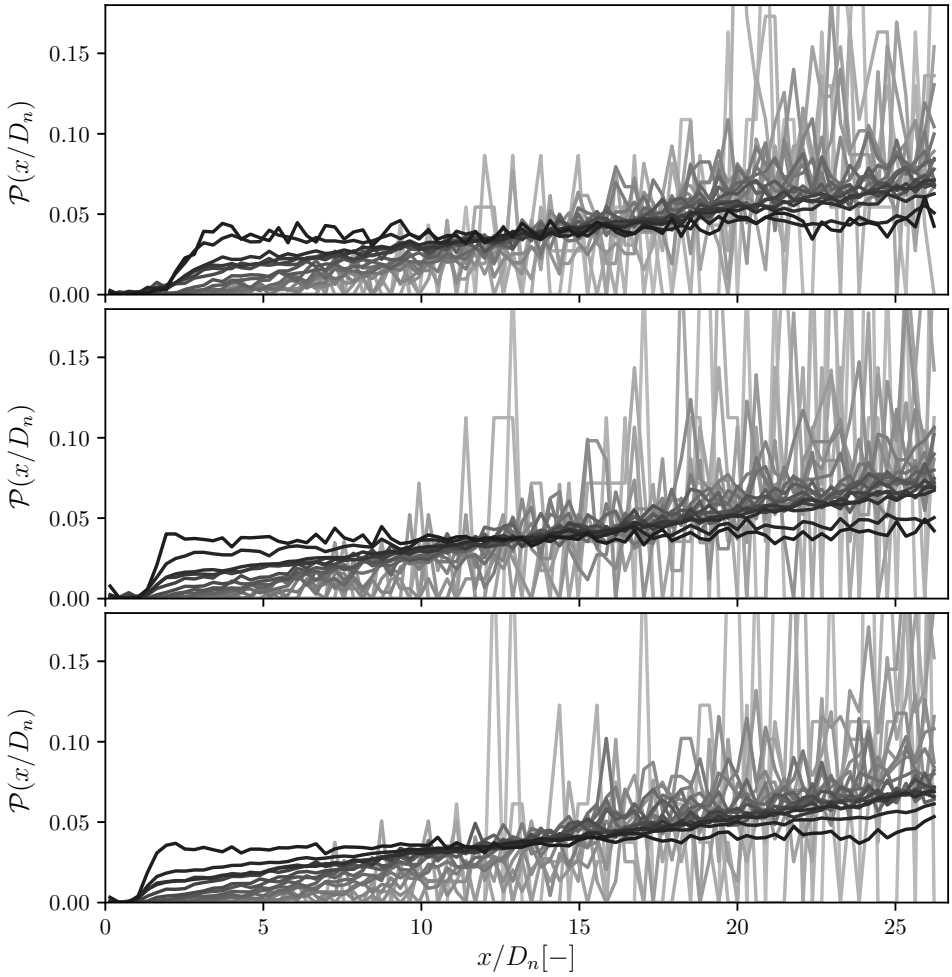

Figure 5.33: Probability Density Function of droplet non-dimensional axial position for different droplet sizes. From black to grey as the droplet size increases. The series correspond to the bars from Figure 5.22.

as the distance from the nozzle increases, where the number of small droplets decreases while the number of bigger liquid structures increases. This is in line with results shown in Figure 5.34, where the amount of smaller droplets remains constant along the axial direction, and the rest of the sizes gradually increase.

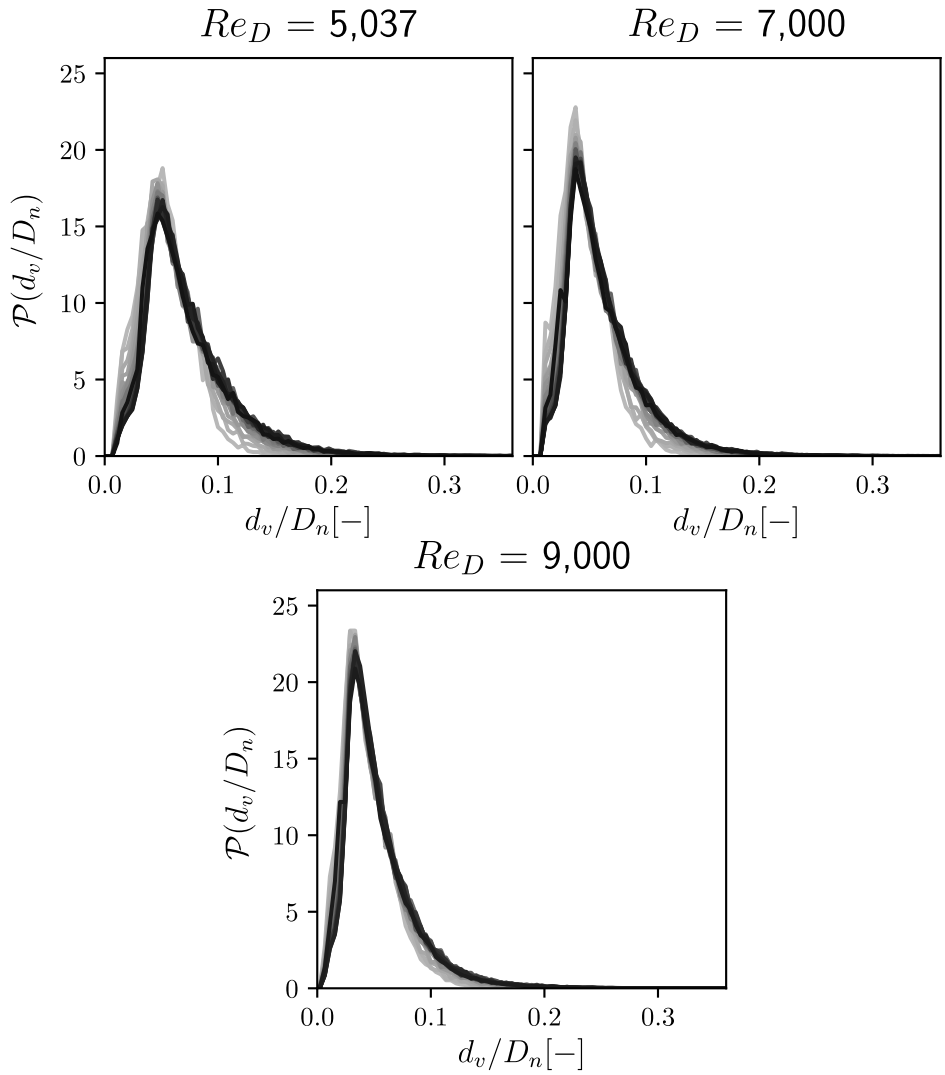

Figure 5.34: Average Probability Density Function of the non-dimensional diameter for different axial positions. From grey to black as increasing the axial distance. The axial distance goes from $x/D_n > 2.5$ to $x/D_n = 25.5$.

Moving to the radial distribution along the axial direction, Figure 5.35

follows the same procedure as for the previous figure, showing the radial distribution for different axial positions. The first detail to notice is that the peak location remains unchanged as the axial position increases, which means that the droplet cloud is spreading away from the spray axis in the same proportion as the $r_{1/2}$, which is also related to the momentum transfer from the liquid to the surrounding gas. Regarding the radial distribution, the peak value decreases with the axial distance, leading to a flattener distribution, increasing the values, especially near the spray axis. This widening of the distribution is caused by the disintegration of the liquid core, which allows droplet production near the spray axis. This does not affect the spray periphery as it remains nearly identical for all axial positions. Overall trends are maintained in terms of Reynolds number influence, but at lower axial positions, the radial distributions are shaper as the Reynolds number increases, and the effect on the spray periphery also increases.

5.5 Conclusions

In this section, the analysis of the influence of the Reynolds number in the atomisation process has been analysed. The inflow boundary conditions have been obtained by mapping LES results computed on a periodical pipe to ensure the correct turbulence field injection in each case. This study has been focused on several aspects of the spray to provide a detailed global view of how the inflow conditions affect its development. First, Section 5.2 highlighted the increase in the droplet cloud density as the Reynolds number increased, showing almost no change in the spray aperture. Both behaviours are consistent with the spray angle study performed on Section 5.3 and the droplet size and radial distributions on Section 5.4. When focusing on the core, the growth of the number of vortexes detected and their shifting towards the liquid surface when increasing the Reynolds number causes an increment of surface perturbations. This effect decreases the external non-perturbed length, triggering the atomisation at higher Reynolds numbers.

Following the morphological study, the flow field has been studied in terms of centreline statistics, axial distributions and an analysis of the turbulence located on a plane far away from the nozzle. Interesting results are obtained when studying the centreline axial distribution for velocity and mass concentration fields. The centreline velocity exhibits two different linear decays in each condition, steeper at a lower Reynolds number. Also, the breakup length is computed and, in contrast with the classical thoughts, increases with the Reynolds number. Furthermore, the spray aperture is estimated by computing both the $r_{1/2}$ and $r_{0.01}$ axial distributions, showing particular behaviours

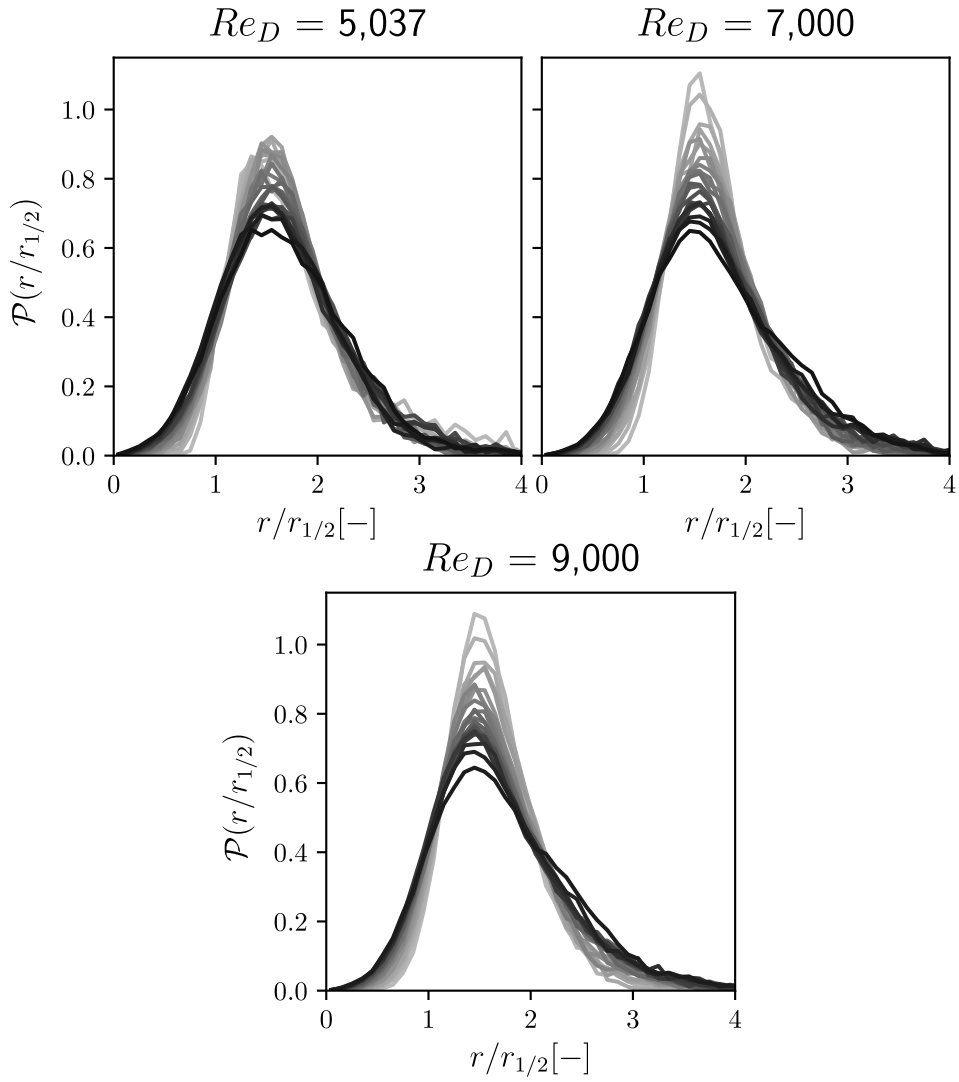

Figure 5.35: Probability Density Function of droplet non-dimensional radial position for different axial positions. From grey to black as increasing the axial distance. The axial distance goes from $x_/D_n > 2.5$ to $x/D_n = 25.5$.

near the nozzle. Although the presented results seem to follow non-intuitive trends, the spotlight is put on the variation of the inflow velocity profile distribution to explain those behaviours. The wall-bounded velocity profile shifts from a parabolic to a squared shape as the Reynolds number increases and the bulk velocity is maintained, leading to higher velocities near the liquid surface and lower velocities at the pipe centre. The velocity profile differences at the inflow condition, the axial evolution of the velocity profile along with the spray, linked to the spray aperture and momentum and mass transfer lead to the belief that, near the nozzle outlet, the turbulence allows to transfer the momentum and mass earlier, disrupting the liquid surface and widening the spray. However, when the momentum transfer moves towards the spray centre, the higher velocities boost it compensating for the initial turbulent mixing and widening the spray aperture.

When focusing on the turbulence located on a plane, it is noticeable that the axial velocity profile follows a Gaussian profile with more accuracy as the Reynolds number increases. As this behaviour is linked to the auto-similar region, it insinuates that as the Reynolds number increases, the axial distance where the spray starts exhibiting this behaviour decreases. The radial velocity profiles show lower values than expected, and the Reynolds number does not have a particular influence when expressed in the non-dimensional radial distance. Regarding the liquid field, the mass transfer in the radial direction seems to decrease as the Reynolds number increases, as expected from the spray contours extracted in earlier sections. However, just like the velocity profile, the mass concentration follows a Gaussian distribution in all cases, although the fit increases again with the Reynolds number. Concluding the plane analysis, both the dissipation rate and the Kolmogorov scale are computed. All cases present similar distributions concerning the dissipation rate, locating their peaks near the mixing region. Furthermore, the maximum value increases with the Reynolds number as high energy has to be dissipated during the mixing process. Then η is calculated to find similar behaviours with the Reynolds number, leading to an $\eta_{min}/d_x \approx 0.25$, which has been proved to leave a negligible percentage of the total energy unresolved in previous works.

Finally, the analysis is focused on the droplet size, location and velocity distribution. The number of droplets detected increases, and the droplet cloud shifts to finer structures when increasing the Reynolds number. All cases present a log-normal distribution that will be further studied in a later chapter. Regarding the droplet location, all conditions show similar radial distribution when compared with the $r_{1/2}$, which means that, even the spray aperture is higher for the lower Reynolds number, the majority of the droplets are located at a radial distance slightly further from the mixing region. The

axial distribution of the droplets also exhibits an early apparition of droplets as the Reynolds number increases, so the atomisation is triggered at lower axial distances. However, after the initial discrepancies, all cases collapse into similar axial distributions, meaning that the droplet generation rate on the axial distance is comparable in all cases. Moving to the droplet velocity, a non-negligible number of droplets present quasi-static behaviour as they are located sufficiently far from the spray axis after the breakup event. For those droplets, the advection is purely radial as the axial velocity is negligible, so, as the radial velocity at those positions is negative, eventually, the droplets will be dragged back to the spray centre.

References

[1] ECN. *Engine Combustion Network*. Online. 2010.

[2] Payri, Raul, Salvador, Francisco Javier, Gimeno, Jaime, and Crialesi-Esposito, Marco. "Comparison of mapped and synthetic inflow boundary conditions in Direct Numerical Simulation of sprays". In: *ILASS - Europe 2019, 29th Conference on Liquid Atomization and Spray Systems*. Paris, France, 2019.

[3] Torregrosa, Antonio J., Payri, Raul, Javier Salvador, F., and Crialesi-Esposito, Marco. "Study of turbulence in atomizing liquid jets". In: *International Journal of Multiphase Flow* 129 (2020), p. 103328. DOI: 10.1016/j.ijmultiphaseflow.2020.103328.

[4] Crialesi-Esposito, Marco, Gonzalez-Montero, L. A., and Salvador, F. J. "Effects of isotropic and anisotropic turbulent structures over spray atomization in the near field". In: *International Journal of Multiphase Flow* 150.November 2021 (2022), p. 103891. DOI: 10.1016/j.ijmultiphaseflow.2021.103891.

[5] Pope, Stephen B. *Turbulent flows*. IOP Publishing, 2001.

[6] Wagner, C., Hüttl, T. J., and Friedrich, R. "Low-Reynolds-number effects derived from direct numerical simulations of turbulent pipe flow". In: *Computers and Fluids* 30.5 (2001), pp. 581–590. DOI: 10.1016/S0045-7930(01)00007-X.

[7] Kastengren, Alan L, Powell, Christopher F, Liu, Z., and Wang, J. "Time resolved, three-dimensional mass distribution of diesel sprays measured with x-ray radiography". In: *SAE Technical Paper 2009-01-0840* 4970 (2009), SAE Paper no. 2009–01–0840.

[8] Kastengren, A. L. et al. "Time-resolved X-ray radiography of sprays from Engine Combustion Network spray a diesel injectors". In: *Atomization and Sprays* 24.3 (2014), pp. 251–272. DOI: 10.1615/AtomizSpr.2013008642.

[9] Trettel, Ben. "Reevaluating the jet breakup regime diagram". In: *Atomization and Sprays* 30.7 (2020), pp. 517–556. DOI: 10.1615/ATOMIZSPR.2020033171.

[10] Trettel, Ben. "Conditional damped random surface velocity model of turbulent jet breakup". In: *Atomization and Sprays* 30.8 (2020), pp. 575–606. DOI: 10.1615/AtomizSpr.2020033172.

[11] Desantes, Jose Maria, Payri, Raul, Garcia-Oliver, Jose Maria, and Salvador, Francisco Javier. "A contribution to the understanding of isothermal diesel spray dynamics". In: *Fuel* 86.7-8 (2007), pp. 1093–1101. DOI: 10.1016/j.fuel.2006.10.011.

[12] Desantes, Jose Maria, Salvador, Francisco Javier, Lopez, Jose Javier, and De la Morena, Joaquin. "Study of mass and momentum transfer in diesel sprays based on X-ray mass distribution measurements and on a theoretical derivation". In: *Experiments in Fluids* 50.2 (2011), pp. 233–246. DOI: 10.1007/s00348-010-0919-8.

[13] Hussein, Hussein J., Capp, Steven P., and George, William K. "Velocity measurements in a high-Reynolds-number, momentum-conserving, axisymmetric, turbulent jet". In: *Journal of Fluid Mechanics* 258 (1994), pp. 31–75.

[14] Desantes, Jose Maria, Payri, Raul, Salvador, Francisco Javier, and Manin, Julien. "Influence on Diesel Injection Characteristics and Behavior Using Biodiesel Fuels". In: *SAE Technical Paper 2009-01-0851* (2009). DOI: 10.4271/2009-01-0851.

Chapter 6

The Influence of Weber Number

6.1 Introduction

As already introduced in Chapter 1, the atomisation process is controlled by different non-dimensional groups that relate to the inertial forces, the surface tension and the density ratio. After studying the influence of the Reynolds number on the spray atomization in the previous chapter, this one puts the spotlight on the Weber number, which relates the inertial forces with the surface tension. So, following a similar procedure as in the last chapter, three different simulations have been performed, ranging the Weber number from 26,600 to 90,000.

Just like in the Reynolds study, a reference simulation, already analysed in [1–3], is taken using the Spray A from the ECN [4] whose properties are gathered on Table 5.1, and corresponds to the lowest Weber number. In order to modify the Weber number without affecting the rest of the parameters, only the surface tension is changed. Table 6.1 present all the physical properties and simulation parameters from all cases. In contrast with the previous study, the inflow turbulence is expected to be the same as the Reynolds number is maintained, so all meshes and domains remain the same.

The procedure followed to analyse the results of these simulations is similar to the ones in Chapter 5. However, the flow field study will be simplified as the primary efforts will be devoted to the droplet cloud study. So, the

Table 6.1: Simulation parameters for the Weber study

Reynolds number	Re [-]	26,600	60,000	90,000
Fuel viscosity	μ_l [kg/m^3]	$1.34 \cdot 10^{-3}$	$1.34 \cdot 10^{-3}$	$1.34 \cdot 10^{-3}$
Fuel density	ρ_g [kg/m^3]	750	750	750
Surface tension	σ [kg/s^2]	0.0253	0.0112	0.0075
x - length	l_x [mm]	2.4	2.4	2.4
y,z - length	l_y, l_z [mm]	1.2	1.2	1.2
Cell size	d_x [µm]	2.34	2.34	2.34
Timestep	d_t [ns]	4	4	4
Number of cells	N_{cells} [-]	$268 \cdot 10^6$	$268 \cdot 10^6$	$268 \cdot 10^6$

morphological study is first presented to check the spray development and the qualitative features of the droplet cloud generated. Then, the flow fields' centreline and axial distribution are investigated to shed light on the velocity decay, liquid breakup, and spray aperture. Similarly to the Reynolds study, the turbulence analysis is performed on a plane located at $x/D_n = 25$, and the efforts are put on the Kolmogorov scale determination and the dissipation rate. Finally, droplet production is studied in-depth, putting emphasis on the droplet location and size distributions, taking into account different parameters.

6.2 Spray morphology study

In the same way as previously done in the Reynolds study, the first analysis of the spray consists of the qualitative observation of the spray morphology. Consequently, Figure 6.1 shows the iso-contour of the VOF for each Weber condition corresponding to the transient phase, in particular at $T = 12.5$ µs. The threshold to extract the contour is set to $C_{th} = 0.05$. Comparing all conditions, the spray aperture and penetration are similar but not exactly equal. The droplet cloud appears to be finer as the Weber number increases. The onset of the atomization takes place at the same axial positions, and all cases present a highly disintegrated spray tip.

Figure 6.2 presents all Weber conditions at $T = 150$ µs, which corresponds to the statistically stationary state. This frame provides useful features of the spray once it is completely developed. So, there are no significant differences

Figure 6.1: Spray morphology during the transient state at $T = 12.5$ μs. Increasing Weber number from top to bottom.

between the studied cases at first sight. The spray aperture and the external non-perturbed length are equal, and only the droplet cloud seems to change. In these terms, the minimum size detected seems to be maintained, but the proportion of smaller droplets increases, leading to a finer droplet cloud. It is worth mentioning that the inflow boundary conditions are the same in all simulations, so the differences between the cases are produced by the decrease of the surface tension as the Weber number increases, which allows an easier breakup of the ligaments.

One of the consequences of using the same inflow conditions is that the injected vortexes are the same. As already stated in the previous chapter, the vortexes are strongly linked to the surface perturbations and, as can be seen in Figures 6.1 and 6.2, all cases seem to have the same perturbations on the

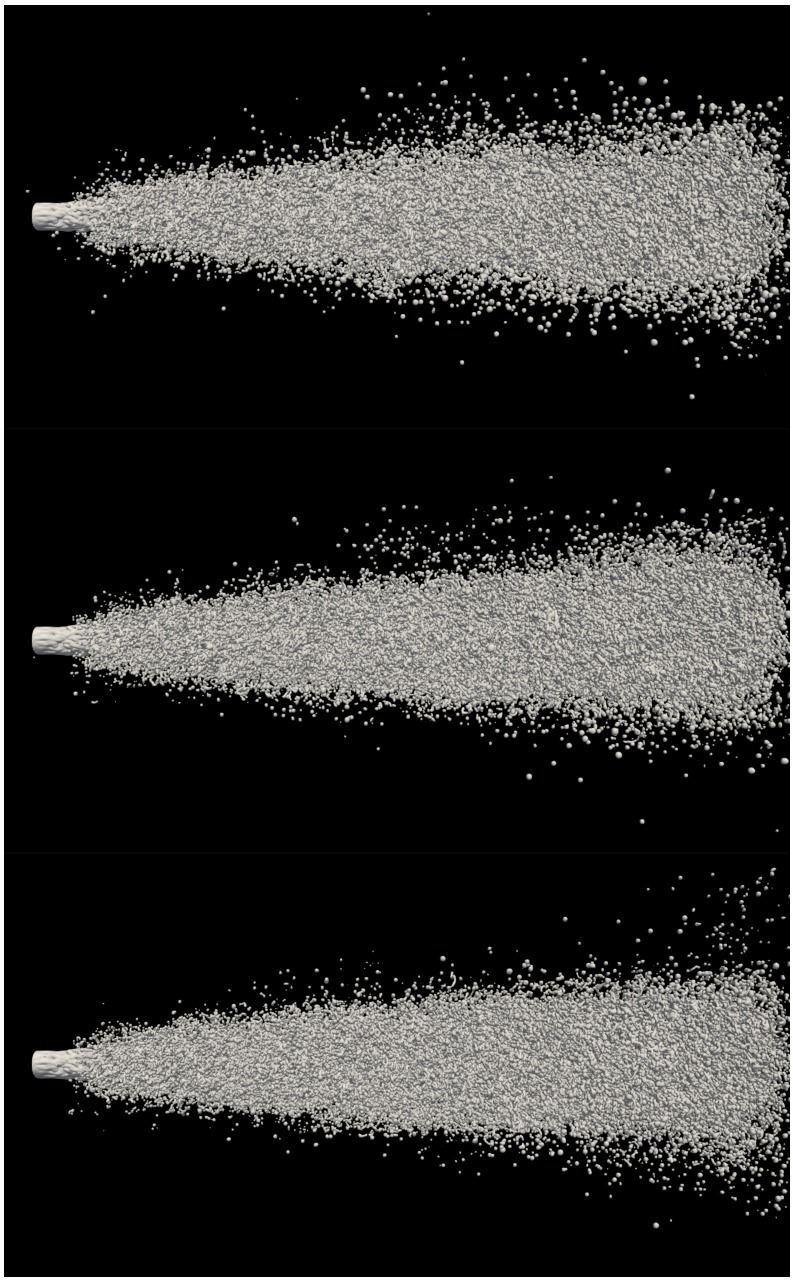

Figure 6.2: Spray morphology during the steady state at $T = 150$ μs. Increasing Weber number from top to bottom.

core surface. Figure 6.3 gathers the contour of the extracted core at $T = 150$ µs for all cases. For this figure the contour is applied with a threshold of $C_{th} = 0.95$. It can be seen that, as hinted previously, the core perturbations are the same in the first microns along the axial direction, so it is reasonable that the start of the atomization takes place at the same axial distance.

Figure 6.3: Spray core extracted from the full spray at $T = 150$ µs. Increasing Weber number from left to right.

With the visualization of the spray development, some conclusions can be extracted. First, the overall morphology of the spray seems to be the same, maintaining the penetration rate and the spray aperture. As the same vortexes are injected, the core perturbations are the same. However, the decrease of the surface tension modifies the development of the breakup event, leading to finer droplet clouds.

6.3 Flow field analysis

This section is devoted to the flow analysis, focusing on the centreline statistics, the spray aperture and the analysis of a plane located at $x/D_n = 25$.

6.3.1 Centreline statistics

The centreline statistics are essential as they can provide helpful information on spray development. The results shown in this section correspond to the temporal average obtained by taking into account the whole statistically stationary state (for T > 60 < µs), sampling the output every timestep.

Starting with the velocity centreline distribution, Figure 6.4 depicts the axial component of the velocity, $u_{x,c}$. As expected, the average centreline velocity of the nozzle outlet coincides in all cases, as the velocity inflow boundary conditions are not modified between the cases. In fact, the centreline axial velocity distribution is nearly the same for all Weber number conditions, exhibiting two clear linear trends along the axial direction, which can be fitted

by linear regressions. These similarities are confirmed in Table 6.2 where are gathered the parameters of the linear regression for each condition. Here, m and n are the regression slope and the intercept point, respectively, R^2 is the coefficient of determination, subscripts 1 and 2 refer to the first and the second linear regions, and d is the non-dimensional axial distance where both regressions intercept. Results show an almost perfect linear fit as the coefficient of determination is above 0.99 in all cases. Although the linear slopes are not exactly equal, the difference is around 4% in the worst case.

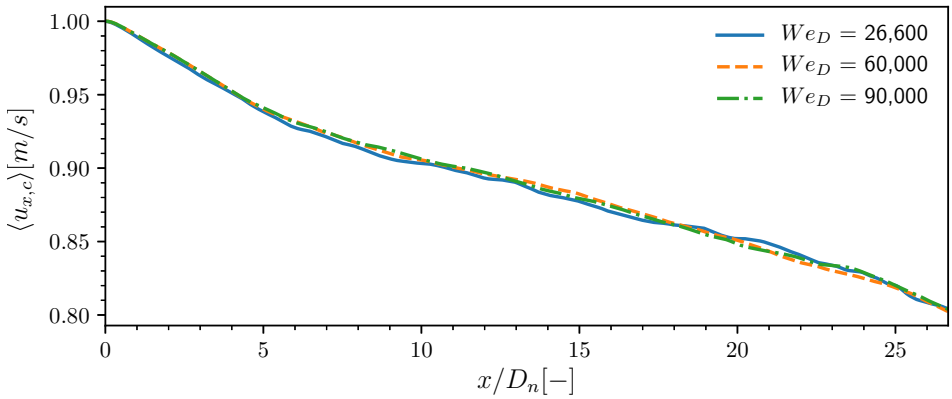

Figure 6.4: Axial distribution of the centreline axial velocity.

Table 6.2: Linear regression parameters of the axial distribution of the centreline velocity for all Weber cases.

$\mathbf{We}_D$	26,600	60,000	90,000
$\mathbf{m}_1$	-1.605	-1.592	-1.574
$\mathbf{n}_1$	127.57	127.96	127.92
$\mathbf{R}_1^2$	0.999	0.999	0.999
$\mathbf{m}_2$	-0.706	-0.751	-0.741
$\mathbf{n}_2$	122.30	123.33	123.19
$\mathbf{R}_2^2$	0.996	0.997	0.998
d	6	5.8	5.8

Moving to the liquid field, the presence of the liquid in the centreline is studied through two parameters, the volume liquid fraction $\langle C \rangle$ depicted in Figure 6.5, and the liquid mass concentration, m_c plotted in Figure 6.6. Like

in the centreline distribution of the axial velocity, there are no significant differences between the cases other than the temporal average for the medium and the highest Weber number are smoother, so the decay trend is collapsed in a single curve.

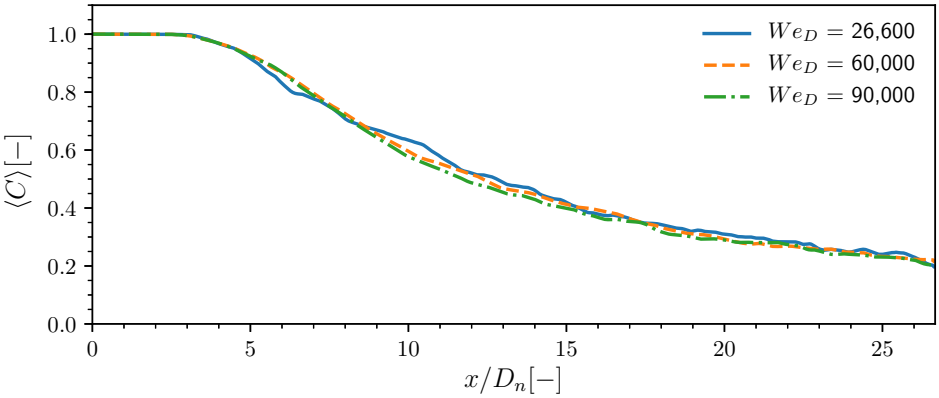

Figure 6.5: Axial distribution of the liquid volume fraction, C.

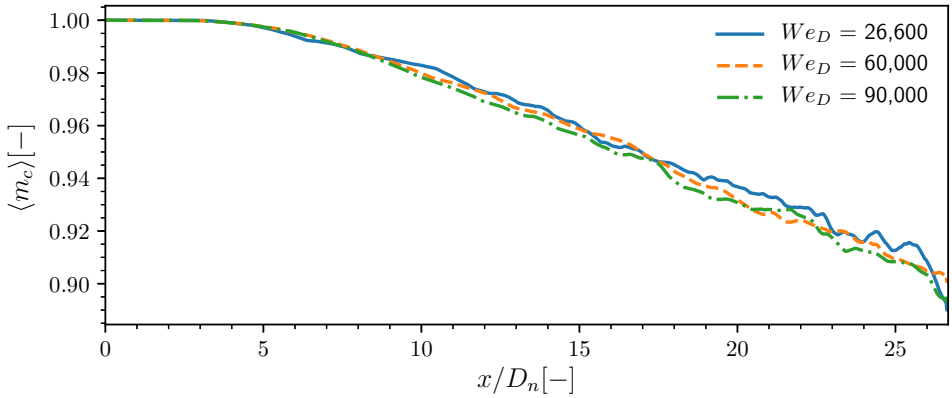

Figure 6.6: Axial distribution of the liquid mass concentration, m_c.

When translating the centreline distributions of the liquid presence to breakup length, the obtained values are nearly the same as can be seen in Table 6.3. Nevertheless, when applying the threshold on the mass concentration at 0.95, it is noticeable that the breakup length decreases by nearly 6%, equivalent to 1 D_n.

Table 6.3: Breakup length using different thresholds on C and m_c.

	C			m_c		
$\mathbf{We}_D$	26,600	60,000	90,000	26,600	60,000	90,000
x_b/D_n $(Th{=}0.99)$	3.36	3.26	3.26	7.52	7.62	7.51
x_b/D_n $(Th{=}0.98)$	3.7	3.64	3.64	10.73	9.97	9.67
x_b/D_n $(Th{=}0.95)$	4.5	4.52	4.48	16.96	16.93	16.07

6.3.2 Axial distributions

Following the centreline results, this section is focused on the study of the spray aperture. The spray angle is analysed through the radial decay of the velocity and the liquid fields along the axial direction. Again, the $r_{1/2}$ and $r_{0.01}$ criteria are used to determine the spray aperture. The first one refers to the radial position where the value of the field decays below the 50% of the centreline value, whereas the $r_{0.01}$ where it drops below 1%. This criteria is usually applied to the velocity field, but also can be applied to the liquid volume fraction ($r_{1/2,C}$ and $r_{0.01,C}$) and the mass concentration ($r_{1/2,m_c}$ and $r_{0.01,m_c}$) fields.

The first approach to the spray aperture is the $r_{1/2}$ criterion applied to the velocity field. Figure 6.7 depicts the $r_{1/2}$ axial distribution for all Weber number conditions. As can be seen, there are no fundamental discrepancies between the cases as they collapse into the same curve.

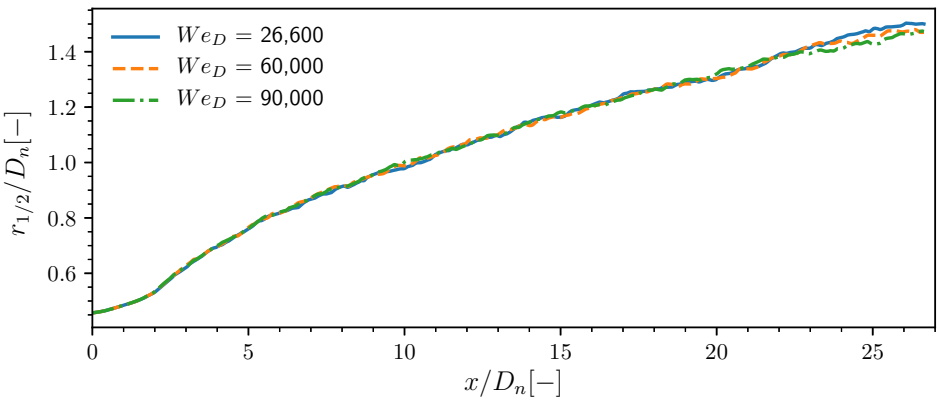

Figure 6.7: Axial distribution of $r_{1/2}$.

Similar results are obtained when using the $r_{0.01}$, $r_{0.01_C}$ and $r_{0.01_{m_c}}$, criteria corresponding to the velocity, liquid volume fraction, and mass concentration,

respectively. Figure 6.8 shows the $r_{0.01}$ for all conditions and variables. Just like on the $r_{1/2}$ criteria, all cases tend to collapse into the same trend. It is important noticing that the characteristic behaviour of the $r_{0.01}$ in the near nozzle field, already reported in Chapter 5 is again shown here for all Weber number conditions.

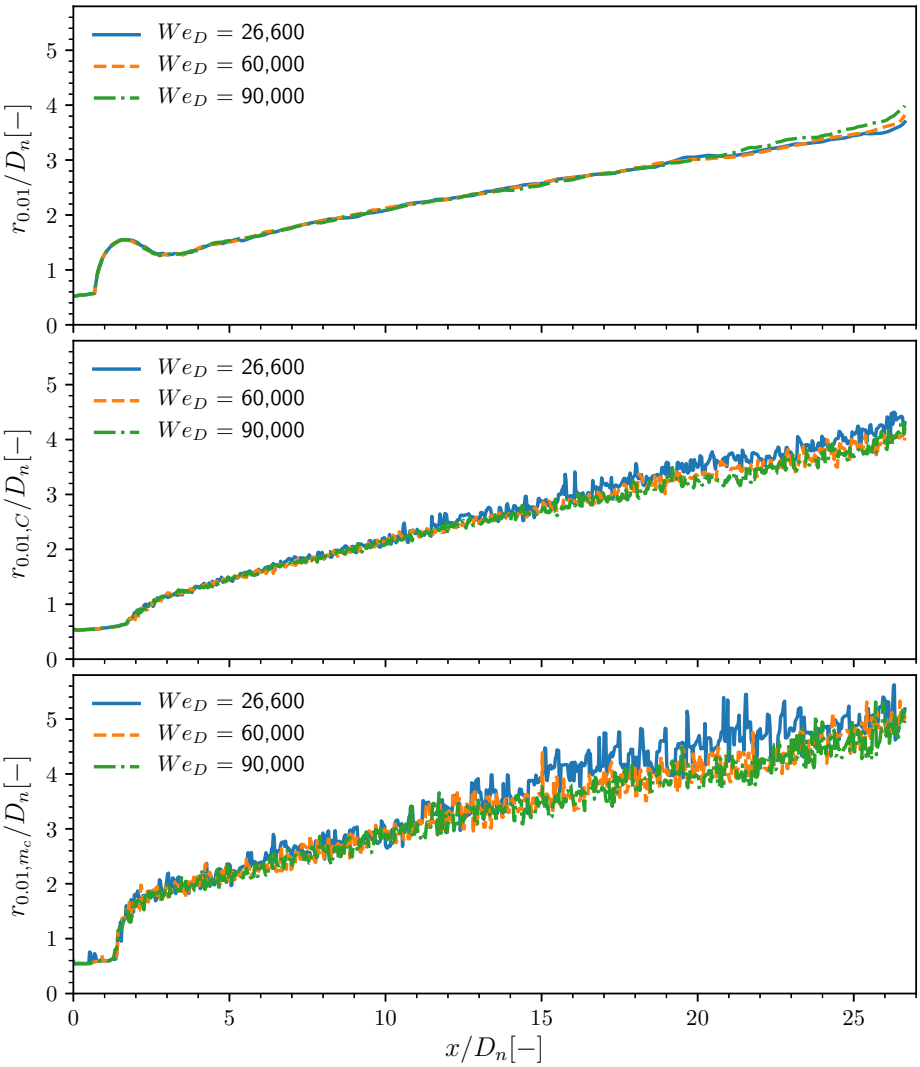

Figure 6.8: Axial distribution of $r_{0.01}$.

6.3.3 Turbulent statistics on $x/D_n \approx 25$

Moving to the plane of study, this study will be mainly centred on the analysis of the Gaussian profile of the axial velocity and the mass concentration, the liquid volume fraction behaviour, and finally, the effect of the Weber number on the computed Kolmogorov scale.

Starting with the axial velocity component, Figure 6.9 presents the non-dimensional average radial profile of the axial velocity component (made dimensionless with the centreline velocity from the corresponding axial position). The radial position is also made non-dimensional, with the $r_{1/2}$, and with the $r_{0.01}$, computed with the temporal average of the plane data. Again, the main interest of this analysis is to compare the profiles with the expected Gaussian distribution obtained by using Equation 5.2 for both r_{ref}. Focusing on the left plot, all cases seem to fit correctly the Gaussian behaviour at radial positions up to than $r_{1/2} = 1.5$. Beyond this point the radial profile present lower values than the Gaussian distribution. However, when computing Sum-Squared Error, SSE, the obtained values are 0.011, 0.007 and 0.006 as the Weber number increases. Different results are obtained when taking into account the $r_{0.01}$ as the reference radial position on the right plot. In this case, there is a clear trend where the velocity profile tends to present a more Gaussian behaviour as the Weber number increases. Furthermore, the Sum-Squared Error increases to 0.24, 0.23 and 0.08 when increasing the Weber number.

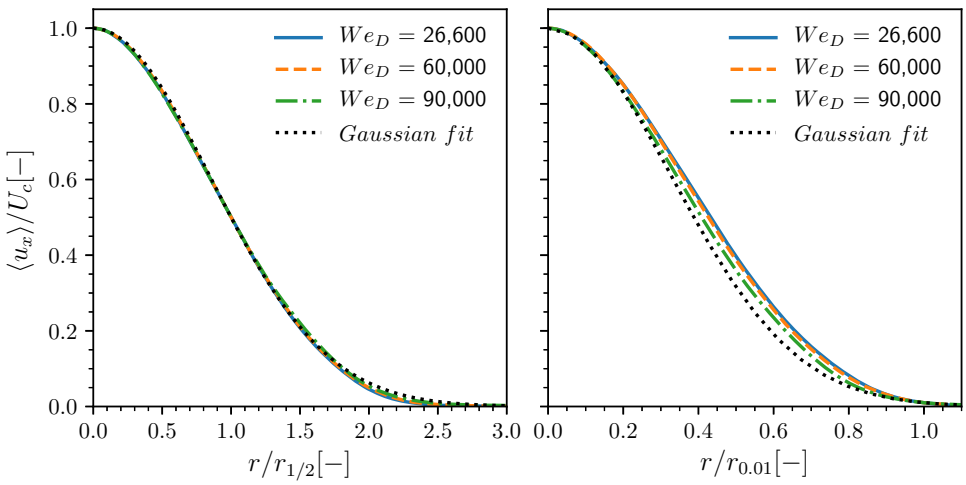

Figure 6.9: Self-similar radial profile of the dimensionless mean axial velocity at $x/D_n = 25$ made non dimensional with: left, $r_{1/2}$ and right, $r_{0.01}$.

Regarding the liquid volume fraction C, Figure 6.10 shows the average of the liquid volume fraction against the non-dimensional radial distance (made non-dimensional with the $r_{1/2}$). Interestingly, all cases collapse for radial distances higher than $r/r_{1/2} = 0.5$, and at lower values, the medium Weber case presents minimally lower values. The centreline values also present different values without a clear dependence on the Weber number. This can be due to the temporal average and the complete convergence of the results. However, the differences are not significant.

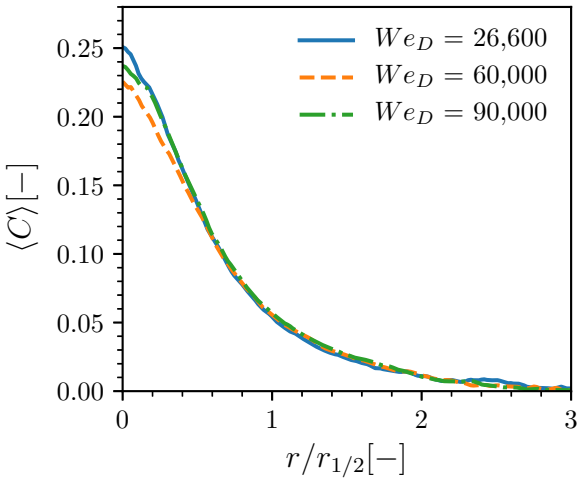

Figure 6.10: Radial profile of the mean radial velocity at $x/D_n = 25$.

Like the axial velocity component, the mass concentration is expected to follow a Gaussian behaviour. So, following the same procedure used on the axial velocity, Figure 6.11 depicts the average radial profile of the mass concentration against the non-dimensional radial distance. Once more, the left plot corresponds to the profile using the $r_{1/2}$ and the right one using the $r_{0.01}$ (both referring to the axial velocity). Starting with the left plot, it can be seen that Gaussian behaviour is fitted until radial positions around $r/r_{1/2} = 1.5$, for all conditions. However, moving to farther radial positions increases the signal noise, and the lowest Weber conditions present the worst fitting. At the same time, the medium and the highest values maintain good agreement with the Gaussian effect. This leads to an SSE values of 0.18, 0.09 and 0.05 as the Weber number increases. Although the discrepancies are higher at the distribution tail, the majority of the spray mass is gathered at $r/r_{1/2} < 1.5$. Regarding the right plot, as the profiles become noisier where the mass concentration drops below 0.2, it is more complex to find the correct shape coefficient. However, the fitting for all Weber number conditions is

slightly higher, presenting the SSE of 0.32, 0.28 and 0.20 as the Weber number increases.

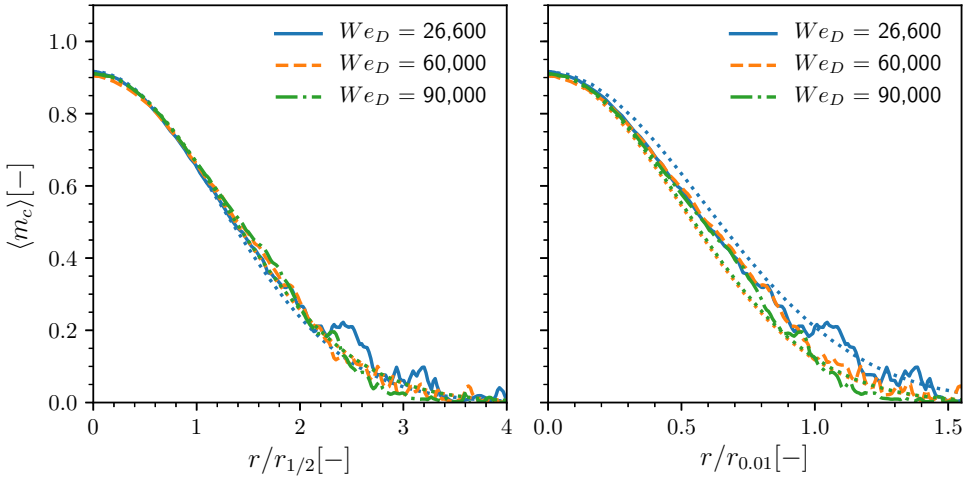

Figure 6.11: Self-similar radial profile of the mean mass concentration at $x/D_n = 25$ made non dimensional with: left, $r_{1/2}$ and right, $r_{0.01}$.

Finally, the Kolmogorov scale η is computed to check the accuracy of the computations. Figure 6.12 shows the radial distribution of η against the non-dimensional radial distance, $r_{1/2}$. As expected, the Weber number does not seem to affect either the radial distribution or the values on radial positions below $r/r_{1/2} = 2$. Although the distributions are not collapsed for higher values, that region is further away from the mixing region where both the axial velocity and mass concentration radial profiles are almost negligible, and thus, there is out of the region of interest.

6.4 Droplet cloud study

Finally, the study is focused on the droplet analysis. This section starts with the total number of droplets detected during all simulations, as shown in Figure 6.13. Similar conclusions from the Reynolds number study can be extracted regarding the peak location and the evolution of the detected droplets. However, the detected droplets during the transient state are quite similar, increasing their discrepancies once the spray reaches the outflow boundary condition, at around $T = 40$ µs. It can be seen that, as the Weber number increases, so do the total droplets detected, especially once all cases have reached the statistically stationary state. Table 6.4 gathers the average number of droplets detected during the statistically stationary state for all Weber

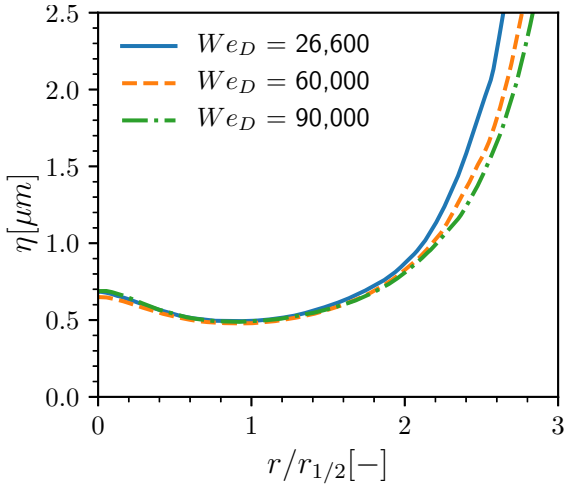

Figure 6.12: Radial profile of the computed Kolmogorov scale at $x/D_n = 25$.

cases. It is also noticeable that the medium Weber number presents an increase of around 25% with respect to the lowest Weber number case. The highest Weber number case presents only a 7% with respect to the medium Weber number case. So, although the increase of the number o droplets generated seems to be decreasing, it is interesting to remark that that the Weber number increases 225% from the lowest case to the medium case and only a 50% between the medium and the highest case.

Table 6.4: Average of droplets detected during the steady state ($T > 60$ μs) for all Weber number conditions.

Weber number	26,600	60,000	90,000
Average droplets detected	17,530	21,980	23,445

As could be seen in the snapshots shown previously in Figures 6.1 and 6.2, the droplet cloud was similar, but the droplet density seemed denser as the Weber number increased. So, in order to further study the implications of the Weber number in the droplet formation, the size, position and velocity distributions will be studied in the following sections.

6.4.1 Size distribution

One of the main parameters that describe the droplet cloud, apart from the total number of droplets, is the size distribution by characterising each droplet

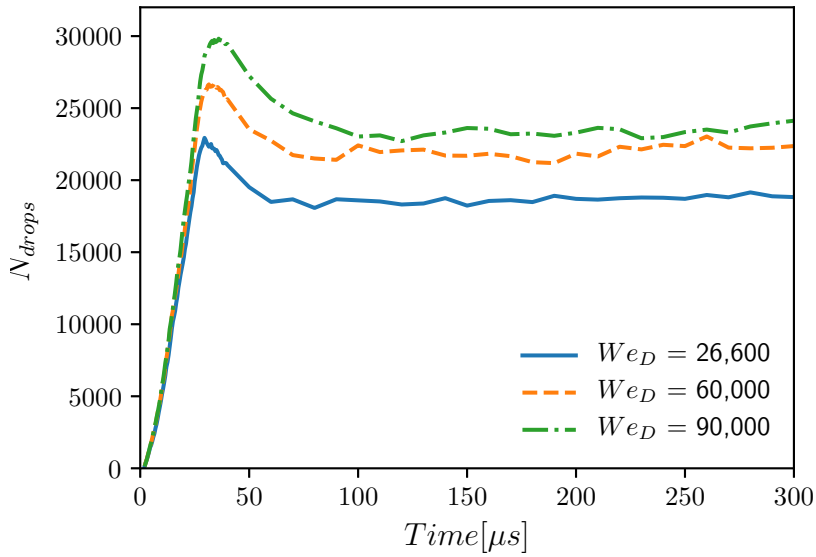

Figure 6.13: Evolution of the number of droplets detected during the whole simulation time.

with its volumetric diameter, d_v. Figure 6.14 shows the temporal average of the number of droplets detected during the statistically stationary state ($T > 60$ µs) for different droplet sizes for all Weber number conditions. Regarding the distributions, it can be seen that in all cases, the maximum is located around 5µm, and as the diameter increases, the number of droplets detected decreases. As the Weber number increases, two different trends are observed. The first range of smaller droplets with d_v lower than 10 µm presents an increase in the total number of droplets detected. At the same time, at higher diameters, that trend inverts, exhibiting less number of droplets when increasing the Weber number. It is worth noticing that the diameter detected with the highest number of droplets coincides with 2 times the cell size of the simulations.

However, as the round jet atomisation is presented under a wide range of configurations, expressing the size distribution in microns cannot be directly comparable as it strongly depends on the nozzle diameter. So, to provide more global information, the droplet sizes are made non-dimensional by dividing by the nozzle diameter. Furthermore, the relative proportion between the bigger and the smaller droplets can be obtained using the PDF of the size distribution. In that terms, Figure 6.15 presents the PDF of the droplet non-dimensional size distribution for all Weber conditions. As the PDF allows finer

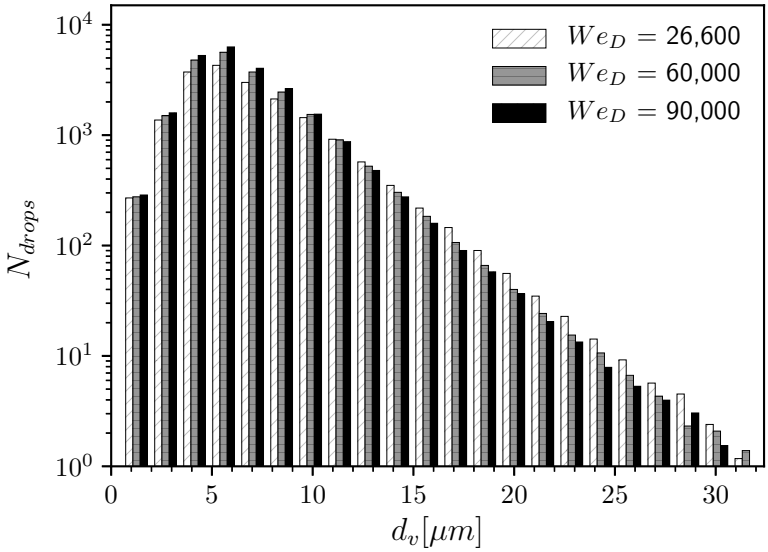

Figure 6.14: Average number of droplets detected for all Reynolds conditions, sorted by their non-dimensional diameter.

discretisation of the size distribution, it can be seen that the peak location is the same in all Weber number conditions and that the droplets with sizes above 10% of the nozzle diameter have a lower probability of appearing and above 15% are almost negligible. In addition, as the Weber number increases, the proportion of having smaller droplets increases. These results mean that the Weber number affects the ligament and drop breakups, favouring the production of smaller droplets as the Weber number increases.

Previously it has been stated that the simulations reach the statistically stationary state around $T = 60$ µs. Nevertheless, it is interesting to check the production ratio of the droplets to ensure that the droplet cloud analysed is not changing during the temporal average. With this objective, the production ratio is computed for each droplet size by comparing the number of droplets detected in each timestep with the number detected on the previous one and then expressed as a percentage of the average number of droplets detected for that size. Figure 6.16 shows the production ratio for each droplet size for all cases. As the droplets are being advected with the flow, if the ratio is zero, the number of droplets generated and those that leave the domain are equal. It can be seen that the ratio is nearly zero for all cases for droplets smaller than 10% of the nozzle diameter, which means that they are practically stabilised. However, as the droplet diameter increases, the distribution becomes noisier

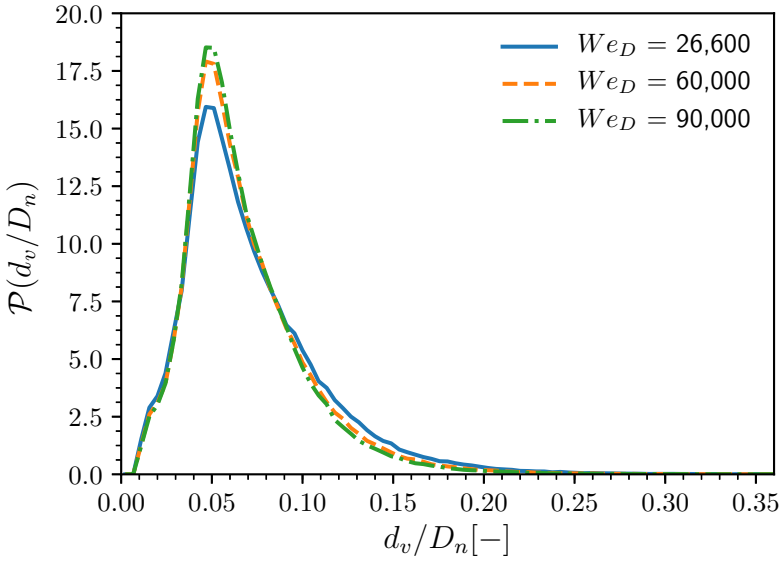

Figure 6.15: Average Probability Density Function of the non-dimensional diameter from the detected droplets for all Reynolds conditions.

due to the less number of droplets detected at diameters above 15% of the nozzle diameter. But as seen in Figure 6.15, those droplet are negligible to the droplet size distributions.

6.4.2 Radial distribution

The following step in the droplet cloud characterisation is the radial distribution. In this section, the radial position of each droplet is taken into account and made non-dimensionless in three different ways: dividing by the outlet nozzle diameter, to relate them to the characteristic size of the problem, then dividing by the $r_{1/2}$ to relate them to the momentum mixing region, and finally with the $r_{0.01}$, to relate them to the spray periphery as it is linked to the nearly zero velocity region.

Figure 6.17 depicts the PDF of the radial position distribution with respect to the nozzle diameter. Regarding the distributions, the medium and the highest Weber number conditions are quite similar, presenting the peak location in the same radial position and exhibiting the same values. On the other hand, the lowest Weber number conditions have the peak shifted towards the spray axis, presenting lower peak values but higher values at the right tail.

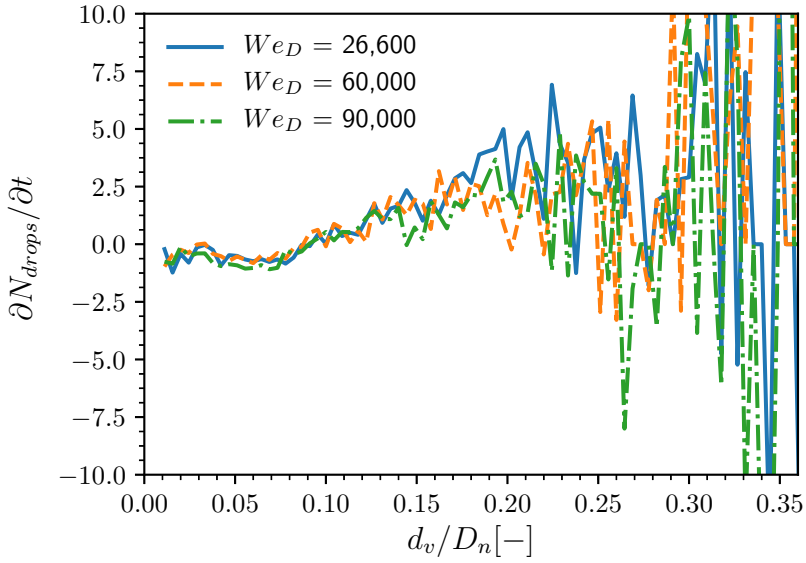

Figure 6.16: Droplet production for the diameters detected within the domain during the steady state. Results expressed as a percentage of the average droplets detected on each size interval.

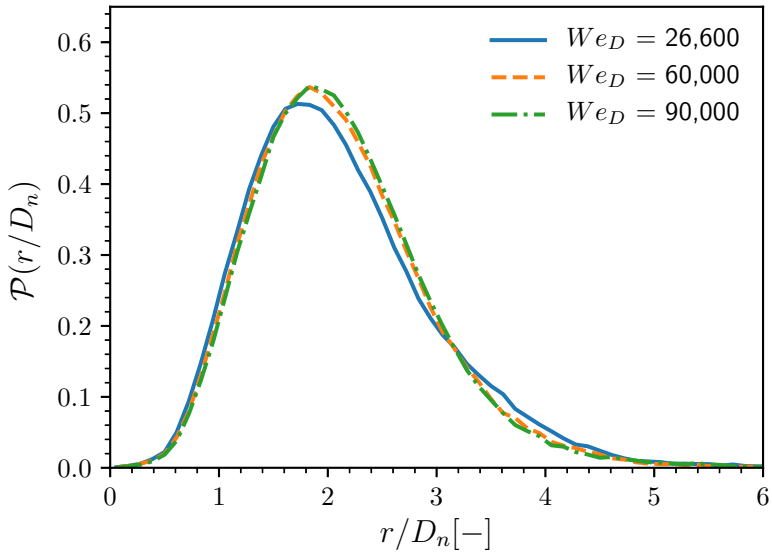

Figure 6.17: Probability Density Function of droplet radial position for all Weber conditions.

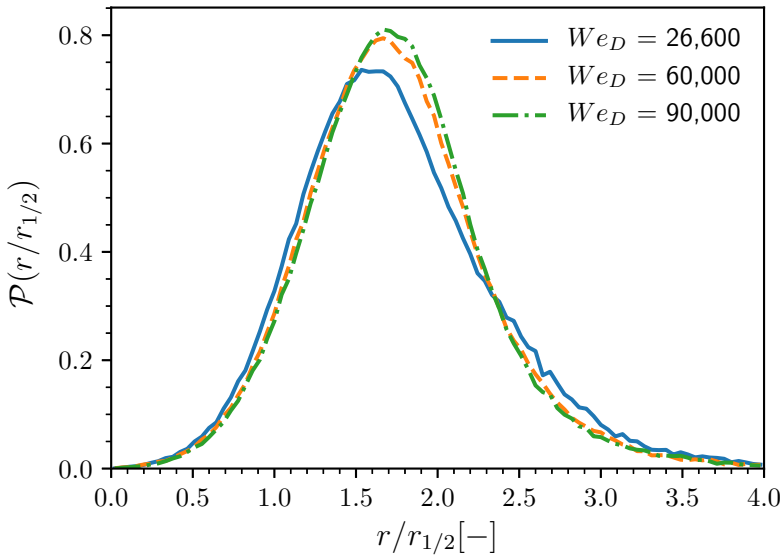

Figure 6.18: Probability Density Function of droplet non-dimensional radial position for all Weber conditions.

Similar trends are found when expressing the radial position made non-dimensional with the $r_{1/2}$, as can be seen in Figure 6.18. Considering the mixing region located around the $r_{1/2}$ distance, the majority of the droplets are placed further from the mixing region, and the distribution tends to a more symmetric shape as the Weber number increases. Again, the medium and highest Weber numbers present almost identical radial distributions having their peaks located at $r/r_{1/2} = 1.75$, while the lowest Weber number condition displaces the maximum to $r/r_{1/2} = 1.58$.

Concerning the $r_{0.01}$, the same trends are observed in Figure 6.19, having sharper, and thus, denser droplet clouds at higher Weber numbers, and moving the peak locations to higher radial positions. In this case, as the peak moves towards $r/r_{0.01} = 1$, the droplet cloud reaches the spray periphery in terms of momentum transfer.

As seen in Figure 6.14, the droplet cloud presents different droplet sizes, so it is interesting to check how the small and the big droplets are distributed through the radial direction. Therefore, Figure 6.20 gathers the radial distribution for different droplet sizes, from grey to black, as the droplet diameter decreases, coinciding with the bars shown on 6.14. Again, the bigger structures present noisy distributions as the population is low. However, the distributions are closer to the spray axis as the bigger structures correspond

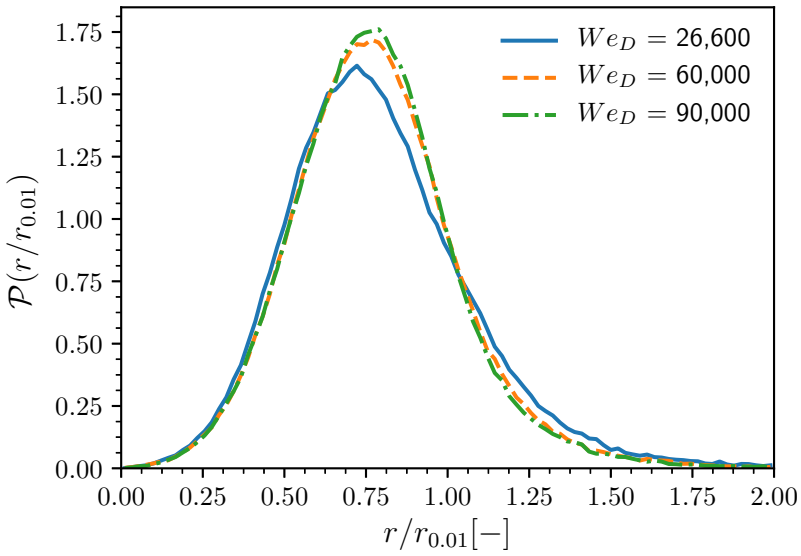

Figure 6.19: Probability Density Function of droplet non-dimensional radial position for all Weber conditions.

to the ligaments previous to the droplet formation. When moving to smaller droplet diameters, the distributions tend to be smoother as the majority of the droplets are located at that size range, shifting the peak towards the spray periphery, from $r/r_{0.01} = 0.72$ to 0.75.

6.4.3 Axial distribution

After studying the radial position of the droplets, the next step is analysing how the droplet statistics change through the axial direction. The first approach is performed by looking at the PDF of the axial position of each droplet, as seen in Figure 6.21. The first thing to notice is that, although the number of droplets generated increases with the Weber number, the distribution of the droplets along the axial direction remains the same. In fact, as hinted in the morphological study back in Section 6.2, the position where the atomisation starts is the same in all conditions, so increasing the Weber number no affect the atomisation onset.

Earlier, when studying the size distribution, the whole domain was considered, giving an overall look at the droplet cloud characteristics. However, as seen on the axial position PDF, the number of droplets increases as moving farther the nozzle exit. Furthermore, as stated earlier, the spray is still in

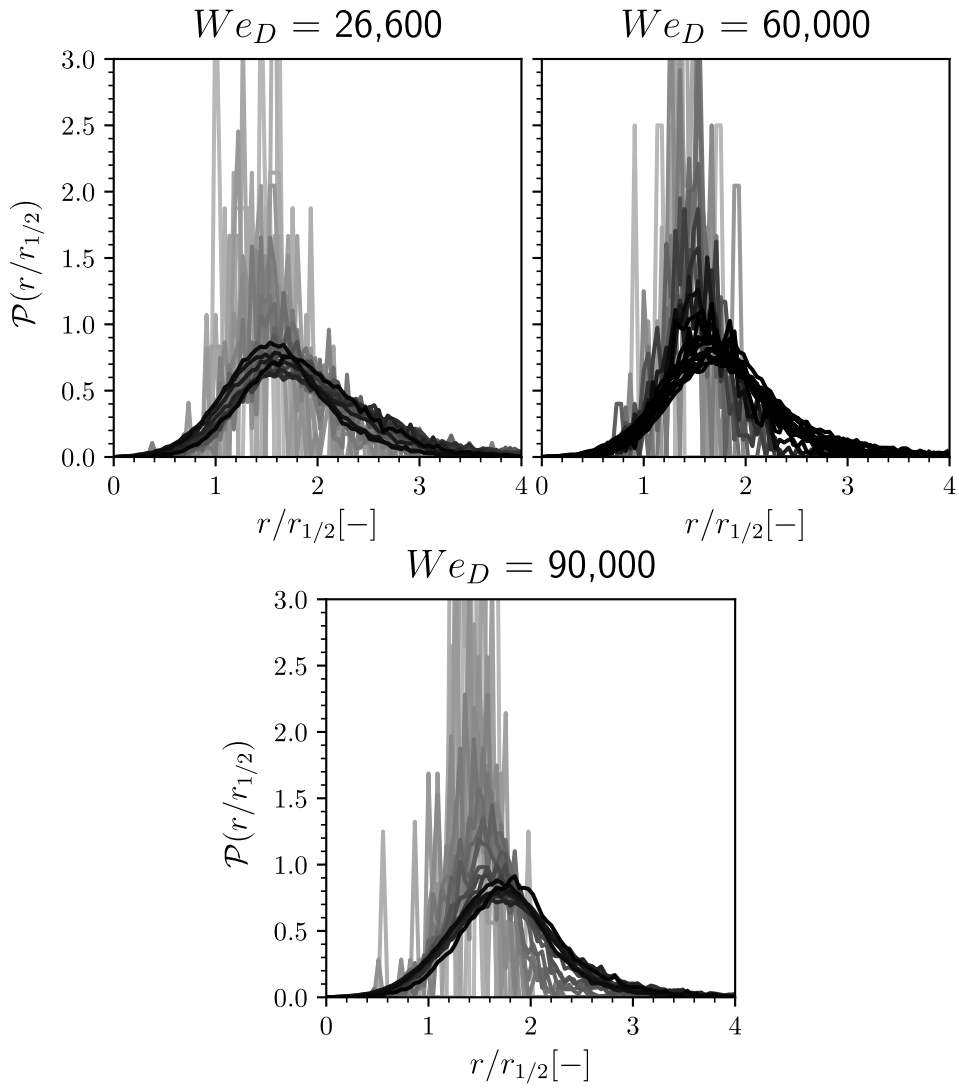

Figure 6.20: Probability Density Function of droplet non-dimensional radial position for different droplet sizes. From black to grey as the droplet size increases. The series correspond to the bars from Figure 6.14.

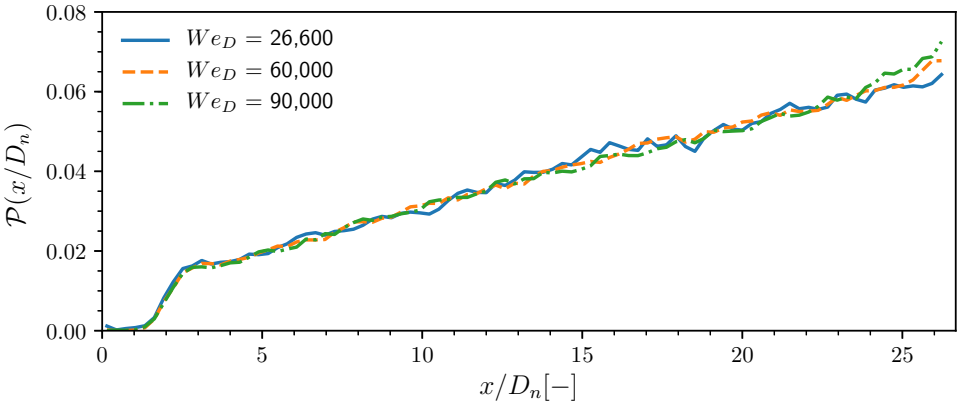

Figure 6.21: Probability Density Function of droplet non-dimensional axial position for all Weber number conditions.

development within the axial range, so it is expected that the droplet size distribution can change as the mixing process advances. So Figure 6.22 presents the size distribution obtained at different axial positions for all Weber number conditions. From grey to black as the axial distance from the nozzle increases. It is noticeable that all cases exhibit a similar trend where near the nozzle exit, the majority of the droplets correspond to the smallest droplet sizes detected. Moving away from the nozzle, the size distribution presents fewer tiny droplets and bigger droplets.

The same approach is applied to the radial distribution to analyse how the droplets are located concerning the spray velocity aperture moving away from the nozzle field. This study will be applied to the radial distance made non-dimensional by the nozzle diameter, D_n, the $r_{1/2}$ and $r_{0.01}$. Starting with the r/D_n, Figure 6.23 presents the radial distribution for different axial position. Same colour guide as the previous figure. The droplets are located at a higher radial position as the spray develops due to the spray aperture. In fact, as the Weber number increases, the PDF radial distribution near the end of the axial domain presents the peak location at slightly higher radial positions.

Following the radial distributions, Figure 6.24 shows similar information to the previous one but expresses the radial distance non-dimensional using the $r_{1/2}$. Interesting behaviour is reported as the peak location remains at the same radial position regardless of the axial position. As the $r_{1/2}$ is related to the mixing region of the spray, that means that the droplet aperture follows the $r_{1/2}$ trend. However, it is noticeable that at higher axial positions, the probability of finding droplets near the spray axis increases while the right

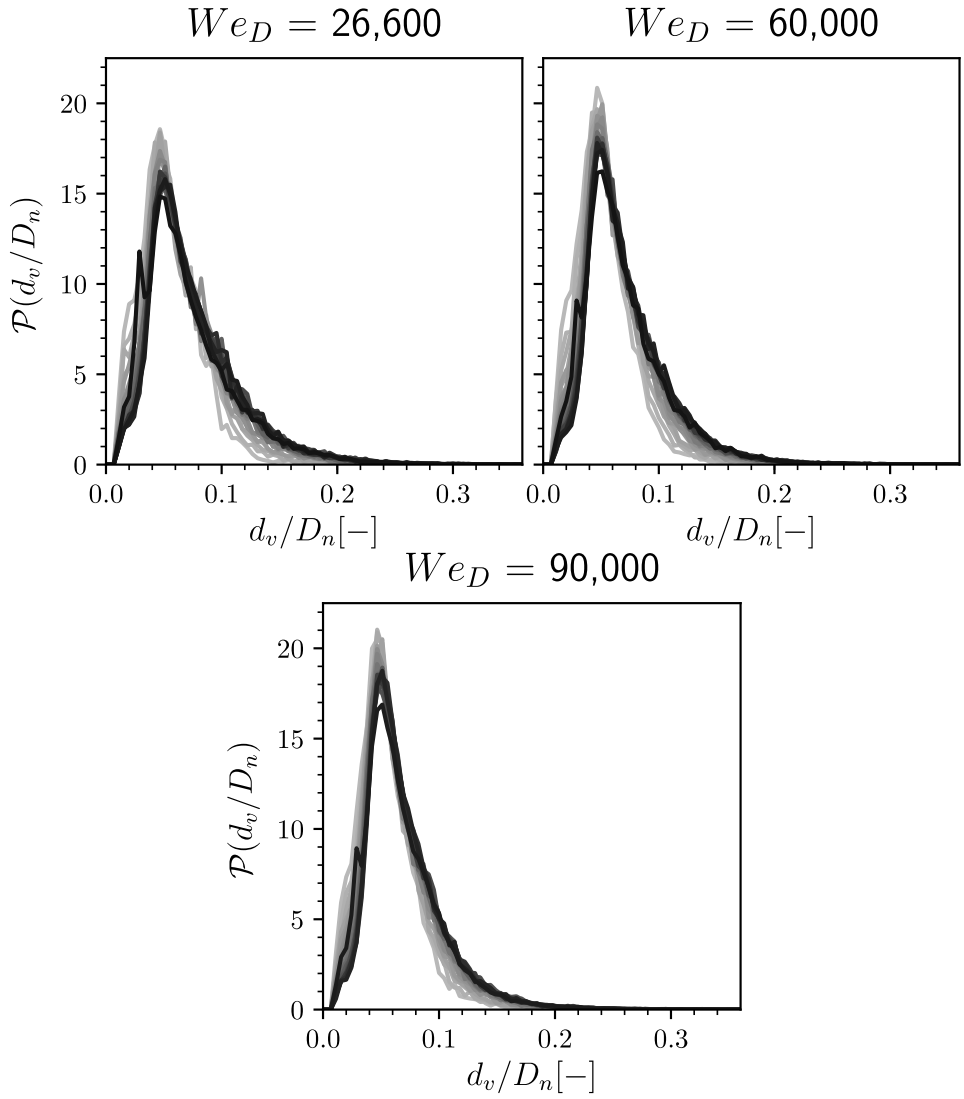

Figure 6.22: Probability Density Function of non-dimensional droplet sizes for different axial positions droplet non-dimensional axial positions. From grey to black as increasing the axial distance. The axial distance goes from $x_/D_n > 2.5$ *to* $x/D_n = 25.5$.

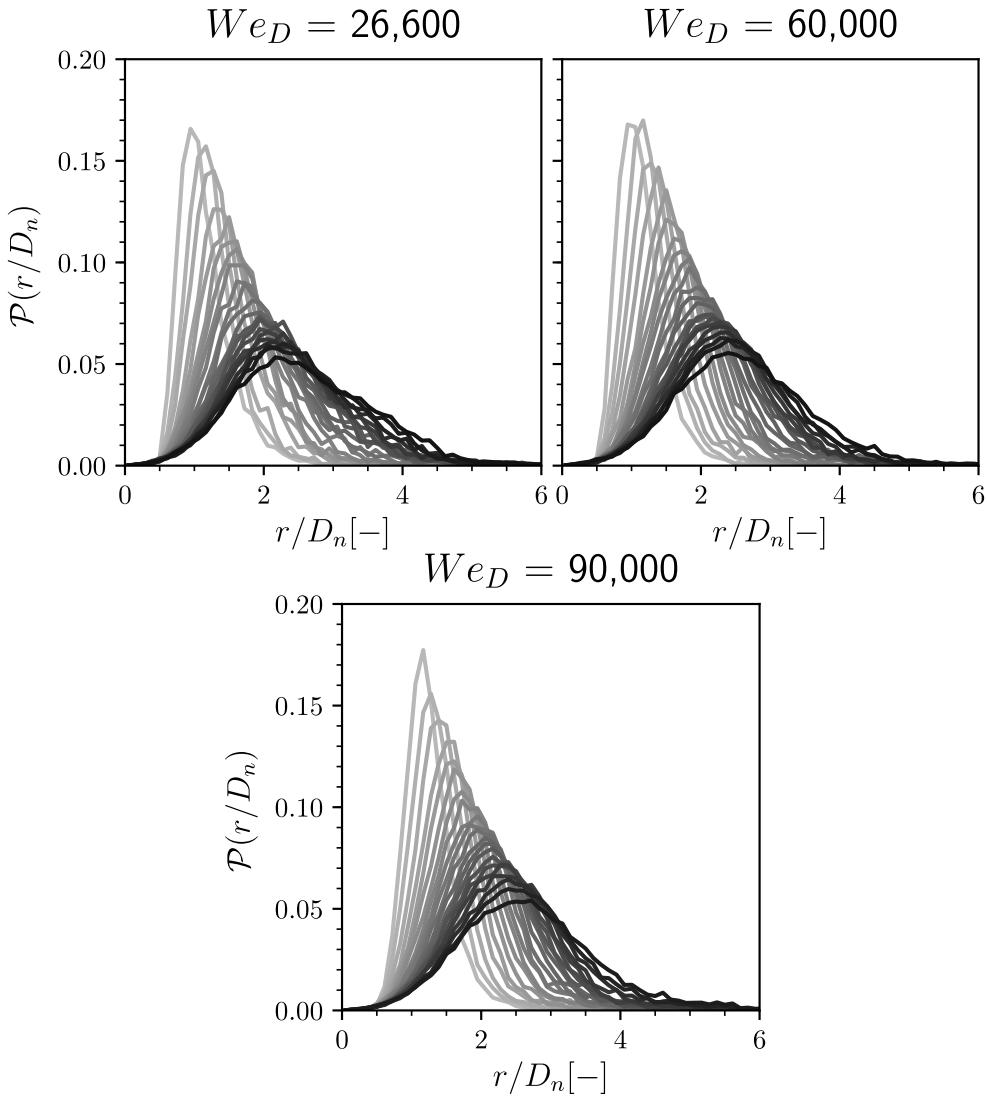

Figure 6.23: Probability Density Function of droplet non-dimensional radial position, r/D_n, for different axial positions. From grey to black as increasing the axial distance. The axial distance goes from $x_/D_n > 2.5$ to $x/D_n = 25.5$.

tail of the distributions seems to collapse into the same trends. The Weber number just shifts the peak location to higher radial positions.

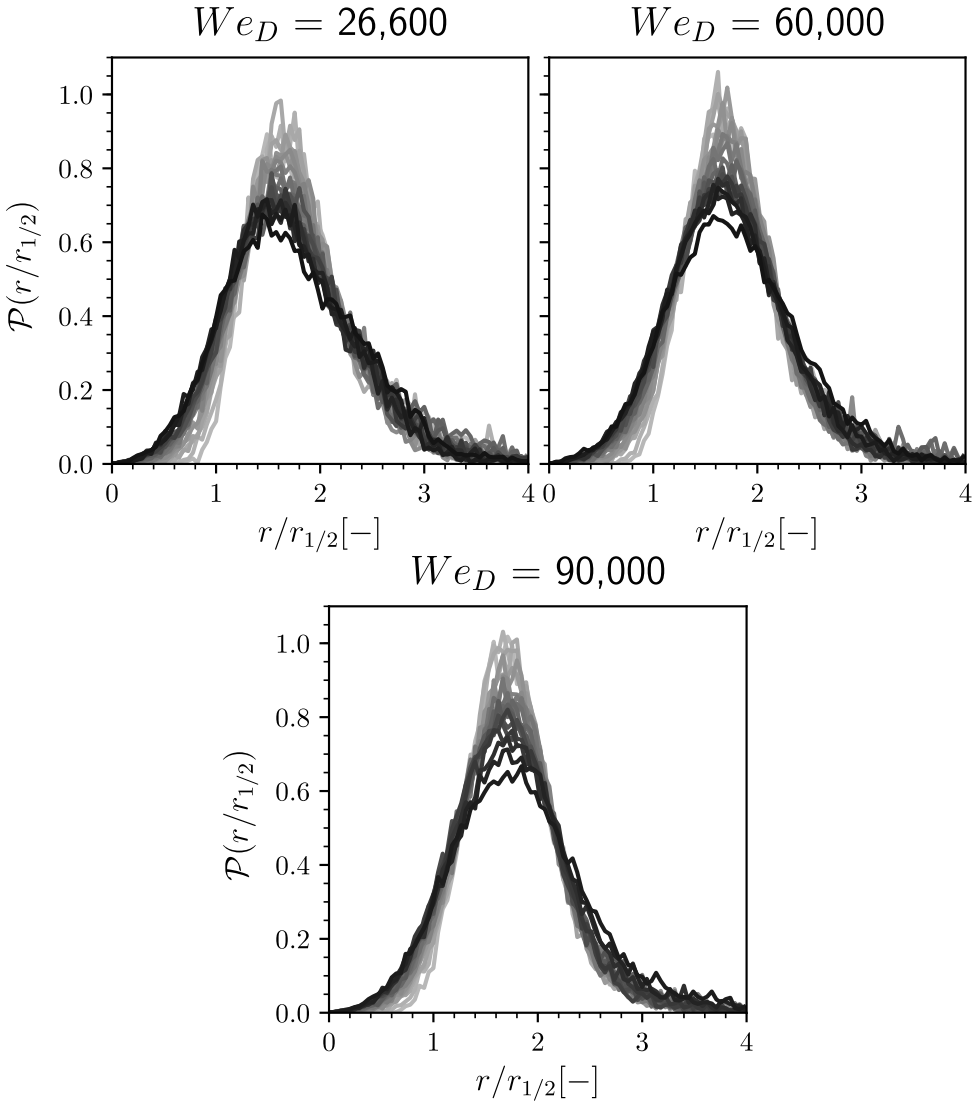

Figure 6.24: Probability Density Function of droplet non-dimensional radial position, $r_{1/2}$, for different axial positions. From grey to black as increasing the axial distance. The axial distance goes from $x_/D_n > 2.5$ to $x/D_n = 25.5$.

Concluding the radial analysis, Figure 6.25 follows the same procedure using the $r_{0.01}$. Similar trends can be observed for all Weber number conditions, where the PDF shifts towards a lower radial position when increasing the axial

distance. This displacement decreases the radial distance where droplets and ligaments can be found as the core disintegrates. Also, the maximum location shifts towards lower $r/r_{0.01}$ and decrease their values, dulling the distribution shape.

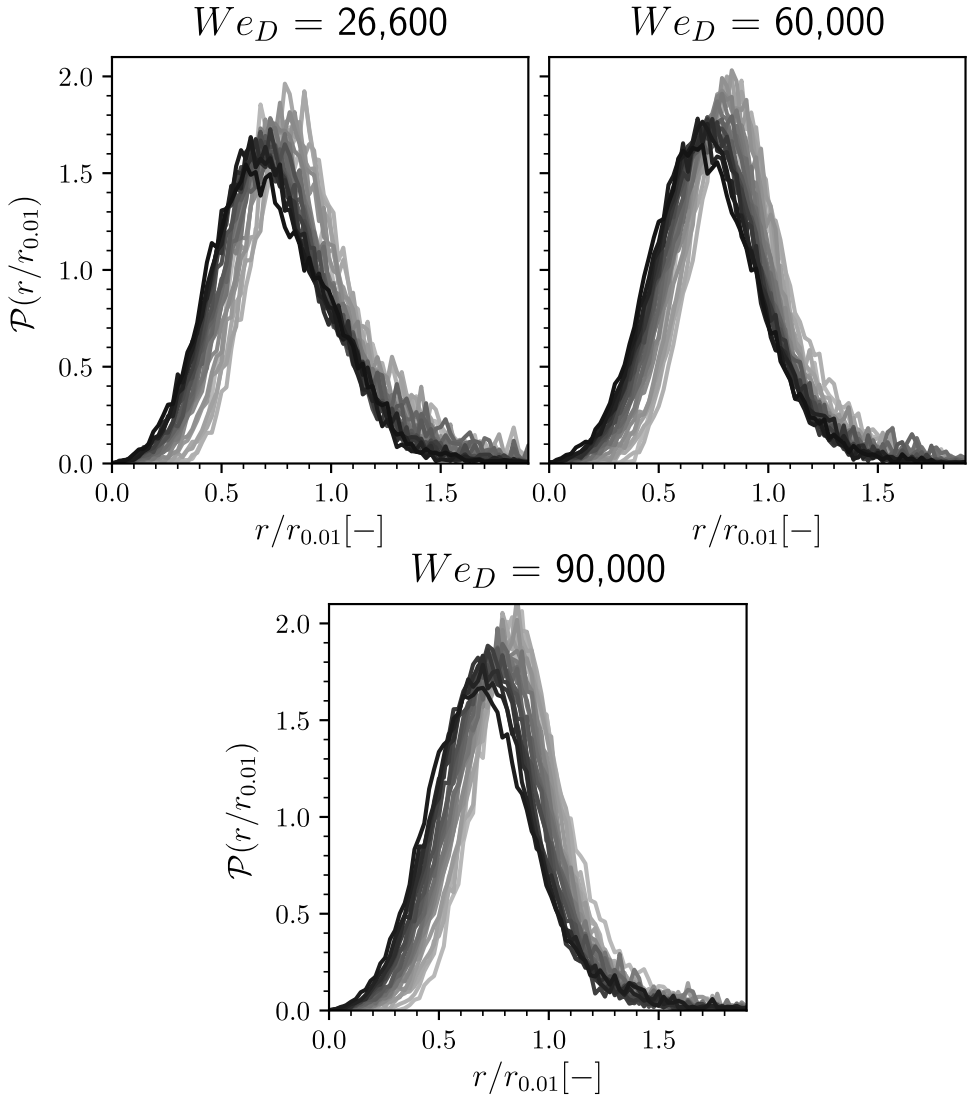

Figure 6.25: Probability Density Function of droplet non-dimensional radial position, $r_{0.01}$, for different axial positions. From grey to black as increasing the axial distance. The axial distance goes from $x/D_n > 2.5$ to $x/D_n = 25.5$.

When studying how those distributions change as the axial distance in-

creases, it is mandatory to keep in mind the spray morphology and that the spray is still in development during the axial sweep. Near the nozzle, the spray is basically a disturbed core with some droplets mainly generated by the spray tip during the transient state. This leads to having mainly small drops located near the spray periphery. Then, as the momentum transfer starts taking place and the atomization develops, the breakup event of the core leads to the ligament appearance, so the droplet size range increases. Furthermore, the droplet position tends to lie inside the spray velocity influence remaining near the mixing region, as can be seen on the $r/r_{1/2}$ distributions.

6.4.4 Velocity distribution

Apart from the droplet position, it is interesting to analyze the droplet velocity to see how the momentum is transferred to them during the atomization process. Figure 6.26 presents the PDF of the non-dimensional axial velocity (made non-dimensional by dividing by the injection bulk velocity). As noticed in the Reynolds number study, an important amount of droplets present axial velocities near zero or negative.

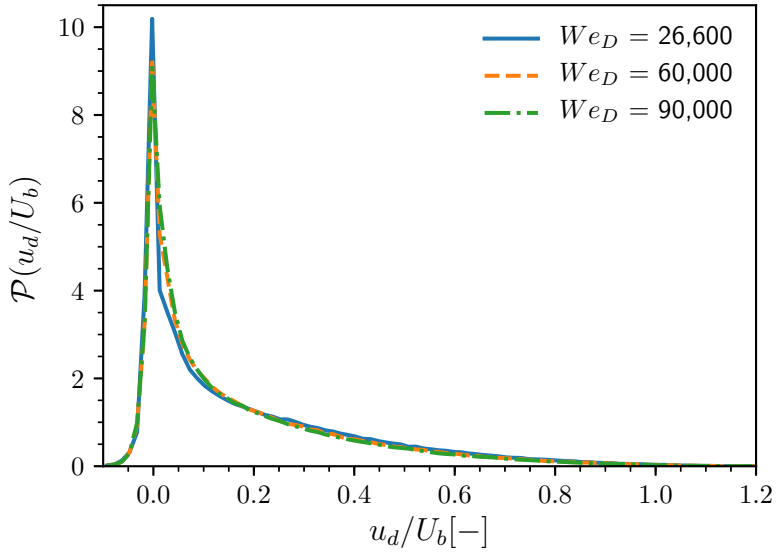

Figure 6.26: Probability Density Function of droplet axial velocity for all Weber conditions.

As already mentioned earlier in the chapter, during the atomization process, there exist some droplets that are advected out from the axial velocity

field; hence, as they lose their inertia and remain static, there are not enough negative radial velocities to attract them again into the spray. To check where are located these droplets, a non-dimensional radial PDF is shown in Figure 6.27 taking into account only the droplets with less than 5% of the U_b. In this case, the PDF is obtained by dividing it into the total amount of droplets. Comparing those results with the ones from Figure 6.19, the peak shifts towards the $r/r_{0.01}$, assuring that is due to the droplets located on the spray periphery.

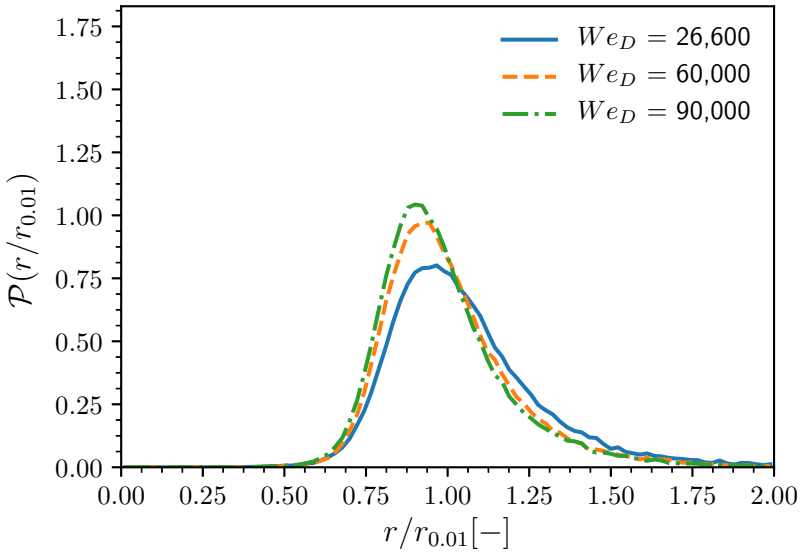

Figure 6.27: Probability Density Function of droplet axial velocity for all Weber conditions.

As done on the size and the radial distributions, it is interesting to see how the velocity is transferred to the droplets along the axial axis. Figure 6.28 shows the PDF of the non-dimensional axial velocity for different axial positions. From grey to black as the axial distance increases. It can be noticed that near the nozzle, the most common velocities around zero. This peak corresponds to the droplets generated during the transient phase that are advected out of the velocity influence region. However, when moving away from the nozzle, the probability of having droplets with velocities higher than the 5% of the injection bulk velocity clearly increases in all Weber number conditions. This is caused by the fact that the region where the velocity is non-zero increases as the spray gains aperture, so the droplets have more inertia. Regarding the Weber number influence, the quasi-static droplets are reduced, although the peak is still located around zero velocity.

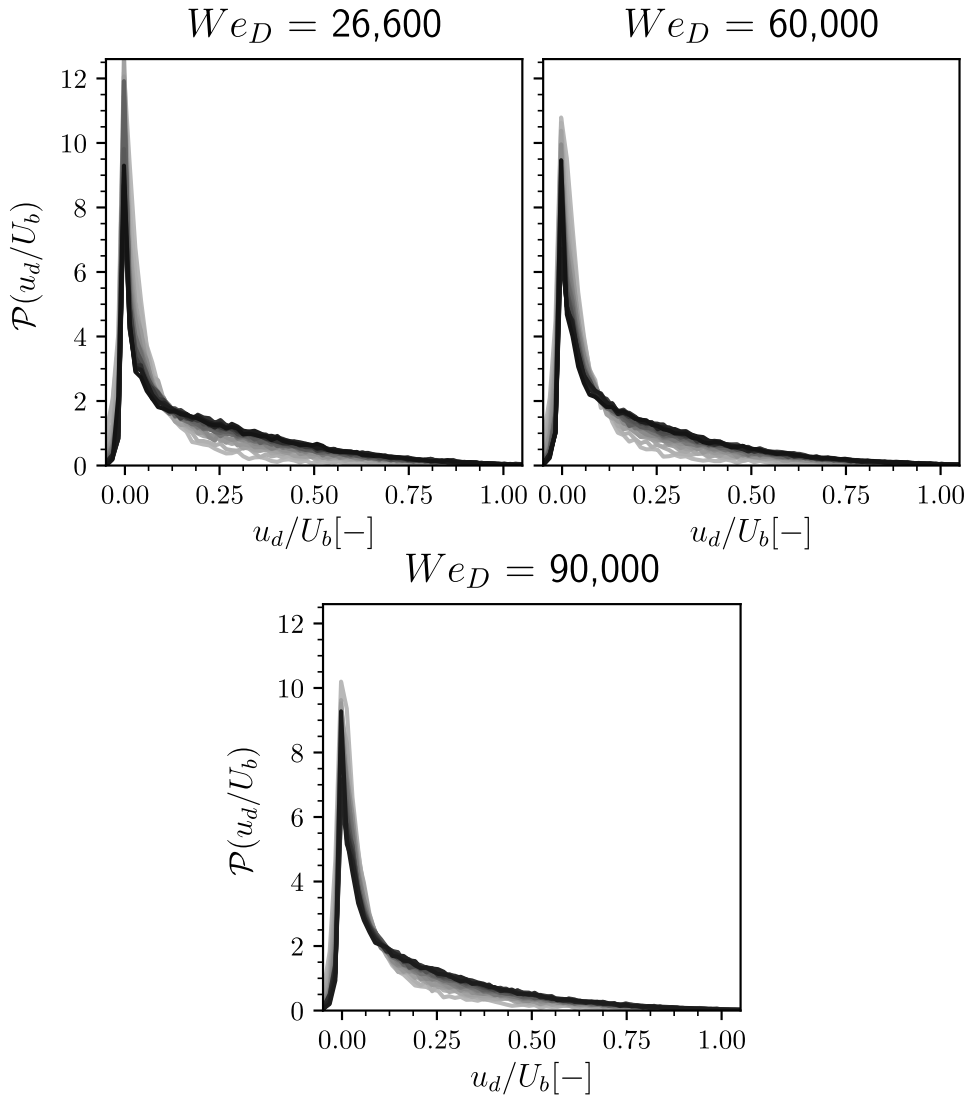

Figure 6.28: Probability Density Function of droplet axial velocity for different axial positions. From grey to black as increasing the axial distance. The axial distance goes from $x/D_n > 2.5$ to $x/D_n = 25.5$.

6.5 Conclusions

This chapter has been focused on studying the influence of the Weber number on the primary atomisation process. Only the surface tension has been modified to vary the Weber number, maintaining the same inflow boundary conditions and most of the physical properties from both the liquid and the gas are used. With this, the Weber number swept from 26,600 to 90,000. This analysis is mainly centred on droplet formation and distribution. Nevertheless, an overall study provides general information on spray development.

The first analysis addresses how the Weber number affects spray development qualitatively. No significant differences have been reported in the penetration or the spray aperture. However, the droplet cloud seems denser as the Weber number increases. Interesting behaviour is noticed when focusing on the liquid core. As all cases use the same inflow conditions, the same perturbations are detected. The effect of decreasing the surface tension is not enough to provoke the core breakup earlier, leading to similar external non-perturbed length.

After the qualitative study of the morphology, the statistically stationary flow field is analysed, focusing on the centreline statistics, axial and radial distributions and the detailed study of a cross-section plane located in the self-similar region. However, unlike in the previous Reynolds number study, where the injection conditions heavily affected the flow field statistics, modifying the Weber number seems not to affect the centreline velocity or mass concentration. Comparable breakup lengths are detected in all applied criteria. Furthermore, all cases exhibit similar spray apertures in terms of velocity, $r_{1/2}$ and $r_{0.01}$; and liquid field, $r_{0.01,C}$ and $r_{0.01,m_c}$. The smoother radial profiles show better Gaussian fit on the axial velocity component and the mass concentration regarding the plane data gathered. Apart from that, similar results regarding the flow field behaviour are reported, and also the Kolmogorov scale exhibit resembling values, maintaining a $\eta_{min}/dx \approx 0.25$ in all cases.

Moving to the droplet cloud analysis, the study is centred on the total number of droplets generated, their size, position and velocity. First, the number of droplets detected increases with the Weber number. The size distribution shows that the population of small droplets increases while the number of bigger liquid structures decreases, accordingly to the qualitative analysis. However, all conditions exhibit a log-normal distribution as expected. Regarding the droplet position, the radial position is analysed in terms of their distance with respect to the D_n, $r_{1/2}$ and $r_{0.01}$. Overall, as the Weber number increases, the droplet cloud displaces to slightly higher radial distances. When

studying the radial distribution of the droplet cloud along the axial direction, as already pointed out in the Reynolds study, the droplet cloud follows the spray aperture of $r_{1/2}$ as the maximum is located at the same non-dimensional radial position. The axial distribution highlights that the smallest droplets are generated evenly along with the axial domain once the atomisation takes place. In contrast, the rest of the droplets increase their number as moving away from the nozzle. This can be translated to modifying the droplet size distribution, decreasing the proportion of the small-to-large droplets as the spray develops in the axial direction. Finally, the axial velocity distribution highlights the droplets that are advected out of the influence of the spray velocity field and remain quasi-static. Also, as the axial distance increases, the spray can provide higher velocities to the droplets, as they are provoked by the natural core jet breakup.

When putting together all the available data from those simulations, it can be noticed that, although the liquid core seems to present a similar size (the breakup length is quite similar), the amount of droplets increases and tends to a finer droplet cloud. As the physical properties and the inflow conditions are kept constant in all cases, it can be stated that the same amount of energy is being added to the process. This means that the surface tension reduction mainly causes the differences in the droplet population. So, the lower the surface tension, the easier the ligaments are disintegrated into droplets, and this seems affecting less to the core breakup.

References

[1] Payri, Raul, Salvador, Francisco Javier, Gimeno, Jaime, and Crialesi-Esposito, Marco. "Comparison of mapped and synthetic inflow boundary conditions in Direct Numerical Simulation of sprays". In: *ILASS - Europe 2019, 29th Conference on Liquid Atomization and Spray Systems*. Paris, France, 2019.

[2] Torregrosa, Antonio J., Payri, Raul, Javier Salvador, F., and Crialesi-Esposito, Marco. "Study of turbulence in atomizing liquid jets". In: *International Journal of Multiphase Flow* 129 (2020), p. 103328. DOI: 10.1016/j.ijmultiphaseflow.2020.103328.

[3] Crialesi-Esposito, Marco, Gonzalez-Montero, L. A., and Salvador, F. J. "Effects of isotropic and anisotropic turbulent structures over spray atomization in the near field". In: *International Journal of Multiphase Flow* 150.November 2021 (2022), p. 103891. DOI: 10.1016/j.ijmultiphaseflow.2021.103891.

[4] ECN. *Engine Combustion Network*. Online. 2010.

Chapter 7

Phenomenological model

7.1 Introduction

As presented in Chapter 1, the primary atomisation models commonly used on round jet low-detailed simulations present a high number of constants that need to be calibrated. Moreover, validating those simulations requires studying the far field, as there is scarce information on the dense region. On account of this, one of the main objectives of this thesis is to shed light on the primary atomisation process, studying the liquid breakup and droplet formation, aiming to help future studies on atomisation without requiring extensive, high-consuming and infeasible DNS.

This chapter is focused on proposing a simple phenomenological model able to predict the droplet size distribution depending on the injection conditions. As the primary atomisation process is expected to provide log-normal distributions of the droplet size, a parametrisation of the main terms of the distribution is performed using the results presented in Chapters 5 and 6.

7.2 Statistical distribution selection

Many efforts have been put into understanding the liquid fragmentation, and different approaches are reviewed by Gorokhovski et al.[1]. However, a simple explanation is worth mentioning to understand the reasons behind the parameters selected to design the phenomenological model. Traditionally, the

size distributions of liquid breakup have been approached with scaling formulations. Kolmogorov's hypothesis assumes [2] that the size of the parent structure does not affect the number of structures directly generated until a specific limit. This fractal behaviour has been noticed in different computational [3, 4] and experimental [5, 6] studies. It has been noticed that results follow log-normal or gamma distributions. The fractal behaviour of the liquid breakup can explain the log-normal behaviour, but as the number of breakups increases, the droplet density increases, leading to the apparition of coalescence. That coalescence affects the size distribution, shifting to a gamma distribution.

So, to find which canonical distribution fits best the computational data, the reference case is chosen. To this end, the temporal PDF of the size distribution is compared to the Log-normal (Equation 7.1)) and the gamma (Equation 7.2) distributions.

$$P_{LN} = \frac{1}{d_v \cdot \hat{\sigma}^2 \cdot \sqrt{2\pi}} \, exp\left(-\frac{(ln\, d_v - \hat{\mu})^2}{2\hat{\sigma}^2}\right) \tag{7.1}$$

$$P_{\Gamma} = \frac{\bar{\beta}^{\bar{\alpha}}}{\Gamma(\bar{\alpha})} \, d_v^{\bar{\alpha}-1} \, exp\left(-\bar{\beta} d_v\right) \tag{7.2}$$

where $\hat{\mu}$ and $\hat{\sigma}$ correspond to the mean and standard deviation of $ln\, d_v$, respectively. $\bar{\alpha} = (\bar{\mu}/\bar{\sigma})^2$ and $\bar{\beta} = \bar{\alpha}/\bar{\mu}$, being $\bar{\mu}$ and $\bar{\sigma}$ the mean and standard deviation of d_v, respectively, and Γ is the Gamma function.

Figure 7.1 presents the PDF of size distributions corresponding to the reference case (Re = 5,037, We = 26,600), along with the Log-normal and Gamma distributions. Those distributions are determined using $\hat{\mu}, \hat{\sigma} = (1.71, 0.51)$, and $\bar{\alpha}, \bar{\beta} = (3.62, 0.57)$ obtained with the computational data. It can be noticed that both distributions present the peak located at the same diameter as the original PDF. Focusing on the Log-normal distribution, a perfect agreement is seen for diameters higher than 5.7 µm. However, at smaller sizes, the distribution shows an under prediction of the number of droplets of the peak but overpredicts the number of droplets with sizes smaller than the peak value. On the other hand, the Gamma distribution presents an even more under prediction of the peak than the Log-normal and an over-prediction at larger droplet sizes.

Results show a better agreement of the Log-normal distribution than the Gamma distribution. This suggests that most droplets generated during the atomisation are due to liquid breakup, and coalescence is not playing an important role up to this point. Additionally, the non-agreement of the smallest

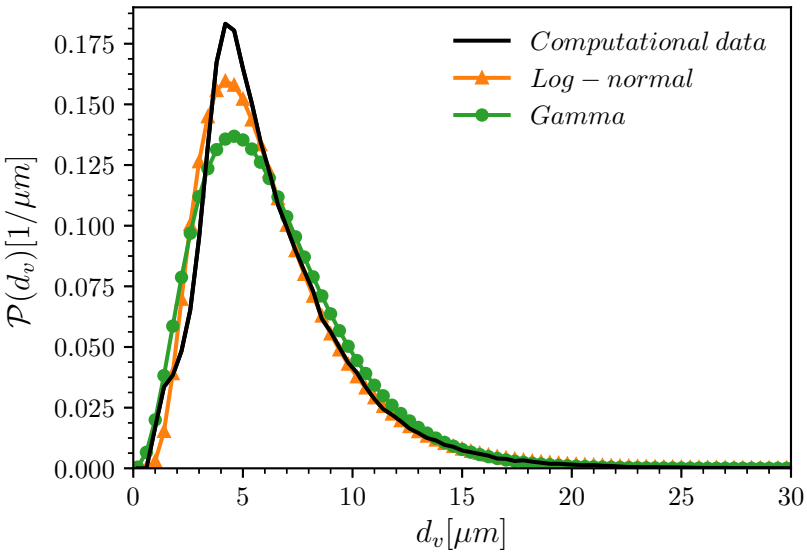

Figure 7.1: PDF of droplet size of the reference case along the Log-normal and Gamma adjusted distributions

sizes can be explained by the spatial discretisation of the domain. As already pointed out in Chapter 4, there is an open topic regarding the minimum droplet size that can be considered resolved. When reaching droplet sizes comparable to the cell size, the calculations of the droplet breakup become more complex, and the code might not be able to handle the disintegration event. This leads to a saturation effect where the number of specific droplet sizes increases and the number of smaller droplet sizes decreases. Taking this into account, the Log-normal distribution explains the droplet formation mechanism of the studied problem and will be selected to define the phenomenological model presented in the following sections.

The following sections will be devoted to defining the parameters that determine the Log-normal distribution for all cases presented earlier in the document. As highlighted in those chapters, the droplet size distribution varies along the axial direction, so apart from studying the whole simulation domain, the last axial portion of the domain ($x > 24.5 \cdot D_n$) will also be analysed as corresponding to the most developed region of the spray.

7.3 Model based on the Reynolds Number

Following the order of appearance on the document, the first non-dimensional number to analyse is the Reynolds number. As can be seen on Equation 7.1, the Log-normal distribution can be defined by its $\hat{\mu}$, $\hat{\sigma}$ and the d_v range. The reference case has already exhibited a good agreement between the data and the Log-normal distribution, so the same procedure is followed for the rest of the cases. Additionally, it is interesting analysing how those parameters change along the axial direction and time.

So before performing the PDF fitting, a temporal and spatial study is performed on $\hat{\mu}$ and $\hat{\sigma}$. In previous chapters, the statistically stationary state has been defined as the moment where the droplet production stabilises, and the droplet generation by size is nearly negligible. However, it is interesting to analyse how the fitting parameters act during this time to see if the distribution is sensitively modified. For this purpose, Figure 7.2 shows the temporal evolution of $\hat{\mu}$ and $\hat{\sigma}$ for the whole domain. It is noticeable that, whereas the $\hat{\mu}$ is practically invariant, the $\hat{\sigma}$ presents a slight increase during the statistically stationary state, similar in all cases. Those trends can be translated into a slight decrease of the small droplets with an increase of the bigger ones, as seen on the obtained droplet size PDFs on Chapter 5. However, these changes are still negligible, so the values presented below are obtained averaging on $T > 150$ µs.

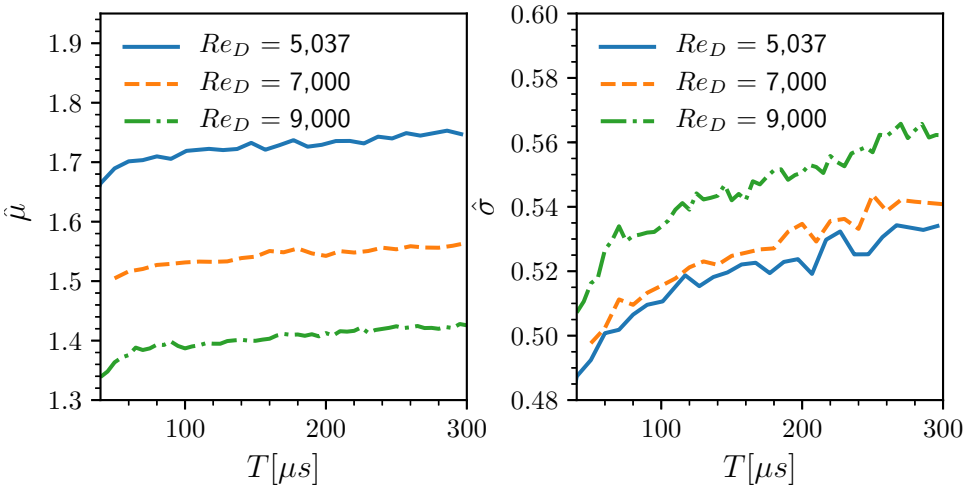

Figure 7.2: Temporal evolution of both the logarithmic mean and standard deviation of d_v for all Reynolds conditions

Once the temporal average is performed, the axial distribution of $\hat{\mu}$ and $\hat{\sigma}$ is done and plotted on Figure 7.3. As in the previous figure, the left plot corresponds to the axial distribution of $\hat{\mu}$, and the right to the $\hat{\sigma}$. It is noticeable that the $\hat{\mu}$ increases with the axial direction, while the $\hat{\sigma}$ is nearly constant. This is consistent with the trends observed in Chapter 5 where near the nozzle, the proportion of smaller droplets was higher than in the most developed region.

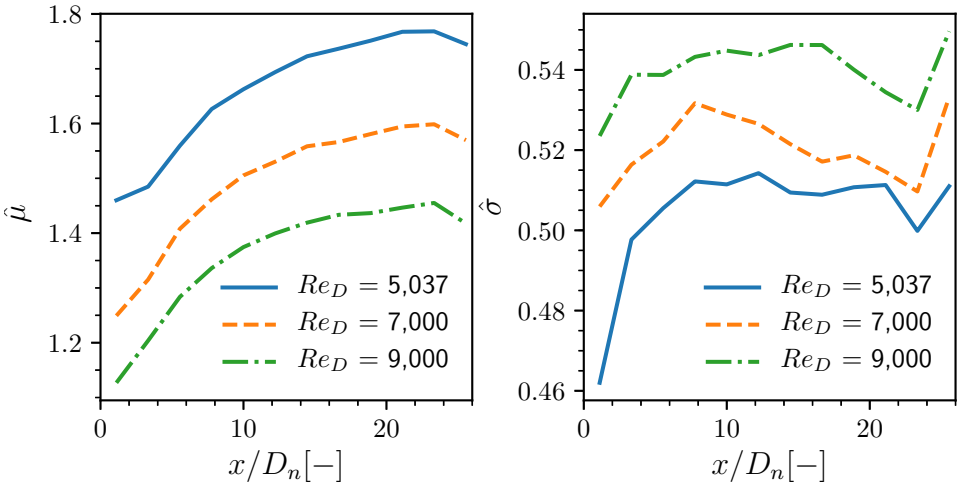

Figure 7.3: Axial distribution of both the logarithmic mean and standard deviation of d_v for all Reynolds conditions

So Table 7.1 gathers all the temporal averaged parameters for all cases and regions of interest. Focusing on the $\hat{\mu}$, it can be seen that, both in the entire domain and in the partial domain, decreases with the Reynolds number and increases when considering only the last region of the domain. In contrast, $\hat{\sigma}$ increases both with the Reynolds number and when considering the domain's end part.

Finally, it is crucial to verify how are the Log-normal distributions obtained using parameters from Table 7.1 to verify how they fit the actual data. Figure 7.4 presents all cases along with the obtained Log-normal distributions. From top to bottom, increasing the Reynolds number, left the full domain fit, and right the end region fit. Solid lines present the PDF of the non-dimensional size obtained from simulations, while the black markers represent the modelled size distribution. Regarding the agreement between the model and the data, the smallest droplet size that can be considered equal are $0.060 \cdot D_n$, $0.051 \cdot D_n$ and $0.043 \cdot D_n$ as the Reynolds number increases for both the whole domain

Table 7.1: Logarithmic mean and standard deviation of d_v for all Reynolds number cases

	Full domain		End domain	
Re	$\hat{\mu}$	$\hat{\sigma}$	$\hat{\mu}$	$\hat{\sigma}$
5,037	1.714	0.511	1.745	0.514
7,000	1.543	0.526	1.57	0.533
9,000	1.403	0.545	1.418	0.550

and the last region. Furthermore, although the obtained PDFs are noisier on the final region, the agreement is slightly better, especially for the reference case where both distributions present almost the same values from $0.043 \cdot D_n$.

Figure 7.4 lacks on providing clear information about the Log-normal fitting at droplet sizes greater than $0.1 \cdot D_n$. Thus, Figure 7.5 expresses the probability values in a logarithmic scale. These results show that the obtained PDF follows the Log-normal trends in all cases and both for the full domain and the end region.

7.4 Model based on the Weber Number

As far as the Weber number is concerned, the same approach as for the Reynolds number is followed. So Figure 7.6 depicts the temporal evolution of both the $\hat{\mu}$ on the left plot, and $\hat{\sigma}$ on the right plot. Just like in the Reynolds study, a slight increase is noticed during the statistically stationary state, so to provide a reliable model fitting, the temporal averaging is performed on $T > 150$ µs. In contrast with the Reynolds number effect, both parameters decrease with the Weber number in this case.

Regarding the axial distribution, on Figure 7.7 are plotted on the left the $\hat{\mu}$, and on the right, the $\hat{\sigma}$. Similarly, as on the Reynolds number, all Weber number cases present an increase of the $\hat{\mu}$ as the axial distance increases. In this case, the Weber number does not seem to significantly affect the $\hat{\mu}$ axial distribution. Moving to the $\hat{\sigma}$, while the reference case presents an axial distribution more or less constant for $x/D_n > 10$, the other cases present a slight decrease as the axial distance increases.

Then, Table 7.2 sums up all the parameters resulting from the computational data for all cases and regions. Regarding the $\hat{\mu}$, although the values decrease with the Weber number, they are maintained in a narrow range. The

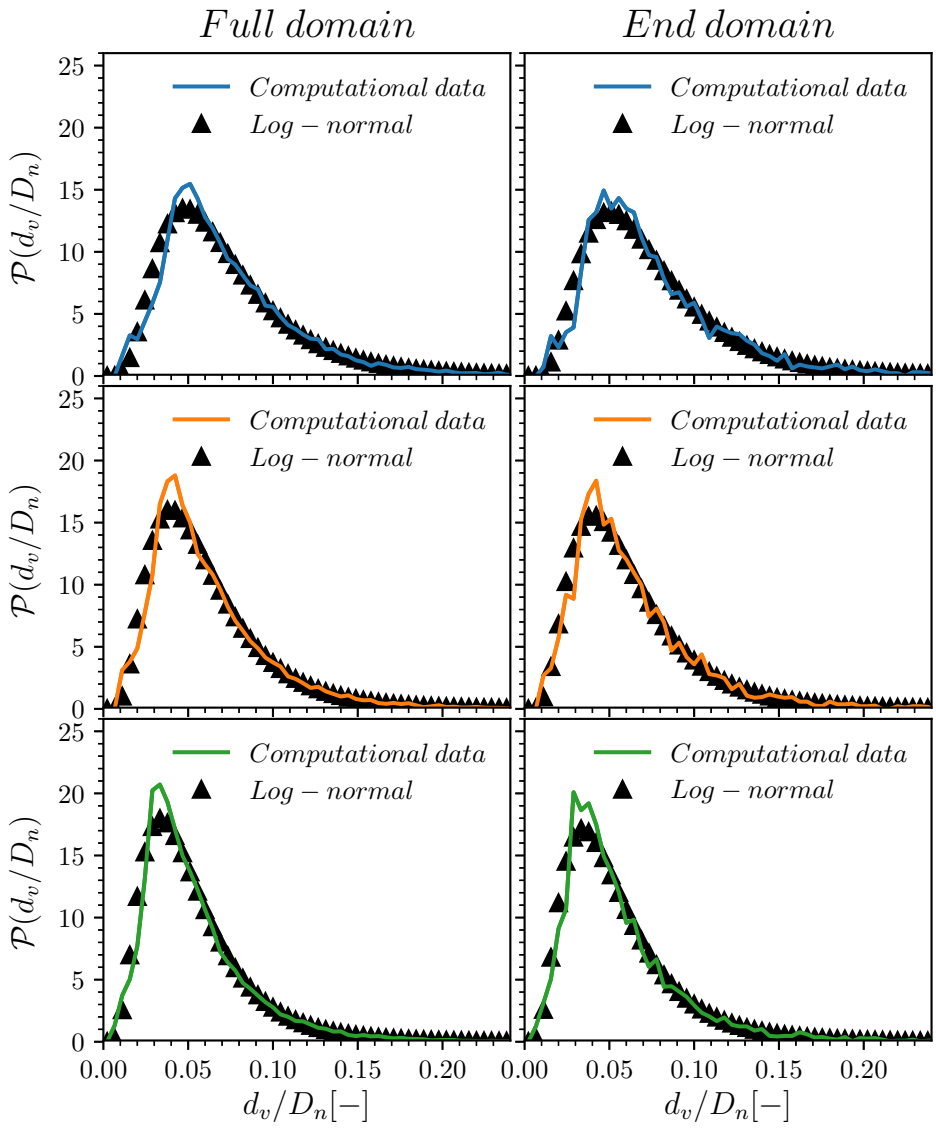

Figure 7.4: PDF of droplet size of all Reynolds number cases along the Log-normal adjusted distributions. From top to bottom as the Reynolds number increases.

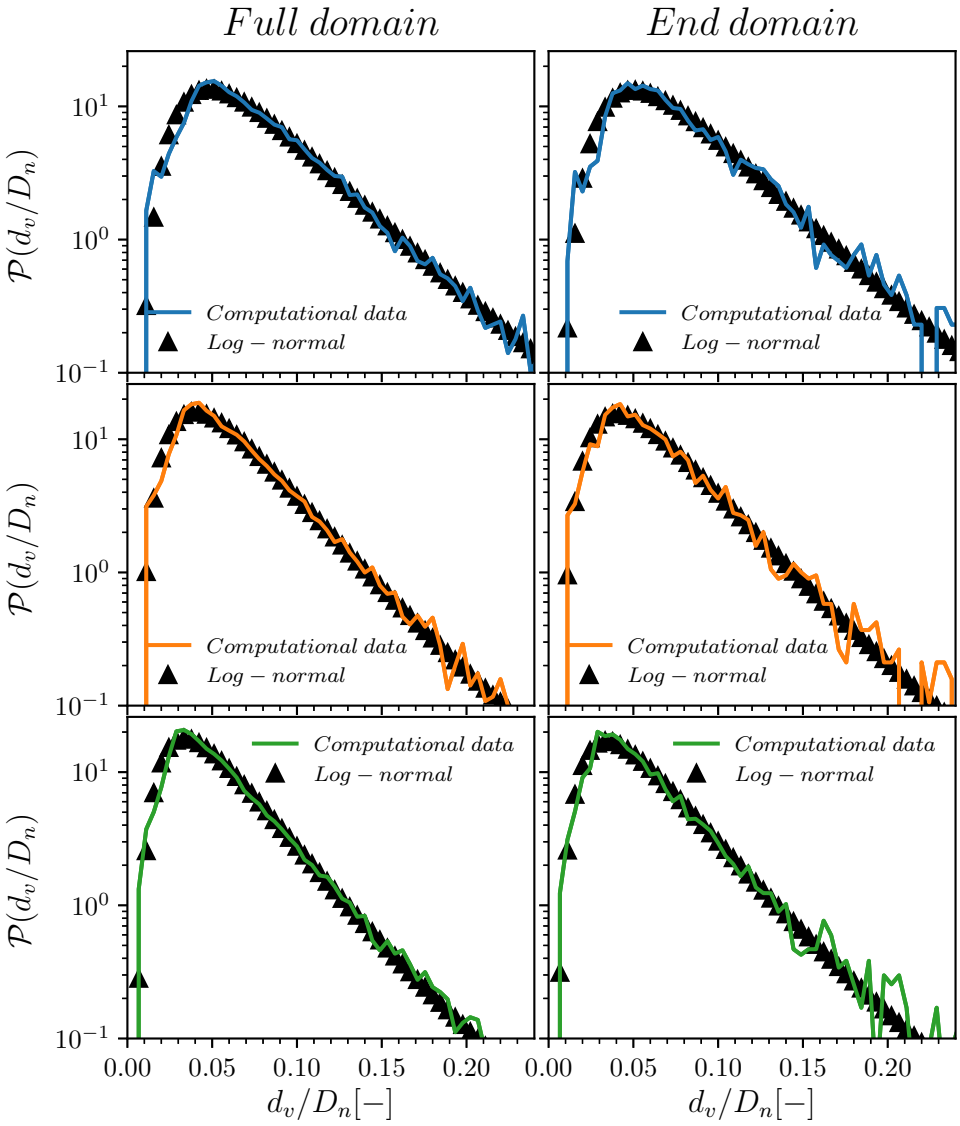

Figure 7.5: PDF of droplet size of all Reynolds number cases along the Log-normal adjusted distributions expressed in logarithmic scale. From top to bottom as the Reynolds number increases.

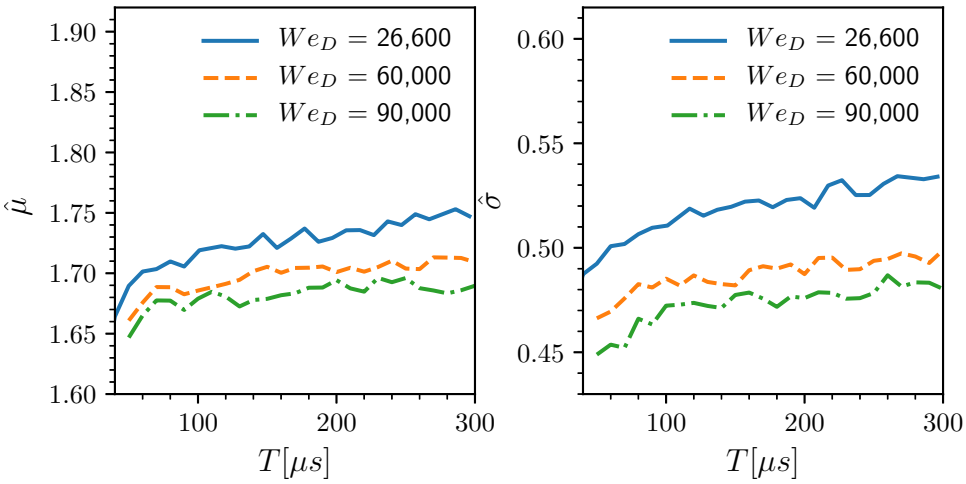

Figure 7.6: Temporal evolution of both the logarithmic mean and standard deviation of d_v for all Weber conditions

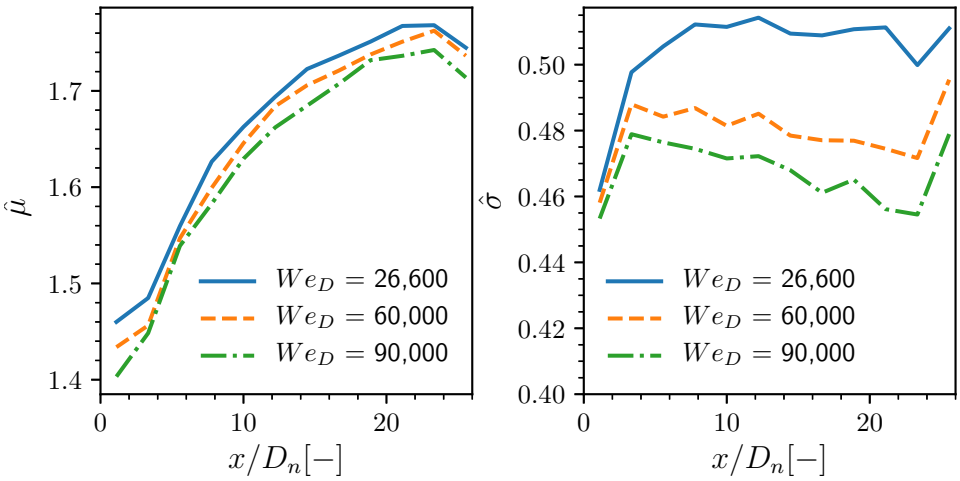

Figure 7.7: Axial distribution of both the logarithmic mean and standard deviation of d_v for all Weber conditions

$\hat{\sigma}$ decreases with the Weber number percentage-wise more than the $\hat{\mu}$. Finally, when considering the most developed region of the spray, a slight increase of both the $\hat{\mu}$ and the $\hat{\sigma}$ is perceived, and the same dependence of the Weber number is noticed.

Table 7.2: Logarithmic mean and standard deviation of d_v for all Weber number cases

	Full domain		End domain	
We	$\hat{\mu}$	$\hat{\sigma}$	$\hat{\mu}$	$\hat{\sigma}$
26,600	1.714	0.511	1.745	0.514
60,000	1.698	0.487	1.736	0.495
90,000	1.682	0.473	0.171	0.479

Finally, Figure 7.8 shows the obtained PDF of the non-dimensional size for all cases and the Log-normal distributions obtained using the parameters from Table 7.2. Following the same structure from Figure 7.4, from top to bottom, the Weber number increases, and the left and right columns correspond respectively to the whole domain and the last region analysis. Solid lines represent the PDF of the simulation results and mark the modelled Log-normal distributions. In this case, all Weber conditions present a reasonably good agreement on the Log-normal models on the computational data obtained. The Log-normal distribution matches the computational data for droplet sizes more significant than $0.06 \cdot D_n$ for all tested conditions, and the peak value is slightly underestimated.

Additionally, to ensure the agreement of the models for droplet sizes where the right tail of the function lacks discretisation, it is interesting to express the probability in logarithmic scale, as presented in Figure 7.9. Even though the bigger structures present noisier results, those comparisons highlight that the logarithmic trend is followed on the obtained computational data, and the Log-normal model successfully predicts the larger droplet population.

7.5 Model definition

In the previous section, the fit capabilities of the Log-normal distribution have been proved for all conditions. This leads to a pair of $\hat{\mu}$ and $\hat{\sigma}$ for each condition. In this section, using the parameters gathered on Tables 7.1 and 7.2, a simple regression will be proposed to predict the size distribution on injection conditions within the Reynolds and the Weber number ranges.

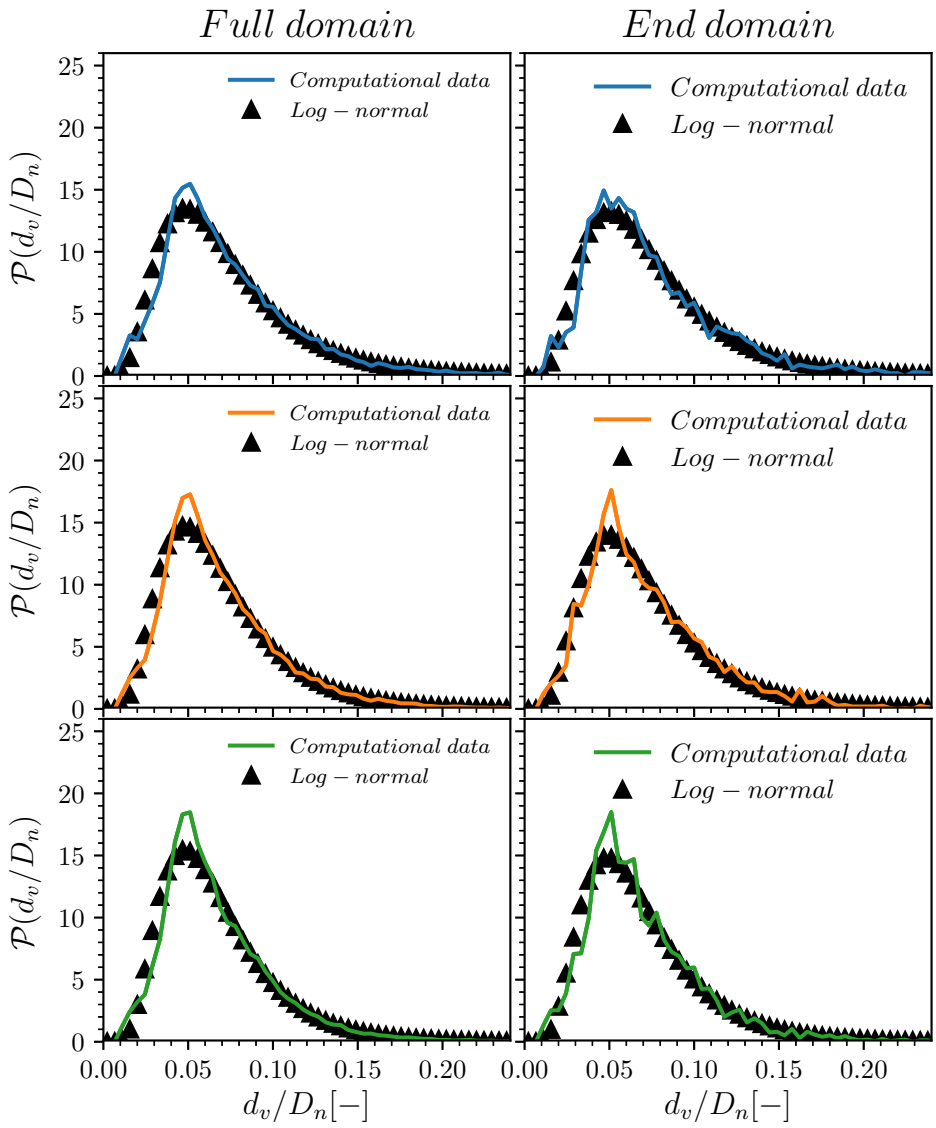

Figure 7.8: PDF of droplet size of all Weber number cases along the Log-normal adjusted distributions. From top to bottom as the Weber number increases.

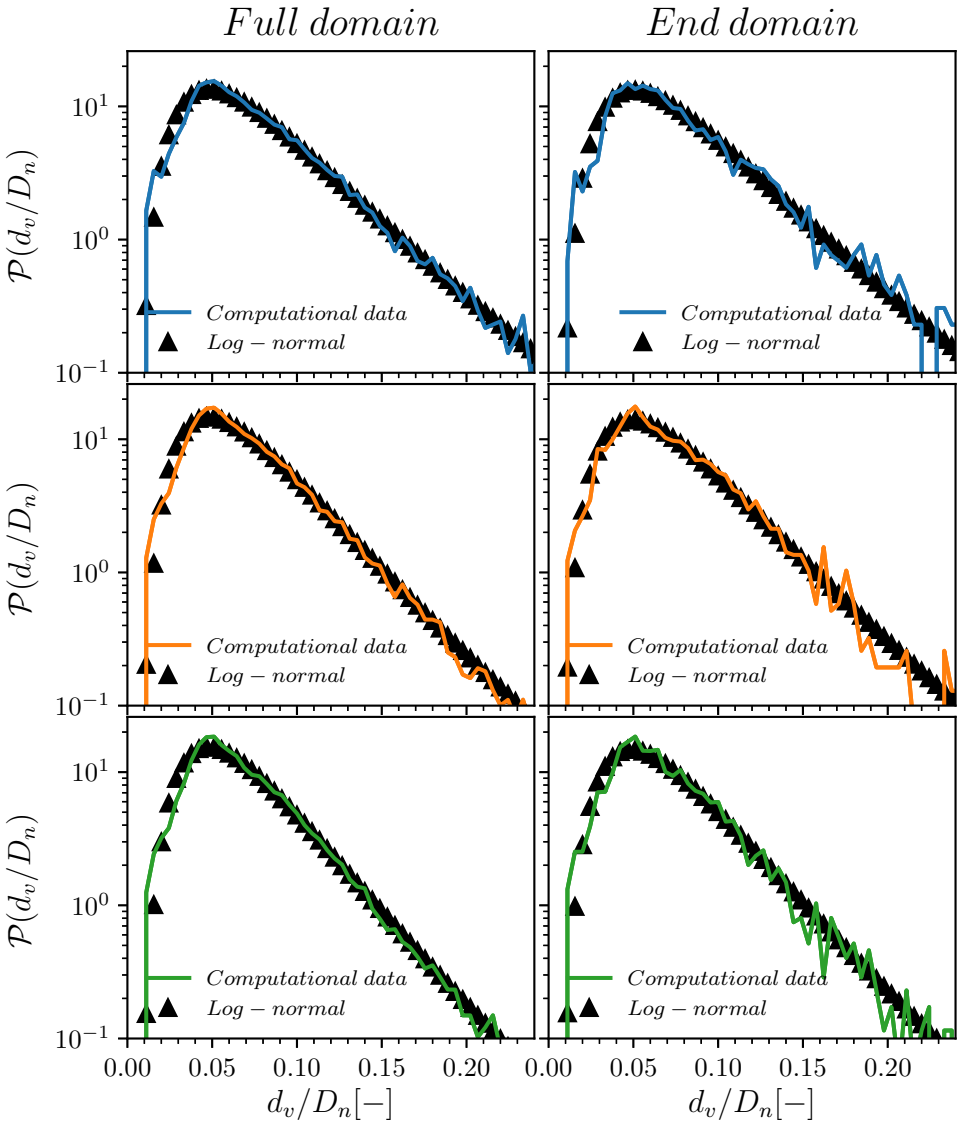

Figure 7.9: PDF of droplet size of all Weber number cases along the Log-normal adjusted distributions expressed in logarithmic scale. From top to bottom as the Weber number increases.

Starting with the Reynolds number model, Table 7.3 gathers all the regressions obtained for $\hat{\mu}$ and $\hat{\sigma}$ for the whole domain and the end region, along with the R^2 coefficient. It can be seen that all cases present a perfect fit with a quadratic regression, so is the one suggested for interpolating purposes.

Table 7.3: Parameter regressions for the Reynolds number phenomenological model

Full domain	$\hat{\mu} = 6.487 \cdot 10^{-9} \cdot Re^2 - 1.722 \cdot 10^{-4} \cdot Re + 2.440$	$R^2 = 1$
	$\hat{\sigma} = 1.541 \cdot 10^{-9} \cdot Re^2 - 1.454 \cdot 10^{-5} \cdot Re + 0.561$	$R^2 = 1$
End domain	$\hat{\mu} = 7.182 \cdot 10^{-9} \cdot Re^2 - 1.898 \cdot 10^{-4} \cdot Re + 2.554$	$R^2 = 1$
	$\hat{\sigma} = 0.882 \cdot 10^{-9} \cdot Re^2 - 0.472 \cdot 10^{-5} \cdot Re + 0.534$	$R^2 = 1$

Figure 7.10 depicts the $\hat{\mu}$ and $\hat{\sigma}$ values corresponding to the Reynolds number study. The left plots refer to the total domain results and the right ones to the most developed region of the spray. All plots present a dotted line representing the obtained regression for each case. As expected, the trends do not change when considering only the end part of the domain. Additionally, as hinted in Table 7.3, the agreement of the regression with the computational data is perfect. Regarding the trends, the $\hat{\mu}$ does not present a high curvature in many cases, but the $\hat{\sigma}$ does exhibit a marked curvature, especially when taking into account the whole domain.

The same procedure is followed in the Weber number analysis. Table 7.4 sums up all the regressions obtained for both $\hat{\mu}$ and $\hat{\sigma}$ along with their respective coefficient of determination. Again, quadratic regressions are used as they provide a perfect fit for a three-point defined function. Compared to the Reynolds number regressions, it can be seen that the model coefficients are far lower, as the Weber numbers used are about one order of magnitude greater than the Reynolds number.

Table 7.4: Parameter regressions for the Weber number phenomenological model

Full domain	$\hat{\mu} = 5.046 \cdot 10^{-12} \cdot We^2 - 1.369 \cdot 10^{-6} \cdot We + 1.770$	$R^2 = 1$
	$\hat{\sigma} = 9.216 \cdot 10^{-12} \cdot We^2 - 1.833 \cdot 10^{-6} \cdot We + 0.569$	$R^2 = 1$
End domain	$\hat{\mu} = 2.907 \cdot 10^{-12} \cdot We^2 - 1.302 \cdot 10^{-6} \cdot We + 1.813$	$R^2 = 1$
	$\hat{\sigma} = 3.035 \cdot 10^{-12} \cdot We^2 - 1.038 \cdot 10^{-6} \cdot We + 0.558$	$R^2 = 1$

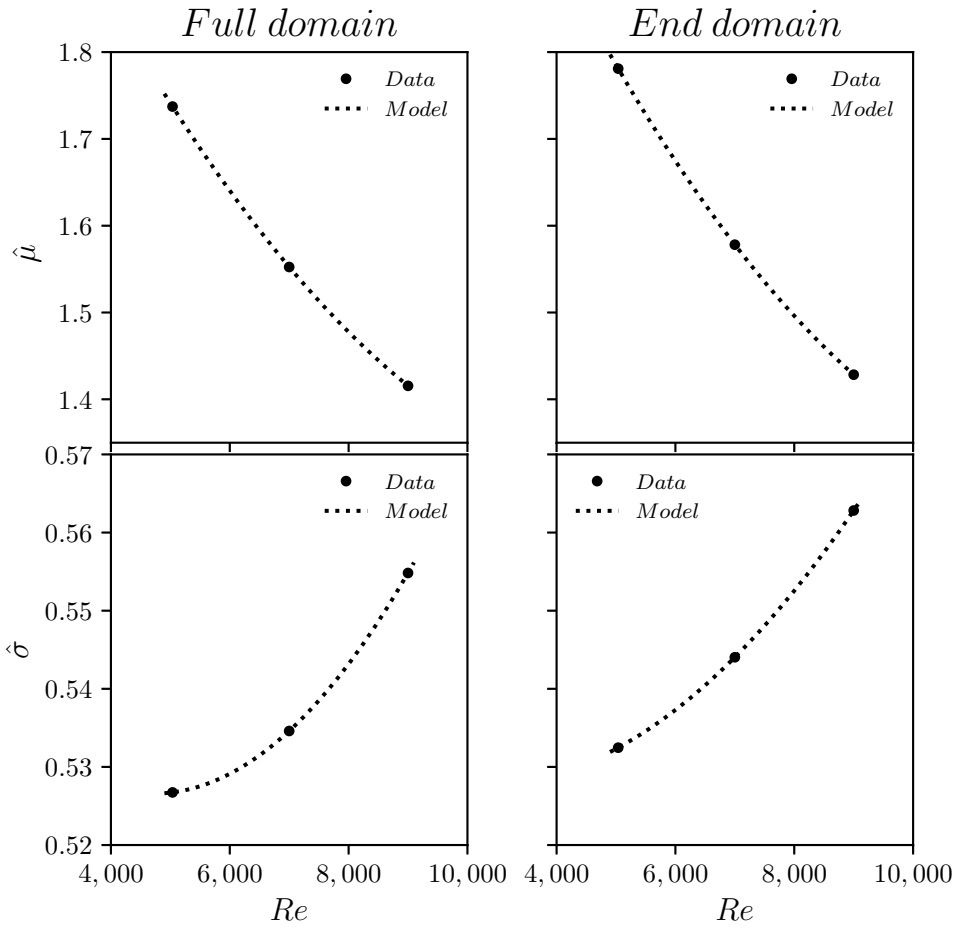

Figure 7.10: Logarithmic mean and standard deviation of the droplet size distributions from all Reynolds number cases along the phenomenological model regressions

Once more, Figure 7.11 shows the obtained values of $\hat{\mu}$ and $\hat{\sigma}$ for the whole domain (on the left plots) and the end region (on the right plots), along with the quadratic regressions presented on Table 7.4. Like in the Reynolds study, the regressions corresponding to the $\hat{\mu}$ present lower curvatures than the $\hat{\sigma}$.

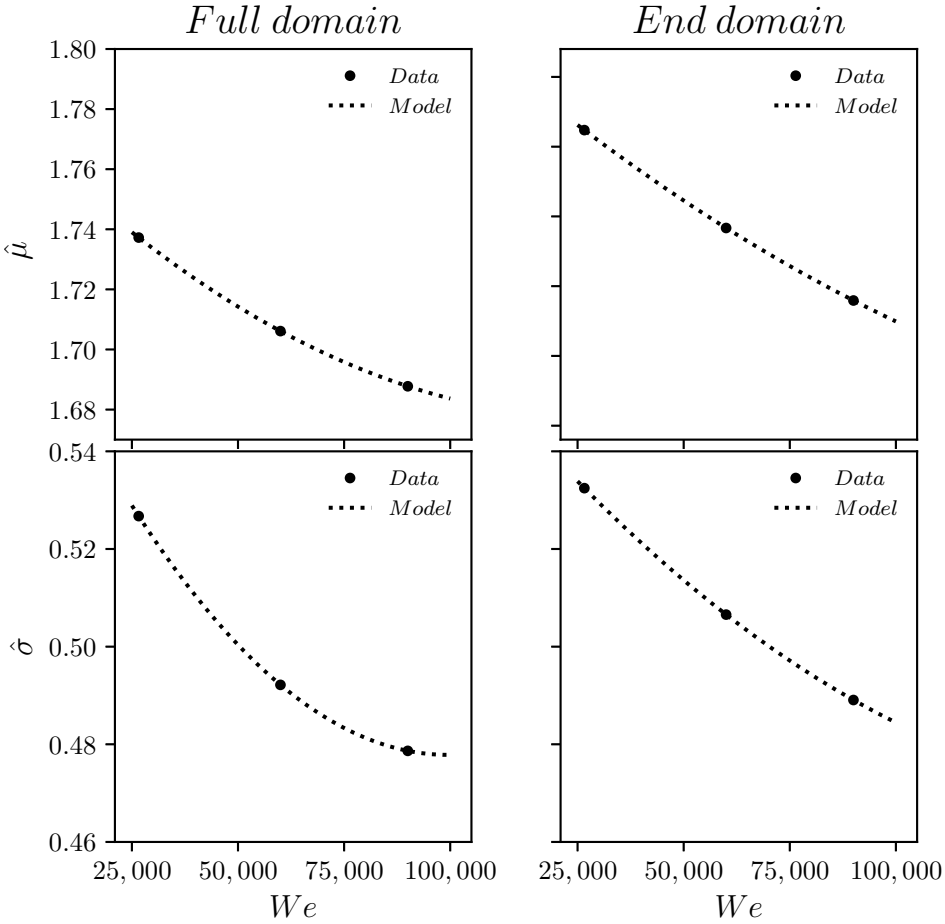

Figure 7.11: Logarithmic mean and standard deviation of the droplet size distributions from all Weber number cases along the phenomenological model regressions

After defining the models for both the Reynolds and the Weber number, a swipe of both parameters is done to analyse how the size distributions vary when interpolating on those models. Figure 7.12 depicts the modelled size distributions obtained by applying the $\hat{\mu}$ and $\hat{\sigma}$ obtained with the presented regressions for different injection conditions. Left plots correspond to swiping from Reynolds number 5,000 to 9,000, and right plots Weber number from

26,600 to 90,000. Top plots correspond to the entire domain and bottom ones to the end region of the domain. The graph series go from grey to black as the non-dimensional number increases. It can be noticed that both models provide smoother transitions between the simulated cases. The Reynolds number model tends to shift the peak location to smaller droplet sizes, increasing its value at the expense of the proportion of bigger droplets. Regarding the Weber number model, it maintains the peak location, also increasing the ratio between the smaller and bigger droplets.

This plot shows how the interpolation affects the droplet size distribution. It is mandatory to emphasise that those regression curves have been obtained at the iso-Weber number (in the case of the Reynolds number model), at the iso-Reynolds number (in the case of the Weber number model) and the iso-density ratio, and are 100% valid only when applied under those conditions. However, it can also be interesting to check how those models behave outside the interpolation range predicting the size distribution at higher Reynolds numbers or lower Weber numbers. With this premise, Figure 7.13 follows the same structure than Figure 7.12, but the Reynolds number swipes from 9,000 to 15,000, and the Weber number from 5,000 to 26,600. Those ranges are selected because the characteristic Reynolds number on most applications is greater than $9,000$, and the Weber number is usually lower than $26,600$.

Regarding the Reynolds number extrapolation, it can be seen that as expected the peak location shifts to lower diameters, from $0.034 \cdot D_n$ at $Re = 9,000$ to $0.27 \cdot D_n$ at $Re = 13,100$ and then, remains constant. When taking into account only the final region of the domain, the same trend is appreciated, converging to the same lowest value, which is reached at $Re = 14,000$. Furthermore, the peak value presents an interesting behaviour as it increases from 18.32 at $Re = 9,000$ to 19.23 at $Re = 11,500$ and then, decreases to 17.70 at $Re = 15,000$, considering the whole domain. Those numbers change to 17.9 at $Re = 9,000$, 19.20 at $Re = 12,000$, and 17.97 at $Re = 15,000$ in the end region. Additionally, the influence of the Reynolds number on droplet sizes greater than $0.1 \cdot D_n$ is nearly negligible. It is worth mentioning that, during the Reynolds study, one of the main features that have been highlighted is that the inflow conditions have not reached the fully developed velocity profile, and that generates particular behaviours on the momentum mixing. Pipe flows exhibit the fully developed velocity profile somewhere between $Re = 12,000$ and $15,000$, so interestingly, the model presents a change in the trends. However, it might be a coincidence that deserves to be analysed in the future.

Moving to the Weber number, it is noticeable that, in contrast with the

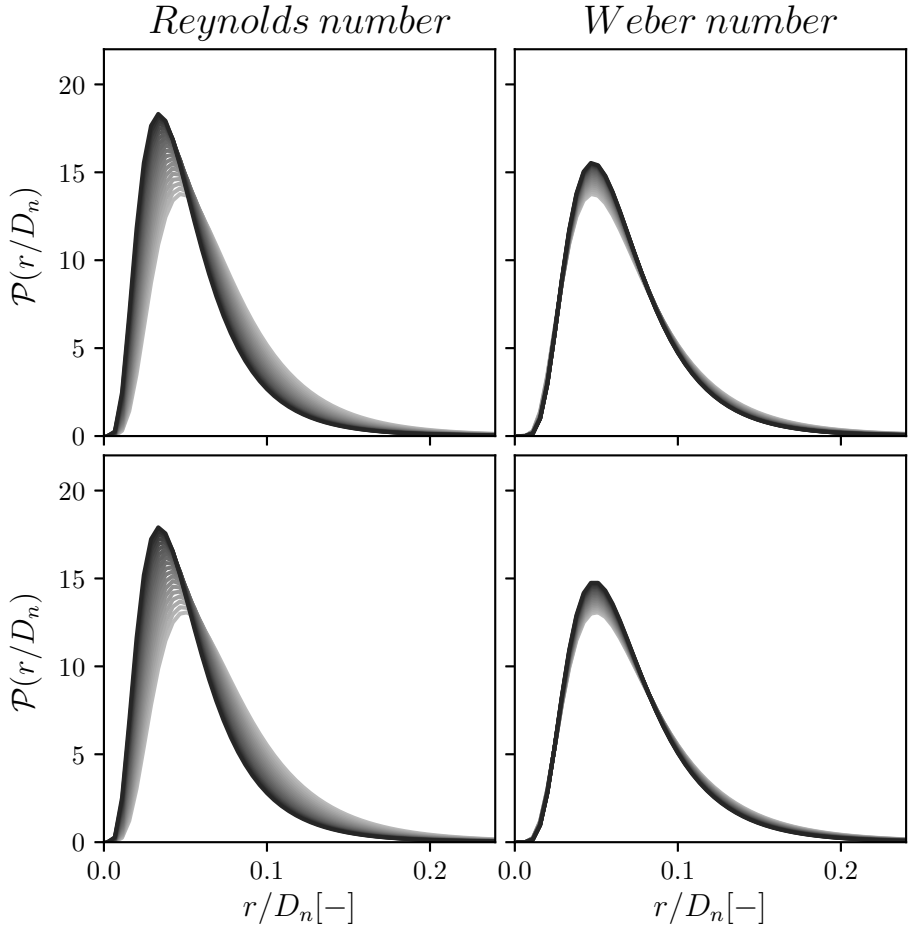

Figure 7.12: PDF of droplet size distribution obtained by interpolating the phenomenological models within the simulated data range. On the left, Reynolds number model from grey Re=5,037 to black Re=9,000. On the right, the Weber number model from grey We=26,600 to black We=90,000. Upper plots correspond to the whole domain, and bottom ones to the end region.

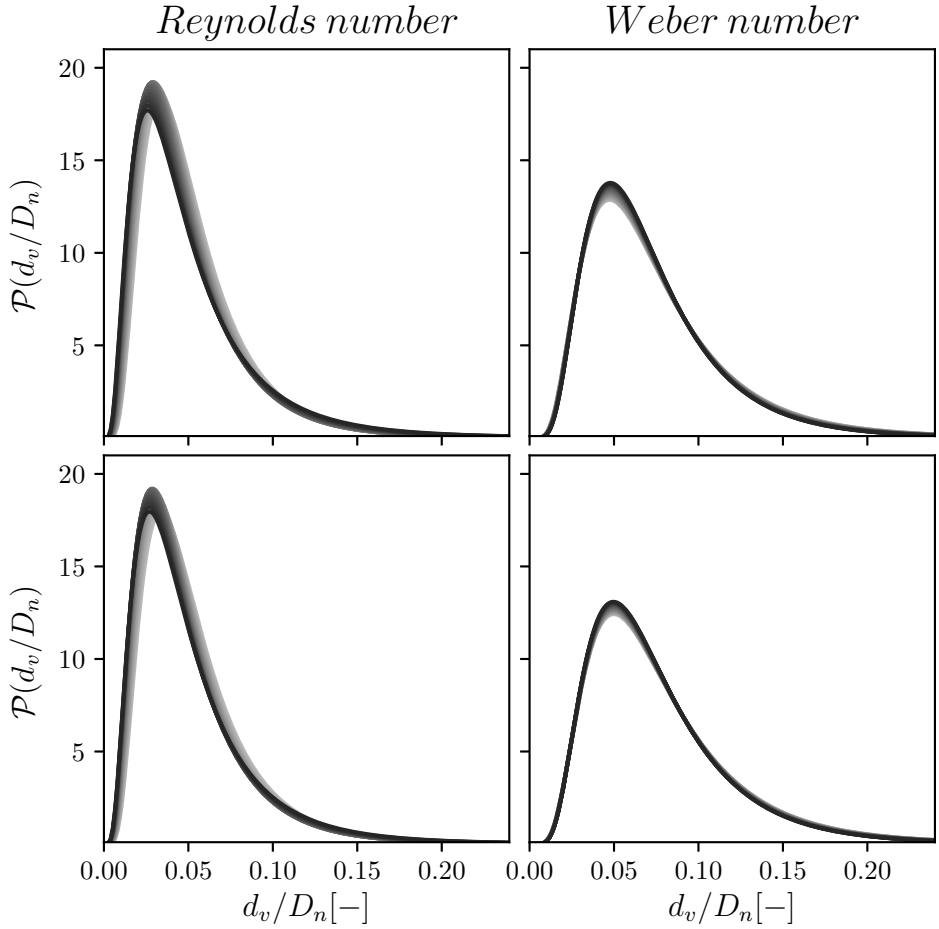

Figure 7.13: PDF of droplet size distribution obtained by extrapolating the phenomenological models outside the simulated data range. On the left, Reynolds number model from grey Re=9,000 to black Re=15,000. On the right, the Weber number model from grey We=5,000 to black We=26,600. Upper plots correspond to the whole domain, and bottom ones to the end region.

Reynolds number model, the extrapolation of the Weber number follows the same trend in the extrapolation range than on the interpolation range. As the Weber number decreases, the peak location remains at the same droplet size, but the value decreases.

Finally, a further step is taken in the extrapolation. The ones presented earlier were done at iso-Weber number in the Reynolds number model and at iso-Reynolds number in the Weber number model. However, a cross extrapolation can be made to extract the droplet size within the Reynolds number interpolated model, but at a different Weber number than the one used to define the model. This extrapolation is made by considering that the effects of the Weber number are constant at different Reynolds number conditions. So, to provide an example, the droplet size distribution will be predicted with an inflow Reynolds number of 6,500 and an inflow Weber number of 50,000. To obtain the $\hat{\mu}$ and $\hat{\sigma}$ of this new condition, first, the $\hat{\mu}$ and $\hat{\sigma}$ are computed for the 6,500 Reynolds number using the Reynolds number model. Then the values are corrected by displacing the Weber number influence of the Weber number model to the preliminary $\hat{\mu}$ and $\hat{\sigma}$. Then the prediction of the final $\hat{\mu}$ and $\hat{\sigma}$ is performed using the Weber number model. Figure 7.14 depicts a scheme of how this cross extrapolation is performed. After applying this procedure, the models provide $\hat{\mu}$ and $\hat{\sigma}$ of 1.57 and 0.50, respectively, for the full domain analysis, and 1.60 and 0.52 when considering only the end region of the domain.

Using the parameters provided by the cross extrapolation method, the droplet size PDF for this new condition is plotted in Figure 7.15, along with the reference case. It can be seen that, as expected, the peak location shifts to lower diameter values (as happens when increasing the Reynolds number), and the ratio between the smaller and bigger droplets increases (here, both models provide similar trends). Even though this assumption is not based on any physical knowledge and may be wrong, it can provide an estimation of the droplet size distributions at injection conditions that are not performed yet.

7.6 Conclusions

This chapter is centred on defining a phenomenological model to predict the droplet size distribution depending on the Reynolds and the Weber number. The first step of this study is finding the correct statistical distribution that fits the computational data obtained. Considering the literature and the preliminary analysis, the Log-normal distribution is chosen, demonstrating its

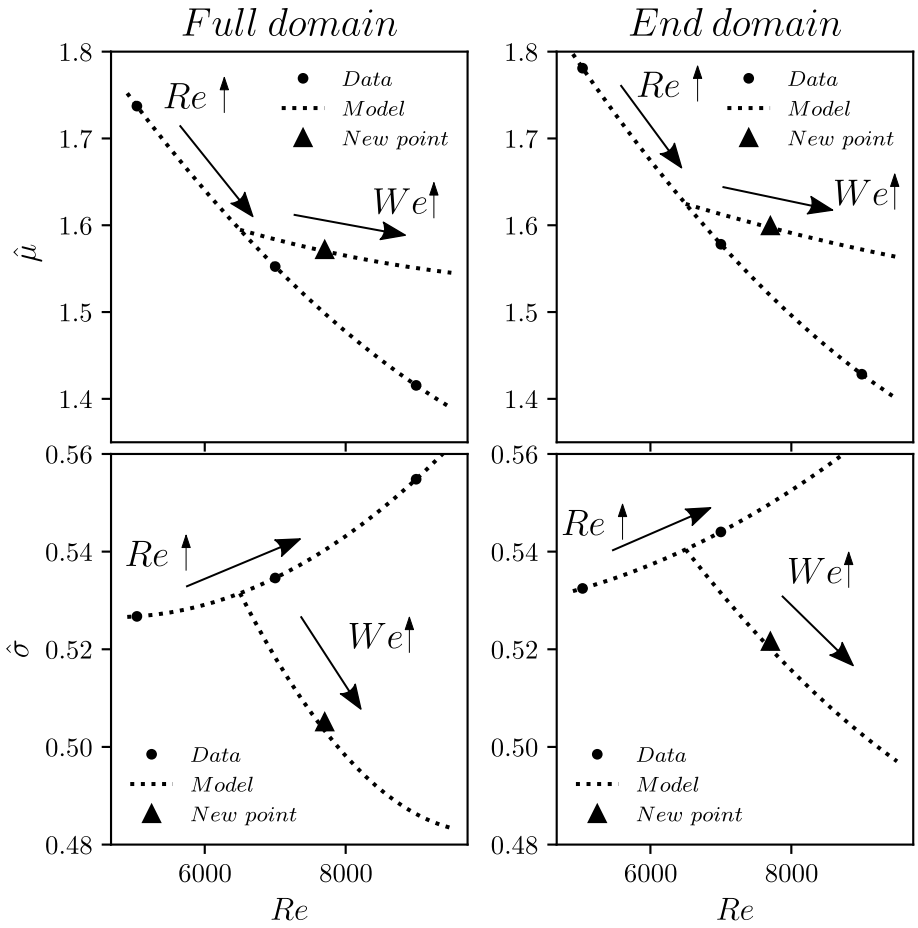

Figure 7.14: Cross extrapolation method to obtain $\hat{\mu}$ and $\hat{\sigma}$ outside the iso-Reynolds and iso-Weber number restrictions. ▲ corresponds to inflow conditions of $Re = 6,500$ and $We = 50,000$. Left plots correspond to the whole domain, and right plots to the end region.

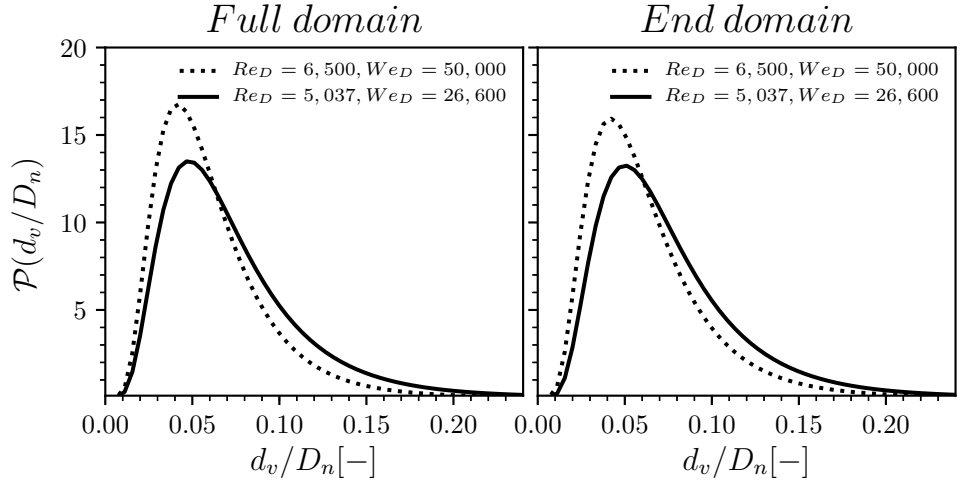

Figure 7.15: PDFs of droplet sizes predicted with the cross extrapolation method compared to the reference case. The left plot correspond to the whole domain, and the right plot to the end region.

capability to predict the droplet size distribution. The Log-normal distribution is defined by two parameters: the $\hat{\mu}$ and $\hat{\sigma}$, which are used to define the phenomenological model. So those parameters are calculated for all simulations presented on the Reynolds number and the Weber number studies. Furthermore, this fit is performed on the whole simulation domain and on the last region of the spray, where the atomization process is more developed.

A characteristic pattern can be noticed when comparing the fitted distribution with the PDF of size distribution provided by the DNS simulations. The peaks of all PDF distributions are located at $2{\cdot}d_x$. So, the mesh refinement affects the droplet breakup when the droplets have comparable sizes to the cell size, leading to an overestimation of droplets with $d_v \approx 2 \cdot d_x$, and an underestimation of smaller droplets. Although this numerical issue is present in all simulations, the overall behaviour of the breakup process of the primary atomization is well-resolved as the overall distributions present a very well agreement in all cases. When expressing the probability on a logarithmic scale, the peak discrepancies are diluted, and the agreement is almost perfect.

After finding the fitting parameters to the computed droplet size distributions, a regression is proposed for the $\hat{\mu}$ and $\hat{\sigma}$ composing the phenomenological model. As a result, two models are formulated to predict how the droplet distributions are affected when modifying the injection conditions.

Finally, the limits of the models are tested by extrapolating the injection

conditions beyond the simulated conditions to check the behaviour in extreme conditions. The quadratic regressions are chosen to define the models that lead to a characteristic behaviour, especially in the Reynolds number study that coincides with the conditions where the internal flow reaches the fully developed velocity profile. On the other hand, the Weber number extrapolation follows similar trends and on the interpolation range.

References

[1] Gorokhovski, Mikhael and Herrmann, Marcus. "Modeling Primary Atomization". In: *Annual Review of Fluid Mechanics* 40.1 (2008), pp. 343–366. DOI: 10.1146/annurev.fluid.40.111406.102200.

[2] Kolmogorov, A. "On the log-normal distribution of particles sizes during breakup process". In: *Dokl. Akad. Nauk.* XXXI.4 (1941), pp. 99–101.

[3] Ling, Yue, Fuster, Daniel, Zaleski, Stéphane, and Tryggvason, Grétar. "Spray formation in a quasiplanar gas-liquid mixing layer at moderate density ratios: A numerical closeup". In: *Physical Review Fluids* 2.1 (2017), p. 014005. DOI: 10.1103/PhysRevFluids.2.014005.

[4] Zhang, Bo, Popinet, Stephane, and Ling, Yue. "Modeling and detailed numerical simulation of the primary breakup of a gasoline surrogate jet under non-evaporative operating conditions". In: *International Journal of Multiphase Flow* 130 (2020), p. 103362. DOI: 10.1016/j.ijmultiphaseflow.2020.103362.

[5] Sotolongo-Costa, Oscar, Moreno-Vega, Yamir, Lloveras-González, Juan J., and Antoranz, J. C. "Criticality in Droplet Fragmentation". In: *Physical Review Letters* 76.1 (1996), pp. 42–45. DOI: 10.1103/PhysRevLett.76.42.

[6] Chehroudi, B and Talley, D. "The fractal geometry of round turbulent cryogenic Nitrogen jets at subcritical and supercritical pressures". In: *Atomization and Sprays* 14.1 (2004), pp. 81–91. DOI: 10.1615/AtomizSpr.v14.i1.50.

Chapter 8

The Influence of nozzle shape

8.1 Introduction

Throughout the document, the emphasis has been put on the influence of the main non-dimensional numbers on the spray development. However, there are still some variables that can modify the spray behaviour. Among them, this chapter puts the spotlight on the nozzle geometry as it varies the injected turbulent distribution. This analysis is performed by simulating two different elliptical sprays under similar injection conditions from the reference simulation already presented in Chapters 5 and 6.

As introduced in Chapter 3, the inflow conditions have been set to match the mass flow rate with the reference simulation by maintaining the bulk velocity, the liquid properties and the injection area. Table 8.1 shows the geometrical parameters of the elliptical nozzles already presented in the boundary conditions study. Additionally, Figure 8.1 also show the cross-section from the elliptical nozzles used.

Regarding the numerical setup, as the bulk velocity is maintained and the higher Reynolds number corresponds to the reference round case, both the cell size and the timestep are maintained in both elliptical configurations and are expected to have a good turbulence resolution. Additionally, the domain of the elliptical configurations has been enlarged on the major axis direction to ensure that all transitional vortex structures are closed within. Table 8.2 sums up all the significant simulation parameters for all cases considered.

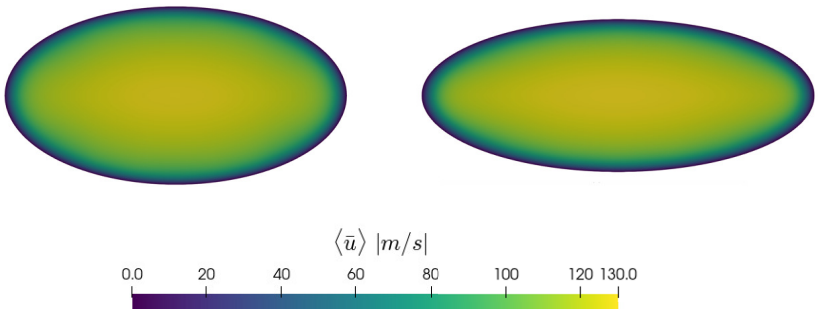

Figure 8.1: Cross section of the elliptical nozzle shapes used, left $e = 0.85$ and right $e = 0.92$.

Table 8.1: Geometric parameters of the elliptical ducts

e	0.85	0.92
a [µm]	63.32	72.65
b [µm]	32.82	28.12
D_h [µm]	84.30	77.28
Re	4,718	4,325

Table 8.2: Simulation parameters for the nozzle shape study

Eccentricity factor	e [-]	0	0.85	0.92
x - length	l_x [mm]	2.4	2.4	2.4
y/z - length	l_y, l_z [mm]	1.2 x 1.2	1.8 x 1.2	1.8 x 1.2
Cell size	d_x [µm]	2.34	2.34	2.34
Timestep	d_t [ns]	4	4	4
Number of cells	N_{cells} [-]	$268 \cdot 10^6$	$402 \cdot 10^6$	$402 \cdot 10^6$

The results will be analysed following the same structure as in previous chapters. As the elliptical spray does not present an axi-symmetric behaviour, the results will be mainly expressed in the directions of both the major and the minor semiaxis and on their transversal distribution when possible. The first analysis will be qualitative and focus on the spray's morphology, emphasising the core perturbations. Then the flow field is studied by the centreline distributions and the spray aperture along the axial direction. Also, a turbulent study on a plane located at $x/D_n = 25$. Finally, the droplet cloud is analysed, centring on the droplet size and position distribution. All those results will be studied considering the secondary flows that emerge on non-axi-symmetric ducts and will affect the spray development, mainly in the transverse direction. Additionally, it is worth mentioning that, when analysing the results, the $e = 0$ case will be referred as the round case or reference case, the $e = 0.85$, will be the lower eccentric case, and the $e = 0.92$ will be named as the highest eccentric case.

8.2 Spray morphology study

To start analysing the effect of the nozzle shape on the spray development, a qualitative approach is followed to observe their morphology. Just like in previous studies, snapshots of both the transient and the steady state phase are considered, and the spray is represented as an iso-surface with $C_{th} = 0.05$.

Beginning with the transient state, Figure 8.2 shows a snapshot corresponding to $T = 12.5\mu s$ for all cases, from top to bottom as the eccentricity factor increases. Regarding the elliptical cases, the left view corresponds to the XZ plane, perpendicular to the minor axis perspective, while the right view is the perspective from the end of the domain, plane ZY. In these snapshots, all cases present the same penetration and a slightly decreasing spray aperture as the eccentricity factor increases. Focusing on the view perpendicular to the axial direction, the spray tip can be seen as the continuous smoother surface visible. This surface, and thus the mushroom tip, decreases as the eccentricity factor of the nozzle increases, meaning that the interaction between the liquid and the gas in this region is heavier in the most eccentric case.

Moving to the steady state, the following snapshots are taken at $T = 150\mu s$ to ensure that the sprays are fully developed. Additionally, as the elliptical sprays are not axi-symmetric, two views are chosen, one perpendicular to the major axis (plane XY) and another to the minor axis (plane XZ). So Figure 8.3 shows the view perpendicular to the major axis for all geometries, again, sorted from top to bottom as the eccentricity factor increases. Focusing on

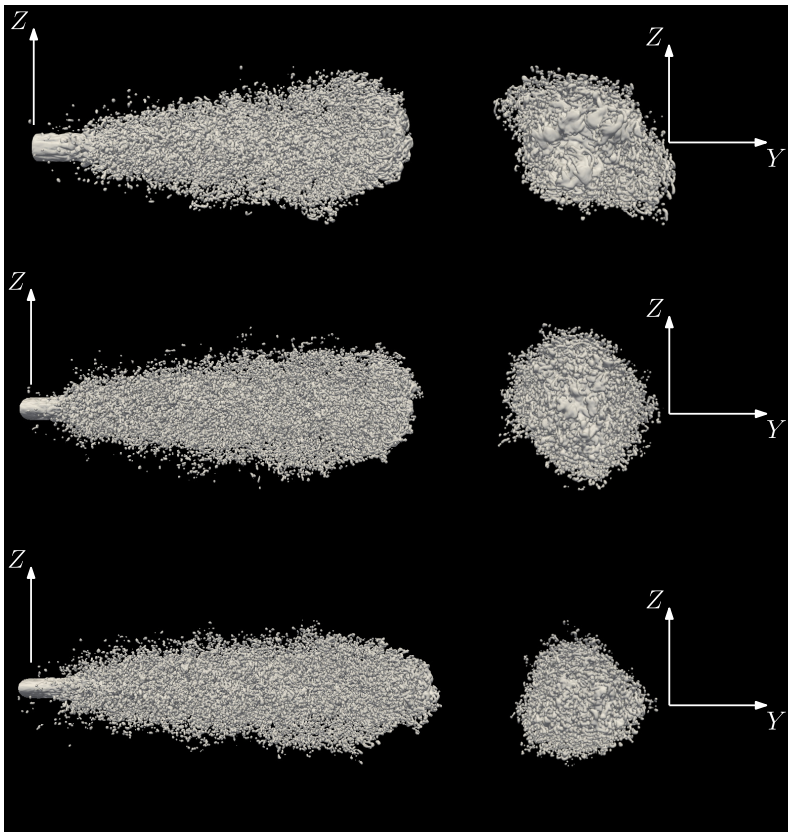

Figure 8.2: Spray morphology during the transient state at $T = 12.5$ μs. Increasing the eccentricity factor from top to bottom.

the liquid core near the nozzle outlet, it can be noticed that the atomisation starts earlier on the elliptical geometries than on the round case. Looking at the droplet cloud, it can be seen that the droplets seem finer when using an elliptical nozzle, but there are not many differences between eccentricities. The spray aperture in this axis also seems similar in all cases, but the round spray exhibits a higher amount of droplets located 'outside' the spray cone.

On the other hand, Figure 8.4 shows the view perpendicular to the minor axis, following the same structure as Figure 8.3. In this case, similar observations can be made on the core breakup. However, although the spray angle seems comparable, the spray aperture on the most developed region of the spray is appreciably lower in the elliptical cases.

To be able to compare the spray morphology along both the minor axis and the major axis perspective, Figure 8.5 shows both elliptical perspectives

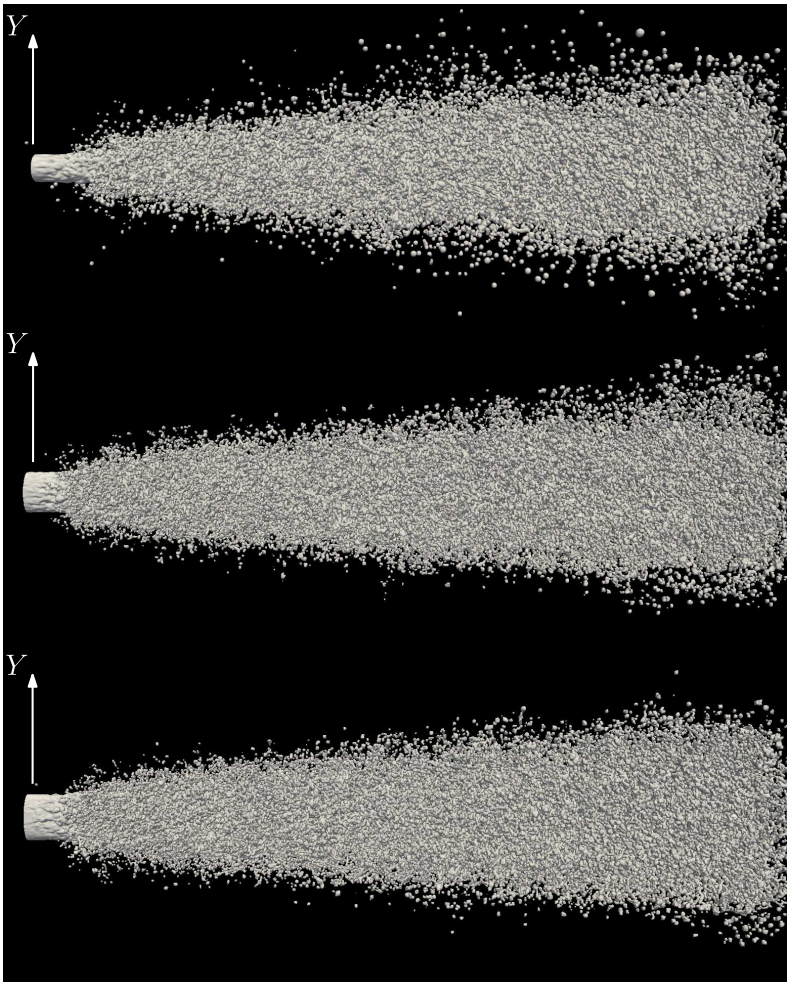

Figure 8.3: Spray morphology during the statistically stationary state at T = 150 μs, taken perpendicular to the major axis. Increasing the eccentricity factor from top to bottom.

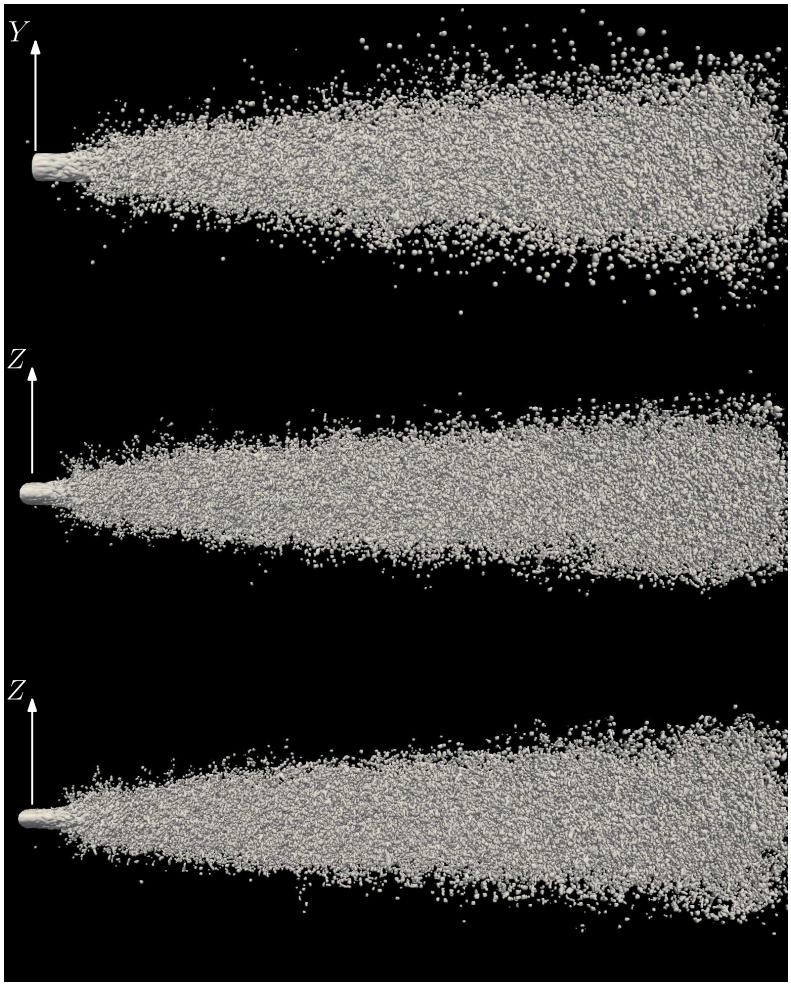

Figure 8.4: Spray morphology during the statistically stationary state at T = 150 μs, taken perpendicular to the minor axis. Increasing the eccentricity factor from top to bottom.

presented in Figures 8.3 and 8.4 merged in only one snapshot. Again top spray corresponds to the medium eccentric case ($e = 0.85$) and the bottom one to the highest eccentricity factor ($e = 0.92$). Each case is split in two: the upper perspective perpendicular to the major axis and the lower perspective perpendicular to the minor axis.

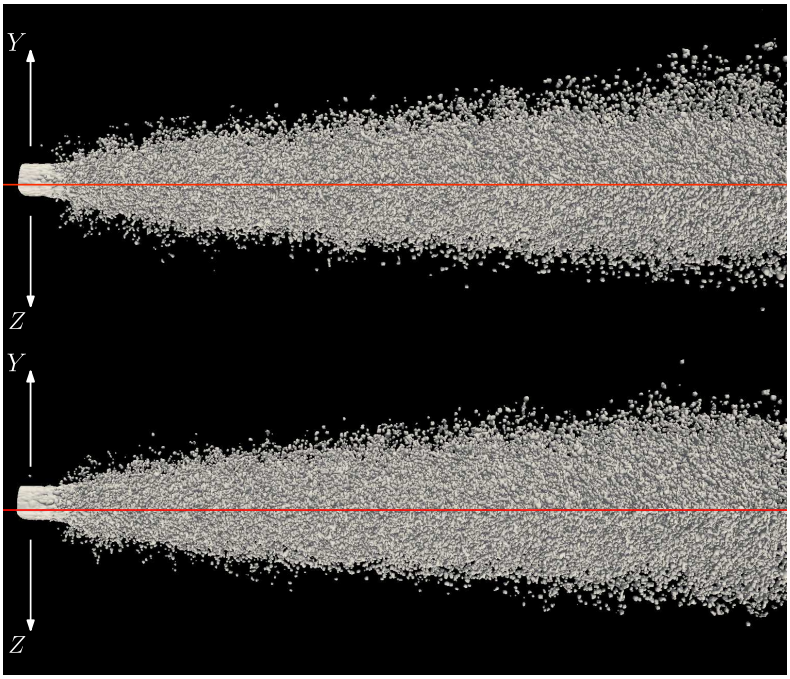

Figure 8.5: Comparison between the apertures perpendicular to the major axis on the top half of each spray and the minor axis on the bottom half. Increasing the eccentricity factor from top to bottom.

Like in previous chapters, observing the core surface hints at how the inflow turbulence affects the subsequent liquid breakup. In this case, Figure 8.6 depicts a zoom of the first microns of the spray core, isolated from the droplet cloud, from left to right as the eccentricity factor increases. The core is represented as an iso-surface with $C_{th} = 0.95$. Here, the external intact length exhibits characteristic behaviours as the eccentricity factor increases. Focusing on the elliptical cases, the minor eccentric nozzle shows higher perturbations near the minor axis while in the major axis presents lower perturbations. This is accentuated when looking at the most eccentric nozzle, where the core breakup starts earlier near the minor axis plane than on the major axis. This is coherent with how the vortex structures are arranged within the internal

flow on the elliptical nozzles already seen in Chapter 3, which showed that the turbulence is located on the top and on the bottom of the nozzle.

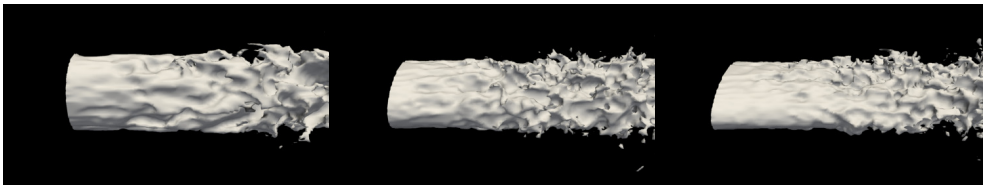

Figure 8.6: Spray core extracted from the full spray at $T = 150$ μs. Increasing the eccentricity factor from left to right.

8.3 Flow field analysis

In this section, the flow field is analysed in terms of centreline statistics, spray aperture, and the statistics on a plane located at $x/D_n = 25$.

8.3.1 Centreline statistics

This subsection is focused on the centreline of the spray. Unfortunately, there is no high frequency sampled statistics of the centreline on the elliptical sprays. So the centreline values are obtained by the temporal average of the domain snapshots. Although those results are rougher than the ones obtained directly with centreline sampling (as in Chapters 5 and 6), they will help to extract interesting information.

In these terms, Figure 8.7 depicts the axial velocity of the centreline for all tested geometries. In order to represent the deviation between the centreline results computed with specific outputs and with the domain snapshots, the round case is plotted two times, being the smoother line than the one obtained with the centreline output. It can be seen that, although the domain results are relatively rougher, the overall trend is well captured, so the comparison between cases will be, at least, qualitatively valid. Moving to the proper comparison, the centreline velocity distribution is practically the same up to around 1.2 mm, and then the elliptical cases present slightly lower values. Those differences coincide with the two different trends that have been already observed in previous studies. So the first section, near the nozzle, exhibits the same slope in all cases, but the next one presents steeper slopes in the elliptical cases. In the end, the elliptical cases do not show enough high discrepancies to be detected without having a well-temporal averaged distribution.

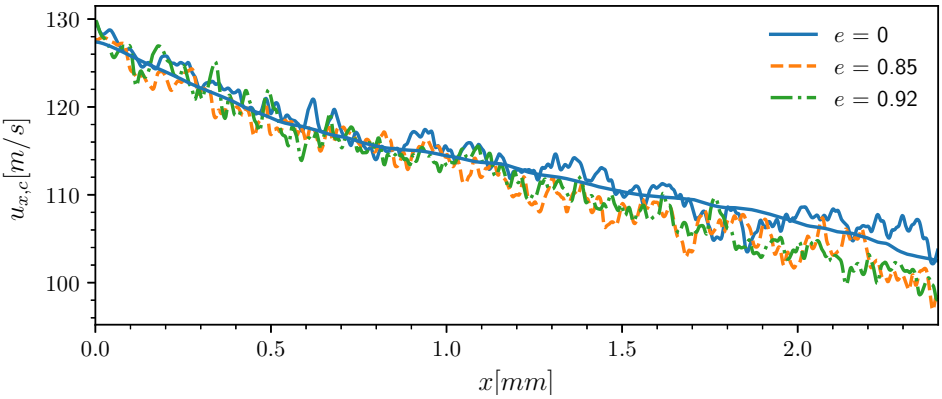

Figure 8.7: Axial distribution of the centreline axial velocity, u_x, for all nozzle geometries.

The same procedure is followed to study the liquid volume fraction distribution along the centreline, as can be observed in Figure 8.8. Here is a noticeable difference in the axial distance where the liquid fraction drops below 1 between the results obtained using the centreline and the domain outputs. However, although the breakup length (i.e. the axial distance for which $\langle C \rangle$ drops below 1) obtained from the domain outputs is higher than that obtained from the centreline results, both cases collapse at higher axial distances. Regarding the elliptical cases, the liquid volume fraction seems agreeing with the round case at axial positions higher than 1 mm. However, right near the nozzle, the elliptical cases drop from 1 at earlier distances. Additionally, the highest eccentric case presents liquid volume fractions lower than 1 at lower axial distances. However, it can be stated that the breakup length decreases with the eccentricity factor as the distributions are not smooth enough.

Finally, the mass concentration is computed based on the liquid volume fraction and plotted in Figure 8.9. The same conclusions can be extracted for the mass concentration as in the liquid volume fraction. The trends far from the nozzle exit are practically the same, being all cases superposed. On the other hand, near the nozzle exit is required a zoom-in to determine the axial position where the mass concentration drops below the unity. Again, it seems to depend on the eccentricity factor, reducing the breakup length as the eccentricity factor increases. Nevertheless, smoother distributions are required to compute this length correctly.

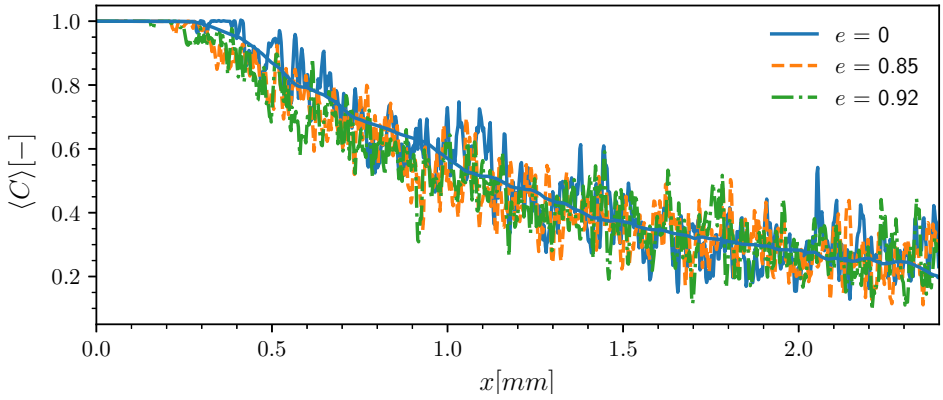

Figure 8.8: Axial distribution of the centreline liquid volume fraction, C, for all nozzle geometries.

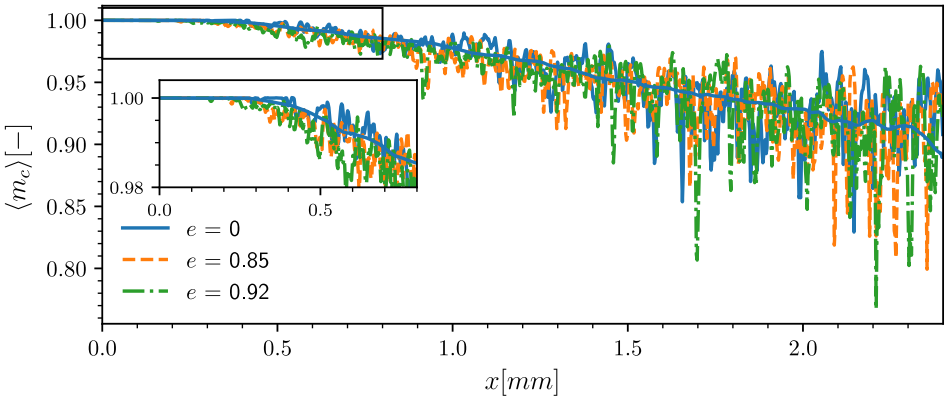

Figure 8.9: Axial distribution of the centreline mass concentration, m_c, for all nozzle geometries.

8.3.2 Axial distributions

Once the centreline statistics have been analysed, the spray aperture provides useful information about how the spray interacts with the surrounding ambient. This spray aperture can be studied based on the velocity or liquid field and imposing different criteria. Here, the axial velocity, the liquid volume fraction and mass concentration are taken into account so that, setting an axial position, the decay of those flow fields along the radial direction (for the round case) and the transversal direction (for the elliptical case) is analysed. Finally, to determine the spray aperture in each axial position, a threshold is set as a proportion of the centreline value of that flow field on that axial posi-

tion. So, $r_{1/2}$ corresponds to the distance to the spray axis where the flow field drops below the 50% of the centreline value, and $r_{0.01}$ sets the threshold where the flow field drops below 1%. It is worth mentioning that the round spray aperture can be collapsed in one radial profile, as its axi-symmetric behaviour allows it to perform an azimuthal direction. Nevertheless, as the elliptical sprays present two main directions (aligned with the major and minor axis), two different aperture profiles will be studied, one for each direction.

The first criterion analysed is the $r_{1/2}$ corresponding to the axial velocity field. Figure 8.10 depicts the spray aperture using the $r_{1/2}$ criterion for all configurations. It can be noticed that the elliptical cases present two different apertures; the upper one corresponds to the major axis plane, while the lower one refers to the minor axis plane. Although the elliptical cases show early discrepancies near the nozzle, caused by the differences in the nozzle geometry, at axial distances greater than 0.5 mm both elliptical sprays show similar aperture on both the major and the minor axis. Additionally, the round case presents aperture values between the major and minor apertures from the elliptical cases, almost their average values. So, when computing the half spray aperture angles $\theta_{r_{1/2}}$ the obtained values are 3.84° for the round spray case; 3.24° and 4.20° for the minor and major axis, respectively, on the $e = 0.85$ case; and 3.87° and 3.65° for minor and major axis of the most eccentric case.

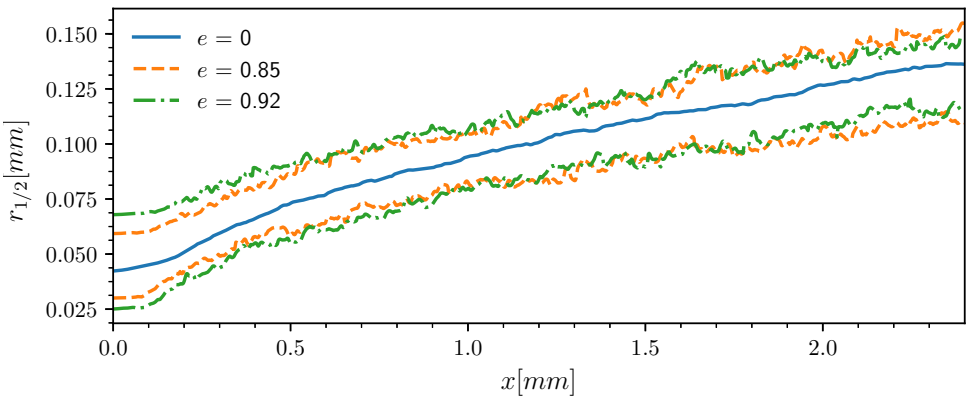

Figure 8.10: Axial distribution of $r_{1/2}$ for all nozzle shapes.

Following the same procedure but using the $r_{0.01}$ criterion on the axial velocity field leads to the distributions plotted in Figure 8.11. As seen in the previous chapters, the velocity profile relaxation leads to a particular behaviour near the nozzle between 0.1 - 0.3 mm, where the spray aperture steeply increases and then is adapted to a more linear trend. This feature is also observed in the elliptical cases in both directions. As on the $r_{1/2}$ aperture, the

round case presents intermediate values between the major and minor axes on both elliptical configurations. Furthermore, the only main difference between the elliptical cases is the higher aperture detected in the last 0.4 mm in the lower eccentric case ($e = 0.85$) which presents a higher aperture on the major axis direction. Note that the spray apertures are computed using the centreline values so if the centreline distribution presents a noisy profile, it can be translated to the aperture computation. As expected, the spray apertures are higher than the ones obtained by using $r_{1/2}$ criteria, and the half spray angle aperture $\theta_{r_{0.01}}$ values are 10.61° for the round case; 9.36° and 12.25° for the minor axis and major axis direction, respectively, for the less eccentric case ($e = 0.85$); and 10.21° and 10.20° for the most eccentric nozzle.

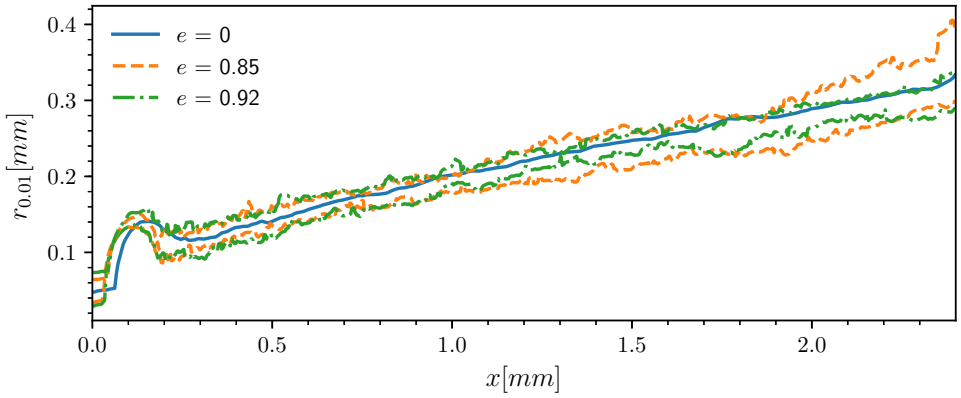

Figure 8.11: Axial distribution of $r_{0.01}$ for all tested nozzles.

Moving to the aperture computed with the liquid field, the first approach is performed by computing the $r_{0.01,C}$ on the liquid volume fraction, as shown in Figure 8.12. The first thing to notice when analysing the liquid volume fraction aperture is the high noise level that presents the axial distribution of $r_{0.01,C}$, especially in the elliptical cases. The elliptic sprays near the nozzle present an earlier aperture than the round case. Nevertheless, as the axial distance increases, the round spray aperture presents a higher slope, resulting in higher aperture values than both axes from the elliptical sprays at the end of the domain. Additionally, the distance where the spray starts opening is lower in the elliptical cases in both directions than in the round spray. When comparing the main directions of the elliptical cases, the roughness of the distributions prevents the extraction of clear conclusions. This behaviour leads to half spray aperture angles $\theta_{r_{0.01,C}}$ of 14.69° on the round spray; 9.25° and 12.03° for the minor and major axis direction on the less eccentric case;

and 10.38° and 10.28° for the minor and major axis, respectively, on the most eccentric case.

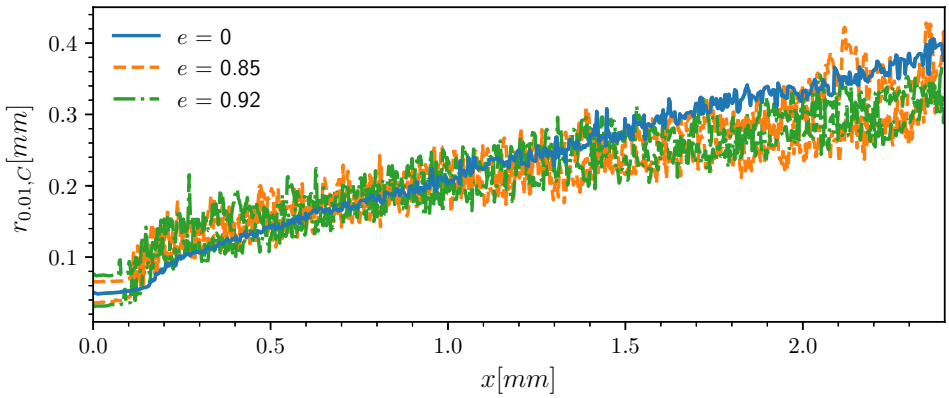

Figure 8.12: Axial distribution of $r_{0.01,C}$ for all nozzle shapes.

Finally, the mass concentration is computed for both the $r_{1/2,m_c}$ and the $r_{0.01,m_c}$ criteria. So, Figure 8.13 depicts the mass concentration aperture using the $r_{1/2,m_c}$ criterion along the axial distance. On the first microns of the spray, it can be seen an adaptation of the mass concentration field where values are almost constant for all cases, and at 200 µm, the spray aperture occurs. Concerning the elliptical cases, it can be noticed that both axes tend to collapse into a single trend, and the eccentricity factor does not affect the spray aperture. Moreover, both the values and the spray aperture angle exhibited by the elliptical sprays are higher than the one presented by the round spray. Specifically, the half spray aperture angle $\theta_{r_{1/2,m_c}}$ is 5.20° for the round case and around 10° for both axis on the elliptical cases.

Then, Figure 8.14 represents the mass concentration aperture computed through the $r_{0.01,m_c}$. It can be appreciated that obtaining the spray aperture using the mass concentration cleans up the distributions compared to Figure 8.12, so the differences between the round and the elliptical sprays are more noticeable. Here, the higher spray aperture angle of the round spray is evident, and the apertures of the elliptical cases collapse into a narrower band, being hard to read the differences between directions and cases. However, the half spray aperture angles obtained, $\theta_{r_{0.01,m_c}}$ are 15.56° on the round nozzle case; 8.68° and 11.83° for the minor and major axis direction, respectively for the less eccentric geometry; and 9.95° and 9.80° for the minor and major axis direction, respectively on the most eccentric case. Comparing these results with those obtained using the $r_{1/2,m_c}$ criterion, a trend change can be spotted

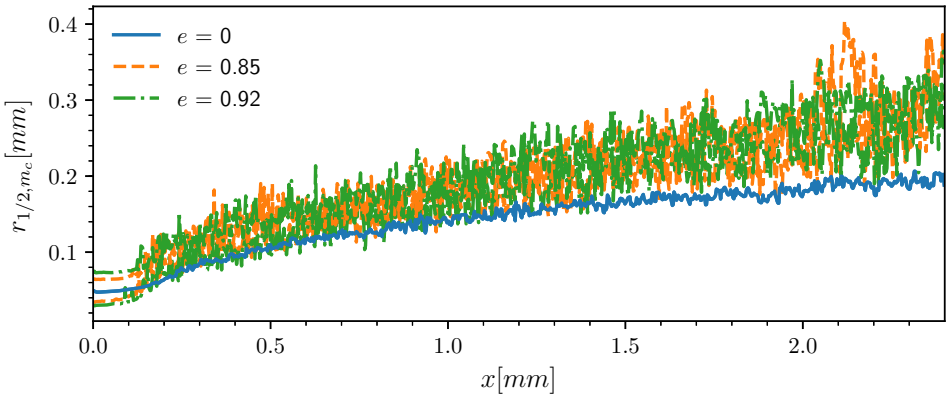

Figure 8.13: Axial distribution of $r_{1/2,m_c}$ for all nozzle geometries.

as the round case presents a higher aperture than the elliptical cases. This is linked with the behaviour seen in Figures 8.3 and 8.4 from the morphology study, where the droplet cloud from the round case presented a higher number of satellite drops than in the elliptical cases where the majority of the drops are located inside the spray cone. This affects the $r_{0.01,m_c}$ calculation, increasing the spray angle for the round case.

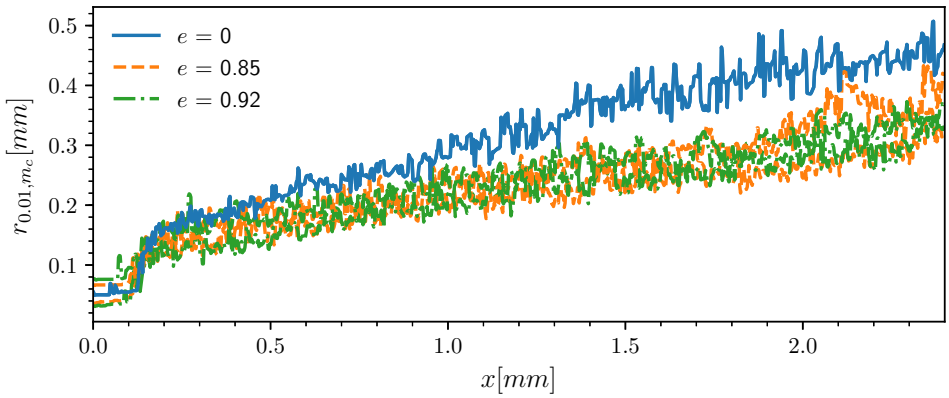

Figure 8.14: Axial distribution of $r_{0.01,m_c}$ for all nozzle geometries.

8.3.3 Plane statistics

Finally, the last analysis of the flow field is focused on a plane located at 2.23 mm. This location corresponds to an $x/D_n \approx 25$ of the round jet case; thus, the flow behaviour should be self-similar. The study will focus on the

axial velocity and the liquid field, and the Kolmogorov scale will be computed. Moreover, in contrast with the previous studies where all the plane information could be collapsed into their radial profiles, the elliptical cases require different results to provide the complete information. To do so, apart from plotting the flow statistics along the major and the minor axis directions, the transversal information will be exposed by the contours of the temporal average fields.

The first field to study is the axial velocity component. Figure 8.15 depicts the axial velocity component contours for all geometries. A spatial average has been performed to reduce the information into a single quadrant to achieve smoother results. It can be seen that the round spray presents a clear axi-symmetric axial velocity field, whereas the elliptical cases present a higher aperture on the major axis than on the minor axis, leading to an elliptical velocity field. Regarding the comparison between geometries, the elliptical cases present higher velocity apertures on the major axis than the round case, while the aperture on the minor axis is slightly lower.

Apart from the transversal plane, the velocity profile is also analysed to check if the elliptical cases present Gaussian behaviour on the axial velocity profile as on the round spray. In Figure 8.16 are depicted, the velocity profiles along the major (left plot) and minor (right plot) axes along with the Gaussian behaviour and the radial profile of the axial velocity component from the round case. The velocity profile is made non-dimensional by dividing by the centreline velocity, and the distance to the axis is also divided by the $r_{1/2}$ computed in each axis in the elliptical cases. Centring on the major axis on the left plot, it can be seen that both elliptical cases do not exhibit a Gaussian behaviour, as they present higher values at positions lower than $r_{1/2}$ and lower values at higher distances. On the other hand, on the minor axis, the velocity decay up to a radial distance around $r_{1/2}$ is very similar to the Gaussian behaviour. However, at higher distances, the values are higher.

Moving to the liquid field, Figure 8.17 presents the transversal distribution of the liquid volume fraction on the plane for all cases. Again, all the information is collapsed into one single quadrant to smooth the average. Just like in the axial velocity field, the round case presents the same aperture along the azimuthal direction, while the elliptical cases exhibit a higher aperture along the major axis direction than on the minor axis direction. Focusing on the elliptical cases, no other differences are noticed. The liquid displays lower apertures in the transversal directions than the velocity apertures.

Figure 8.18 depicts the liquid volume fraction along the minor and the major axis for the elliptical cases along with the radial profile from the round spray, the distance from the spray axis is made dimensionless by dividing by

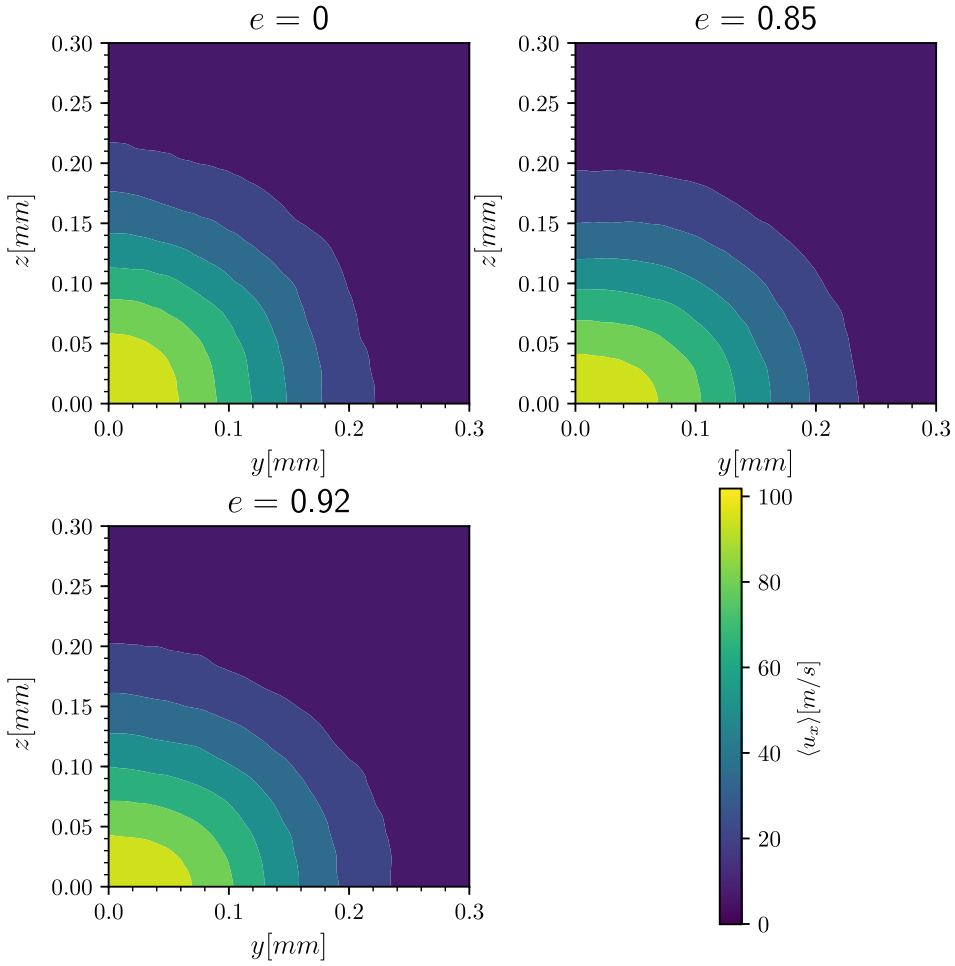

Figure 8.15: Transversal axial velocity field distribution, collapsed into a single quadrant, for all studied conditions.

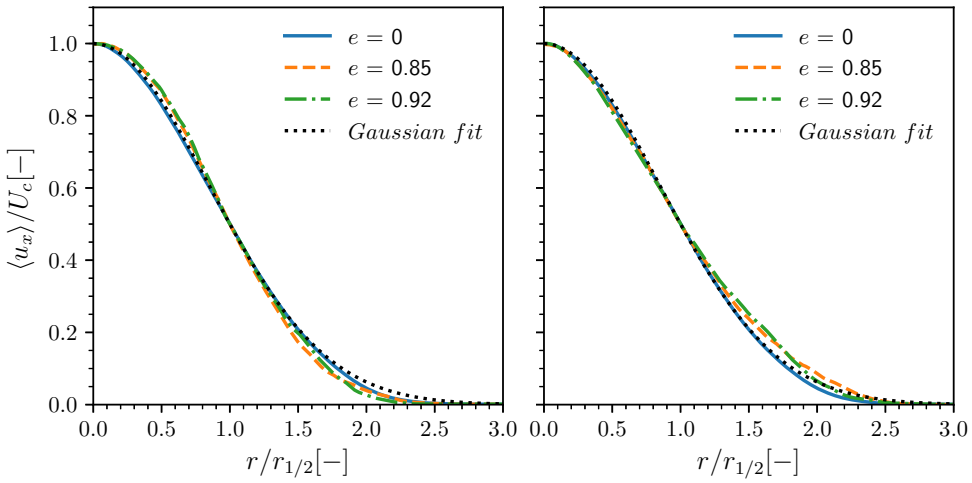

Figure 8.16: Self-similar profile of the non-dimensional axial velocity along: left, the major axis direction, and right the minor axis direction. All distances are made dimensionless with $r_{1/2}$.

the $r_{1/2}$, computed with the axial velocity profile and refers to the mixing region of the spray. The left plot corresponds to the major axis direction, and the right plot to the minor axis direction. As expected, there is no Gaussian behaviour in any of the directions as it decays rapidly near the spray axis. Starting with the major axis profile, two clear trends can be seen: first, for transversal positions lower than $r_{1/2}$, the elliptical cases present higher liquid volume concentration than the round case, whilst at higher distances, the trend inverts exhibiting the round spray higher values spreading further on the spray axis. This means that, proportionally, the round case advects more liquid farther the mixing region. However, as seen in Figures 8.10 and 8.17, the elliptical cases show a higher aperture on the major axis direction than the round spray. Regarding the minor axis, the liquid volume fraction profile presents better agreement between the round and the elliptical cases.

The liquid distribution is expected to have the Gaussian distribution when using the mass concentration instead. Figure 8.19 shows the mass concentration profiles, just as did in Figure 8.18, using $r_{1/2}$ to make non-dimensionless the distance to the spray axis and plotting on the left the major axis direction profile and on the right the minor axis one. Both plots agree on the Gaussian behaviour up to $r_{1/2}$. However, the elliptical cases exhibit a steeper drop at higher distances, even though the agreement is slightly better on the minor axis direction.

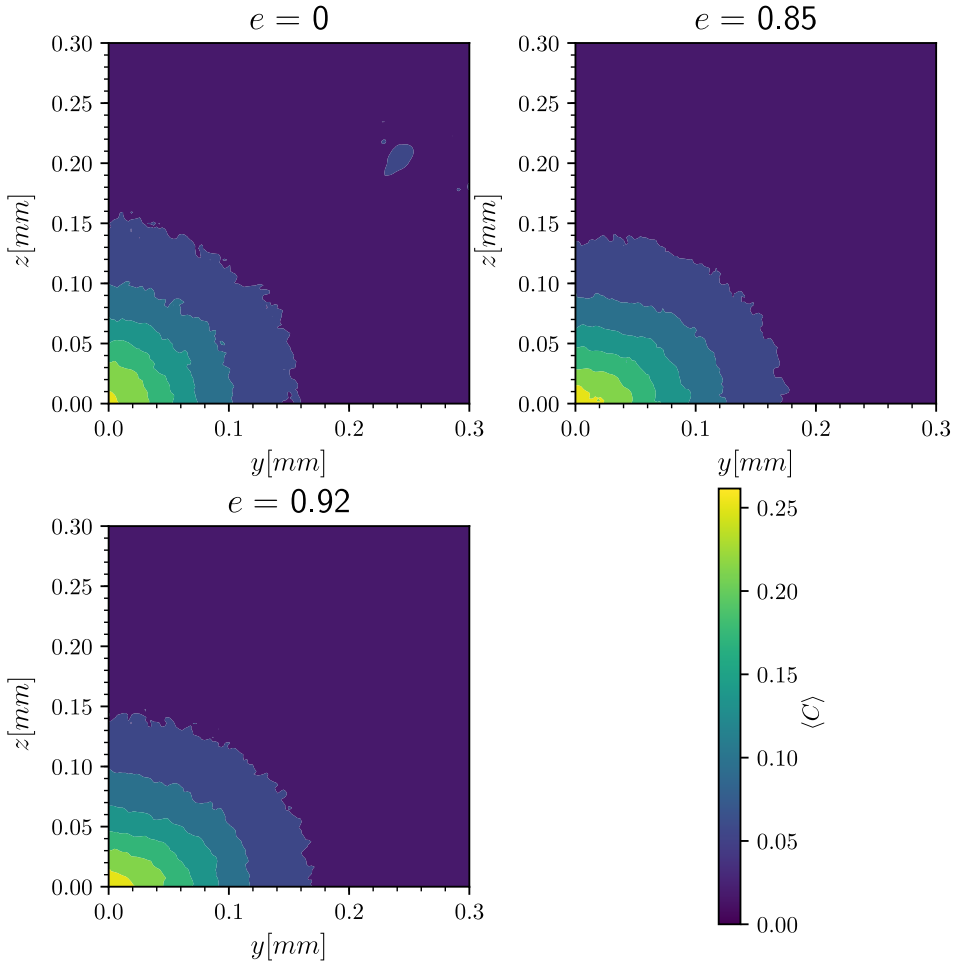

Figure 8.17: Transversal liquid volume fraction field distribution, collapsed into a single quadrant, for all nozzle configurations.

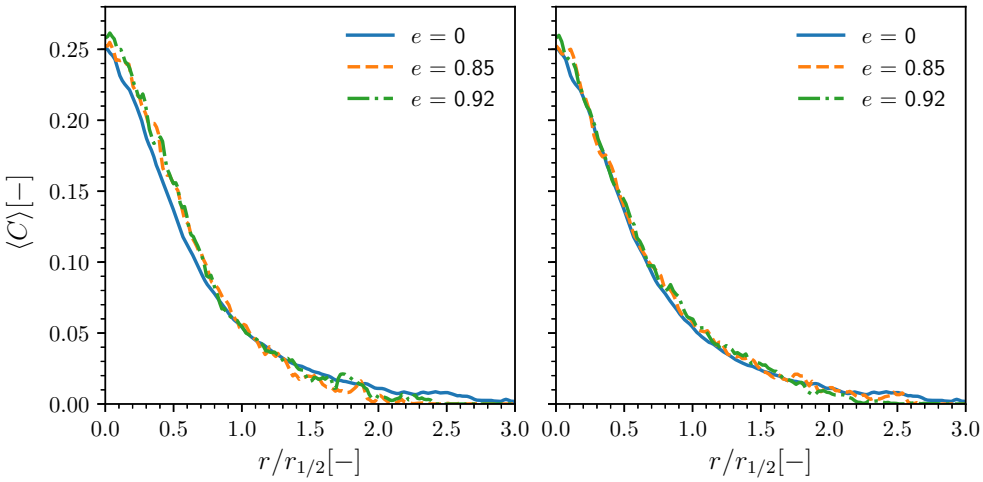

Figure 8.18: Liquid volume fraction profile along: left, the major axis direction, and right the minor axis direction. All distances are made dimensionless with $r_{1/2}$.

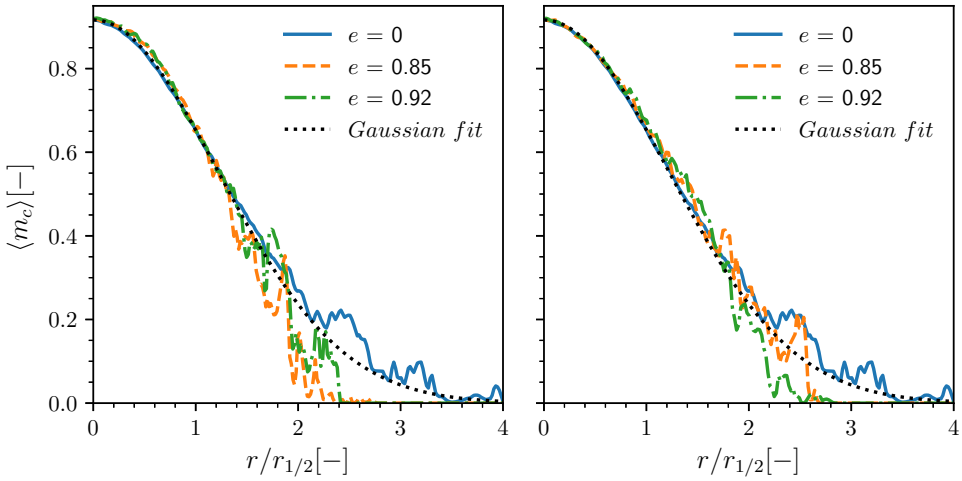

Figure 8.19: Self-similar profile of the mass concentration along: left, the major axis direction, and right the minor axis direction. All distances are made dimensionless with $r_{1/2}$.

Finally, the last field to analyse the plane is the Kolmogorov scale η to assess the quality of the computations. First of all, Figure 8.20 depicts the transversal field of the η, computed with the mean viscosity field and the strain tensor s_{ij}. Focusing on the lowest values, it can be noticed that the round spray presents an axi-symmetric distribution. In contrast, the elliptical cases present the minimums at similar distances on the major axis and lower distances on the minor axis.

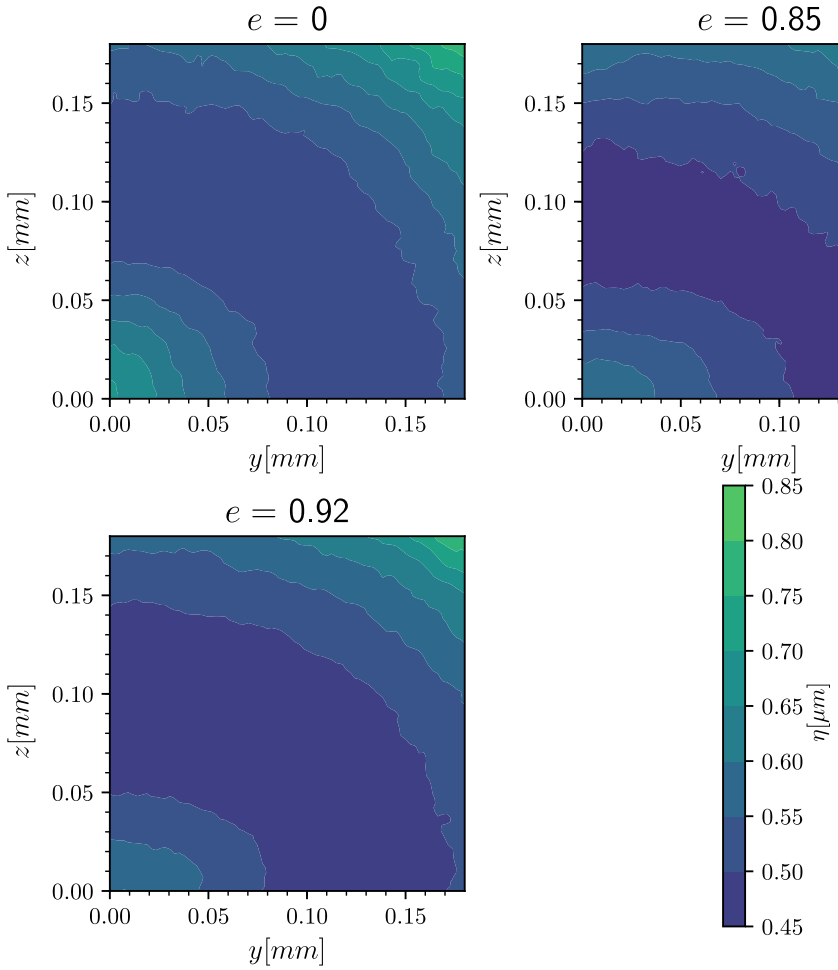

Figure 8.20: Transversal Kolmogorov scale distribution, collapsed into a single quadrant, for all studied conditions.

Centring on the major and minor axis directions, Figure 8.21 shows the η distribution along the radial direction in the case of the round spray, on

the major axis direction on the left plot, and in the minor axis direction in the right plot. In both cases, the η is plotted against a distance to the spray axis, made non-dimensional by dividing by $r_{1/2}$. On the spray axis, the obtained values are slightly lower on the elliptical cases, but when moving to the mixing region, all cases tend to collapse. The minimums are around $r_{1/2}$ on both axis directions, where flow presents higher turbulence intensity. The elliptical nozzles on the major axis direction present almost the same η distribution as the round geometry at distances higher than $r_{1/2}$. However, at those higher distances, elliptical sprays show lower along the minor axis direction. To conclude, the minimum values obtained for all cases are still around 0.25 times the cell size, which has been proven [1] to be sufficiently low to resolve the majority of the energy, being negligible the amount left unresolved.

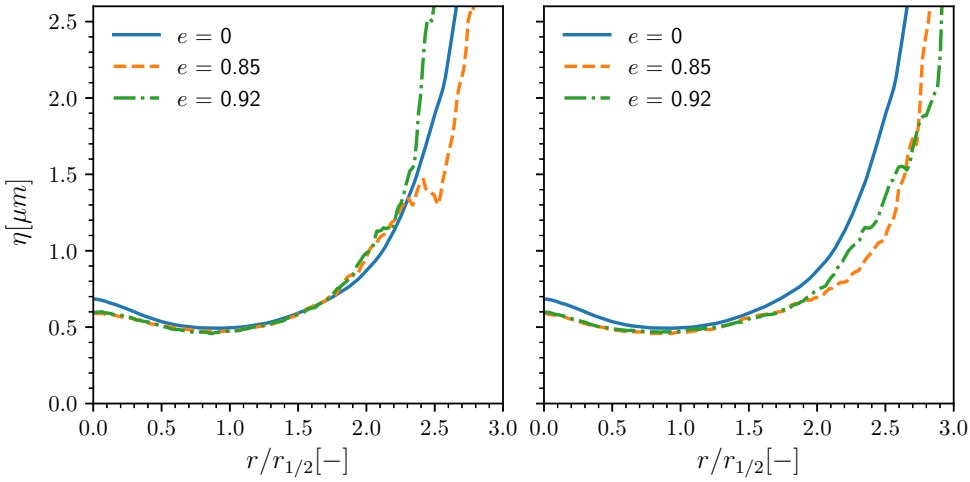

Figure 8.21: Kolmogorov scale profile along: left, the major axis direction, and right the minor axis direction. All distances are made dimensionless with $r_{1/2}$.

8.4 Droplet cloud study

Following the same structure as previous results chapters, most of the analysis efforts are put on the droplet cloud characterisation. To start this study, the temporal evolution of the number of droplets detected by the algorithm is plotted in Figure 8.22. It is noticeable that the droplet production during the transient phase is practically the same in all cases. As already pointed out

in previous analyses of the temporal evolution of the number of droplets, the peak value is firmly dependent on the spray tip, where the strongest interaction between the liquid and the gas occurs. This means that the increase of the maximum droplets detected with the eccentricity factor is due to the delay in reaching the outflow boundary condition of the domain (around 3 µs later for the most eccentric case). In fact, this behaviour is corrected when looking to the statistically stationary state where all the cases decrease the number of droplets until the stabilisation. Furthermore, eccentric nozzles present a higher number of droplets than the round nozzle. However, Table 8.3 gathers the average number of droplets detected during the steady state. It can be seen that using an elliptical nozzle with $e = 0.85$ leads to an increase of 19.4% compared with the round nozzle. However, barely 100 more droplets are counted at the highest eccentricity factor nozzle between both elliptical cases.

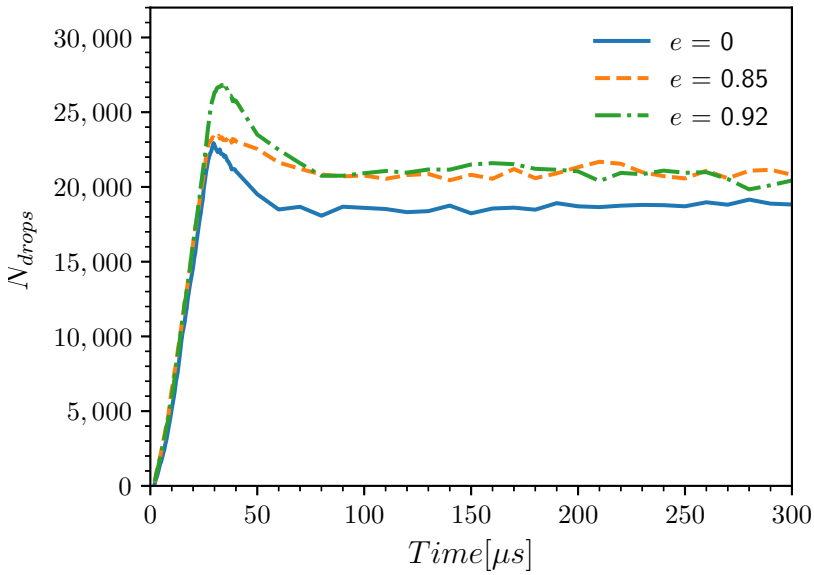

Figure 8.22: Evolution of the number of droplets detected during the whole simulation time.

Table 8.3: Average of droplets detected during the steady state ($T > 60$ µs) for all nozzle geometries.

Eccentricity	0	0.85	0.92
Average droplets detected	17,530	20,900	20,980

8.4.1 Size distribution

Again, the first parameter to be studied is the droplet size distribution based on each droplet's volumetric diameter d_v. Figure 8.23 presents the temporal average number of droplets detected of each size during the statistically stationary state for all tested geometries. It can be seen that the significant differences are presented when comparing the round jet case with the elliptical cases where the diameters lower than 7 µm present an increase in the number of droplets detected whilst the round jet presents a higher number of bigger droplets. Nevertheless, when comparing both elliptical sprays, it can be seen that the discrepancies are nearly negligible as they appear at sizes greater than 13 µm.

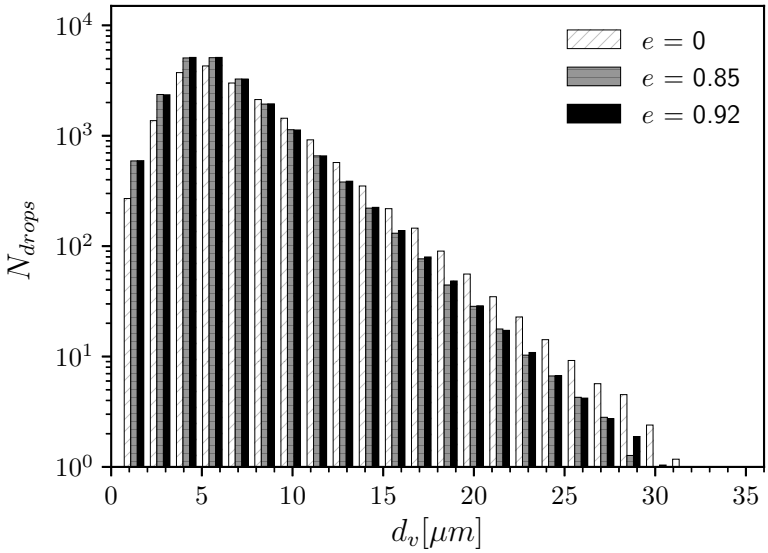

Figure 8.23: Average number of droplets detected for all nozzle geometries, sorted by their non-dimensional diameter.

In order to avoid the influence of the total number of droplets on the size distributions, the PDF is computed and plotted in Figure 8.24. The PDFs of the size distribution confirm the trends observed in Figure 8.23, as the round jet present a higher probability of having droplets with diameters greater than 6.5 µm but lower probability on the smallest droplets. Here the earlier discrepancies observed between the elliptical cases practically disappear, leading to the same PDF of size distribution. This means both cases present similar breakup mechanisms as the droplet clouds are similar in size distributions. However, it is crucial having in mind that the highest eccentricity case presents

a decrease in the Reynolds number of 8.3 % compared to the lower eccentric case, so the decrease of the inflow turbulence can cover up the effects of the non-axisymmetry that appear on the elliptical case.

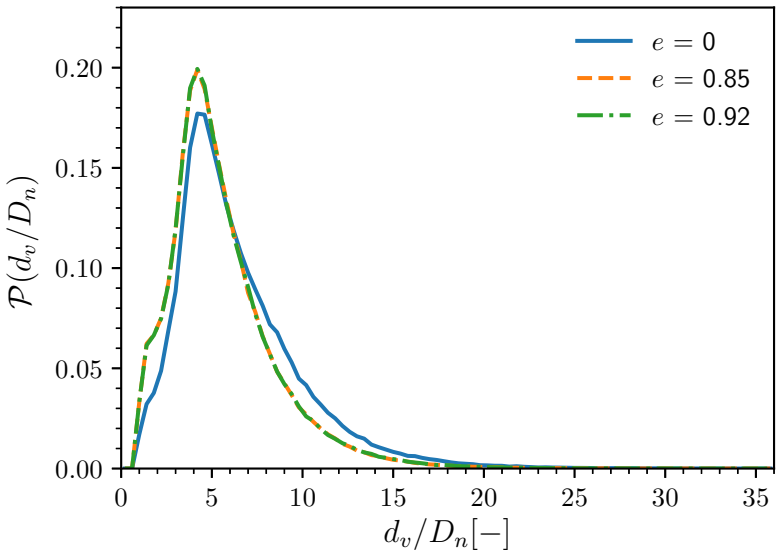

Figure 8.24: Average Probability Density Function of the non-dimensional diameter from the detected droplets for all nozzle geometries.

Finally, the production ratio is analysed to check if the droplet size distribution is, in fact, stabilised during the statistically stationary state. As shown in Figure 8.23, the most numerous droplets can be counted up to 6,000, while bigger ligaments can be around a few hundreds or even tens. To overcome the effect of having that wide range of the number of droplets between the smallest and the biggest droplet sizes, the droplet production is expressed as a percentage of the average number of droplets detected of each size. As the droplets are being advected with the flow, a production ratio of 0 does not mean that there is no droplet production. However, the same quantity is being produced and driven out of the computational domain. In these terms, Figure 8.25 depicts the droplet production ratio of each droplet diameter for all tested geometries. It can be noticed that the droplet production for diameters lower than 15 µm is almost negligible in all cases. So being that those droplets correspond to nearly the 99% of the total number of droplets, it can be stated that the droplet production during the steady state is zero. However, it is interesting pointing out that the higher values on the bigger liquid structures are due to the lower droplet population and are not significant to the overall count.

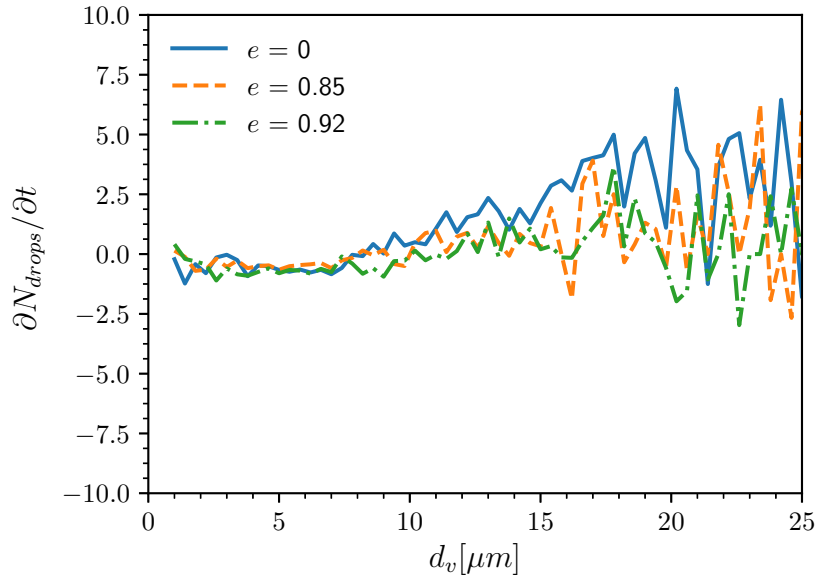

Figure 8.25: Droplet production ratio for each droplet size during the steady state for all nozzle shapes. Results expressed as a percentage of the average of droplets detected in each size interval.

8.4.2 Transversal distribution

The principal aspect that is different when studying elliptical configurations is that, in contrast with the Reynolds and Weber number studies, there is no axi-symmetric flow behaviour. This feature is addressed in Chapter 3 pointing out the appearance of secondary movements within the elliptical ducts. Therefore, as the radial distribution loses its sense, to analyse how the droplets are arranged on the transversal plane is by studying the PDF of the azimuthal position of all the droplets as plotted in Figure 8.26. In this case, the angle θ starts at the major axis at 0° and ends at the minor axis at 90°. It is worth mentioning that the droplet angle is moved to the first quadrant to collapse all data between 0-90°. It can be seen that the round case presents a reasonably constant distribution as predicted, but slightly higher values are obtained at around 45°. Regarding the elliptical nozzles, a clear trend is found as most of the droplets are near the major axis and reduce as moving to the minor axis.

However, the azimuthal distribution does not present a clear droplet disposition on the transversal plane. So, another way to analyse how the droplets are arranged on the transversal plane is by performing a 2D probability function. To this end, the cross-section is divided into squared parcels, so the

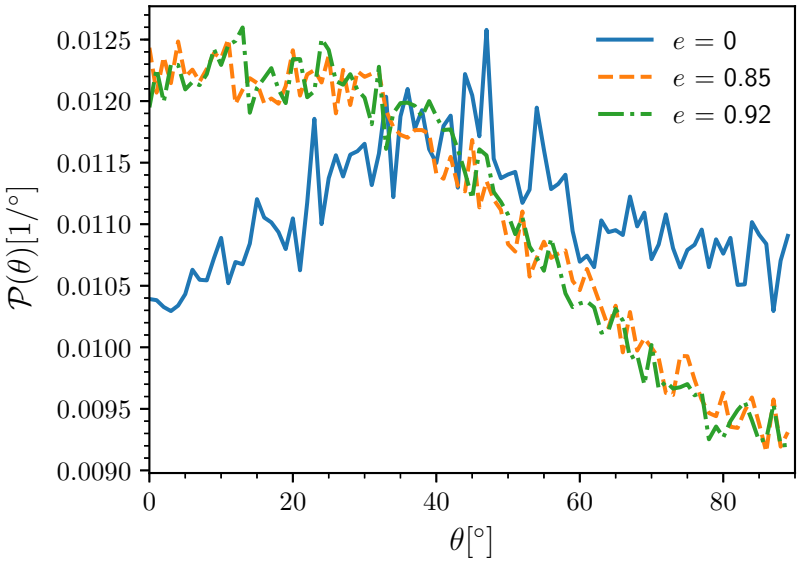

Figure 8.26: Probability Density Function of droplet azimuthal position for all nozzle geometries. From 0 to 90 as moving from the major to the minor axis.

number of droplets located in each parcel, divided by the total number of droplets, provides the probability of finding a droplet in that location. This bi-dimensional probability function can be interpreted as a heat map of droplet location in the cross-section direction. Furthermore, all the information is collapsed into a single quadrant to achieve smoother results.

Figure 8.27 shows the bi-dimensional PDF of the transversal location for all geometries obtained when considering the whole domain. To provide more comparable data, all cases have been non-dimensionalised by their maximum value. Additionally, for clarity, the nozzle shape is plotted in white. As expected, the round case provides an axisymmetric pattern of droplet position, and the distribution is almost constant along the azimuthal direction. Moving to the elliptical cases, the lower eccentricity case exhibits an elliptical droplet cloud, and different aspects can be pointed out. On the one hand, focusing along the major axis direction, the spray aperture is similar to the round case, reaching distances around 0.29 mm. However, the maximum location moves to slightly higher positions as the peak can be estimated at 0.15 mm while the round case is located at around 0.125 mm. On the other hand, along the minor axis direction, the spray aperture is lower than the round case as it reaches 0.25 mm, but the peak is located at the same position as the round

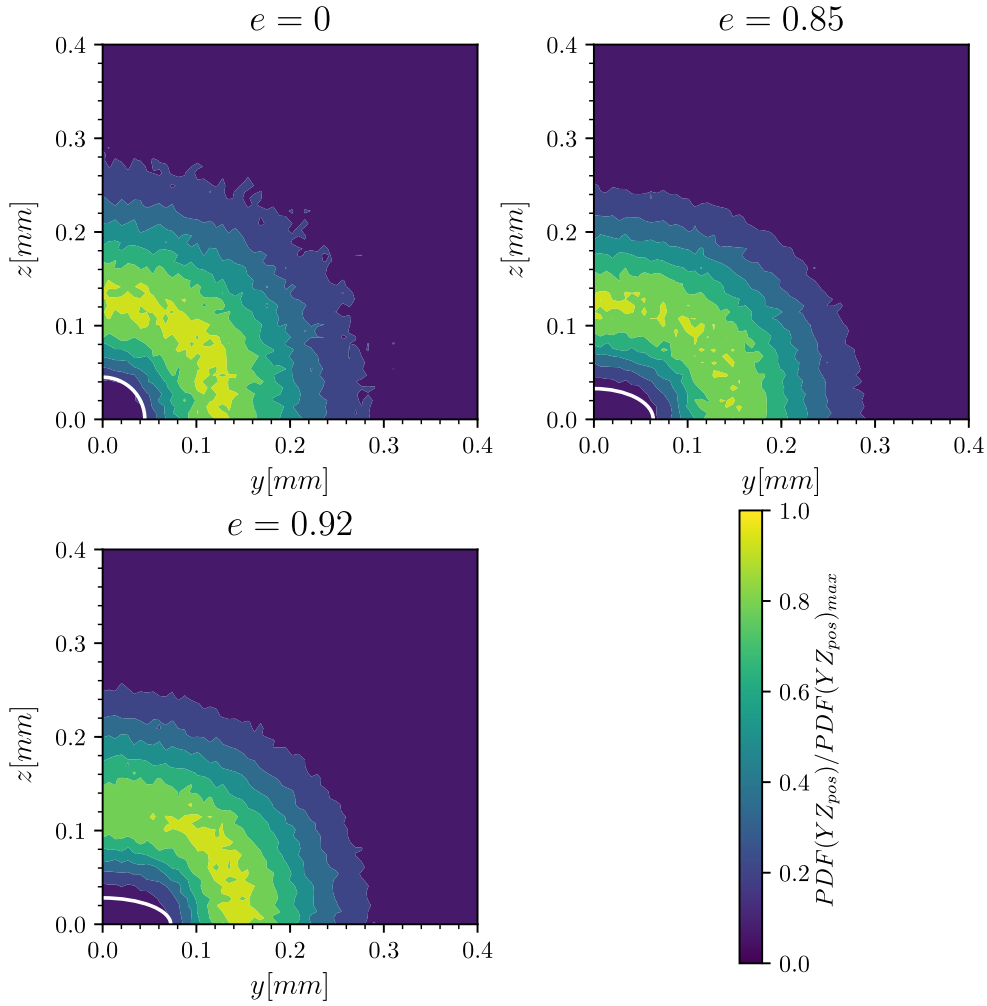

Figure 8.27: Bi-dimensional Probability Density Function of transversal droplet position (plane YZ) for all cases. In white are plotted the nozzle shapes for comparison.

case.

Regarding the droplet location, the most eccentric case presents similar values to the other elliptical case. Nevertheless, the nozzle geometry plays an important role when considering the spray aperture since the same distance from the spray axis on the minor axis direction leads to higher spray angles as the eccentricity increases. On the contrary, increasing the eccentricity leads to lower spray angles at similar distances from the spray axis. Back in Chapter 3 and in section 8.2, it was noticed that the turbulence is located near the minor axis of the elliptical ducts, leading to higher perturbations on that region along the core surface, so it can be anticipated that the earlier droplet formation and momentum transfer displace the droplets farther away along the minor axis than along the major axis. Furthermore, the droplet clouds tend to present lower eccentricity than the nozzle geometry in both cases, and this behaviour has been already addressed in experimental [2] and computational [3] studies, where under different conditions, elliptical sprays tend to exhibit the same angle in both axes within 1-5 mm.

To conclude the transversal analysis, the PDF of droplet size distribution is evaluated in different azimuthal portions to check if there is any effect derived from having elliptical-shaped droplet clouds. Again, the droplet angle is moved to one quadrant to collapse all the information. With this explained, Figure 8.28 presents the PDF of droplet sizes for different azimuthal positions, from grey to black moving from the major axis to the minor axis direction. In this case, it can be seen that the droplet size distribution seems constant along the azimuthal direction for the round case and the lowest eccentric nozzle. Regarding the most eccentric nozzle, minor changes are noticed on the peak value, where a marginal decrease is noticed near the minor axis direction.

8.4.3 Axial distribution

This section focuses on how the axial position affects the droplet cloud's most important characteristics. So the first parameter to study is how the droplets are arranged along the axial direction. Figure 8.29 presents the PDF of the axial droplet position for all geometries. It can be observed that the elliptical cases present earlier atomization as the axial position where it is expected to start having droplets is around 0.1 mm, while the round case delays it to 0.15 mm. Once all cases are stabilized, they exhibit a clear increasing trend. This trend is almost the same in the elliptical cases and a bit irregular in the round case. However, all geometries present a similar growth rate of the droplet axial position PDF. The appearance of droplets earlier in the axial

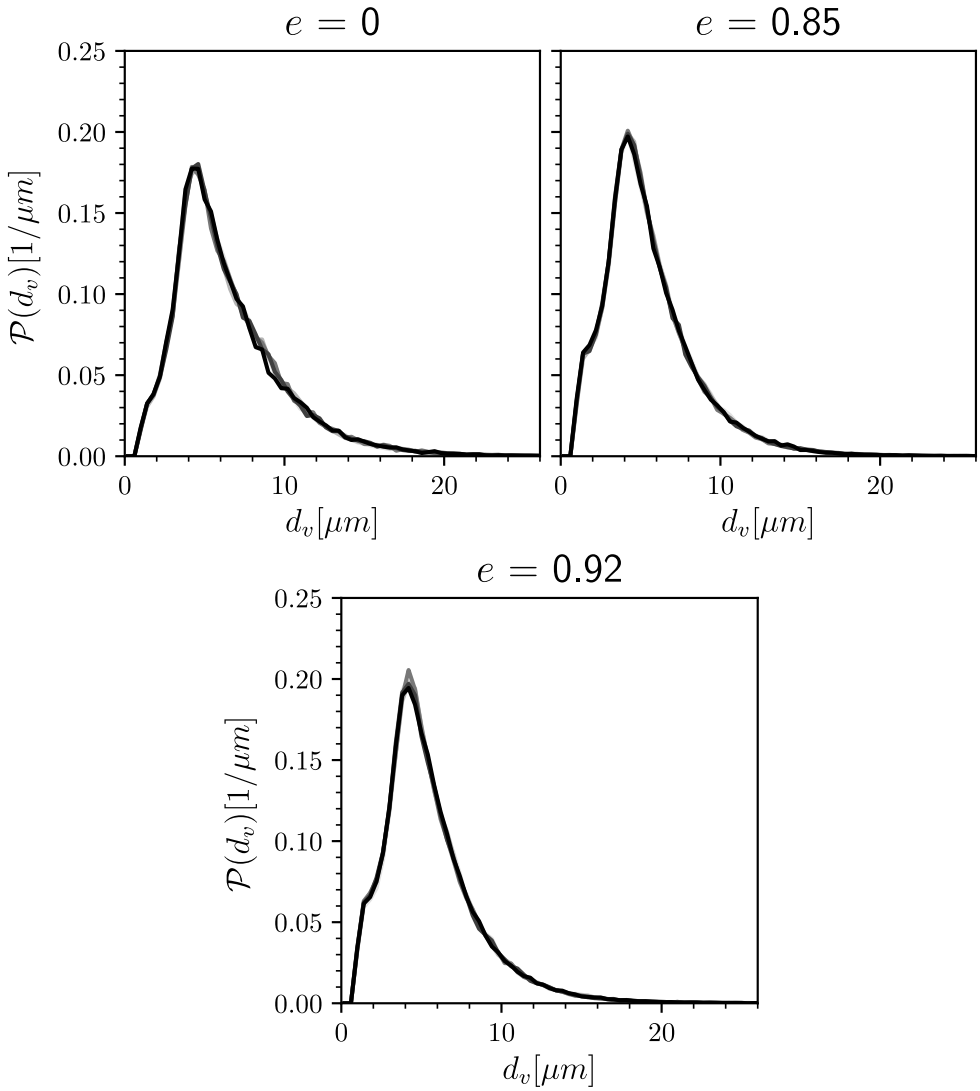

Figure 8.28: Probability Density Function of droplet size for different azimuthal regions. From black to grey as moving from the major to the minor axis.

direction is coherent with the snapshots seen in Section 8.2, where droplets were appreciated in lower axial positions, especially around the minor axis.

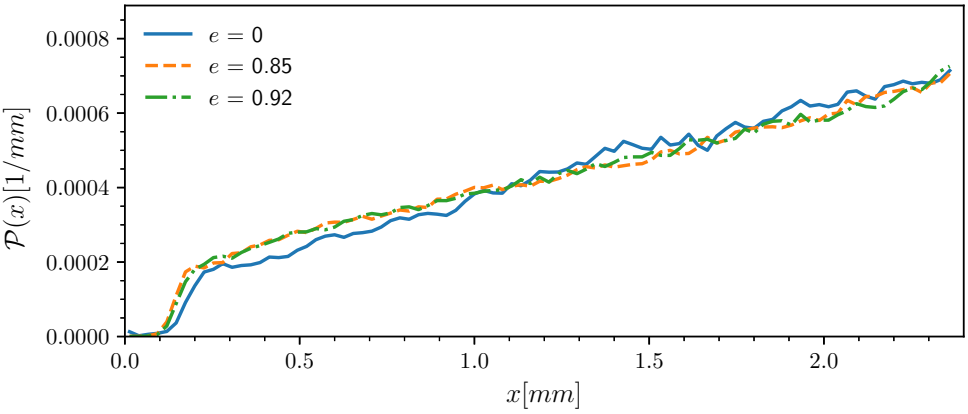

Figure 8.29: Average Probability Density Function of droplet axial position for all geometries.

As seen on the PDF of axial droplet distance, the number of droplets and the spray becomes more developed as the distance from the nozzle increases. Consequently, it is relevant to study if the droplet size distribution is modified as the mass and momentum occur. To study this influence, the domain has been divided along the axial axis into portions of 0.1 mm. Figure 8.30 gathers the PDF of droplet size distributions for each axial division from all cases. From grey to black as the distance from the nozzle outlet increases. As already noticed in the Reynolds and Weber number studies back in Chapters 5 and 6, it can be seen that, as the spray develops, the number of smaller droplets decreases and the bigger liquid structures increases for all geometries.

Moving to the azimuthal distribution, it is expected to see changes in the droplet distribution as the spray develops. Figure 8.31 depicts the PDF of the azimuthal position of the droplets, only considering the droplets located at the last 0.2 mm of the domain. Again, 0° corresponds to the major axis direction and 90° to the minor axis direction. Regarding the round nozzle, it can be seen that the droplet distribution along the azimuthal direction is perfectly constant, as expected. The elliptical nozzles present similar behaviours as the probability of finding droplets is higher near the major axis direction than in the minor axis direction. However, comparing these results with those obtained after studying the whole domain, it can be noticed that the round nozzle does not present a slightly higher probability at 45○. On the other hand, although the same trends are visible in the elliptical case regardless

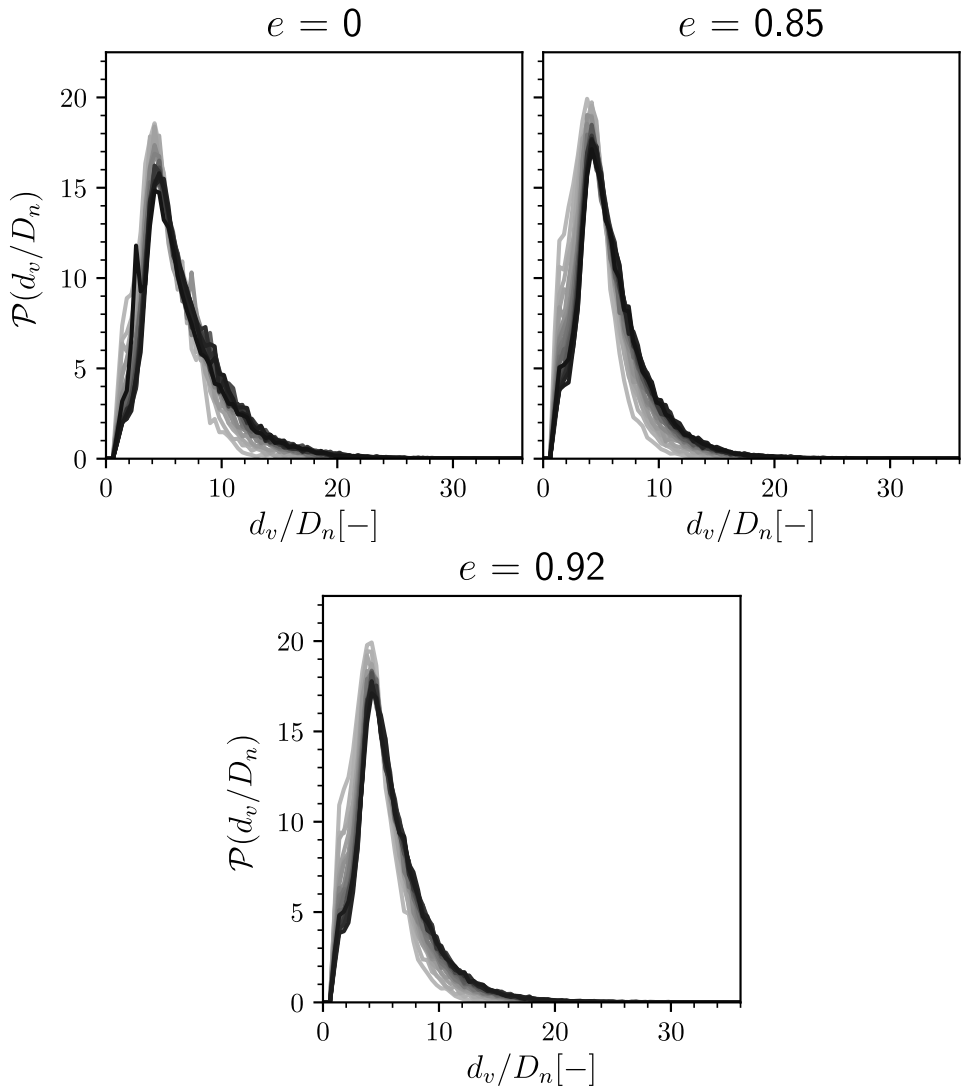

Figure 8.30: Probability Density Function of droplet diameter for different axial positions. From grey to black as the axial distance increases. The axial distance goes from 0.25 mm to 2.4 mm.

of studying the whole domain or the end region, it is appreciable that the difference between the probability of finding droplets near the major and minor axis decreases. Hence, the droplet arrangement tends to have a more uniform distribution.

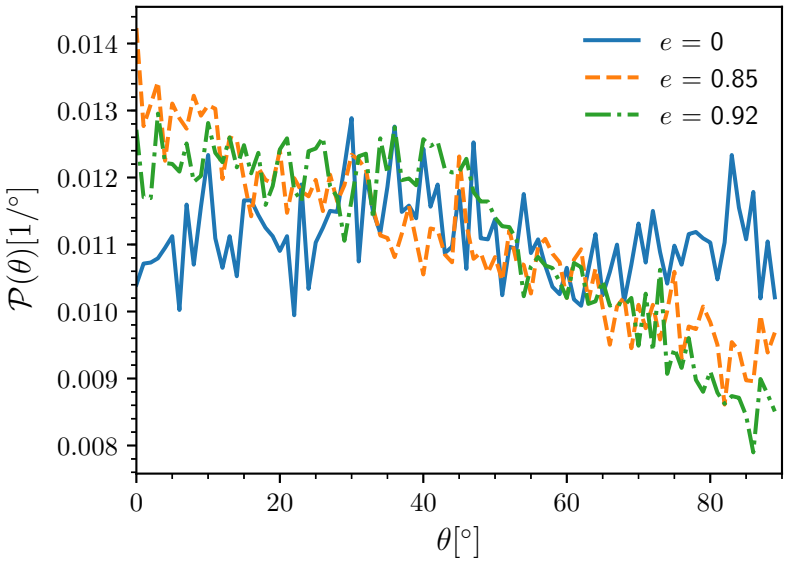

Figure 8.31: Probability Density Function of the azimuthal position from the droplets located at axial positions between 2.2 and 2.4 mm. From 0 to 90 as moving from the major to the minor axis.

Additionally, in the same manner as presented in the transversal study, the 2D probability distribution is computed with the same approach as shown in Figure 8.27 but applied to the most developed region of the domain, the same as used to obtain the Figure 8.31. As anticipated, similar conclusions on the overall domain can be extracted as the round nozzle presents axisymmetric behaviour and the elliptical cases exhibit a less eccentric droplet cloud. However, it can be seen that the probability spreads to higher distances to the spray axis, reaching 0.4 mm on the round case and 0.3 and 0.35 on the minor and major axis directions for both elliptical cases.

8.4.4 Velocity distribution

The last aspect analysed on the droplet cloud is the axial velocity, as a monitor to check how the momentum is transferred to the droplets during the breakup process. Figure 8.33 depicts the PDF of the non-dimensional axial

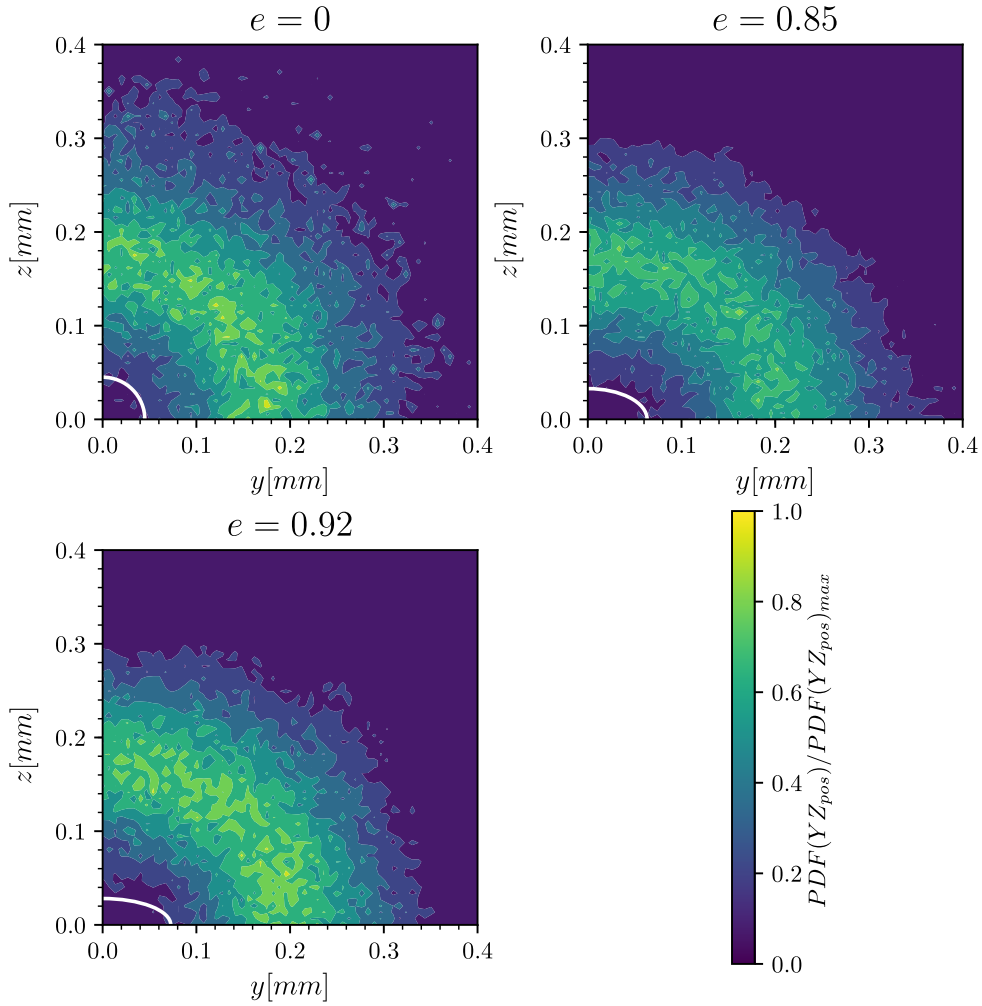

Figure 8.32: Bi-dimensional Probability Density Function of transversal position (plane YZ) from the droplets located at axial positions between 2.2 and 2.4 mm. In white are plotted the nozzle shapes for comparison.

droplet velocity. The velocity is made dimensionless by dividing by the injection bulk velocity. This plot shows similar trends than already noticed in previous studies, as there are a significant number of droplets that present axial velocities near zero. The peak value decreases in the elliptical cases, and a slightly higher probability is found between 0.1 - 0.3 u_d/U_b.

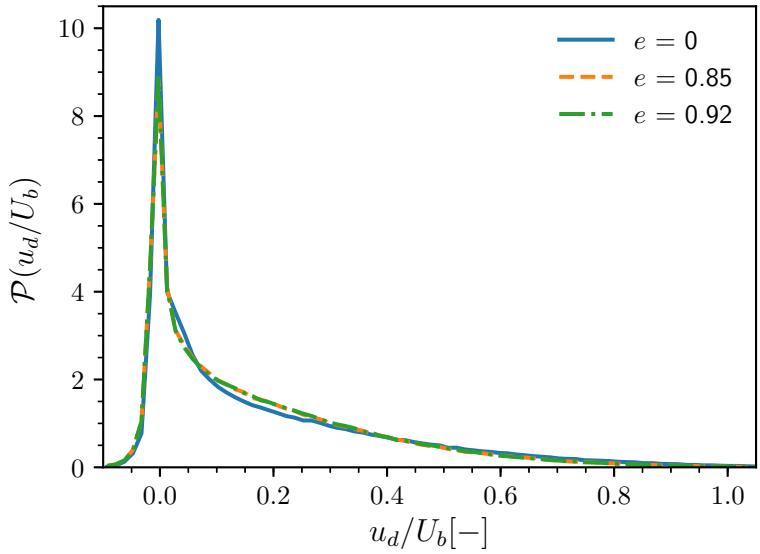

Figure 8.33: Average Probability Density Function of the droplet non-dimensional axial velocity for all nozzle geometries.

Focusing on the peak, it is important to point out that the fact of having that sharp peak near the zero velocity means that there are an important number of droplets condensed in a narrow velocity interval. In fact, the droplets with axial velocities lower than $u_d/U_b = 0.025$ represent around 28-30% of the total number of droplets, depending on each case. At this point, to explain the apparition of those droplets, the transverse location is studied, taking into account the last 0.2 mm of the domain as it is where the spray is most developed. To this end Figure 8.34 gathers the transversal bi-dimensional PDF of having a droplet with $u_d < 0.025 \cdot U_b$ located at the last 0.2 mm. The PDF is divided by the total number of droplets to be directly comparable with Figure 8.32. Comparing both figures, it can be noticed that the highest PDF values for droplets with low axial velocity are located farther away than the maximums obtained when taking into account all droplets in that axial region. This means that the quasi-static droplets are located on the spray periphery, where the axial velocity profile loses its influence. In fact, comparing

this results with the axial velocity contours from Figure 8.16 it can be noticed that they start exhibiting non-zero values almost when the velocity contours drop to zero.

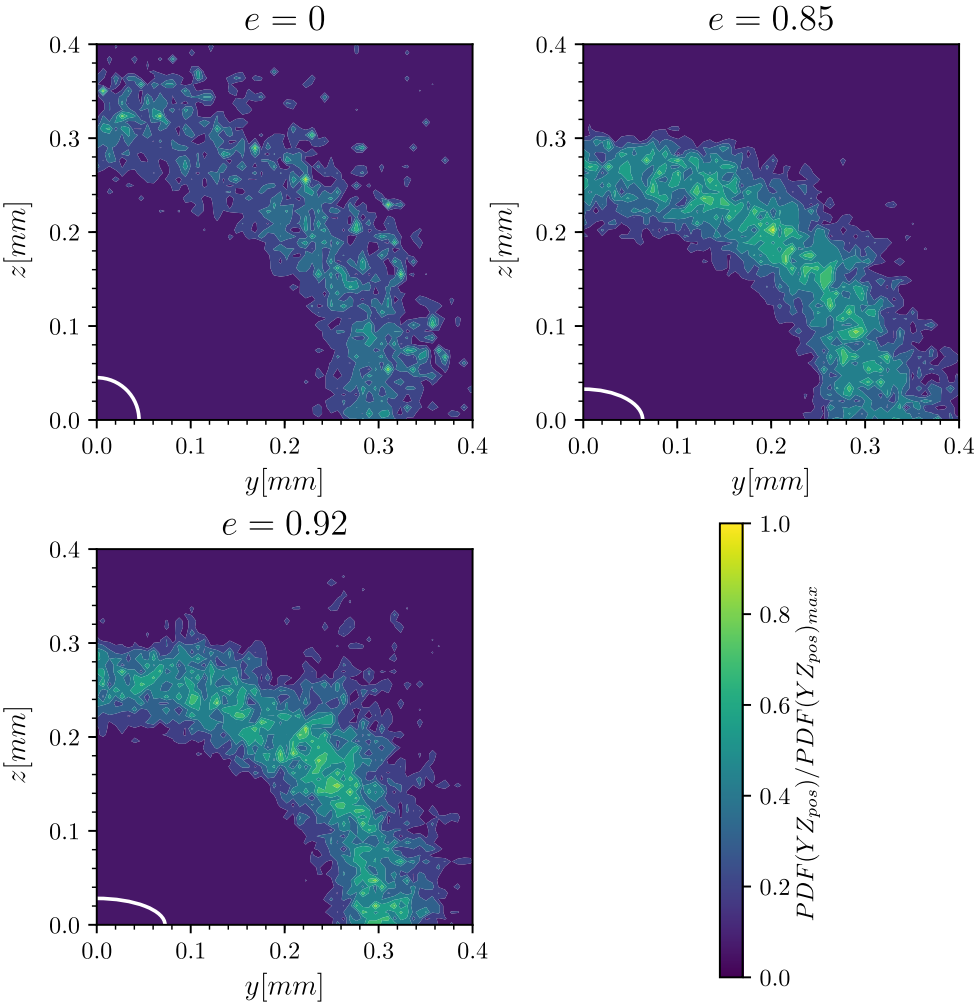

Figure 8.34: Bi-dimensional Probability Density Function of transversal position (plane YZ) from the droplets located at axial positions between 2.2 and 2.4 mm with axial velocities lower than 2.5 m/s. In white are plotted the nozzle shapes for comparison.

Finally, as the spray develops in the axial direction, the velocity transference to the droplets is affected. To analyse this effect, and just like done on the droplet size, Figure 8.35 shows the PDF of the non-dimensional axial

velocity for different axial positions. From grey to black as the axial distance increases. Centring near the nozzle, it can be seen that most of the droplets have zero velocity and just a tiny amount exhibit velocities up to $0.1 \cdot U_b$. Having droplets almost static near the nozzle means that they have been advected to a radial position too high to be attracted again to the spray. This hints that they may have been produced during the transient phase. Moving to higher axial positions, the probability of having quasi-static droplets decreases, increasing the probability of having droplets with higher velocities. So, as the spray develops, the momentum transfer to the droplets increases as the momentum mixing leads to a broader velocity profile. Additionally, the air entrainment increases, so the droplets located on the spray periphery can be advected again to the spray easier, and thus, the amount of quasi-static droplets decreases. Regarding the effect of the nozzle shape, it can be noticed that the peak decreases with the eccentricity factor, which is in agreement with the morphological analysis where the number of 'satellite drops' decreases when moving to elliptical nozzles. Furthermore, while the round spray shows a smoother profile when moving to higher velocities from the peak, the elliptical cases exhibit a sudden change in the distribution.

8.5 Conclusions

The main objective of this chapter is to study how the nozzle shape affects the primary atomisation process. To do so, two elliptical nozzles with different eccentricity factors have been designed to maintain the injection area with respect to a round spray reference case. Also, the liquid and discharge properties and the injection bulk velocity are maintained. This leads to a decrease in the Reynolds and Weber number as the eccentricity factor increases. This analysis primarily focuses on the macroscopic spray features such as the spray aperture and the droplet formation and characterisation.

The first approach to this study is through the macroscopic visualisation of the spray using iso-contours of the liquid volume fraction. Regarding the transient state, no differences were found in the spray penetration, but higher disintegration of the spray tip is reported as the eccentricity factor increases. When analysing the steady state, early atomisation can be found in the elliptical cases, and the droplet cloud generated seem denser with smaller droplets. Additionally, the spray aperture of the elliptical cases on the major axis is higher than the round spray and slightly lower on the minor axis direction. Furthermore, the droplet cloud generated by the elliptical sprays appears to be condensed within the spray cone, exhibiting fewer satellite drops at high radial positions than the round spray. An interesting behaviour is reported when

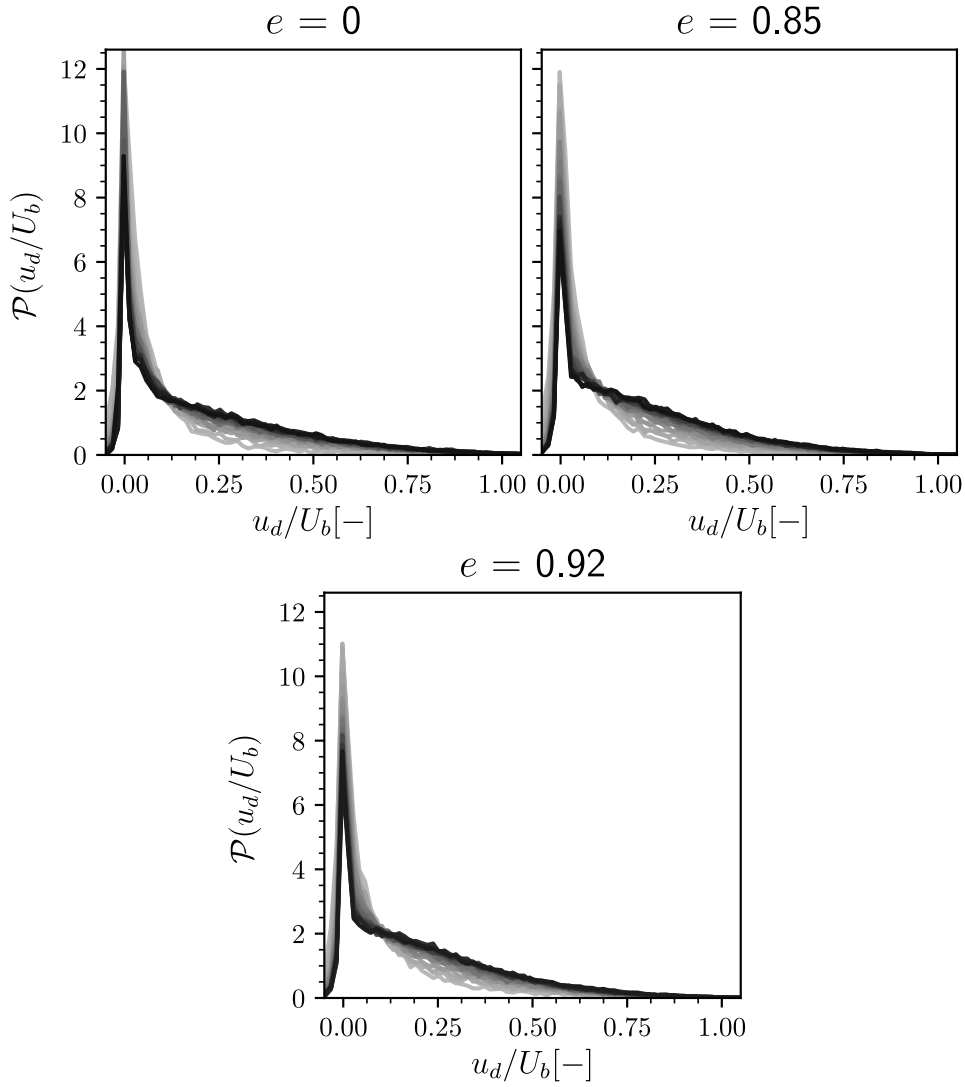

Figure 8.35: Probability Density Function of droplet dimensionless axial velocity for different axial positions. From grey to black as the axial distance increases. The axial distance goes from 0.25 mm to 2.4 mm.

focusing on the liquid core topology. The surface near the minor axis presents more perturbations than near the major axis. This behaviour is accentuated as the eccentricity factor increases. It is explained by the vortex distribution on the internal flow analysed in Chapter 3, where it was pointed out that the vortex structures are located near the minor axis. However, although most perturbations are located near the minor axis, the higher curvature of the surface near the major axis favours the surface breakup, leading to a similar external non-perturbed length.

After analysing the sprays' morphology, the velocity and liquid fields are studied, addressing the centreline statistics, the spray aperture along the axial direction, and the transversal statistics on a plane located near the outflow boundary condition. The main issue with the centreline statistics is the lack of high temporal resolution on the elliptical cases, which prevents obtaining accurate measurements. However, the axial distributions of the axial velocity and liquid distribution on the centreline are good enough to provide clear trends. Starting with the axial velocity, it can be observed that near the nozzle, both elliptical and round cases present a similar decay rate. However, from 1.2 mm, the elliptical cases present lower values. Regarding the liquid distribution, the liquid volume fraction distributions show a decrease in the breakup length when increasing the eccentricity factor. However, moving away from the nozzle, all cases tend to collapse in the same trend.

Following the centreline statistics, the spray aperture study is performed by analysing the radial decay of the axial velocity, the liquid volume fraction and the mass concentration for all axial positions. So the aperture subscript is defined with $r_{1/2}$ or $r_{0.01}$ depending on the 50% or the 1% of the centreline value. The comparison between the elliptical sprays and the round case shows that, in terms of the axial velocity component and $r_{1/2}$, the spray aperture of the elliptical sprays is higher in the major axis direction and lower at the minor axis direction than the one exhibited in the round case. However, when computing the spray angle, all cases present similar aperture angles of around $10°$, except for the major axis of the $e = 0.85$ case that presents the highest angle aperture of $12°$, that can be caused by the poor average of the centreline results. Interesting results are obtained when studying the spray aperture in terms of mass concentration. It is seen that using the $r_{1/2,m_c}$ criterion, the spray angles and profiles of the elliptical cases tend to collapse into a single spray aperture, and also the values are higher than the round spray case. However, when applying the $r_{0.01,m_c}$ criterion, that trend reverts, showing a higher aperture on the round spray case than on the elliptical sprays. This behaviour, along with the morphological study, explains why the droplet cloud

from the elliptical nozzles seems denser and fewer satellite droplets are found far away from the spray axis.

The last analysis of the flow field statistics is centred on a plane located sufficiently far from the nozzle outlet. Here, focusing on the transversal direction, it can be seen that the elliptical cases tend to present elliptical velocity and liquid fields. However, the eccentricity of those fields decreases, slowly turning into rounded profiles. Additionally, the minor and the major axis profiles of the axial velocity and mass concentration are compared to the round case and the hypothetical Gaussian profile. From that, the major axis distribution from both the axial velocity and mass concentration does not precisely agree with the Gaussian behaviour as present higher values at distances lower than $r_{1/2}$ and lower values at higher distances. Nevertheless, the minor axis does show a Gaussian behaviour at distances lower than $r_{1/2}$, but the agreement at higher distances is poor. Finally, the Kolmogorov scale η is computed and follows similar patterns to the previous fields analysed. The elliptical sprays present elliptical distributions, while the round spray has an axi-symmetric arrangement. Regarding the lowest values detected, all cases present the same lowest value, which is sufficiently high to diminish the unresolved energy to levels that do not affect the spray resolution.

Moving to the main objective of this chapter, the droplet cloud is characterised. First, the number of droplets detected increases when using elliptical geometries, but no substantial differences are obtained between eccentricities. The droplet size PDFs for the elliptical cases collapse into the same distribution, presenting a higher probability of having smaller droplets and a lower probability of bigger ones than the round spray. Regarding the droplet distribution in the azimuthal direction, the droplet size distribution is nearly constant for all eccentric cases. However, it shows a higher number of droplets near the major axis than near the minor axis. However, this difference decreases when taking into account just the most developed region of the domain, meaning that the droplet distribution tends to be axi-symmetric as it moves far from the nozzle. As expected after analysing the morphological study, the elliptical geometries present droplets at lower axial distances, and, as the axial distance increases, the droplet size presents a log-normal distribution. Finally, the PDF of the axial velocity component presents a lower number of 'quasi-static' droplets on the elliptical cases, consistent with the fact that there are fewer 'satellite droplets' on the elliptical sprays.

Those results show that using elliptical nozzles leads to finer atomisation and a similar spray aperture. However, they are subject to the fact that, due to the design strategy of the elliptical nozzles, the non-dimensional numbers

decrease with the eccentricity factor. So the benefits of having elliptical nozzles that can be noticed when comparing the round case and the $e = 0.85$, could be diminished by the decrease of turbulence injected, leading to an optimum eccentricity factor.

References

[1] Torregrosa, Antonio J, Payri, Raul, Salvador, Francisco Javier, and Crialesi-esposito, Marco. "Numerical evidences of universal energy cascade in multiphase flows". In: (2018).

[2] Yu, Shenghao et al. "Experimental study on the spray characteristics discharging from elliptical diesel nozzle at typical diesel engine conditions". In: *Fuel* 221.February (2018), pp. 28–34. DOI: 10.1016/j.fuel.2018.02.090.

[3] Yu, Shenghao et al. "Numerical investigation on effects of elliptical diesel nozzle on primary spray characteristics by large eddy simulation (les)". In: *Atomization and Sprays* 28.8 (2018), pp. 695–712. DOI: 10.1615/AtomizSpr.2018026642.

Chapter 9

Experimental study of the influence of the turbulence on the spray angle variability in the near field

9.1 Introduction and experimental setup

This chapter will expose the experimental study in the near field. Among the different optical techniques presented back in Chapter 1, the Near-Field Microscopy is the one that will be used to perform the spray characterisation on the dense region accordingly to a specific test matrix. The selection of this technique is because it does not need the modification of the injector as in the case of the Optical Connectivity and access to a high-frequency laser or a Synchrotron is not plausible. As explained earlier, the possibility of obtaining the same results using experimental techniques than using DNS is nearly impossible. Also, performing the experiments under the same conditions from the DNS studies is complex, as the used injector is not able to inject with low bulk velocities. However, using Near-field Microscopy is possible to study the macroscopic features of the spray in the dense region.

In this line, the study exposed in the following pages is a detailed analysis of the influence between the operating conditions on the spray opening angle, specifically on the standard deviation of the spray contour, when the injection

has reached the steady state. The main objective that pursues this work is the relation of the inlet turbulence (increased by the injection pressure) with the stability of the spray angle.

Starting with the proper experimental setup, the injector is introduced into a constant volume chamber, pressurized with Nitrogen under non-evaporative conditions. The illumination is provided by a high-speed Light Emitting Diode (LED), which is able to supply light pulses of 70 ns of duration. In order to collide the light beams, a light pipe homogenizing rod is used to focus the maximum amount of beams into the measuring area. On the other side, a high-speed Photron Fastcam SA-Z CMOS camera is coupled to a long-distance K2 DistaMax microscope with a CF-2 objective. This combination allows acquiring 175,000 frames per second with an imaging window of 512x168 pixels, which corresponds to visualizing the first 2 millimetres of the spray, with approximately 247 pixels per millimetre of resolution. Also, in order to set the microscope closer to the spray, a special sapphire window is used. Figure 9.1 shows schematics of the experimental setup used for the experimental study.

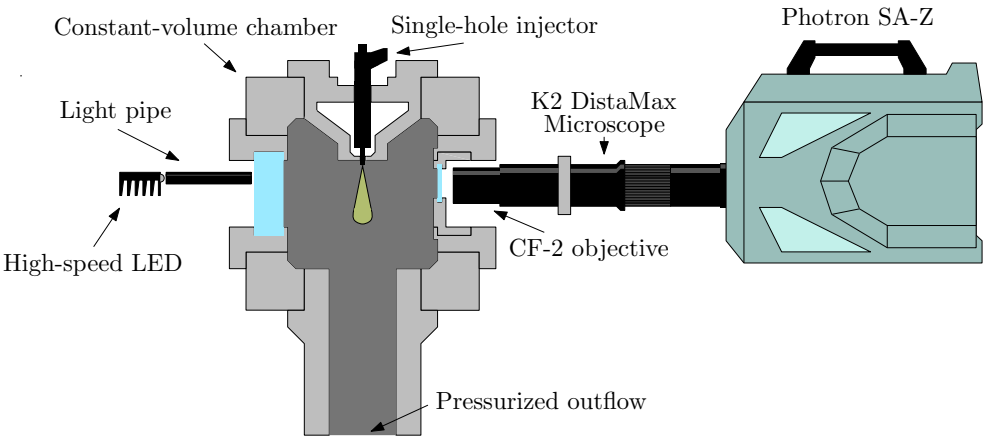

Figure 9.1: Near-Field Microscopy visualization setup sketch.

With this arrangement, a test matrix is designed with 5 levels of injection pressure (50, 80, 100, 120 and 150 MPa) and 2 levels of discharge pressure (1 and 4 MPa), making a total of 10 operating conditions. To ensure the accuracy of the results, each operating condition is repeated 10 times. The injector used in this study is a piezoelectric-driven diesel fuel injector, with a single-hole nozzle with a nominal outlet diameter of 90 μm and a high degree of conicity to avoid the apparition of cavitation inside the nozzle. The fuel selected for performing the tests is the n-dodecane, whose properties at the nozzle outlet depend on the discharge pressure and are gathered in Table 9.1.

These properties have been obtained using the expressions found in Salvador et al. [1], but adapted for this fuel based on the data provided by Caudwell et al. [2]. Finally, the electric pulse duration to open the piezoelectric injector is 2 ms to ensure that the flow reaches the steady state and provide enough frames to achieve smoother averages.

Table 9.1: N-dodecane fuel density and viscosity properties as a function of discharge pressure

$\mathbf{P}_{back}$ **[MPa]**	1	4
$\boldsymbol{\rho}$ **[kg/m^3]**	746.21	748.38
$\boldsymbol{\mu}$ **[mPa·s]**	1.36	1.38

Additionally, using Bernouilli's equation the theoretical velocity on the nozzle exit can be estimated as $u_{theo} = \sqrt{2\Delta p/\rho_l}$ and with the physical properties de Reynolds number at the nozzle outlet can be computed. That data has been gathered in Table 9.2 to be compared with DNS computations.

Table 9.2: Theoretical velocity and injection Reynolds number for all tested conditions.

$\mathbf{P}_{back}$ **[MPa]**			1		
$\mathbf{P}_{inj}$ **[MPa]**	50	80	100	120	150
$\mathbf{u_{Teo}}$ **[m/s]**	362.4	460.2	515.1	564.8	631.9
$\mathbf{Re_{Teo}}$ **[-]**	17,636.2	22,393.5	25,068.4	27,484.1	30,754

$\mathbf{P}_{back}$ **[MPa]**			4		
$\mathbf{P}_{inj}$ **[MPa]**	50	80	100	120	150
$\mathbf{u_{Teo}}$ **[m/s]**	350.6	450.7	506.5	556.8	624.6
$\mathbf{Re_{Teo}}$ **[-]**	17,112.7	21,996.1	24,721.5	27,174.9	30,487.1

9.2 Spray contour detection methodologies

Figure 9.2 depicts two instantaneous frames as an example of what kind of images are provided with the aforementioned experimental arrangement. As can be seen, the position of the nozzle can vary between cases due to the setup calibration between measurements. Furthermore, during the same injection

event, the vibrations of the setup and the movement of the injector can displace the nozzle. All those variations of the nozzle tip position are automatically fixed by an automatic nozzle tip detector, which aligns all the frames used to perform this study. With this alignment, the coordinate system for all cases is located at the position related to the first pixel of the spray detected (corresponding with the nozzle exit).

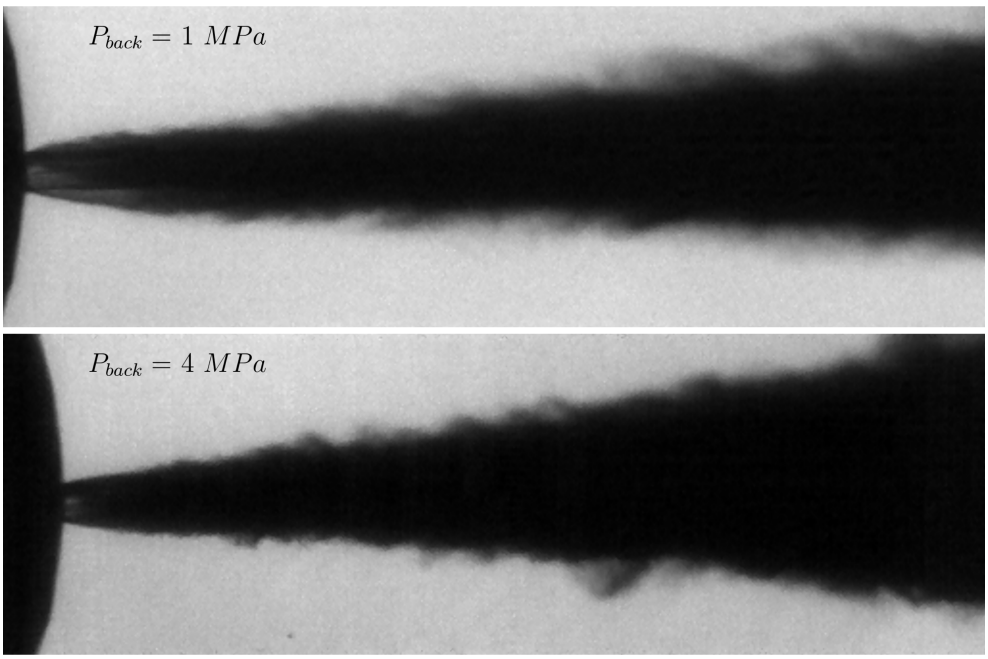

Figure 9.2: Instantaneous frames from two different injection events with P_{inj} = 150 MPa and top: P_{back} = 1 MPa and bottom: P_{back} = 4 MPa.

The main idea is to detect the contour of the spray in each image to be able to study its variability during the injection. To this end, two contour detecting methodologies are evaluated. The first one is based on the Beer-Lambert-Bougher law [3], which relates the decrease of the light intensity received by the CMOS sensor with the attenuation caused by the light travelling through the media. This law can be expressed as Equation 9.1 already used in previous works [4].

$$KL = -ln\left(\frac{I}{I_0}\right) \tag{9.1}$$

Where KL is the optical thickness, I is the intensity detected by the CMOS sensor, and I_0 is the background illumination registered by the CMOS

sensor obtained by averaging in each repetition the frames previous to the injection event. It is crucial to remember that, as this methodology depends on the absolute intensity level detected, it is sensitive to the cleanliness of the windows from the vessel, where tiny droplets can deposit during the tests. Moreover, the KL method requires a threshold to distinguish between spray and background, slightly modifying the spray contour.

A second methodology is proposed using the intensity derivative along the cross direction (dI/dy) instead of its absolute value to avoid these uncertainties. So that, after a signal treatment to reduce the noise, the spray contour can be detected by the maximum values of the derivative profile, which can be automatically detected without any calibration required. Both methodologies are applied in the cross direction profiles for each pixel in the axial direction.

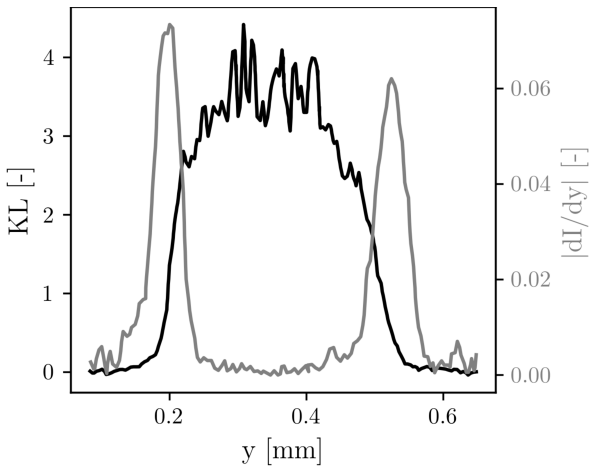

Figure 9.3: Comparison between contour detection methodologies on a cross section profile at $P_{inj} = 150$; $P_{back} = 1$ MPa; $x = 1.15$mm. Black the Optical thickness method and grey the derivative method.

Figure 9.3 shows an example of the profiles from which the contours are detected for each methodology having in black the results for the KL method and grey the results for the derivative method. These profiles, in particular, correspond to an axial distance of 1.15 mm from the nozzle exit and 150 MPa of injection pressure, and 1 MPa of discharge pressure. On the one hand, regarding the KL method, the obtained values are around zero when the light does not trespass the spray. Still, as the interaction between the LED and the spray starts, the KL values increase rapidly until having their maximum in the spray center where the KL variability is high. Therefore, to set a coherent threshold is mandatory to perform an average on the flat area of the spray

center in order to obtain an approximate value of the maximum KL for each axial position and frame. In this study, the threshold is set to 5% of the local KL maximum value obtained. On the other hand, the absolute derivative of the intensity profile shows two clear peaks, with a width of around 50 μm, which correspond to the maximum intensity variation caused by the light absorption of the spray in its both sides. This means that these peaks will always be located in the boundary of the spray.

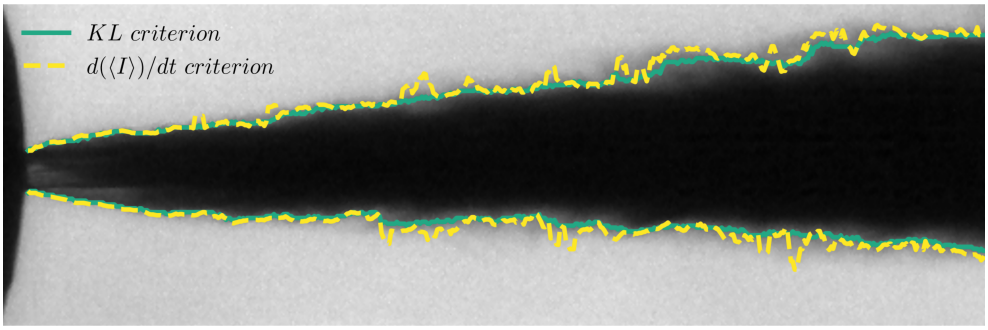

Figure 9.4: Instantaneous frame processed with both methodologies with P_{inj} = 150; P_{back} = 1 MPa. Green shows the KL criterion; Yellow depicts the intensity derivative criterion.

When applying both methods in each axial position in a frame, the spray contour can be depicted as shown in Figure 9.4. The green line represents the contour obtained by using the KL method, whereas the yellow line distinguishes the outline provided by the derivative criterion. It can be seen that the KL method present a less noisy contour while the intensity derivative seems to have a more fluctuating shape. However, both criteria seem to provide very similar results.

9.3 Spray angle results

As already introduced before in this Chapter, the main objective of this research is to study the spray angle under different operating conditions and analyse its variability. The first step required to be able to quantify the contour variation is measuring the detected mean spray angle for each frame and repetition and performing an average for each test condition. Once smoother contours are obtained for both the upper and the lower spray boundaries, a linear fit is done within 0.3 to 1.5 mm from the nozzle exit. Finally, the spray opening angle is calculated as the difference between the slopes from the linear approximations.

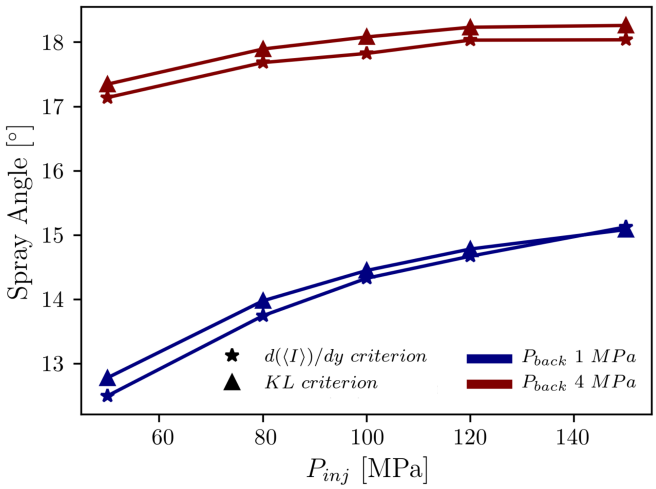

Figure 9.5: Mean spray angle as a function of injection pressure and discharge pressure. Each symbol corresponds to a different contour detection method.

Figure 9.5 gathers the mean spray angles for all tested conditions, presenting different line colours for each discharge pressure and different symbols for each contour detection method. The trends show a stronger influence of the discharge pressure, which is in agreement with the gas-jet prediction analogy, widely used in high pressure sprays [5]. As the discharge pressure increases, the ambient density increases, leading to higher aerodynamic interaction between the liquid and the gas. This increase in the interaction enhances the air entrainment, opening the spray angle. On the other hand, increasing the injection pressure also increases the spray angle, although it is lower than the one shown by the discharge pressure. Increasing the injection pressure also increases the liquid momentum and velocity. This combination leads to a favourable effect on the fuel-air mixing and seems more important for lower discharge pressure conditions, showing a saturation at higher values. At lower discharge densities, the increase of the spray angle induced by the inflow turbulence is significant, but at higher discharge pressures the increase of the aerodynamic forces drive the air entrainment. In the end, both criteria show similar results of mean spray angle, demonstrating both their capability to detect the spray contour.

The standard deviation of the spray contour is studied to quantify the instabilities produced by the inflow turbulence on the spray morphology. Each instantaneous contour is compared against the mean spray profile to compute this parameter. Figure 9.6 show the results for 1 MPa of discharge pressure

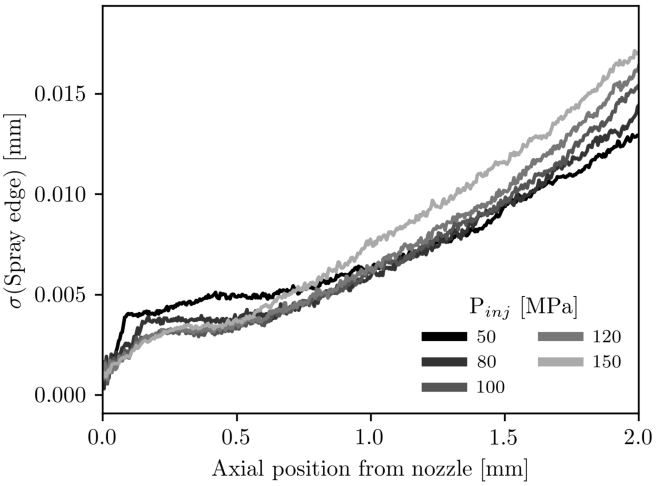

Figure 9.6: Axial distribution of the standard deviation of the spray contour for P_{back} = 1MPa.

using the KL threshold criterion. It can be noticed that, near the nozzle exit and up to around 0.7 mm, the standard deviation is higher for the lower injection pressure (50 MPa) while tends to collapse for higher injection pressures. This behaviour is caused because the amount of atomized liquid in this region is lower at low injection pressures. The lower the atomization is, the slightly the light dissipation is, as can be seen in Figure 9.7 where the spray at 50 MPa shows a lighter grey when compared with the 150 MPa injection pressure condition. Being both methods dependant on the light intensity, the sharper the contour is, the better contour capturing offers. So that, the contour detection provides higher variability, not because of the variation of the spray contour itself, but for the complexity of the methodologies to detect it. Nevertheless, this effect is only appreciated near the nozzle field when calculating the standard deviation and does not affect the average spray detection used to compute the spray angle. Actually, when moving far from the nozzle exit, the standard deviation shows a clear trend, increasing with the injection pressure. Using Bernoulli's equation to calculate the theoretical velocity on the nozzle exit, the estimated Reynolds numbers range when increasing the injection pressure as seen in Table 9.2, confirming the increase of the inflow turbulence. Considering the results obtained, the turbulence intensity can be related to the spray contour stabilities on the first millimetres of the atomization process.

Just like for the lowest discharge pressure, Figure 9.8 depicts the standard deviation of the spray contour when increasing the discharge pressure to 4

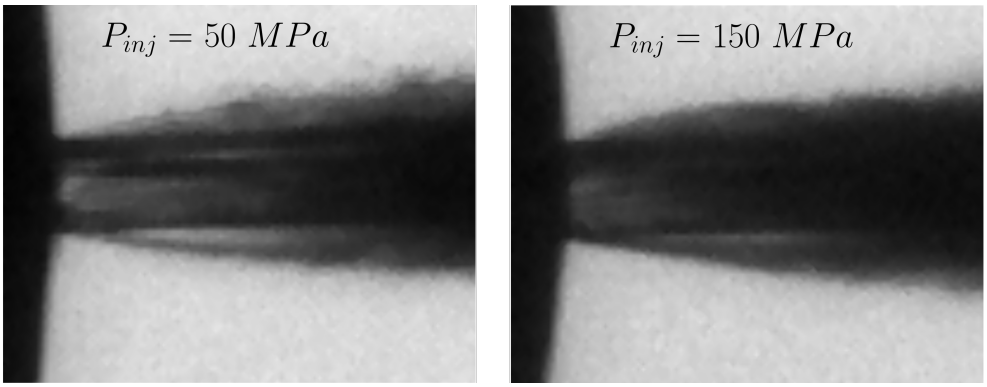

Figure 9.7: Zoom to the near nozzle region of instantaneous frames of two injection events with P_{back} = 1 MPa and left: P_{inj} = 50 MPa and right: P_{inj} = 150 MPa.

MPa. The near field presents higher standard deviation values for the lowest injection pressure, but it rapidly drops because the higher discharge density enhances the gas-liquid interaction, reducing the non-perturbed length and thus, obscuring the spray shadow. Between 0.25 and 1.2 mm, the standard deviations are again aligned with the injection pressure as expected, but when moving forward, the results tend to collapse into the same trend (excluding the 50 MPa case). This is caused by the rise of the secondary atomization, where the aerodynamic interaction between the ambient gas and the ligament and droplets detached becomes more significant. Therefore, the oscillations caused by the inflow turbulence give way to the oscillations caused by the secondary atomization.

Finally, to finish off the spray angle study, the standard deviation shown can be traduced to an angle deviation. To compute the standard deviation of the angle, the opening angle is computed for each frame once the spray has reached the quasi-steady state, and also for the 10 repetitions from each test condition, and then, compared to the mean opening angle from Figure 9.5. The obtained results for the 1 MPa discharge pressure operating conditions are depicted in Figure 9.9 for both methodologies. Those results show that increasing the injection pressure not only increases the spray opening because of the improvement in the gas-liquid mixing but also its variability. Indeed, it is worth mentioning that the higher growth on the angle deviation is measured between 50 MPa and 80 MPa of injection pressure, and then the slope decreases with higher injection pressures. This behaviour can be a consequence of a non-fully developed flow regime at lower injection pressures [6, 7]. In fact, it agrees with the trends seen in the discharge coefficient that presents lower

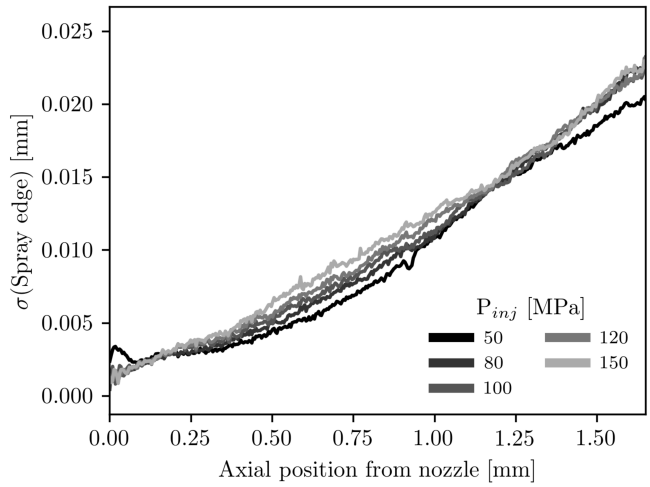

Figure 9.8: Axial distribution of the standard deviation of the spray contour for P_{back} = 4MPa.

values at moderate injection pressures. Once more, both methods present the same conclusions.

9.4 Conclusions

In this chapter, a study of the effect of the operating conditions on the near-nozzle spray morphology has been carried out. To fulfil this purpose, a single-hole injector is coupled into a constant-volume chamber pressurized with nitrogen, and a high-speed Near-field Microscopy has been chosen to magnify the injection event. The test conditions vary in injection pressure (from 50 to 150 MPa) and in discharge pressure (from 1 to 4 MPa), and the main efforts are focused on their influence on the spray opening angle and its temporal variability.

The images provided by the Near-Field Microscopy are processed in order to detect the spray contour using two different criteria: on the one hand, a threshold based on the optical thickness KL, and on the other hand, one based on the intensity derivative in the cross direction. Using both methods, different parameters based on the spray contour are calculated and analysed against the injection and discharge pressures. First, the average spray contour is detected, and the spray angle is fitted. Then the standard deviation of the contour and the spray angle is computed, taking the averaged contour as a

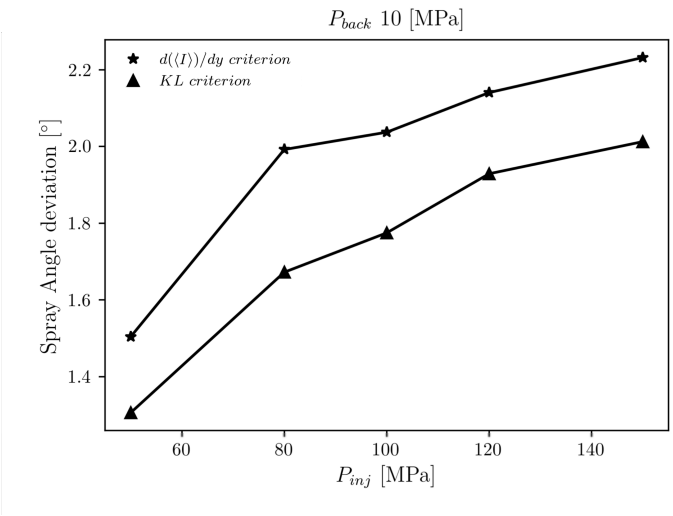

Figure 9.9: Mean spray angle as a function of injection pressure and discharge pressure. Each symbol corresponds to a different contour detection method.

reference. From all the obtained results, the following conclusions can be extracted:

- Although the intensity derivative methodology for the contour capturing is more sensitive and detect a noisier profile. Nevertheless, when averaging in time, the macroscopic spray aspects obtained are practically similar to the KL threshold method.
- The spray opening angle measured agrees with the expected trends, increasing with the discharge pressure due to the improvement of the gas-liquid mixture. However, the same trend (but lower in values) is observed with the injection pressure, specially at low discharge pressure.
- The obtained standard deviation is mainly related to the injection pressure, and therefore, the outflow turbulence. This effect is more critical at low discharge pressures, where the induced oscillations of the spray contour are induced by the turbulence and not by gas-liquid aerodynamic interaction. It should be noted that the near nozzle field presents higher perturbations at low injection pressures due to the non-development of the flow.

- The standard deviation of the spray angle increases with the injection pressure due to the induced-turbulence intensity. This effect is more important between 50 MPa and 80 MPa, having a higher increase among these values.

References

[1] Salvador, Francisco Javier, Carreres, Marcos, De la Morena, Joaquin, and Martínez-Miracle, E. "Computational assessment of temperature variations through calibrated orifices subjected to high pressure drops: Application to diesel injection nozzles". In: *Energy Conversion and Management* 171 (2018), pp. 438–451. DOI: 10.1016/j.enconman.2018.05.102.

[2] Caudwell, D. R., Trusler, J. P M, Vesovic, Velisa, and Wakeham, William A. "The viscosity and density of n-dodecane and n-octadecane at pressures up to 200 MPa and temperatures up to 473 K". In: *International Journal of Thermophysics* 25.5 (2004), pp. 1339–1352. DOI: 10.1007/s10765-004-5742-0.

[3] Berrocal, Edouard, Sedarsky, David L., Paciaroni, Megan E., Meglinski, Igor V., and Linne, Mark. "Laser light scattering in turbid media Part I: Experimental and simulated results for the spatial intensity distribution". In: *Optics Express* 15.17 (2007), p. 10649. DOI: 10.1364/oe.15.010649.

[4] Payri, Raul, Gimeno, Jaime, Cardona, Santiago, and Ayyapureddi, Sridhar. "Experimental study of the influence of the fuel and boundary conditions over the soot formation in multi-hole diesel injectors using high-speed color diffused back-illumination technique". In: *Applied Thermal Engineering* 158 (2019), p. 113746. DOI: 10.1016/J.APPLTHERMALENG.2019.113746.

[5] Spalding, D B. *Combustion and mass transfer*. Pergamon Press, 1979.

[6] Lichtarowicz, A K, Duggins, R K, and Markland, E. "Discharge coefficients for incompressible non-cavitating flow through long orifices". In: *Journal of Mechanical Engineering Science* 7.2 (1965), pp. 210–219. DOI: 10.1243/JMES_JOUR_1965_007_029_02.

[7] Desantes, Jose Maria, Lopez, Jose Javier, Carreres, Marcos, and López-Pintor, Darío. "Characterization and prediction of the discharge coefficient of non-cavitating diesel injection nozzles". In: *Fuel* 184 (2016), pp. 371–381. DOI: 10.1016/j.fuel.2016.07.026.

Chapter 10

Conclusions and Future Works

Although each result chapter has presented their own conclusion section, this section is thought as a final discussion with an overall frame to treat all the findings along an unifying thread to provide a more global conclusion of all the work presented on this document. Consequently, for more detailed conclusions the reader is referred to the individual conclusions at the end of each chapter. Additionally, this chapter presents future works that arise from the open questions that present this kind of studies.

10.1 Overall conclusions

As presented in the first chapter of this document, the main objective of this thesis is to analyse how the injection conditions affect the primary atomisation process. To conduct this task, two approaches have been selected. On the one hand, the computational standpoint has been founded on using Detailed Numerical Simulations to perform primary atomisation simulations using different inflow conditions. On the other hand, experimental efforts have been put into using Near-Field Microscopy to overcome the complex task of characterising the spray optically in the dense region. However, in the end, both approaches are incomparable, so the conclusions must be separated.

10.1.1 Considerations on the effects of the inflow conditions on the primary atomisation process using DNS

The DNS research is divided into three different studies depending on how the inflow boundary conditions are changed. The first one considers a change in the injection Reynolds number, the next one a variation in the Weber number, and finally, a modification of the nozzle geometry, using elliptical shapes. All those studies followed a similar analysis structure as the same outputs were sampled and post-processed. So, to provide a complete view of the conclusions reached along those studies, different aspects and parameters have been selected, and one by one, the conclusions of each study will be presented. Allowing an easy comparison between the effects provoked by each of the parameters.

The first results correspond not to the atomisation simulations but to the simulations carried out to generate the inflow boundary conditions. However, as they will play an essential role in the spray development is mandatory highlighting some details. Apart from validating the results from the LES performed on the internal flow, further efforts were put into analysing the vortex core distribution along the transversal plane. Here, increasing the Reynolds number ended in increasing the number of turbulent structures, especially the minor ones, and also shifting towards the wall. Regarding the elliptical ducts, increasing the eccentricity factor leads to a decrease in the Reynolds number. However, the apparition of secondary movements rearranged the vortex distribution, resulting in a transversal pattern where most of the vortexes were located at the top and bottom of the ducts, coinciding with the minor axis.

Moving to the DNS atomisation results, the analysis will be centred on the statistically stationary state. The first parameters to analyse are related to the overall spray morphology. One of the most common macroscopic parameters analysed when working with sprays is the external non-perturbed length. Here, the following conclusions are noticed:

- An important reduction is observed when increasing the Reynolds number, which is linked with the inflow vortex rearrangement. As the turbulence increases, so do the number of perturbations injected, and also, they are located nearer the liquid surface.
- Increasing the Weber number does not affect the inflow vortexes number, size, or distribution. Moreover, the decrease of the surface tension is not enough to provoke an earlier breakup of the core surface, leading to the same external non-perturbed length for all cases.

- The elliptical sprays present a characteristic behaviour caused by the distribution of the vortex structures on the elliptical nozzles. As the turbulent structures are mainly located near the minor axis, the perturbations on the liquid core surface are present in that region. Nevertheless, although near the major axis, the perturbations are lower, the higher curvature enhances the liquid breakup, leading to a similar external non-perturbed length in both planes. Additionally, droplets are detected at lower axial distances on the elliptical cases than on the round case, so the external non-perturbed length decrease in this kind of configuration.

Regarding the mean flow field, essential information can be extracted by simultaneously analysing the centreline distribution and spray aperture along the axial direction. First, the centreline values of mass concentration and liquid volume fraction are used to extract the breakup length by setting different thresholds. Depending on the inflow variations, the following observations are gathered:

- When increasing the Reynolds number, the breakup length increases regardless of the chosen threshold. Even though this behaviour is contrary to the one expected in the full atomisation regime, it is explained by the fact that the inflow axial velocity profile is not fully developed within the Reynolds number range sweep in the study. This translates into an increasing C_a with the Reynolds number, and, as the breakup length is proportional to this coefficient, the breakup length increases.

- The Weber number seems not to affect the breakup length as similar values are obtained for all cases. This is again linked to the fact that the decrease of the surface tension is not enough to influence the ligament breakup from the core at the lowest Reynolds number condition.

- Although the centreline statistics from the elliptical cases are not smoother enough to provide reliable quantified values of the breakup length, the results aim to decrease the breakup length on the elliptical sprays with respect to the round geometry.

The breakup length already hints at some particularities in the Reynolds number study, as it might be affecting the development of the inflow axial velocity profile on the spray evolution. So, analysing the velocity decay along

the centreline along with the spray aperture in the axial direction allows an understanding of how the velocity profile relaxation affects the spray momentum transfer:

- Considering the Reynolds number variation, the centreline axial velocity decay presents two different linear trends, a steeper one near the nozzle outlet followed by a lower slope. The change on the slope is related to the region where the liquid core starts breaking up, and the mixing on the centreline occurs. As already pointed out, as the Reynolds number increases, the nozzle outflow centreline velocity decreases, and so does the decay ratio along the axial direction in both regions. Regarding the spray apertures, the overall trend shows a decrease in the spray angle when increasing the Reynolds number. Nevertheless, it can be noticed that the spray starts opening earlier at a higher Reynolds number. This is related to the position of the injected vortex structures. Hence, as they increase in number and move towards the liquid surface, the momentum transfer starts earlier, providing the surrounding air with axial velocity. Then when the momentum transfer moves towards the spray centre, where the lower Reynolds condition presents higher velocities, a boost in the spray aperture takes place, increasing the spray aperture angle as the Reynolds number decreases.

- The axial velocity profile relaxation behaves the same regardless of the Weber number, as no differences are reported at the centreline axial velocity decay and the spray aperture, considering both $r_{1/2}$ and $r_{0.01}$ criteria.

- In the elliptical cases, the centreline axial velocity decay is similar to the round reference case near the nozzle but with a steeper slope from axial distances of 1.2 mm, suggesting a higher momentum transfer on the elliptical sprays. Two clear directions can be studied regarding the spray aperture, aligned with the major and minor axes. Here an interesting behaviour is noticed depending on using the $r_{1/2,m_c}$ or the $r_{0.01,m_c}$ criterion. If using the $r_{1/2,m_c}$ criterion, the elliptical cases show similar apertures on both axes with and spray aperture angle, which is higher than the round case. However, when using the $r_{0.01,m_c}$ criterion, this trend inverts, showing a considerable higher spray aperture angle on the round spray. Although this may seem non-intuitive, it agrees with the observations done in the morphological analysis. A considerable number of 'satellite droplets' can be found outside the dense spray cone in the

round spray case. In contrast, on the elliptical sprays, most droplets are within this spray cone, and fewer' satellite droplets' are found. This could be related to the fact that the transversal velocity field on the elliptical cases is fairly different from the round cases, as the secondary movements can trap the droplets within the spray core. If not, they would be advected far away from the spray axis. So those 'satellite droplets' are the ones that are providing the round spray case with a wider spray aperture.

The last analysis focused on the average flow field is performed on a plane located at $x/D_n \approx 25$, where the spray should exhibit a self-similar behaviour. Additionally, the Kolmogorov scale is computed to ensure the suitability of the chosen cell size. From this study, the following conclusions are obtained:

- Regarding the radial profile of the axial velocity, all Reynolds number conditions present a Gaussian behaviour when adjusting it with the $r_{1/2}$. However, when using $r_{0.01}$ as the radial reference, the Gaussian fit improves as the Reynolds number increases, having higher values on the lowest and medium Reynolds number cases, and a perfect agreement on the highest Reynolds number condition. This suggests that as the Reynolds number increases, the flow exhibits the self-similar behaviour earlier in the axial direction. As far as concerned to mass concentration, similar conclusions can be extracted. A good agreement is found in all cases when using $r_{1/2}$ as a reference, and a slightly poorer agreement is found using $r_{0.01}$. However, the medium Reynolds number level also presents a good agreement in this case. Finally, the Kolmogorov scale along the radial direction presents similar distribution for all cases. Being the minimum value located at $r_{1/2}$ and $\eta_{min}/d_x \approx 0.25$ in all cases leads to a negligible amount of energy left unresolved.

- When analysing the influence of the Weber number on the radial profile of the axial velocities, it can be observed that all cases exhibit a decreasing Sum-Squared Error (SSE) with the Reynolds number when compared to a Gaussian distribution, using $r_{1/2}$ as the reference radial value. Nevertheless, the SSE values increased when using $r_{0.01}$ as the reference, worsening the Gaussian fit in all cases, but as increasing the Weber number, the fit improves. Moving to the radial distribution of the mass concentration, Similar behaviour is reported, with higher SSE in all cases. Finally, the Kolmogorov scale distribution remains invariant when increasing the Weber number, locating the minimum value

at $r_{1/2}$ and only affecting radial positions higher than $2{\cdot}r_{1/2}$ where the values decrease with the Weber number. So, the plane analysis pointed out that the velocity, liquid and turbulent field are influenced by their average statistics at the periphery of the spray.

- As far as the elliptical cases are concerned, the plane analysis is centred on the velocity, liquid, and Kolmogorov scale along both major and minor axes and the transversal distribution by obtaining the contours to check their behaviour along the azimuthal direction. Regarding the axial velocity field, the round case presents an axi-symmetric velocity distribution along the azimuthal direction. However, the elliptical cases show an elliptical velocity field with lower eccentricity than the nozzle outlet. Analysing the radial velocity profile along the major and the minor axes, using $r_{1/2}$ as the radial reference value, it can be noticed that the elliptical cases do not show a proper Gaussian fitting. The same behaviour is observed when analysing the mass concentration field. Here, reasonably good agreement is reported in both axes for radial distances from the spray axis up to $r_{1/2}$. Beyond this point, the elliptical cases' mass concentration in both axes presents a sudden decrease. This is linked with the observations of the spray morphology, where the limits on the spray profile are sharper in the elliptical cases due to the lack of the 'satellite droplets'. Finally, all eccentricities exhibit a similar value of the minimum Kolmogorov scale, also located at $r_{1/2}$ on both axes.

Once all conclusions regarding the macroscopic features of the spray and the flow field analysis have been exposed, the spotlight is moved to the droplet cloud generated in each case and their characterisation. The first approach to the droplet cloud is made by counting the average droplets detected in each case, and their droplet size distribution:

- Increasing the Reynolds number increases the number of droplets generated significantly. Increasing the Reynolds number from 5,037 to 9,000 almost duplicates the number of droplets generated. Additionally, as the inflow turbulence increases, the droplet clouds tend to present a higher quantity of smaller droplets and a lower amount of bigger liquid structures. Additionally, the droplet size exhibits a Log-normal distribution, where the peak location shifts to smaller sizes as the Reynolds number increases. This leads to a denser and finer droplet cloud as increasing the Reynolds number.

- Similar trends are obtained when modifying the Weber number, as the number of detected droplets also increases. This time, the difference between the lowest and the highest Weber number cases is around 35%. Regarding the droplet size distribution, again, all cases present Log-normal distributions and an increase in the smaller droplets is observed at the expense of the bigger ones. However, in this case, the peak location remains at the same droplet diameter.

- When it comes to the elliptical study, an increase in the number of droplets detected within the domain is reported. However, no other differences are found between elliptical cases as they show an increase of 20% with respect to the round spray. Additionally, the droplet size distributions from the elliptical cases are almost identical, again showing an increase in the smaller droplets and a decrease in the bigger ones. This can be related to the fact that when increasing the eccentricity factor, the Reynolds number, and thus the inflow turbulence, decreases, diminishing the effects of having higher eccentric nozzles. This suggests that the injection velocity has to increase with the eccentricity factor to overcome this effect.

Apart from analysing the droplet size distribution, it is also important to study how those droplets are arranged within the domain. To do so, the radial (or transversal in the elliptical cases) and axial directions are chosen to check how the droplet characteristics change:

- When analysing the radial position distribution of all droplets, all Reynolds number conditions exhibit similar behaviour when referred to the $r_{1/2}$, presenting the majority of the droplets in a radial position slightly further from the mixing region. Furthermore, the peak of the radial distribution remains at the same radial distance regardless of the axial position, suggesting that the droplet cloud aperture is related to the $r_{1/2}$ angle. Following the axial direction analysis, as expected, the number of droplets increases as moving away from the nozzle outlet, and the distance where the droplets start appearing decreases. However, the most interesting behaviour is noticed in the droplet size distribution. Here, as the spray develops along the axial direction, the ratio between the small and big droplets decreases, dulling the peak of the distributions but maintaining the Log-normal shape.

- Increasing the Weber number moves the droplet cloud slightly to higher radial distances. The influence of the axial direction on the radial posi-

tion is similar to the one reported in the Reynolds analysis. The droplet cloud aperture follows the $r_{1/2}$ profile, whereas the peak moves to lower values of $r_{0.01}$ as moving away from the nozzle. Finally, the droplet size distributions turn to less sharp peaks as the spray develops in the axial direction.

- As expected after the flow field analysis, the elliptical cases also present elliptical transversal cloud distribution, showing droplets farther on the major axis than on the minor axis. Comparing the spray aperture in terms of droplets between the round and the ellipticals cases, similar values around the minor axis are obtained. However, higher apertures are reported near the major axis on the elliptical cases. Analysing the droplet distribution along the azimuthal direction, the round case presents an almost constant pattern, as expected, being axi-symmetric in that direction. Nevertheless, the elliptical cases present a higher probability of having droplets near the major axis than on the minor axis. This difference reduces when taking into account only the last region of the spray, meaning that the droplet cloud tends to present lower disequilibrium between axis directions, moving to a more axi-symmetric droplet cloud. The droplet size presents the same distribution regardless of the azimuthal position. Moving to the axial direction, earlier atomisation is observed in the elliptical cases. Furthermore, the droplet size presents the same trend along the axial direction reported in the previous studies.

Finally, all simulations find a peak near zero velocity when addressing the axial droplet velocities. When analysing where those droplets are located within the droplet cloud, they are near the spray periphery, where the axial velocity profile drops, so they are not advected back to the flow. Furthermore, the proportion of 'satellite droplets' decreases as increasing the Reynolds number, the Weber number and when using elliptical nozzles.

10.1.2 Considerations on the phenomenological model

One of the main objectives of this document is to propose a phenomenological model that can predict the droplet size distribution depending on the inflow boundary conditions. To do so, the results from the Reynolds and the Weber number studies are considered.

The Log-normal distribution is chosen to fit all the data, leading to the definition of a model based on $\hat{\mu}$ and $\hat{\sigma}$ parameters that change for each inflow condition. However, although the excellent agreement between the computed

droplet size distribution and the modelled Log-normal pattern at droplet sizes bigger than 5% of D_n, the resulting peak is sharper than the modelled one. This is caused by the simulation's cell size, which prevents generating droplets smaller than $2{\cdot}d_x$ easily. So, considering the observed trend of the droplet size distribution with the axial distance, where the peak value decreases at the expense of increasing the tail values, the model is also applied only to the droplets located in the last region of the domain.

Once all cases are characterised with their $\hat{\mu}$ and $\hat{\sigma}$ for both the whole domain and the last region, a quadratic regression is performed to provide the relation between those parameters and the inflow Reynolds and Weber number conditions. Testing the usability of the model, different distributions are plotted within the interpolation range to ensure that the model accurately shows a smooth transition between the simulated cases. Additionally, some extrapolation to higher Reynolds number conditions is performed. Here is noticed a change of trends on the peak location and value near the Reynolds condition where the internal flow would reach the fully-developed axial velocity profile.

10.1.3 Considerations on the near region spray angle variability using NFM

Although the experimental study and the computational study can not match the operating conditions (typical Spray A conditions are infeasible for computational studies, and the injector needle does not work at the low injection pressures from the computational study), many efforts were put into performing an experimental study in the same thread than the computational analysis. In this terms, as the computational studies put into the spotlight how the turbulent inflow field affects the spray development, the same approach is followed by analysing how the injection pressure, and therefore the inflow turbulence, affects the spray.

So using Near-Field Microscopy, the spray aperture is characterised for different injection and discharge pressures using two different criteria: on the one hand, setting a threshold on the optical thickness field, KL, and on the other hand, one based on the intensity derivative in the cross-section. This characterisation comprehends not only the temporal average spray opening angle but also its temporal variation, leading to the following conclusions:

- Both spray contour detection methodologies provide the same macroscopic results when averaging in time. However, the KL method detects a smoother contour.

- Regarding the average opening spray angle, the expected trends are spotted, regardless of the methodology. The angle increases with the discharge pressure as the air-liquid interaction enhances. Additionally, a similar trend, to a lesser extent, is also seen when increasing the injection pressure, especially at lower discharge pressures.

- The axial standard deviation of the spray contour increases with the injection pressure and is related to the injected frequencies and, thus, the nozzle outflow turbulence. This effect is more prominent at low discharge pressures as the aerodynamic gas-liquid interaction is lower, and the turbulent processes drive the spray contour oscillations. However, near the nozzle, the standard deviation is higher at lower injection pressures because of the non-development of the flow.

- Focusing on the spray angle deviation, an increase is noticed with the injection pressure, especially between 50 MPa and 80 MPa of injection pressure.

10.2 Future Works

10.2.1 Further analysis on the influences of non-dimensional numbers, using DNS with AMR

The Reynolds study and the inflow boundary conditions pointed out that the injected turbulent field is not fully developed within the simulated range. This lead to a characteristic behaviour as it can not be stated that the simulations are in the fully atomised regime. In this context, to assess that the simulations would behave as expected on the fully atomised regime, the Reynolds number inflow conditions should be increased above at least 12,000. Additionally, a minimum of two simulations of that regime would be necessary to check the trends. This implies increasing the simulation domain while decreasing notably the cell size, reaching computational costs almost infeasible.

In this context, software as the *Basilisk code* rises as a suitable tool to perform this study as it works with Adaptive Mesh Refinement, which reduces considerably the number of cells required to perform the computations. Hence, both the computational cost and storage size required substantially decrease. Nevertheless, using AMR implies new aspects that were straightforward with *PARIS*. The cartesian mesh used on *PARIS* makes post-processing routines easy to implement, and *Basilisk* uses an octree grid structure where the cell size varies spatially and temporally. Moreover, the adaptive algorithm requires

selecting field variables, such as the liquid volume fraction or velocity, and a certain threshold to decide whether the code refines the cell into 2^n cells, where n is the dimensions of the problem.

Additionally, the phenomenological model presented in this document is initially validated within the different conditions computed. That is, the Reynolds number model is valid for a constant Weber number and density ratio of 26,600 and 33, respectively. Similarly, the Weber number model is validated for a Reynolds number and density ratio of 5,037 and 33, respectively. Some simple extrapolations have been shown both for Reynolds and Weber number conditions to enlarge the applicability of the model. Even crossing influences between both models can provide information on new conditions. However, additional parameters such as the density ratio can not be extrapolated with the available data. So, improving and validating the phenomenological model further the current points requires carrying out an extensive matrix of simulations that, if performed in Cartesian meshes, can be unreachable.

10.2.2 Approaching the experimental and computational operating conditions

The previous section exposed the possibility of increasing the simulated Reynolds number, which, apart from allowing to reproduce an atomisation process in the Fully atomised regime, would be closer to the lowest injection pressure presented in the experimental analysis. Apart from increasing the computational Reynolds number, the injection Reynolds condition from the experimental standpoint can be also diminished by decreasing the injection pressure to match the same injection conditions. Nevertheless, as already mentioned in the document, commercial injectors limit the lower injection pressure, as they are designed to work at high injection pressures. Combined with the fact that the injector's nozzle length is not long enough to let the flow reach a fully developed turbulent profile, it may not be the best option to replicate the DNS simulations. One of the possibilities is using perforated plates with higher length to diameter ratios. However, this solution requires designing new hardware to precisely control the injection event.

Additionally, when achieving reproducing the same injection conditions in the computational and experimental studies, different optical techniques should be used, such as the X-ray or optical connectivity that can provide results than can be directly compared.

10.2.3 Analysis of aeronautical burners pressure-swirl atomisers using DNS

All the post-processing tools and analysing methodologies can be applied to different injector configurations. In this case, the pressure-swirl atomisers are gaining popularity as the increasing pollutant restrictions start affecting the aeronautical sector. Furthermore, this configuration has been chosen as the near-field region of the spray is notably less dense than the one from the round sprays. This allows obtaining reliable measured droplet information nearer than on the canonical round sprays, making easier the validation of the DNS simulations. So, in this context, the objective would be computing DNS simulations with AMR of pressure-swirl atomisers using inflow conditions obtained from LES simulations of the internal flow.

Global Bibliography

Battistoni, Michele et al. "Experimental and Computational Investigation of Subcritical Near-Nozzle Spray Structure and Primary Atomization in the Engine Combustion Network Spray D". In: *SAE Technical Paper* 2018-01-0277 (2018), pp. 1–15. DOI: 10.4271/2018-01-0277 (cited on pages 29, 30).

Beau, Pierre-Arnaud et al. "Numerical jet atomization: part II-modeling information and comparison with DNS results". In: *Fluids Engineering Division Summer Meeting*. Vol. 47500. 2006, pp. 555–563 (cited on page 13).

Bell, John B, Colella, Phillip, and Glaz, Harland M. "In this paper we develop a second-order projection method for the incom- pressible Navier-Stokes equations". In: *Journal of Computational Physics* 283 (1989), pp. 257–283 (cited on page 50).

Berrocal, E., Kristensson, E., Hottenbach, P., Aldén, M., and Grünefeld, G. "Quantitative imaging of a non-combusting diesel spray using structured laser illumination planar imaging". In: *Applied Physics B: Lasers and Optics* 109.4 (2012), pp. 683–694. DOI: 10.1007/s00340-012-5237-9 (cited on page 23).

Berrocal, Edouard, Kristensson, Elias, Richter, Mattias, Linne, Mark, and Aldén, Marcus. "Multiple scattering suppression in planar laser imaging of dense sprays by means of structured illumination". In: *Atomization and Sprays* 20.2 (2010), pp. 133–139. DOI: 10.1615/AtomizSpr.v20.i2.30 (cited on pages 22, 23).

Berrocal, Edouard, Sedarsky, David L., Paciaroni, Megan E., Meglinski, Igor V., and Linne, Mark. "Laser light scattering in turbid media Part I: Experimental and simulated results for the spatial intensity distribution". In: *Optics Express* 15.17 (2007), p. 10649. DOI: 10.1364/oe.15.010649 (cited on pages 18, 244).

Bharadwaj, N., Rutland, C. J., and Chang, S. "Large eddy simulation modelling of spray-induced turbulence effects". In: *International Journal of Engine Research* 10.2 (2009), pp. 97–119. DOI: 10.1243/14680874JER02309 (cited on page 10).

Brackbill, J.U U, Kothe, D.B B, and Zemach, C. "A continuum method for modeling surface tension". In: *Journal of Computational Physics* 100.2 (1992), pp. 335–354. DOI: 10.1016/0021-9991(92)90240-Y (cited on page 57).

Cai, Wenyi et al. "Quantitative analysis of highly transient fuel sprays by time-resolved x-radiography". In: *Applied Physics Letters* 83.2003 (2003), pp. 1671–1673. DOI: 10.1063/1.1604161 (cited on page 28).

Canu, Romain et al. "Where does the droplet size distribution come from?" In: *International Journal of Multiphase Flow* 107.January 2019 (2018), pp. 230–245. DOI: 10.1016/j.ijmultiphaseflow.2018.06.010 (cited on page 13).

Caudwell, D. R., Trusler, J. P M, Vesovic, Velisa, and Wakeham, William A. "The viscosity and density of n-dodecane and n-octadecane at pressures up to 200 MPa and temperatures up to 473 K". In: *International Journal of Thermophysics* 25.5 (2004), pp. 1339–1352. DOI: 10.1007/s10765-004-5742-0 (cited on page 243).

Celik, I., Klein, M., and Janicka, J. "Assessment measures for engineering LES applications". In: *Journal of Fluids Engineering, Transactions of the ASME* 131.3 (2009), pp. 0311021–03110210. DOI: 10.1115/1.3059703 (cited on page 70).

Charalampous, Georgios, Hadjiyiannis, C, Hardalupas, Yannis, and Taylor, A.M.K.P. "Measurement of continuous liquid jet length in atomizers with optical connectivity, electrical conductivity and high-speed photography techniques". In: *ILASS Europe 2010*. September. Brno, Czech Republic, 2010, pp. 1–10 (cited on pages 24, 25).

Charalampous, Georgios, Hardalupas, Yannis, and K. P. Taylor, A. M. "Novel Technique for Measurements of Continuous Liquid Jet Core in an Atomizer". In: *AIAA Journal* 47.11 (2009), pp. 2605–2615. DOI: 10.2514/1.40038 (cited on page 24).

Chehroudi, B and Talley, D. "The fractal geometry of round turbulent cryogenic Nitrogen jets at subcritical and supercritical pressures". In: *Atomization and Sprays* 14.1 (2004), pp. 81–91. DOI: 10.1615/AtomizSpr.v14.i1.50 (cited on page 180).

Chin, C., Ooi, A. S.H., Marusic, I., and Blackburn, H. M. "The influence of pipe length on turbulence statistics computed from direct numerical simulation data". In: *Physics of Fluids* 22.11 (2010). DOI: 10.1063/1.3489528 (cited on pages 66, 75).

Chorin, Alexandre Joel. "Numerical solution of the Navier-Stokes equations". In: *Mathematics of Computation* 22 (1968), pp. 745–762. DOI: 10.2307/2004575 (cited on page 47).

CORIA. *Archer code*. 2005 (cited on page 44).

Corrsin. *SPECTRA AND DIFFUSION IN A ROUND TURBULENT JET*. Tech. rep. 8. 1943, pp. 399–405 (cited on page 95).

Craske, John, Debugne, Antoine L R, and Van Reeuwijk, Maarten. "Shear-flow dispersion in turbulent jets". In: *Journal of Fluid Mechanics* 781 (2015), pp. 28–51. DOI: 10.1017/jfm.2015.417 (cited on page 95).

Crialesi-Esposito, Marco. "Analysis of primary atomization in sprays using Direct Numerical Simulation". PhD thesis. Universitat Politècnica de València, 2019 (cited on pages 16, 31, 44, 59, 87, 94, 95, 99, 102).

Crialesi-Esposito, Marco, Gonzalez-Montero, L. A., and Salvador, F. J. "Effects of isotropic and anisotropic turbulent structures over spray atomization in the near field". In: *International Journal of Multiphase Flow* 150.November 2021 (2022), p. 103891. DOI: 10.1016/j.ijmultiphaseflow.2021.103891 (cited on pages 16, 17, 95, 99, 101, 105, 147).

Crua, Cyril, Heikal, Morgan R, and Gold, Martin R. "Microscopic imaging of the initial stage of diesel spray formation". In: *Fuel* 157 (2015), pp. 140–150. DOI: 10.1016/j.fuel.2015.04.041 (cited on pages 19, 20).

Cummins, Sharen J, Francois, Marianne M, and Kothe, Douglas B. "Estimating curvature from volume fractions". In: *Computers & structures* 83.6-7 (2005), pp. 425–434 (cited on page 57).

DeBar, R. "Fundamentals of the KRAKEN code". In: *Technical Report UCIR-760* (1974) (cited on page 53).

Den Toonder, J. M.J. and Nieuwstadt, F. T.M. "Reynolds number effects in a turbulent pipe flow for low to moderate Re". In: *Physics of Fluids* 9.11 (1997), pp. 3398–3409. DOI: 10.1063/1.869451 (cited on pages 65, 74, 75).

Desantes, Jose Maria, Lopez, Jose Javier, Carreres, Marcos, and López-Pintor, Darío. "Characterization and prediction of the discharge coefficient of non-cavitating diesel injection nozzles". In: *Fuel* 184 (2016), pp. 371–381. DOI: 10.1016/j.fuel.2016.07.026 (cited on page 249).

Desantes, Jose Maria, Payri, Raul, Garcia-Oliver, Jose Maria, and Salvador, Francisco Javier. "A contribution to the understanding of isothermal diesel spray dynamics". In: *Fuel* 86.7-8 (2007), pp. 1093–1101. DOI: 10.1016/j.fuel.2006.10.011 (cited on pages 116, 117, 123).

Desantes, Jose Maria, Payri, Raul, Salvador, Francisco Javier, and Manin, Julien. "Influence on Diesel Injection Characteristics and Behavior Using Biodiesel Fuels". In: *SAE Technical Paper 2009-01-0851* (2009). DOI: 10.4271/2009-01-0851 (cited on page 123).

Desantes, Jose Maria, Salvador, Francisco Javier, Lopez, Jose Javier, and De la Morena, Joaquin. "Study of mass and momentum transfer in diesel sprays based on X-ray mass distribution measurements and on a theoretical derivation". In: *Experiments in Fluids* 50.2 (2011), pp. 233–246. DOI: 10.1007/s00348-010-0919-8 (cited on pages 116, 117, 123).

Desjardins, Olivier, Moureau, Vincent, and Pitsch, Heinz. "An accurate conservative level set/ghost fluid method for simulating turbulent atomization". In: *Journal of Computational Physics* (2008). DOI: 10.1016/j.jcp.2008.05.027 (cited on pages 13, 55).

Duran, S P, Porter, J M, and Parker, T E. "Ballistic Imaging of Sprays at Diesel Relevant Conditions". In: *ICLASS 2012*. 2012, pp. 1–5 (cited on page 22).

Duret, B, Reveillon, J, Menard, T, and Demoulin, François-Xavier. "Improving primary atomization modeling through DNS of two-phase flows". In: *International Journal of Multiphase Flow* 55 (2013), pp. 130–137. DOI: 10.1016/j.ijmultiphaseflow.2013.05.004 (cited on pages 11, 13).

ECN. *Engine Combustion Network*. Online. 2010 (cited on pages 16, 105, 147).

El Khoury, George K. et al. "Direct numerical simulation of turbulent pipe flow at moderately high reynolds numbers". In: *Flow, Turbulence and Combustion*. Vol. 91. 3. 2013, pp. 475–495. DOI: 10.1007/s10494-013-9482-8 (cited on pages 65, 66, 73–75).

Fedkiw, Ronald P., Aslam, Tariq, Merriman, Barry, and Osher, Stanley. "A Non-oscillatory Eulerian Approach to Interfaces in Multimaterial Flows (the Ghost Fluid Method)". In: *Journal of Computational Physics* 152.2 (1999), pp. 457–492. DOI: 10.1006/jcph.1999.6236 (cited on page 55).

Fuster, Daniel and Popinet, Stéphane. "An all-Mach method for the simulation of bubble dynamics problems in the presence of surface tension". In: *Journal of Computational Physics* 374 (2018), pp. 752–768. DOI: 10.1016/j.jcp.2018.07.055 (cited on page 43).

Fuster, Daniel et al. "Simulation of primary atomization with an octree adaptive mesh refinement and VOF method". In: *International Journal of Multiphase Flow* 35.6 (2009), pp. 550–565. DOI: 10.1016/j.ijmultiphaseflow.2009.02.014 (cited on pages 16, 44).

Gavtash, B. et al. "A model of transient internal flow and atomization of propellant/ethanol mixtures in pressurized metered dose inhalers (pMDI)". In: *Aerosol Science and Technology* 52.5 (2018), pp. 494–504. DOI: 10.1080/02786826.2018.1433814 (cited on page 2).

Gorokhovski, Mikhael and Herrmann, Marcus. "Modeling Primary Atomization". In: *Annual Review of Fluid Mechanics* 40.1 (2008), pp. 343–366. DOI: 10.1146/annurev.fluid.40.111406.102200 (cited on page 179).

El-Hannouny, Essam M. et al. "Near-Nozzle Spray Characteristics of Heavy-Duty Diesel Injectors". In: *SAE Technical Paper 2003-01-3150* 724 (2003) (cited on page 28).

Harlow, Francis H and Welch, J Eddie. "Numerical calculation of time-dependent viscous incompressible flow of fluid with free surface". In: *The physics of fluids* 8.12 (1965), pp. 2182–2189 (cited on page 49).

Hasslberger, Josef, Ketterl, Sebastian, Klein, Markus, and Chakraborty, Nilanjan. "Flow topologies in primary atomization of liquid jets: A direct numerical simulation analysis". In: *Journal of Fluid Mechanics* 859 (2019), pp. 819–838. DOI: 10.1017/jfm.2018.845 (cited on pages 16, 44).

Herrmann, Marcus. "A parallel Eulerian interface tracking/Lagrangian point particle multi-scale coupling procedure". In: *Journal of Computational Physics* 229.3 (2010), pp. 745–759. DOI: 10.1016/j.jcp.2009.10.009 (cited on page 98).

Herrmann, Marcus. "On Simulating Primary Atomization Using the Refined Level Set Grid Method". In: *Atomization and Sprays* 21.4 (2011), pp. 283–301. DOI: 10.1615/AtomizSpr.2011002760 (cited on pages 15, 98).

Herrmann, Marcus. "The influence of density ratio on the primary atomization of a turbulent liquid jet in crossflow". In: *Proceedings of the Combustion Institute* 33.2 (2011), pp. 2079–2088 (cited on pages 11, 98).

Hines, R. L. "Electrostatic Atomization and Spray Painting". In: *Journal of Applied Physics* 37 (1966), pp. 2730–2736 (cited on page 2).

Hirt, C.W W and Nichols, B.D D. "Volume of fluid (VOF) method for the dynamics of free boundaries". In: *Journal of Computational Physics* 39.1 (1981), pp. 201–225. DOI: 10.1016/0021-9991(81)90145-5 (cited on page 53).

Hussein, Hussein J., Capp, Steven P., and George, William K. "Velocity measurements in a high-Reynolds-number, momentum-conserving, axisymmetric, turbulent jet". In: *Journal of Fluid Mechanics* 258 (1994), pp. 31–75 (cited on pages 95, 123, 125).

Ilavsky, Jan and Jemian, Peter R. "Irena: Tool suite for modeling and analysis of small-angle scattering". In: *Journal of Applied Crystallography* 42.2 (2009), pp. 347–353. DOI: 10.1107/S0021889809002222 (cited on page 29).

Ilavsky, Jan et al. "Ultra-small-angle X-ray scattering at the Advanced Photon Source". In: *Journal of Applied Crystallography* 42.3 (2009), pp. 469–479. DOI: 10.1107/S0021889809008802 (cited on page 29).

Issa, R I. *Solution of the Implicitly Discretised Fluid Flow Equations by Operator-Splitting*. Tech. rep. 1985 (cited on page 67).

Jarrahbashi, D. and Sirignano, W. A. "Invited Article: Vorticity dynamics for transient high-pressure liquid injection". In: *Physics of Fluids* 26.10 (2014). DOI: 10.1063/1.4895781 (cited on page 12).

Jarrahbashi, D., Sirignano, W. A., Popov, P. P., and Hussain, F. "Early spray development at high gas density: hole, ligament and bridge formations". In: *Journal of Fluid Mechanics* 792 (2016), pp. 186–231. DOI: 10.1017/jfm.2016.71 (cited on page 12).

Jeong, Jinhee and Fazle, Hussain. *On the identification of a vortex*. Tech. rep. 1995, pp. 69–94 (cited on page 79).

Jiménez, Javier and Hoyas, Sergio. "Turbulent fluctuations above the buffer layer of wall-bounded flows". In: *Journal of Fluid Mechanics* 611 (2008), pp. 215–236. DOI: 10.1017/S0022112008002747 (cited on page 66).

Kaiser, Max, Heilig, Ansgar, and Dinkelacker, Friedrich. "Application of the Optical Connectivity Method to a Real Size Heavy Duty CIDI-Injector". In: *COMODIA 2012*. Comodia. 2012, pp. 506–511 (cited on page 25).

Kastengren, A. L. et al. "Time-resolved X-ray radiography of sprays from Engine Combustion Network spray a diesel injectors". In: *Atomization and Sprays* 24.3 (2014), pp. 251–272. DOI: 10.1615/AtomizSpr.2013008642 (cited on pages 28, 114).

Kastengren, Alan L and Powell, Christopher F. "Spray density measurements using X-ray radiography". In: *Proceedings of the Institution of Mechanical Engineers, Part D: Journal of Automobile Engineering* 221.6 (2007), pp. 653–662. DOI: 10.1243/09544070JAUTO392 (cited on page 28).

Kastengren, Alan L, Powell, Christopher F, Liu, Z., and Wang, J. "Time resolved, three-dimensional mass distribution of diesel sprays measured with x-ray radiography". In: *SAE Technical Paper 2009-01-0840* 4970 (2009), SAE Paper no. 2009–01–0840 (cited on pages 28, 114).

Kastengren, Alan L et al. "Measurements of droplet size in shear-driven atomization using ultra-small angle x-ray scattering". In: *International Journal of Multiphase Flow* 92 (2017), pp. 131–139. DOI: 10.1016/j.ijmultiphaseflow.2017.03.005 (cited on pages 29, 30).

Kastengren, Alan L. et al. "Determination of diesel spray axial velocity using X-ray radiography". In: *SAE Technical Papers* 2007.724 (2007). DOI: 10.4271/2007-01-0666 (cited on page 28).

Kim, J and Moin, P. "Application of a fractional-step method to incompressible Navier-Stokes equations". In: *Journal of Computational Physics* 59.2 (1985), pp. 308–323. DOI: 10.1016/0021-9991(85)90148-2 (cited on page 48).

Kim, K. C. and Adrian, R. J. "Very large-scale motion in the outer layer". In: *Physics of Fluids* 11.2 (1999), pp. 417–422. DOI: 10.1063/1.869889 (cited on page 66).

Klein, M. "Direct numerical simulation of a spatially developing water sheet at moderate Reynolds number". In: *International Journal of Heat and Fluid Flow* 26.5 (2005), pp. 722–731. DOI: 10.1016/j.ijheatfluidflow.2005.01.003 (cited on page 11).

Klein, M., Sadiki, A., and Janicka, J. "A digital filter based generation of inflow data for spatially developing direct numerical or large eddy simulations". In: *Journal of Computational Physics* 186.2 (2003), pp. 652–665. DOI: 10.1016/S0021-9991(03)00090-1 (cited on pages 13, 16).

Klewicki, J., Chin, C., Blackburn, H. M., Ooi, A., and Marusic, I. "Emergence of the four layer dynamical regime in turbulent pipe flow". In: *Physics of Fluids* 24.4 (2012). DOI: 10.1063/1.3702897 (cited on pages 66, 75).

Kolmogorov, A. "On the log-normal distribution of particles sizes during breakup process". In: *Dokl. Akad. Nauk.* XXXI.4 (1941), pp. 99–101 (cited on pages 93, 180).

Kristensson, E., Berrocal, E., Richter, M., Pettersson, S.-G., and Aldén, M. "High-speed structured planar laser illumination for contrast improvement of two-phase flow images". In: *Optics Letters* 33.23 (2008), p. 2752. DOI: 10.1364/ol.33.002752 (cited on page 23).

Kristensson, Elias, Berrocal, Edouard, and Aldén, Marcus. "Two-pulse structured illumination imaging". In: *Optics Letters* 39.9 (2014), p. 2584. DOI: 10.1364/ol.39.002584 (cited on page 22).

Lebas, R., Menard, T., Beau, P.A., Berlemont, A., and Demoulin, François-Xavier. "Numerical simulation of primary break-up and atomization: DNS and modelling study". In: *International Journal of Multiphase Flow* 35.3 (2009), pp. 247–260. DOI: 10.1016/j.ijmultiphaseflow.2008.11.005 (cited on pages 11, 13, 14).

Lefebvre, Arthur H and McDonell, Vincent G. *Atomization and Sprays*. 2nd Ed. Boca Raton, FL: CRC Press, 2017 (cited on pages 4, 6, 7).

Leonard, B.P. Brian P. "A stable and accurate convective modelling procedure based on quadratic upstream interpolation". In: *Computer methods in applied mechanics and engineering* 19.1 (1979), pp. 59–98. DOI: 10.1016/0045-7825(79)90034-3 (cited on page 49).

Levy, N., Amara, S., and Champoussin, J. C. "Simulation of a diesel jet assumed fully atomized at the nozzle exit". In: *SAE Technical Papers* 724 (1998). DOI: 10.4271/981067 (cited on page 10).

Li, Jie. "Calcul d'interface affine par morceaux". In: *Comptes rendus de l'Académie des sciences. Série II, Mécanique, physique, chimie, astronomie* 320.8 (1995), pp. 391–396 (cited on pages 54, 60).

Liang, Gangtao and Mudawar, Issam. "Review of spray cooling - Part 1: Single-phase and nucleate boiling regimes, and critical heat flux". In: *International Journal of Heat and Mass Transfer* 115 (2017), pp. 1174–1205. DOI: 10.1016/j.ijheatmasstransfer.2017.06.029 (cited on page 1).

Liang, Gangtao and Mudawar, Issam. "Review of spray cooling - Part 2: High temperature boiling regimes and quenching applications". In: *International Journal of Heat and Mass Transfer* 115 (2017), pp. 1206–1222. DOI: 10.1016/j.ijheatmasstransfer.2017.06.022 (cited on page 1).

Lichtarowicz, A K, Duggins, R K, and Markland, E. "Discharge coefficients for incompressible non-cavitating flow through long orifices". In: *Journal of Mechanical Engineering Science* 7.2 (1965), pp. 210–219. DOI: 10.1243/JMES_JOUR_1965_007_029_02 (cited on page 249).

Ling, Y et al. "A two-phase mixing layer between parallel gas and liquid streams: multiphase turbulence statistics and influence of interfacial instability". In: *Journal of Fluid Mechanics* 859 (2019), pp. 268–307. DOI: 10.1017/jfm.2018.825 (cited on page 97).

Ling, Y., Zaleski, Stéphane, and Scardovelli, Ruben. "Multiscale simulation of atomization with small droplets represented by a Lagrangian point-particle model". In: *International Journal of Multiphase Flow* 76 (2015), pp. 122–143. DOI: 10.1016/j.ijmultiphaseflow.2015.07.002 (cited on page 98).

Ling, Yue, Fuster, Daniel, Zaleski, Stéphane, and Tryggvason, Grétar. "Spray formation in a quasiplanar gas-liquid mixing layer at moderate density ratios: A numerical closeup". In: *Physical Review Fluids* 2.1 (2017), p. 014005. DOI: 10.1103/PhysRevFluids.2.014005 (cited on pages 97, 180).

Linne, Mark. "Imaging in the optically dense regions of a spray: A review of developing techniques". In: *Progress in Energy and Combustion Science* 39.5 (2013), pp. 403–440. DOI: 10.1016/j.pecs.2013.06.001 (cited on pages 2, 24–27).

Linne, Mark, Paciaroni, Megan E, Hall, Tyler, and Parker, Terry. "Ballistic imaging of the near field in a diesel spray". In: *Experiments in Fluids* 40.6 (2006), pp. 836–846. DOI: 10.1007/s00348-006-0122-0 (cited on page 21).

Linne, Mark, Sedarsky, David, Meyer, Terrence, Gord, James, and Carter, Campbell. "Ballistic imaging in the near-field of an effervescent spray". In: *Experiments in Fluids* 49.4 (2010), pp. 911–923. DOI: 10.1007/s00348-010-0883-3 (cited on pages 21, 22).

Linne, Mark et al. "Correlation of internal flow and spray breakup for a fuel injector used in ship engines". In: *8th US National Combustion Meeting 2013* 2 (2013), pp. 1–8 (cited on page 22).

Liu, Xu-Dong, Osher, Stanley, and Chan, Tony. "Weighted Essentially Non-oscillatory Schemes". In: *Journal of Computational Physics* 115.1 (1994), pp. 200–212. DOI: 10.1006/jcph.1994.1187 (cited on page 50).

Lozano, Antonio, García-Olivares, Antonio, and Dopazo, César. "The instability growth leading to a liquid sheet breakup". In: *Physics of Fluids* 10.9 (1998), pp. 2188–2197. DOI: 10.1063/1.869740 (cited on page 11).

Manin, Julien, Bardi, Michele, Pickett, Lyle M, Dahms, R N, and Oefelein, Joseph C. "Development and mixing of diesel sprays at the microscopic level from low to high temperature and pressure conditions". In: *THIESEL 2012 Conference on Thermo and Fluid-dynamic Processes in Diesel Engines*. 2012 (cited on page 19).

Manin, Julien, Pickett, Lyle M, and Yasutomi, K. "Transient cavitation in transparent diesel injectors". In: *ICLASS 14th Triennial International Conference on Liquid Atomization and Spray Systems*. Chicago, 2018, pp. 1–9 (cited on page 19).

Marusic, I. et al. "Wall-bounded turbulent flows at high Reynolds numbers: Recent advances and key issues". In: *Physics of Fluids* 22.6 (2010), pp. 1–24. DOI: 10.1063/1.3453711 (cited on page 65).

Mates, S. P. and Settles, G. S. "A study of liquid metal atomization using close-coupled nozzles, part2: atomization behavior". In: *Atomization and Sprays* 15 (2005), pp. 41–60 (cited on page 2).

Ménard, T, Tanguy, S, and Berlemont, A. "Coupling level set/VOF/ghost fluid methods: Validation and application to 3D simulation of the primary break-up of a liquid jet". In: *International Journal of Multiphase Flow* 33.5 (2007), pp. 510–524. DOI: 10.1016/j.ijmultiphaseflow.2006.11.001 (cited on pages 13, 14).

Meyer, Terrence R, Brear, Michael, Jin, Seong Ho, and Gord, James R. "Formation and diagnostics of sprays in combustion". In: *Handbook of Combustion: Online* (2010), pp. 291–322 (cited on page 21).

Milenkovic, Jovana, Alexopoulos, Aleck H., and Kiparissides, Costas. "Optimization of a DPI Inhaler: A Computational Approach". In: *Journal of Pharmaceutical Sciences* 106.3 (2017), pp. 850–858. DOI: 10.1016/j.xphs.2016.11.008 (cited on page 2).

Moin, Parviz and Mahesh, Krishnan. "DIRECT NUMERICAL SIMULATION: A Tool in Turbulence Research". In: *Annual Review of Fluid Mechanics* 30.1 (1998), pp. 539–578. DOI: 10.1146/annurev.fluid.30.1.539 (cited on page 43).

Moody, LF and Princeton, NJ. "Friction Factors for Pipe Flow". In: *Transactions of the ASME* 66.8 (1944), pp. 671–684 (cited on page 75).

Moon, S. et al. “Ultrafast X-ray Phase-Contrast Imaging of High-Speed Fuel Sprays from a Two-Hole Diesel Nozzle”. In: *22nd Annual Conference on Liquid Atomization and Spray Systems (ILASS Americas 2010)* May (2010) (cited on pages 26, 27).

Mukundan, Anirudh Asuri et al. “DNS and LES of primary atomization of turbulent liquid jet injection into a gaseous crossflow environment”. In: *Proceedings of the Combustion Institute* 38.2 (2021), pp. 3233–3241. DOI: 10.1016/j.proci.2020.08.004 (cited on page 11).

Nagib, Hassan M. and Chauhan, Kapil A. “Variations of von Kármán coefficient in canonical flows”. In: *Physics of Fluids*. Vol. 20. 10. American Institute of Physics Inc., 2008. DOI: 10.1063/1.3006423 (cited on page 74).

Narasimha, R and Lumley, J. “Whither turbulence? Turbulence at the crossroads”. In: *Lecture Notes in Physics, Proceedings of a workshop held at Cornell University, Ithaca New York, March*. 1989, pp. 22–24 (cited on page 43).

Nicoud, F. and Ducros, F. “Subgrid-Scale Stress Modelling Based on the Square of the Velocity Gradient Tensor”. In: *Flow, Turbulence and Combustion* 62.3 (1999), pp. 183–200. DOI: 10.1023/A:1009995426001 (cited on pages 67, 69).

Nikitin, Nikolay and Yakhot, Alexander. “Direct numerical simulation of turbulent flow in elliptical ducts”. In: *Journal of Fluid Mechanics* 532 (2005), pp. 141–164 (cited on pages 66, 76, 78).

Noh, W.F. and Woodward, P. *SLIC (simple line interface calculation). [Usable in 1, 2, or 3 space dimensions]*. Tech. rep. Livermore, CA: Lawrence Livermore National Laboratory (LLNL), 1976. DOI: 10.2172/7261651 (cited on page 53).

Ogrodnik, Nicholas, Azzi, Victor, Sprigge, Elizabeth, Fiset, Sandra, and Matida, Edgar. “Nonuniform deposition of pressurized metered-dose aerosol in spacer devices”. In: *Journal of Aerosol Medicine and Pulmonary Drug Delivery* 29.6 (2016), pp. 490–500. DOI: 10.1089/jamp.2015.1257 (cited on page 2).

OpenFOAM v3.0.0. 2015 (cited on page 66).

Örlü, R. et al. “Reynolds stress scaling in pipe flow turbulence - First results from CICLoPE”. In: *Philosophical Transactions of the Royal Society A: Mathematical, Physical and Engineering Sciences* 375.2089 (2017). DOI: 10.1098/rsta.2016.0187 (cited on pages 65, 66).

Pandal, Adrian. “Implementation and Development of an Eulerian Spray Model for CFD simulations of diesel Sprays”. PhD thesis. 2016 (cited on page 10).

Patil, Shirin and Sahu, Srikrishna. “Liquid jet core characterization in a model crossflow airblast atomizer”. In: *International Journal of Multiphase Flow* 141 (2021), p. 103688. DOI: 10.1016/j.ijmultiphaseflow.2021.103688 (cited on page 25).

Payri, Francisco, Bermúdez, Vicente, Payri, Raul, and Salvador, Francisco Javier. “The influence of cavitation on the internal flow and the spray characteristics in diesel injection nozzles”. In: *Fuel* 83.4-5 (2004), pp. 419–431. DOI: 10.1016/j.fuel.2003.09.010 (cited on page 7).

Payri, Raul, Gimeno, Jaime, Cardona, Santiago, and Ayyapureddi, Sridhar. “Experimental study of the influence of the fuel and boundary conditions over the soot formation in multi-hole diesel injectors using high-speed color diffused back-illumination technique”. In: *Applied Thermal Engineering* 158 (2019), p. 113746. DOI: 10.1016/J.APPLTHERMALENG.2019.113746 (cited on page 244).

Payri, Raul, Salvador, Francisco Javier, Gimeno, Jaime, and Crialesi-Esposito, Marco. “Comparison of mapped and synthetic inflow boundary conditions in Direct Numerical Simulation of sprays”. In: *ILASS - Europe 2019, 29th Conference on Liquid Atomization and Spray Systems*. Paris, France, 2019 (cited on pages 15, 16, 44, 99, 105, 147).

Pendar, Mohammad Reza and Páscoa, José Carlos. “Numerical modeling of the distribution of virus carrying saliva droplets during sneeze and cough”. In: *Physics of Fluids* 32.8 (2020). DOI: 10.1063/5.0018432 (cited on page 2).

Pickett, Lyle M., Manin, Julien, Kastengren, Alan L, and Powell, Christopher F. “Comparison of Near-Field Structure and Growth of a Diesel Spray Using Light-Based Optical Microscopy and X-Ray Radiography”. In: *SAE Technical Paper 2014-01-1412* 7.2 (2014), pp. 1044–1053. DOI: 10.4271/2014-01-1412 (cited on pages 19, 28).

Pilliod Jr, James Edward and Puckett, Elbridge Gerry. “Second-order accurate volume-of-fluid algorithms for tracking material interfaces”. In: *Journal of Computational Physics* 199.2 (2004), pp. 465–502 (cited on page 54).

Pope, Stephen B. *Turbulent flows*. IOP Publishing, 2001 (cited on pages 93, 94, 106, 123).

Popinet, Stéphane. "An accurate adaptive solver for surface-tension-driven interfacial flows". In: *J. Comput. Phys.* 228.16 (2009), pp. 5838–5866. DOI: 10.1016/j.jcp.2009.04.042 (cited on page 16).

Popinet, Stéphane. "An accurate adaptive solver for surface-tension-driven interfacial flows". In: *J. Comput. Phys.* 228.16 (2009), pp. 5838–5866. DOI: 10.1016/j.jcp.2009.04.042 (cited on pages 57, 58, 60).

Popinet, Stéphane. *Gerris code*. 2010 (cited on pages 44, 50).

Popinet, Stéphane. *Basilisk code*. 2014 (cited on pages 44, 50, 99).

Popinet, Stéphane. "Numerical Models of Surface Tension". In: *Annual Review of Fluid Mechanics* 50.1 (2017), pp. 49–75. DOI: 10.1146/annurev-fluid-122316-045034 (cited on page 56).

Rayleigh, Lord. "On The Instability Of Jets". In: *Proceedings of the London Mathematical Society* s1-10.1 (1878), pp. 4–13. DOI: 10.1112/plms/s1-10.1.4 (cited on page 4).

Reitz, Rolf D. and Bracco, Frediano V. "Mechanism of atomization of a liquid jet". In: *Physics of Fluids* 25.10 (1982), pp. 1730–1742. DOI: 10.1063/1.863650 (cited on pages 4, 6).

Reitz, Rolf D. and Diwakar, Ramachandr. "Structure of high-pressure fuel sprays". In: *SAE Paper 870598* (1987) (cited on page 10).

Renardy, Yuriko and Renardy, Michael. "PROST a parabolic reconstruction of surface tension for the volume-of-fluid method". In: *Journal of computational physics* 183.2 (2002), pp. 400–421 (cited on page 57).

Richardson, Lewis F. "Weather prediction by numerical process, second edition". In: *Weather Prediction by Numerical Process, Second Edition* (1922), pp. 1–236. DOI: 10.1017/CBO9780511618291 (cited on page 93).

Rudman, Murray. "Volume-tracking methods for interfacial flow calculations". In: *Int. J. Numer. Meth. Fluids* 24.7 (1997), pp. 671–691. DOI: 10.1002/(SICI)1097-0363(19970415)24:7<671::AID-FLD508>3.0.CO;2-9 (cited on page 54).

Ruzycki, Conor A., Javaheri, Emadeddin, and Finlay, Warren H. "The use of computational fluid dynamics in inhaler design". In: *Expert Opinion on Drug Delivery* 10.3 (2013), pp. 307–323. DOI: 10.1517/17425247.2013.753053 (cited on page 2).

Sagaut, Pierre. *Large eddy simulation for incompressible flows: an introduction*. Springer Science & Business Media, 2006 (cited on page 70).

Salvador, Francisco Javier, Carreres, Marcos, De la Morena, Joaquin, and Martínez-Miracle, E. "Computational assessment of temperature variations through calibrated orifices subjected to high pressure drops: Application to diesel injection nozzles". In: *Energy Conversion and Management* 171 (2018), pp. 438–451. DOI: 10.1016/j.enconman.2018.05.102 (cited on page 243).

Salvador, Francisco Javier, Ruiz, Santiago, Crialesi-Esposito, Marco, and Blanquer, Ignacio. "Analysis on the Effects of Turbulent Inflow Conditions on Spray Primary Atomization in the Near-Field by Direct Numerical Simulation". In: *International Journal of Multiphase Flow* 102 (2018), pp. 49–63. DOI: 10.1016/j.ijmultiphaseflow.2018.01.019 (cited on pages 14, 16).

Santos, F. dos and Moyne, L. le. "Spray atomization models in engine applications, from correlations to direct numerical simulations". In: *Oil and Gas Science and Technology* 66.5 (2011), pp. 801–822. DOI: 10.2516/ogst/2011116 (cited on page 10).

Sauer, B., Sadiki, A., and Janicka, J. "Embedded DNS concept for simulating the primary breakup of an airblast atomizer". In: *Atomization and Sprays* 26.3 (2016), pp. 187–217. DOI: 10.1615/AtomizSpr.2014011019 (cited on page 11).

Scardovelli, R and Zaleski, S. "Interface Reconstruction with Least-Square Fit and Split Lagrangian-Eulerian Advection". In: *Int J. Numer. Meth. Fluids* 41 (2003), pp. 251–274 (cited on page 54).

Sedarsky, David, Gord, James, Carter, Campbell, Meyer, Terrence, and Linne, Mark. "Fast-framing ballistic imaging of velocity in an aerated spray." In: *Optics letters* 34.18 (2009), pp. 2748–50. DOI: 10.1364/OL.34.002748 (cited on page 22).

Shinjo, J. and Umemura, Akira. "Simulation of liquid jet primary breakup: Dynamics of ligament and droplet formation". In: *International Journal of Multiphase Flow* 36.7 (2010), pp. 513–532. DOI: 10.1016/j.ijmultiphaseflow.2010.03.008 (cited on pages 12–15, 44, 97, 98).

Shinjo, J. and Umemura, Akira. "Surface instability and primary atomization characteristics of straight liquid jet sprays". In: *International Journal of Multiphase Flow* 37.10 (2011), pp. 1294–1304. DOI: 10.1016/j.ijmultiphaseflow.2011.08.002 (cited on page 14).

Shinjo, J., Xia, J., and Umemura, Akira. "Droplet/ligament modulation of local small-scale turbulence and scalar mixing in a dense fuel spray". In: *Proceedings of the Combustion Institute* 35.2 (2015), pp. 1595–1602. DOI: 10.1016/j.proci.2014.06.088 (cited on page 14).

Shu, Chi-Wang and Osher, Stanley. "Efficient implementation of essentially non-oscillatory shock-capturing schemes, II". In: *Journal of Computational Physics* 83.1 (1989), pp. 32–78. DOI: 10.1016/0021-9991(89)90222-2 (cited on page 50).

Silk, Eric A., Golliher, Eric L., and Paneer Selvam, R. "Spray cooling heat transfer: Technology overview and assessment of future challenges for micro-gravity application". In: *Energy Conversion and Management* 49.3 (2008), pp. 453–468. DOI: 10.1016/j.enconman.2007.07.046 (cited on page 1).

Sjöberg, Henrik, Manneberg, Göran, and Cronhjort, Andreas. "Long-working-distance microscope used for diesel injection spray imaging". In: *Optical Engineering* 35.12 (1996), p. 3591. DOI: 10.1117/1.601113 (cited on page 19).

Sotolongo-Costa, Oscar, Moreno-Vega, Yamir, Lloveras-González, Juan J., and Antoranz, J. C. "Criticality in Droplet Fragmentation". In: *Physical Review Letters* 76.1 (1996), pp. 42–45. DOI: 10.1103/PhysRevLett.76.42 (cited on page 180).

Spalart, P. R., Garbaruk, A., and Stabnikov, A. "On the skin friction due to turbulence in ducts of various shapes". In: *Journal of Fluid Mechanics* 838 (2018), pp. 369–378. DOI: 10.1017/jfm.2017.911 (cited on page 66).

Spalding, D B. *Combustion and mass transfer*. Pergamon Press, 1979 (cited on page 247).

Speziale, Charles G. "On turbulent secondary flows in pipes of noncircular cross-section". In: *International Journal of Engineering Science* 20.7 (1982), pp. 863–872. DOI: 10.1016/0020-7225(82)90008-8 (cited on page 66).

Stein, Stephen W., Sheth, Poonam, Hodson, P. David, and Myrdal, Paul B. "Advances in metered dose inhaler technology: Hardware development". In: *AAPS PharmSciTech* 15.2 (2014), pp. 326–338. DOI: 10.1208/s12249-013-0062-y (cited on page 2).

Subramaniam, S. "Statistical representation of a spray as a point process". In: *Physics of Fluids* 12.10 (2000), pp. 2413–2431. DOI: 10.1063/1.1288266 (cited on page 97).

Subramaniam, S. "Statistical modeling of sprays using the droplet distribution function". In: *Physics of Fluids* 13.3 (2001), pp. 624–642. DOI: 10.1063/1.1344893 (cited on page 97).

Sussman, Mark. "A second order coupled level set and volume-of-fluid method for computing growth and collapse of vapor bubbles". In: *Journal of Computational Physics* 187.1 (2003), pp. 110–136 (cited on page 57).

Sussman, Mark and Puckett, Elbridge Gerry. "A Coupled Level Set and Volume-of-Fluid Method for Computing 3D and Axisymmetric Incompressible Two-Phase Flows". In: *Journal of Computational Physics* (2000). DOI: 10.1006 (cited on page 55).

Sweby, Peter K. "High resolution schemes using flux limiters for hyperbolic conservation laws". In: *SIAM journal on numerical analysis* 21.5 (1984), pp. 995–1011 (cited on page 50).

Torregrosa, Antonio J, Payri, Raul, Salvador, Francisco Javier, and Crialesi-esposito, Marco. "Numerical evidences of universal energy cascade in multiphase flows". In: (2018) (cited on page 221).

Torregrosa, Antonio J., Payri, Raul, Javier Salvador, F., and Crialesi-Esposito, Marco. "Study of turbulence in atomizing liquid jets". In: *International Journal of Multiphase Flow* 129 (2020), p. 103328. DOI: 10.1016/j.ijmultiphaseflow.2020.103328 (cited on pages 16, 17, 95, 105, 106, 128, 147).

Torrey, Martin D, Cloutman, Lawrence D, Mjolsness, Raymond C, and Hirt, C W. "NASA-VOF2D: a computer program for incompressible flows with free surfaces". In: *NASA STI/Recon Technical Report N* 86 (1985), p. 30116 (cited on page 57).

Townsend, A. A. *The Structure of Turbulent Shear Flow*. 2nd. Cambridge University Press, 1976 (cited on page 65).

Trettel, Ben. "Conditional damped random surface velocity model of turbulent jet breakup". In: *Atomization and Sprays* 30.8 (2020), pp. 575–606. DOI: 10.1615/AtomizSpr.2020033172 (cited on pages 5, 6, 116).

Trettel, Ben. "Reevaluating the jet breakup regime diagram". In: *Atomization and Sprays* 30.7 (2020), pp. 517–556. DOI: 10.1615/ATOMIZSPR.2020033171 (cited on pages 5, 116).

Tryggvason, G. et al. "A Front-Tracking Method for the Computations of Multiphase Flow". In: *Journal of Computational Physics* 169.2 (2001), pp. 708–759. DOI: 10.1006/jcph.2001.6726 (cited on page 56).

Tryggvason, Grétar, Scardovelli, Ruben, and Zaleski, Stéphane. *Direct Numerical Simulations of Gas-Liquid Multiphase Flows*. 1st ed. Cambridge University Press, 2011 (cited on pages 45–47, 49–51, 54, 56, 58).

Umemura, Akira and Shinjo, Junji. "Detailed SGS atomization model and its implementation to two-phase flow LES". In: *Combustion and Flame* 195 (2018), pp. 232–252. DOI: 10.1016/j.combustflame.2018.01.026 (cited on page 14).

University of Stuttgart. *FS3D code*. 2010 (cited on page 44).

Unverdi, S O and Tryggvason, G. "A front-tracking method for viscous, incompressible, multi-fluid flows". In: *J. Comput. Phys.* 100 (1992), pp. 25–37 (cited on page 56).

Vallet, A., Burluka, A. A., and Borghi, Roland. "Development of a eulerian model for the "atomization" of a liquid jet". In: *Atomization and Sprays* 11.6 (2001), pp. 619–642. DOI: 10.1002/fld.1650080906 (cited on page 10).

Versteeg, H K and Malalasekera, W. *An introduction to computational fluid dynamics*. 2nd. Pearson Education Limited, 2007 (cited on pages 43, 51).

Voronova, T. V. and Nikitin, N. V. "Results of direct numerical simulation of turbulent flow in a pipe of elliptical cross-section". In: *Fluid Dynamics* 42.2 (2007), pp. 201–211. DOI: 10.1134/S0015462807020068 (cited on pages 66, 76, 78).

VTK (cited on page 100).

Wagner, C., Hüttl, T. J., and Friedrich, R. "Low-Reynolds-number effects derived from direct numerical simulations of turbulent pipe flow". In: *Computers and Fluids* 30.5 (2001), pp. 581–590. DOI: 10.1016/S0045-7930(01)00007-X (cited on pages 73, 113, 118).

Wan, Yuepeng and Peters, Norbert. "Scaling of spray penetration with evaporation". In: *Atomization and Sprays* 9.2 (1999), pp. 111–132. DOI: 10.1615/AtomizSpr.v9.i2.10 (cited on page 10).

Wang, Yujie et al. "Ultrafast X-ray study of dense-liquid-jet flow dynamics using structure-tracking velocimetry". In: *Nature Physics* 4.4 (2008), pp. 305–309. DOI: 10.1038/nphys840 (cited on pages 26, 27).

Warncke, K. et al. "Experimental and numerical investigation of the primary breakup of an airblasted liquid sheet". In: *International Journal of Multiphase Flow* 91 (2017), pp. 208–224. DOI: 10.1016/j.ijmultiphaseflow.2016.12.010 (cited on pages 11, 97–99).

Youngs, David L. "Time-dependent multi-material flow with large fluid distortion". In: *Numerical Methods for Fluid Dynamics* (1982) (cited on page 53).

Youngs, David L. "An interface tracking method for a 3D Eulerian hydrodynamics code". In: *Atomic Weapons Research Establishment (AWRE) Technical Report* 44.92 (1984), p. 35 (cited on page 54).

Yu, Shenghao et al. "Experimental study on the spray characteristics discharging from elliptical diesel nozzle at typical diesel engine conditions". In: *Fuel* 221.February (2018), pp. 28–34. DOI: 10.1016/j.fuel.2018.02.090 (cited on page 228).

Yu, Shenghao et al. "Numerical investigation on effects of elliptical diesel nozzle on primary spray characteristics by large eddy simulation (les)". In: *Atomization and Sprays* 28.8 (2018), pp. 695–712. DOI: 10.1615/AtomizSpr.2018026642 (cited on page 228).

Zaleski, S, Tryggvason, G, and Scardovelli, R. *ParisSimulator code*. 2013 (cited on pages 44, 59).

Zandian, A., Sirignano, W. A., and Hussain, F. "Planar liquid jet: Early deformation and atomization cascades". In: *Physics of Fluids* 29.6 (2017). DOI: 10.1063/1.4986790 (cited on page 12).

Zandian, A., Sirignano, W. A., and Hussain, F. "Understanding liquid-jet atomization cascades via vortex dynamics". In: *Journal of Fluid Mechanics* 843 (2018), pp. 293–354. DOI: 10.1017/jfm.2018.113 (cited on page 12).

Zandian, Arash, Sirignano, William A., and Hussain, Fazle. "Length-scale cascade and spread rate of atomizing planar liquid jets". In: *International Journal of Multiphase Flow* 113 (2019), pp. 117–141. DOI: 10.1016/j.ijmultiphaseflow.2019.01.004 (cited on page 12).

Zhang, Bo, Popinet, Stephane, and Ling, Yue. "Modeling and detailed numerical simulation of the primary breakup of a gasoline surrogate jet under non-evaporative operating conditions". In: *International Journal of Multiphase Flow* 130 (2020), p. 103362. DOI: 10.1016/j.ijmultiphaseflow.2020.103362 (cited on pages 16, 17, 44, 97, 99, 180).

Ziaee, Ahmad et al. "Spray drying of pharmaceuticals and biopharmaceuticals : Critical parameters and experimental process optimization approaches". In: *European Journal of Pharmaceutical Sciences* 127.November (2018), pp. 300–318. DOI: 10.1016/j.ejps.2018.10.026 (cited on page 2).